Analysis of circular bond-type anchorages for prestressing composite rods under quasi-static, fatigue and time-dependent loads.

Thesis by:

Francesc Puigvert Cobos

directed by:

Lluís Gil Espert

Thesis submitted for the degree of Doctor at the Universitat Politècnica de Catalunya

Tesi presentada per obtenir el títol de Doctor per la Universitat Politècnica de Catalunya

Terrassa, june 2014

Universitat Politècnica de Catalunya, BARCELONA**TECH**
Escola Tècnica Superior d'Enginyeries Industrial i Aeronàutica de Terrassa
Departament de Resistència de Materials i Estructures a l'Enginyeria
Laboratori per a la Innovació Tecnològica d'Estructures i Materials

Acknowledgements

Foremost, I would like to express my special appreciation and thanks to my supervisor Dr. Lluís Gil Espert for involving me in this project, for his continuous support of this investigation, for his enthusiasm, motivation and knowledge. His advice on both research as well as on my career have been priceless.

I am grateful to the Universitat Politècnica de Catalunya for the scholarship FPI-UPC which enabled me to undertake the PhD program. I would also like to thank the support from BASF Chemical Company for providing the material utilised in the experimental campaign which has made this work possible.

A special mention is addressed to the Faculty of Engineering and Physical Sciences of the University of Surrey, UK, for accepting me as a visiting student. My sincere thanks also goes to Professor Dr. Andrew Crocombe, for supervising my research during my stay at the University of Surrey. Without his guidance, constant feedback and expert knowledge this research would not have been achievable.

I would like to thank my department colleagues and research partners, Ernest Bernat, Christian Escrig, Marco Antonio Perez, Jordi Marcè, Catalin Andrei, Juan Jose Cruz, Sonia Segura and Vicenç Andreu for their expert contributions to this research.

I am truly thankful to Sigrid Söldner for her comments and improvements to my English writing and also her invaluable support towards the culmination of this research.

Finally, I would like to express my gratitude to my family and friends for their support which helped me to complete this work.

Francesc Puigvert Cobos

June 2014

Abstract

In prestressed structures subjected to corrosive environments, consideration is being given to replacing the steels tendons with non-corrosive tendons. In this respect, Fibre Reinforced Polymer (FRP) materials are a durable option in the design of prestressed concrete structures for use in corrosive environments due to their high mechanical properties, light weight and high resistance to corrosion. However, one of the challenges associated with this option lies in developing a suitable anchorage system for FRP tendons.

In the present work, the mechanical response of circular adhesively bonded anchorages for FRP tendons has been investigated under quasi-static, time-dependent and fatigue loading. This has been achieved through a combination of an experimental campaign and finite element modelling work.

Experimental quasi-static tests of adhesively bonded anchorages were undertaken with failure occurring in the adhesive-tendon interface. The main variables assessed were the adhesive thickness and the bonded length. In order to investigate the quasi-static response of the bonded anchorage and its failure mechanism, a campaign of numerical modelling was carried out with different material models of increasing complexity for the adhesive layer. A cohesive zone model with progressive damage in the bonded joint was found to be in reasonable agreement with the experimentally recorded data.

Additionally, an analytical formulation was developed (and validated against experimental data) with the aim to provide an approximate shear stress distribution in the bonded joint for circular anchors with adhesives which mainly behave linearly elastic up to failure.

The adhesively bonded anchor for FRP tendons was also investigated under the time-dependent phenomena. Creep tests on Single Lap Joints (SLJs) were conducted in order to obtain an experimental creep law whereas stress relaxation tests were conducted on adhesively bonded anchorages to study the load loss in time.

Furthermore, the restressing technique was assessed during the stress relaxation tests by restressing the specimens, to the original tensioning load, when the load loss was stabilised and constant. It was found that the restressing technique allows for the working load of the composite tendon to be reached with a minimum load loss.

A visco-plastic material model, based on the Bailey-Norton law, was calibrated with the experimental data obtained from the creep tests and utilised to predict the creep time to failure of SLJs and anchorages. The creep damage was modelled by degrading the plastic yield stress of the adhesive. The viscoelastic model

was also used to predict the load loss of the anchors under the stress relaxation phenomenon. The predicted load loss results were found to be in good agreement with the experimental results recorded.

Finally, the fatigue response of the bonded anchorages was investigated. Anchorages with four different adhesive thicknesses were evaluated under three constant amplitude fatigue loadings. The experimental fatigue response of adhesively bonded anchorages was discussed and an experimental load-life average curve was obtained for all the anchorages.

The fatigue behaviour was also predicted using Finite Element Analysis. A multi-linear traction-separation cohesive zone model was implemented at the adhesive-tendon interface. The cohesive law obtained in the quasi-static analysis was utilised in the fatigue model. The fatigue damage model utilised in this research was based on the degradation of the cohesive elements taking into account the fatigue damage evolution. The damage model was able to successfully predict the fatigue damage evolution and failure life experimentally observed.

From the experimental and numerical work conducted in this investigation, the most relevant recommendations are proposed for a potential use of adhesively bonded anchorages for CFRP tendons in prestressing applications.

Resum

En estructures pretesades sotmeses a ambients corrosius, s'està estudiant la possibilitat de substituir els tendons d'acer per tendons que no pateixin els efectes de la corrosió. En aquest sentit, els materials compostos *Fibre Reinforced Polymer* (FRP) són una opció duradora en el disseny d'estructures de formigó pretesat degut a les seves altes propietats mecàniques, pes lleuger i alta resistència a la corrosió. No obstant, un dels reptes associats amb aquesta opció es troba en el desenvolupament d'un sistema d'ancoratge adequat per als tendons de FRP .

Per això aquesta investigació ha estudiat la resposta mecànica d'ancoratges d'unió adhesiva per a tendons de FRP sota càrregues quasi-estàtiques, de fatiga i en funció del temps. Aquest objectiu s'ha aconseguit mitjançant la combinació d'una campanya experimental i un treball de modelatge amb el mètode dels elements finits.

En aquest sentit s'han dut a terme assaigs experimentals quasi-estàtics en els ancoratges d'unió adhesiva, observant que la ruptura del sistema es produïa en la unió adhesiva entre l'adhesiu i el tendó. En conseqüència, les principals variables estudiades van ser l'espessor de l'adhesiu i la longitud d'adhesió. A través d'una campanya de modelatge numèric amb diferents models, de complexitat creixent, del material adhesiu, es va investigar la resposta quasi-estàtica de l'ancoratge i el seu mecanisme de fallada. El model numèric va ser capaç de predir les dades enregistrades experimentalment quan el modelatge de l'adhesiu es va realitzar amb elements cohesius amb dany progressiu.

A més, s'ha desenvolupat una formulació analítica (i validat amb èxit) amb l'objectiu de proporcionar una distribució aproximada de les tensions de tall que es produeixen en la capa adhesiva per ancoratges amb adhesius que es comporten principalment elàstic lineal fins a ruptura.

D'altra banda l'ancoratge d'unió adhesiva també es va investigar sota els fenòmens dependents del temps. Per això es van dur a terme assaigs de fluència en unions simples *Single Lap Joints* (SLJs), per tal d'obtenir una llei experimental de fluència, i es van realitzar assaigs de relaxació de la tensió en els ancoratges per estudiar la pèrdua de càrrega en funció del temps. Durant aquests assaigs de relaxació es va estudiar la tècnica del retesat amb l'objectiu d'estudiar l'evolució de les pèrdues de tensió. Es va observar que la tècnica del retesat permet assolir càrregues de treball superiors amb una pèrdua de càrrega mínima.

A més a través d'un model visco-plàstic es va predir el temps de fallada a fluència de les SLJs i els ancoratges, basat en la llei de Bailey-Norton i calibrat amb les dades experimentals obtingudes en els assaigs de fluència de les SLJs. El dany de fluència es va modelar mitjançant la degradació de la tensió de fluència plàstica de l'adhesiu i el model numèric es va utilitzar per predir la pèrdua de càrrega dels ancoratges sota

el fenomen de relaxació de la tensió. Els resultats enregistrats experimentalment van ser predits adequadament amb el model numèric proposat.

Finalment, es va investigar la resposta a la fatiga dels ancoratges d'unió adhesiva. Es van avaluar quatre configuracions d'ancoratge sota tres càrregues de fatiga d'amplitud constant. Els resultats experimentals van permetre l'obtenció d'una corba de vida a fatiga dels ancoratges en funció del nombre de cicles.

Mitjançant el mètode d'elements finits, també es va investigar el comportament a fatiga. La llei cohesiva obtinguda en l'anàlisi quasi-estàtic es va utilitzar en el model de la fatiga, on el dany per fatiga s'ha basat en la degradació de les propietats dels elements cohesius. El model numèric va predir amb èxit l'evolució dany per fatiga i la vida per fatiga observada experimentalment .

A partir del treball experimental i numèric realitzat en aquesta recerca, es proposen les recomanacions més pertinents per a un possible ús dels ancoratges d'unió adhesiva per tendons FRP en aplicacions de pretensat.

Publications

1. **Puigvert F**, Crocombe AD, Gil L. Static analysis of adhesively bonded anchorages for CFRP tendons. Construction and Building Materials 2014; 61: p. 206-215. DOI: 10.1016/ j.conbuildmat.2014.02.072

2. **Puigvert F**, Crocombe AD, L.Gil. Fatigue and creep analyses of adhesively bonded anchorages for CFRP tendons. In Press, Accepted Manuscript for Publication in International Journal of Adhesion and Adhesives 2014. DOI: 10.1016/j.ijadhadh.2014.05.013.

3. **Puigvert F**, L.Gil, Escrig C, Bernat E. Stress relaxation analysis of adhesively bonded anchorages for CFRP tendons. In Press, Accepted Manuscript for Publication in Construction and Building Materials 2014. DOI: 10.1016/j.conbuildmat.2014.05.082.

4. **Puigvert F**. Chapter 8, Estructuras pretensadas con tendones de material compuesto. In: Pérez M.A., editor. Aplicaciones avanzadas de los materiales compuestos en la obra civil y la edificación, ISBN: 978-84-941872-9-2, Omnia Publisher; 2014, p. 183-204. DOI: 10.3926/oms.206.

5. **Puigvert F**, Crocombe AD, L.Gil. Assessing bond anchorage for CFRP in post-tensioned structures. Adhesion ’13 Twelfth International Triennial Conference on the Science and Technology of Adhesion and Adhesives, York, UK: 2013, p. 267-270.

6. **Puigvert F**, L.Gil. Anclaje químico para barras de fibra de carbono. Aproximación experimental. Primeiro Encontro Nacional de Materiais e Estruturas Compósitas, Porto, Portugal: 2010.

Table of Contents

List of Figures

List of Tables

Chapter 1. Introduction

1.1 Motivation

One of the primary causes of deterioration of prestressed concrete structures is the corrosion of the steel reinforcement. This is dependent on the environment, the protection of the reinforcement as well as the thickness of the concrete cover. In reality, the reinforcement suffers corrosion in aggressive environments which may weaken the mechanical properties of the material and thus the durability of the structure. Due to the high prestress of steel tendons (generally around 60% of the tensile strength), corrosion may be the cause of a brittle fracture of the tendons. Therefore, in large infrastructures such as bridges, maintenance campaigns exist which renew and repair the concrete cover and replace the steel tendons when this is possible.

In the last decades, researchers around the world have conducted studies in order to incorporate alternative materials for the traditional reinforcing in prestressed concrete structures. Fibre Reinforced Polymers (FRPs) were found to be some of the best candidates for non-metallic reinforcement for concrete structures. The use of FRP composite materials is particularly common in the aeronautical and naval sectors. The employment of these materials is currently being increased in civil engineering as they have high mechanical properties, are light in weight and, perhaps most importantly, have high resistance to corrosion. In some applications where corrosion protection for reinforcement becomes less cost efficient, using tendons of composite materials provides a reasonable alternative.

However, due to the high production costs of composites materials in comparison to conventional materials, the use of FRP reinforcement is intended for applications where the characteristics are unique to composites.

The results of research carried out so far indicate that FRP materials are a durable option in the design of prestressed concrete structures for use in corrosive environments. Moreover, because of their high mechanical properties, higher tensile strength can be reached and a better performance under fatigue loads and time-dependent behaviour can be achieved.

Although composite materials have highly suitable properties for use in prestressed structures, further research into their anchoring system is required. Due to the large anisotropy of FRP materials, the normal forces produced by traditional anchors may damage the composite tendon transversally. This implies that conventional anchoring systems for steel tendons are not entirely suitable, as they give rise to premature

failure in the rods. Adhesively bonded joints for composite tendons, however, are considered more efficient for composite materials as the stress distribution on the interface is more uniform. For this reason, adhesively bonded anchorages are being investigated in order to allow composite material tendons to be attached to the concrete structure. However, even though adhesively bonded joints have previously been studied, there remains a lack of research on their behaviour related to anchors for prestessing tendons.

1.2 Objectives

This research aims to investigate the mechanical response of circular adhesively bonded joints for composite materials as well as the development of a reliable predictive model capable of simulating their behaviour. In order to accomplish the main aim of this work, the following objectives were established:

1. To undertake a literature review concerning the anchoring systems for composite materials. This will provide the basic fundamentals of the prestressing method, which must be considered in the anchorage analysis, and the different alternatives to anchor FRP tendons. Experimental, analytical and numerical methods employed to investigate the anchorage will be also reviewed in order to initiate this investigation from the state of the art. Particular attention will be paid to the bond-type anchoring systems and bonded joints as these anchorage systems do not damage the composite tendon during prestressing, unlike other anchoring systems.
2. To study the mechanical anchorage for FRP tendons. The most relevant parameters, which affect the mechanical anchorage for composite materials, will be assessed with the aim to discuss and compare the results with the main conclusions considered in the literature review.
3. To develop an analytical formulation for straight bond-type anchorages. An analytical formulation based on the existent analytical solutions and adapted for straight bond-type anchorages will provide an approximate distribution of stresses of the bonded joint for anchorages. Knowledge of the adhesive stresses is particularly significant important as the failure of these anchorages is mainly caused by adhesion failure.
4. To study the mechanical response of straight bond-type anchorage under quasi-static loading. This analysis will determine the quasi-static strength of the anchorages depending on the geometric configuration, the behaviour of the whole up to failure as well as the failure mechanism itself.
5. To investigate the mechanical response of straight bond-type anchorage under time-dependent loading. Both creep and stress relaxation phenomena will be studied and discussed with the aim to describe the long-term effects on adhesively bonded anchorages depending on the magnitude of the applied stress and its duration.
6. To study the mechanical response of straight bond-type anchorage under constant amplitude fatigue loading. The analysis of the anchorage subjected to cyclic loading will focus on the fatigue lifespan

as well as the fatigue damage initiation and propagation in order to develop a consistent predictive model capable of simulating the anchorage under fatigue loading.

1.3 Research methodology

In order to achieve the objectives of this investigation, the scope of this project includes the following:

To experimentally study the mechanical anchorage for FRP tendons.

- Split-wedge mechanical anchorages were experimentally tested under quasi-static loading up to failure in order to study the failure mode of the tendon and the ultimate load achieved by the anchoring system. The effect of introducing a sleeve material, between the tendon and the wedges, and the effect of the clamping wedges were also assessed.

To develop an analytical formulation for straight bond-type anchorages.

- Double lap joints (DLJs) were considered for the quasi-static experimental investigation of the joint where laminated plates of Carbon Fibre Reinforced Polymer (CFRP) were used as a substrate for different adhesive systems. The specimens were instrumented with strain gauges bonded onto the outside of the laminated plates in order to analyse the shear stress distribution on the adhesive-laminate interface and compare the results with the existent analytical formulations.
- An analytical formulation was developed in order to provide an approximate distribution of shear stress in the bonded joint for circular anchors for adhesives with primarily elastic behaviour. The formulation was developed from the analytical solution that best matched the shear stress distribution on the adhesive-adherent interface in DLJs. The analytical formulation was validated against the experimental results of an anchor externally instrumented with strain gauges.

To study the mechanical response of straight bond-type anchorage under quasi-static loading.

- Adhesively circular bonded anchors for CFRP rods were tested under quasi-static loading and the behaviour of the anchorages was assessed experimentally. The parameters assessed include the bonded length and the adhesive thickness. In the quasi-static analysis, ten different adhesives were investigated.
- A finite element static model was developed for all the circular adhesive anchor geometries. Different adhesive material models of increasing complexity were investigated. Initially the adhesive was modelled with linear elastic properties. Following this, adhesive yielding was modelled using both von Mises plasticity and Drucker-Prager plasticity. Finally, progressive damage modelling with a cohesive zone was investigated where the elements followed a multi-linear traction-separation response.

To investigate the mechanical response of straight bond-type anchorage under time-dependent loading.

- Experimental creep tests on Single Lap Joints (SLJs) with different adhesive thicknesses were undertaken at different loads with failure occurring in the bond. The experimental creep tests provided a creep power law which was used to simulate the anchors under the same conditions.
- A finite element creep model was developed to predict the creep time to failure for SLJs. A visco-plastic model was implemented where the creep strains were used to degrade the adhesive plastic yield stress in order to include progressive damage leading to the creep local failure when a given strain was reached.
- Adhesively bonded anchors for CFRP tendons were investigated under the stress relaxation phenomenon. Four different adhesive thicknesses were assessed at three initial tensioning forces. The long-term behaviour of the anchorages was assessed experimentally. The behaviour after restressing, once the load loss was stabilised, was also studied.
- A finite element stress relaxation model was utilised to simulate the first load drop of stress relaxation and compared with the experimental data recorded where the creep power law provided by the experimental creep test on SLJs was used. Similarly to the creep model, visco-plastic and elastic-perfectly plastic von Mises response properties were assumed in the adhesive layer.

To study the mechanical response of straight bond-type anchorage under constant amplitude fatigue loading.

- Experimental fatigue tests on anchorages with four different adhesive thicknesses were conducted at different fatigue loading spectra with failure occurring in the bond line. The experimental fatigue data of the adhesively bonded CFRP tendon anchors were utilised to calibrate the predicted fatigue model.
- The fatigue response of the adhesively bonded CFRP tendon anchors was predicted using Finite Element analysis. A multi-linear traction-separation cohesive zone model was incorporated at the adhesive-rod interface. Also, a fatigue damage model based on the degradation of the cohesive elements was implemented to take into account the fatigue damage evolution.

1.4 Outline of the content

This investigation has mainly included experimental and numerical research. The experimental campaign has been conducted in a laboratory environment in the Laboratory for the Technological Innovation of Structures and Materials research group (LITEM) in the department of Strength of Materials and Structural Engineering of Terrassa (Barcelona) at the Polytechnic University of Catalonia (UPC). Moreover, the computer simulation has been carried out using the Finite Element Method (FEM) where the commercial

Abaqus/CAE v6.11 software has been utilised in all the modelling work. The structure of the thesis is summarised below:

Chapter 2 reviews the most relevant research concerning to the anchorage systems for prestressing composite materials. The fundamentals of the prestressing method are first described, followed by the description of the main anchorage systems studied for composite materials. Current knowledge on the anchorage systems under quasi-static, fatigue and time-dependent loading is assessed. Finally, a brief summary of prestressed concrete structures with FRP tendons is presented.

In Chapter 3, the manufacturing procedure of single lap joints, double lap joints and straight bond-type anchorages is presented. This includes the materials and geometries tested experimentally in this research. Also, the most significant manufacturing details are described.

Chapter 4 presents the quasi-static analysis of mechanical and bonded anchorages. A preliminary work was undertaken where the split-wedge anchorage was experimentally studied to determine the main parameters which influence the strength of the anchorage. Also, the shear stress distribution of adhesively bonded joints (DLJs) were assessed and compared with current analytical formulations. Moreover, the straight bond type anchorage was more extensively investigated through experimental tests and numerical modelling. First, an analytical approach was developed for straight bond-type anchorage from the data obtained in the preliminary work. This analytical formulation is proposed to determine the shear stress distribution on the adhesive-tendon interface when an adhesive which mainly behaves linear-elastic is used. Secondly, bond anchorages were experimentally tested using different adhesive systems. The adhesive thickness and the bonded length were assessed. Finally, the bonded anchorage was numerically modelled using different adhesive material models and compared with the experimental data available.

In Chapter 5, the investigation of time-dependent behaviour of the straight bond-type anchorage is presented. Single lap joints were experimentally tested in order to obtain a creep law to predict the creep time to failure of the adhesively bonded joints tested. The creep law was numerically implemented to predict the lifetime of straight bond-type anchorages where the yield stress of the adhesive layer was degraded with a subroutine to simulate the effect of creep damage. Also, straight bond-type anchorages were experimentally studied and numerically modelled under stress relaxation using the same parameters used in the creep model. Four anchorage geometries were evaluated under three different initial tensioning forces. In addition, the stress relaxation test setup is proposed for long-term tests for anchorages.

Chapter 6 presents the fatigue analysis of straight bond-type anchorage. The anchors were experimentally studied under three different fatigue loading spectra where four different geometric cases were assessed. Also, a fatigue damage model based on the degradation of a multi-linear traction-separation cohesive zone model was implemented to take into account the fatigue damage evolution and compared with the experimental results.

To conclude, Chapter 7 presents the main conclusions obtained of each chapter from this investigation and provides suggestions for the future research.

Chapter 2. State of the art

2.1 Introduction

The advantages of a unidirectional Fibre Reinforced Polymer (FRP) tendon system for prestressing concrete structures are well recognized where their high mechanical properties, light weight and high resistance to corrosion can provide an efficient design. However, the main concern lies in the anchoring system which attaches the tendons to the structure in order to achieve the highest efficiency of the composite material. Bonded and non-bonded anchorages have been studied over the last decades under different loading modes. Although these systems have been widely studied through experimental quasi-static work, additional research regarding the failure mechanism of the anchoring system and its numerical modelling using the finite element method is still required. Time-dependent behaviour and fatigue resistance also need to be investigated further.

The present chapter summarises the current state of the art regarding anchoring systems for FRP tendons. The chapter consist of two main parts. In the first part, the basic fundamentals of the prestressing method, anchoring systems for composite materials and the behaviour of the materials involved are outlined. The second part reviews the most recent experimental investigations in mechanical and bonded anchorages. The central focus of the present thesis lies in the bond-type anchorage, which is more extensively investigated under quasi-static, fatigue and time-dependent loading. Analytical and numerical methods employed to study the anchors are also reviewed.

2.2 Fundamentals of prestressing

Concrete is a material with a high compressive strength, but also with a low tensile strength. The tensile strength is usually 10 times lower than the compressive strength. Hence, concrete is generally reinforced with stronger materials in tension in order to enhance the strength of the structure. Steel bars are the most common material for strengthening concrete. This is known as ordinary reinforcement.

However, it is possible to achieve higher strength than it is practical with ordinary reinforced concrete by prestressing method. Prestressed concrete is a method for increasing concrete structures' strength in tension. It is mainly used in civil engineering to increase the span length in numerous applications such as beams, floors, bridges, underground structures and nuclear reactor vessels. The prestressed concrete method is based on the introduction of stresses (compressive stresses) to counteract those produced by the external loads and own weight, in order to reduce the final tensile stresses. Figure 2.1 shows the concrete section

stress distribution when prestressing a simple beam under bending moment. By means of external loads and its own weight, the structure's tensile limit may be reached far before its compressive limit. Prestressed tendons placed on the tensile area introduce compressive stresses that reduce the resultant tensile stress. This allows concrete structures to increase their strength.

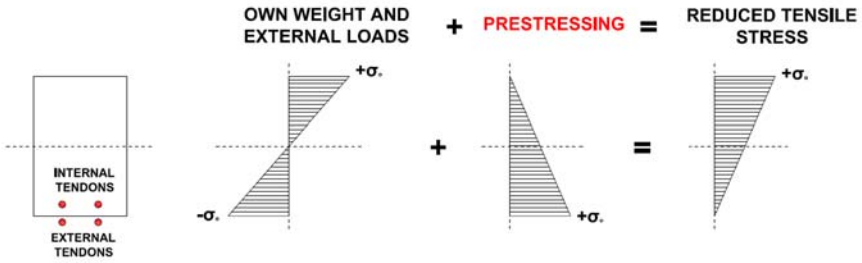

Figure 2.1. Concrete section stress distribution

Prestressing not only enhances concrete structure strength, but also has several other advantages. Increasing the strength also allows for greater span length. Furthermore, the effect of cracks in concrete elements is reduced when the structure is compressed. Prestressing allows for an efficient design by reducing the depth of beams and slabs. Consequently, the cost is reduced and the members are lighter. In addition, these advantages enable mass production in a laboratory environment and structures to be formed by a number of precast units.

Prestressing can principally be carried out in two ways: pre-tensioning concrete and post-tensioning concrete.

Pre-tensioning concrete refers to cables or rods that are tensioned prior to casting of the concrete (see Figure 2.2).

- Step 1. Cables or rods are tensioned and anchored in external supports (A and B).
- Step 2. The mould and the ordinary reinforcement is placed. Afterwards, the concrete is cast into the mould.
- Step 3. Once the placed concrete has developed enough compressive strength, the mould is removed and the structure is prepared to the load transfer of tendons from the external supports to the concrete structure itself.
- Step 4. The load is transferred to the concrete structure by releasing the cables or rods from the external support. Through the static friction between the cables or rods and the concrete, the structure is in a permanent state of prestress.

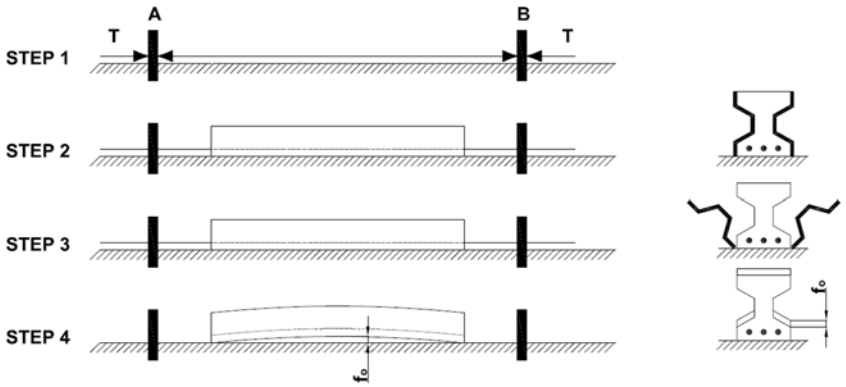

Figure 2.2. Pre-tensioning process.

Post-tensioning concrete refers to cables or rods that are tensioned at any given point in time after casting (see Figure 2.3).

- Step 1. The mould and the ordinary reinforcement is placed.
- Step 2. Ducts that will allocate tendons after casting are placed into the mould. Different paths can be assigned according to the areas with higher tensile stresses.
- Step 3. The concrete is cast into the mould.
- Step 4. The mould is removed when the cast concrete has developed enough compressive strength.
- Step 5. The tendons are passed through ducts and are tensioned. Eventually, the stressed tendons are locked with mechanical anchors at the ends of the structure and thus, the load is transferred to the structure.

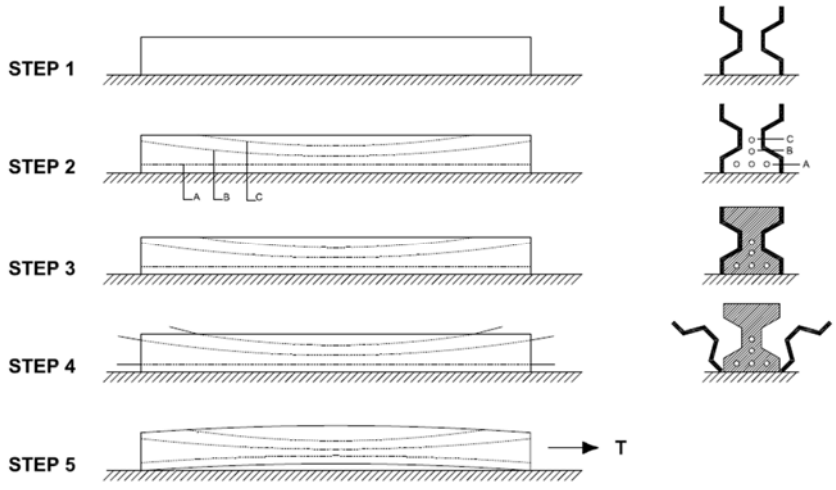

Figure 2.3. Post-tensioning process.

2.3 Anchorage systems

Either in the first step of pre-tensioning or in the last step of post-tensioning, tendons must be tensioned by anchors. Using composite materials for prestressing reinforcement introduces a notable concern related with their anchor because of the anisotropic nature of the composite materials. Unidirectional composite materials intended for prestressing concrete structures offer their highest mechanical strength in the direction of the fibre. Due to the low transverse mechanical properties of the FRP rods, the traditional mechanical anchorage for steel prestressing tendons cannot be used [1]. Furthermore, an anchoring system based on holes and bolts would introduce discontinuity in the fibres and generate a stress concentration which could damage the joint [2]. Also, Jones [3] indicated that the non-uniform stress distribution around the hole may cause unexpected cracks, eventually leading to the premature failure of the joint. For this reason, two main anchor systems for composite materials are generally considered: mechanical anchors and adhesively bonded anchors (see Figure 2.4).

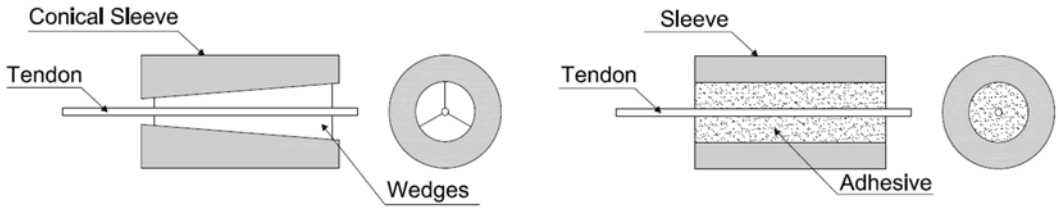

Figure 2.4. General scheme of a mechanical anchor (left) and an adhesively bonded anchor (right).

2.3.1 Tendon properties

The most suitable composite materials for prestressing applications are principally Carbon Fibre Reinforced Polymers (CFRP), Glass Fibre Reinforced Polymers (GFRP) and Aramid Fibre Reinforced Polymers (AFRP). As mentioned earlier, the high mechanical properties, light weight and high resistance to corrosion of FRP tendons can provide an efficient design for prestressed structures in aggressive environments. However, the stress-strain response of these materials can vary significantly depending on the fibre material, the matrix and the fibre/matrix fraction. As it can be seen in Figure 2.5, CFRP has normally superior properties and high strength compared to GFRP and AFRP. Also, the elastic moduli of GFRP and AFRP tendons are three times lower than steel tendons while CFRP tendons have a similar modulus to steel tendons. Nevertheless, unlike steel tendons, FRP tendons have a linear elastic response until sudden and explosive failure whereas the yield of steels tendons provides ductility in the structure at its ultimate limit state.

Whilst fibres provide a high tensile strength to the composite material, the matrix of the composite material primarily aims to bind the fibres together in a unique solid, protect the fibres from potentially damaging

environments and transfer the forces amongst the fibres. The most usual polymeric matrices for FRP tendons are polyester, vinyl ester and epoxy.

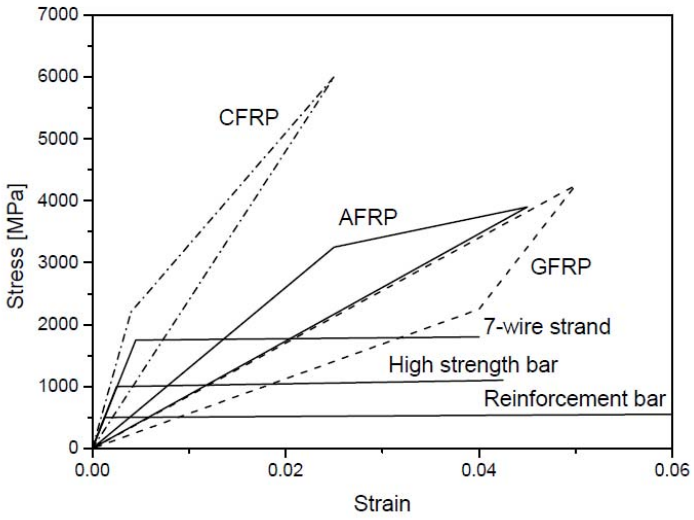

Figure 2.5. Stress-strain curves of composite tendon systems and steel varieties [4].

Even though the mechanical properties of composite materials also depend on the fibre orientation, for prestressing applications the fibres are generally provided throughout the longitudinal direction of the bar or rod. A pultrusion process is the most widely used technique to manufacture FRP tendons, which allows for the manufacturing of a continuous material with a constant cross-section, usually circular.

Another important factor is the fibre/matrix fraction. Generally, the more fibre used, the better strength tensile properties of the tendon will be achieved. However, the maximum percent of fibre mainly depends on the manufacturing process. Usually a fibre percent greater than 70% by volume is not recommended for pultruded products such as rods and bars. The typical amount of fibre for prestressing tendons is 35% by volume.

According to the American Concrete Institute (ACI) [5], CFRP can develop the same mechanical properties as steel tendons when used to prestress concrete structures with a similar stiffness. For this reason, CFRP are normally suggested for prestressed applications.

2.3.2 Mechanical anchors

2.3.2.1 Mechanical anchorage systems

Mechanical anchors for FRP tendons are based on the current mechanical anchors for steel prestressing rods. However, several modifications have been introduced during the last decades in order to achieve greater efficiency for composite materials. The mechanical anchorage generally consists of a barrel housing or steel plates system which grips the tendon through a transverse force. As the weakest mechanical

properties of the composite materials lie upon the transverse direction, the tendon-anchor interface has been extensively studied and modified. One of the most accepted adaptations is the modification of the contact surface roughness of the anchorage. Current anchoring systems have hardened teeth to increase the load transfer. In systems with composite materials, these teeth must be removed due to the damage they would cause in the FRP tendon. The two most widely used systems are described as follows:

- *Clamp anchorage*. This system consists of two steel plates sandwiching the composite material. Through mechanical joints, normally bolts, the steel plates are fixed together. The load is transferred by a shear-friction mechanism. This system allows for the prestressing of tendons with a circular or rectangular section. If local damage occurs in the tendon before reaching its optimal workload, a sleeve material with a lower elastic modulus can be introduced between the composite rod and plates. As indicated by Malvar and Bish [6], this intermediary material distributes the stresses smoother avoiding stress concentrators.
- *Split-wedge anchorage*. Because of their similarity with the current systems for steel, compactness, ease of assembly, reuse and reliability, these anchors are generally more used to date. They commonly consist of a barrel housing which uses several wedges to grip the tendon. The clamping mechanism is based on the friction generated between the inner wedges and FRP tendon during tensioning. The conical shape of the barrel and wedges must develop enough friction to transfer the load properly from the tendon to the anchor. However, as mentioned by Schmidt et al. [1], these wedges generate a high radial pressure and tend to dig into the surface of the tendon causing a premature failure in the anchorage zone. To avoid these effects, the length of the anchor is generally increased to reduce the transverse stress of the tendon. Also, a sleeve material, usually copper, can be placed between the wedges and the tendon in order to smoothen the stress distribution.

2.3.2.2 Failure modes of mechanical anchorage systems

According to ACI code 440.4R-04 [7], there are generally two failure modes when using mechanical anchorages for prestressing FRP tendons; failure of the anchorage system and failure of the tendon.

- *Failure of the anchorage system*. This is the most common kind of failure and the most observed failure modes are described as follows:
  - *Slip of the tendon*. When there is an insufficient grip of the wedges/plates and the friction generated is not able to keep the longitudinal force balance.
  - *Slip of the sleeve and tendon together relative to the wedges/plates*. Slip of the sleeve and tendon together caused by an insufficient shear force between the sleeve and the wedges/plates.
  - *Rupture of the rod inside the anchorage*. Because of either the tapered shape of the barrel and wedges or the transverse force generated by the plates, a high stress is generated at the loading

end of the anchor. This stress concentration may cause the premature failure of the composite material due to its high transverse stress component.

- *Failure of the tendon.* It is considered that the tendon reaches its maximum tensile strength when the rupture is located within its free length (beyond three diameters of the tendon from the loading end of the anchorage). In this particular case, the anchorage does not contribute to the failure of the tendon and enables the reaching of the maximum capacity of the composite material.

2.3.2.3 Quasi-static response of mechanical anchorage systems

Nanni et al. [8] studied the behaviour of the split-wedge anchorage for composite bars. Several pull-out tests were conducted on rods and laminates. Also, different wedge materials were assessed. It was found that a higher value of load can be reached when a material with a lower elastic modulus was introduced into the interface between the composite rod and the wedges as indicated earlier. In this case, the local damage was produced in this material instead of the FRP tendon. In addition, it was observed that premature failures were mainly caused by the continuous slip between the tendon and wedges during testing when semi cylindrical tapered wedges made of polyamide PA6 were used and by the high radial stress generated at the loading end of the anchor. However, anchorages with steel wedges and intermediary sleeve exceeded 95% of the ultimate tensile strength of the rods reported by the manufacturers.

As mentioned by Nanni et al. [8], transverse forces acting on the tendon may collapse the matrix of the composite rod. Determining this component is essential for the design of a split-wedge anchorage that allows the developing of the full tensile strength of the tendon. In their study, Taha et al. [9] determined the forces interacting among the components involved in the split-wedge anchorage (see Figure 2.6).

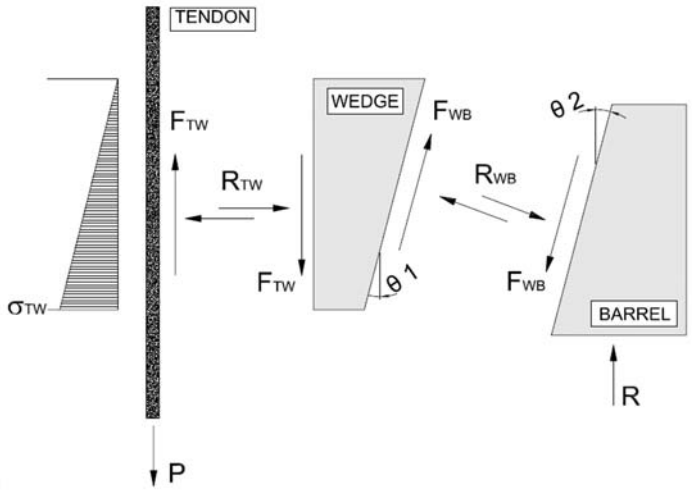

9

Figure 2.6. Static model for a preliminary design of type-wedge anchorages.

According to this model, to ensure static equilibrium the loading force of the tendon, P, must be equal to the static friction generated between the tendon and the wedges, F_{TW} (see Equation 2.1).

$$P = F_{TW} \qquad \text{(Equation 2.1)}$$

Also, the static friction force can be expressed through the normal force between the tendon and the wedges, R_{TW} (see Equation 2.2)

$$F_{TW} = \mu_{TW} \cdot R_{TW} \qquad \text{(Equation 2.2)}$$

in which μ_{TW} is the static coefficient of friction between the tendon and the wedges. In the same way, the equation of friction between the wedges and the barrel can be obtained through Equation 2.3.

$$F_{WB} = \mu_{WB} \cdot R_{WB} \qquad \text{(Equation 2.3)}$$

where F_{WB} is the static friction force between the wedges and the barrel, R_{WB} is the normal force and μ_{WB} is the static coefficient of friction. Moreover, the action P and reaction R can be obtained by a longitudinal force balance on the wedges (see Equation 2.4).

$$F_{TW} = P = R = F_{WB} \cdot \cos\theta_2 + R_{WB} \cdot \sin\theta_2 \qquad \text{(Equation 2.4)}$$

Considering a linear radial stress distribution exerted on the wedge-tendon surface, from zero at the end of the anchor to a maximum value at the loading end, the maximum radial stress, σ_{TW}, is expressed in Equation 2.5.

$$\sigma_{TW} = 2 \cdot \frac{R_{TW}}{2 \cdot \pi \cdot r_t \cdot L_W} = \frac{R_{TW}}{\pi \cdot r_t \cdot L_W} \qquad \text{(Equation 2.5)}$$

where r_t is the FRP tendon radius and L_W is the length of the wedge. Therefore, the matrix of the composite material must be capable of resisting the maximum radial stress shown in Expression 2.5.

A new steel split-wedge anchorage system for post-tensioning applications using CFRP was presented by Sayed-Ahmed et al. [10,11] which introduced two new concepts in order to decrease the high stress concentration that occurs near the leading edge of the tendon (see Figure 2.7). First, a small differential slope between the barrel and the wedges was introduced (difference of 0.1º). This allowed for the distributing of the stresses on the prestressing tendon more evenly over the length of the anchorage, avoiding the high stress concentration at the loading end of the anchor that occurs when all the components have the same angle. The second concept was the rounding of the sharp inner edges of the wedges. This enables a smoother stress distribution at the end of the anchor.

Pincheira and Woyak [12] presented a similar anchor based on the metal split-wedge system with a sleeve as described above, that instead employed a cold swaged sleeve to prevent the slip of the rod when prestressing. The process consisted of the reduction of the tendon diameter through the use of a mandrel to

permanently attach the sleeve to the rod. The system allowed the maximum tensile strength of the rod to be developed when a minimum swaging length of 14 rod diameters was used.

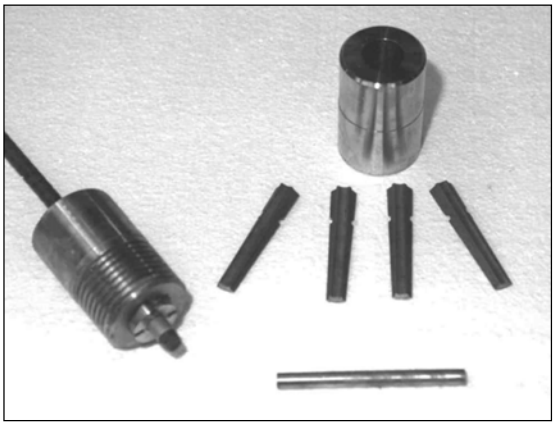

Figure 2.7. Steel split-wedge anchorage system for post-tensioning FRP tendons [10].

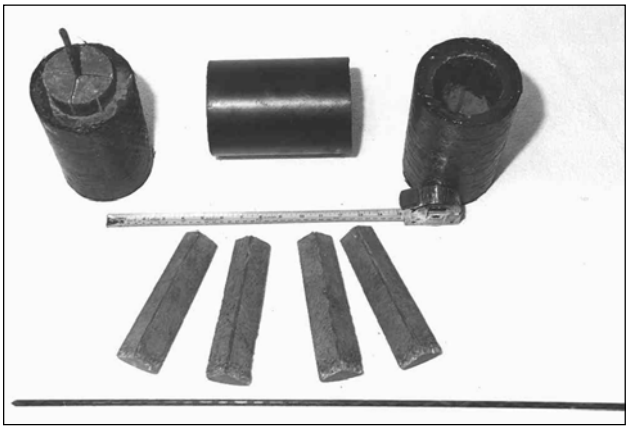

Figure 2.8. A non-metallic wedge-type anchor for fibre reinforced polymer tendons [13].

Later, in 2000, Campbell et al. [13] investigated a solution for the galvanic reaction that potentially may occur between the components of the anchorage. A non-metallic wedge-type anchor for fibre reinforced polymer tendons made with ultra-high performance concrete (UHPC) was developed (see Figure 2.8). The authors concluded that size reductions and a better manufacturing process were required. However, this anchor was shown to be a potential completely metal-free (corrosion-free) post-tensioning system. It is worth noticing that no sleeve was used with this anchorage, and thus the UHPC wedges gripped the tendon directly.

The split-wedge anchorage for FRP tendons made with ultra-high performance concrete (UHPC) was also studied by Taha and Shrive [9,14]. A concrete with compressive strength in excess of 200MPa was developed specifically for this anchorage. Different parameters of the anchor were modified including the anchor geometry, a number of composite layers needed for wrapping the barrel and the anchor seating load. The non-metallic anchor showed suitable mechanical performance by assessing the anchor in quasi-static and fatigue conditions.

Figure 2.9. Unibody clamp anchorage for prestressing CFRP rods [15].

Although the main studies focus on the split-wedge anchorage because of its similarity with the current systems for prestressing steel tendons, the clamp anchorage system was also investigated. A unibody clamp anchorage for prestressing CFRP rods was recently investigated by Burningham [15]. Different models of the anchor were assessed experimentally and numerically. The author concluded that the unibody clamp anchors proposed could be used for pre-tensioning or post-tensioning CFRP rods (see Figure 2.9).

Recently, the work of Schmidt et al. [4] collected the latest developments concerning mechanical anchors for composite materials. The researchers studied different configurations of the components mentioned previously. Also, anchorages were assessed through the finite element method consistent with the experimental load-displacement data. The study concluded that the current mechanical anchor for FRP tendons does not allow the maximum strength of the tendons to be developed.

2.3.3 Adhesively bonded anchors

2.3.3.1 Bond-type anchorage systems

Bond-type anchorages have been widely studied with the aim to replace mechanical anchorages for prestressing composite materials. An adhesive bond-type anchorage consists of a metallic housing inside which single or multiple rods are bonded with a resin or cement. The performance of a bond-type anchorage depends mainly on the geometry of the steel housing and bond length of the tendon, and the mechanical properties of the components involved. In contrast to mechanical anchorages, bond-type adhesive anchors must be manufactured prior to prestressing. This allows for the developing of anchors in a controlled laboratory environment with the possibility of obtaining a high execution quality as well as a mass production process. However, unlike mechanical anchorages, adhesively bonded anchors require an adhesive curing time before the anchor reaches its maximum strength. There are three types of bond-type anchorage between which the main difference lies on either the inner shape of the metallic housing or the adhesive stiffness.

- *Straight bond-type anchorage*. The metallic housing is tubular and therefore the housing inner surface remains parallel to the tendon surface throughout the bonded length. The load-transfer mechanism depends mostly on the adhesive bond between the anchorage components.
- *Tapered bond-type anchorage*. The metallic housing provides a varied profile of the inner surface, which is usually linear or parabolic. In this case, the load-transfer mechanism depends on the adhesive bond and the radial stress produced by the variation of the adhesive material section. The high radial compression generates a better bond stress distribution over the bonded length and improves the anchorage performance. Nevertheless, manufacturing tapered housings is costly and a larger cross-section of the housing is needed to make the internal geometry.

- *Mixed adhesive anchorage*. Using diverse adhesives with different elasticity moduli along the bonded length can optimize the stress distribution. With this technique, a reduction of the highest peaks of shear stress can be achieved. However, a manufacturing process of an anchor with various adhesives may result in high costs and, in practice, is not used.

2.3.3.2 Failure modes of bond-type anchorage systems

Through experimental tests, many researchers have observed two different failure modes when using adhesively bonded anchorages for FRP tendons;

- *Failure of the tendon*. The FRP rod reaches its ultimate tensile strength and the failure of the tendon is produced on its free length. This failure mode assures that the anchor does not detract from the mechanical properties of the FRP tendon.
- *Pull-out of the tendon*. This is the most observed type of failure. Slippage of the composite rod relative to the adhesive occurs due to the bonded surface failure. When the tendon is pulled, the bonded interfaces are mainly loaded by shear forces because of its symmetry. Thus, researchers have focused on the analysis of the shear stress distribution on the adhesive-rod interface.

2.3.3.3 Quasi-static response of adhesively bonded joints

Experimental analyses

As mentioned by Katz [16], the bonded joint properties are determined by the chemical bond or adhesion, and bearing forces, depending on the surface of the composite material and the stage of bond development. The adhesion is the molecular force of attraction between dissimilar materials. The strength of attraction is mostly determined by the surface energy of the material which is a function of the contact angle between the adhesive and the rod. The higher the surface energy, the greater the molecular attraction. The lower the surface energy, the weaker the attractive forces [17].

During the loading of the tendon, the chemical bond or adhesion is the primary resisting mechanism which depends on the chemical interlock between the tendon and the adhesive. The shear stress on the adhesive-rod interface transfers the load throughout the bonded joint. The higher shear stresses are usually located at the ends of the anchor, particularly at the loading end, whereas the lower shear stresses are located in the centre of the bonded joint. Once the loading end of the anchor reaches its maximum shear strength, shear cracks are initiated in the resin-rod interface and are rapidly propagated to the bottom of the bonded joint. At this stage of bond development, the chemical bond is no longer the main resisting mechanism in the parts of the interface where the adhesive failure has been initiated and bearing forces perpendicular to the interface arise as the rod is loaded and attempts to slide.

Bearing forces can be classified in two groups: mechanical friction and mechanical interlock. The first one consists in the static and dynamic friction develop between the adhesive and the rod for either plain tendons or deformed tendons with bearing face angles of up to 30°. The latter involves the strength and mechanical action of deformations on the tendon surface for the rods with bonded fibre spirals or with bearing face angles greater than 30°. In this case, the effect of chemical adhesion is small, and the tendon is principally sustained by the mechanical interaction between the tendon roughness and the adhesive. Also, friction occurs once there is a slip between the tendon and the adhesive [18].

The bond between the anchorage components can be enhanced by surface modifications. This includes braiding, twisting or the introduction of ribs on the tendon to enhance the adhesive-tendon interface, whereas increasing the housing-adhesive interface bonded properties can be reached through using an internal thread in order to increase the roughness of the inner surface of the housing. Also, joints with adhesives allow an easy handling and accurate adjustment of the anchorage components. Furthermore, bond-type anchorages have a somewhat more uniform stress distribution than mechanical anchors. For this reason, adhesively bonded joints generally show higher efficiencies with FRP materials as indicated by Bahei-El-Din and Dvorak [19].

Nanni et al. [8] also studied the behaviour of tubular adhesive bond-type anchorages. The researchers used different composite tendons and adhesives in their work. All the anchors were tensioned until failure occurred. It was observed that potted anchorages often fail because of the pull-out of the tendon from the adhesive component instead of by rupture of the tendon. The maximum load achieved was lower than the ultimate tensile strength of the tendons reported by the manufacturers. Pincheira and Woyak [12] found that the optimal bond length was 50 times the diameter of the FRP tendon. With this consideration, the failure should occur in the FRP tendon as it would reach the maximum value of tensile strength. However, this depends on the mechanical properties of the FRP material used.

Benmokrane et al. [20] presented in their study a comprehensive research concerning the tensile characteristics, bond strength and pull-out behaviour of FRP rods embedded in straight bond-type anchorages. In agreement with the research of Pincheira and Woyak, the ultimate tensile strength of the tendons was reached when a bond length of 50 times the diameter of the FRP tendon was used. For those specimens which failed before reaching the maximum capacity of the tendon, the pull-out of the tendon occurred along the bond length. Bond failure started at the loading end of the anchor and was propagated rapidly to the bottom throughout the adhesive-rod interface. Also, different external housing materials were investigated and it was observed that a higher elastic modulus of the external housing allowed for an increase in the pull-out capacity and stiffness of the FRP anchorage.

The resins used for these anchorages are usually methacrylate, polyurethane or epoxy resins since the shear strength is higher. However, these resins often show a loss of strength at high temperatures or in moist

environments. They may also show drawbacks due to the excessive creep degradation. This fact has motivated several researchers who have studied the use of mortar as an adhesive material. Zhang and Benmokrane [21] studied the use of cement-based grout as a bonding component with mono-tendon and multi-tendon anchorages. The researchers determined through monotonic experimental tests that there was an interaction effect when a multi-tendon system was used due to the load transfer mechanism among the tendons (see Figure 2.10). The results showed that a double bonded length was needed when multi-tendons were inserted in the same anchor to achieve the same ultimate tensioning force as a mono-tendon anchor. Therefore, using multi-tendon system anchorage did not optimize the joint. However, it was found that the investigated cement-grouted anchorage system provided an adequate and simple mechanism for anchoring the FRP rods.

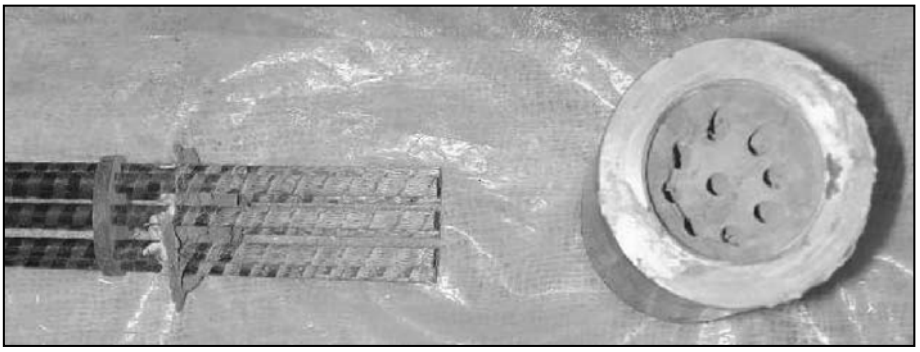

Figure 2.10. Failure bond detail of multi-tendon system [21].

The multi-tendon anchorage was also studied by Fang et al. [22]. Several quasi-static tests were conducted until the bonds of the multi-tendon anchorage system failed. The experimental data showed that the capacity reduction resulting from non-uniformities in multi-tendon anchoring systems must be considered. The capacity reduction of the system was analysed and a reduction factor for multi-tendon anchorage systems was provided.

Analytical and numerical modelling

It has been experimentally observed that the failure in adhesively bonded joints for composite materials occurs in or around the composite-adhesive interface. Thus, researchers have focused on the analysis of the stresses in the adhesive bonded length. Völkersen [23] was the first to study the shear stress distribution in double lap joints introducing the concept of differential shear. Völkersen's analysis considers the adhesive to be deformed by shear stress and the substrates by tension. The highest shear stress occurs at the ends of the joint and is lowest in the centre. This analysis is adequate for double lap joints but does not include the effect of a substrate bending moment caused by the eccentric loading that is more dominant in single lap joints. The shear stress distribution along the bonded joint predicted by Völkersen's analysis can be obtained through Equations 2.6 - 2.10.

$$\tau_i = \frac{T}{b \cdot l} \cdot \frac{w}{2} \cdot \frac{Cosh(w \cdot X)}{Sinh\left(\frac{w}{2}\right)} + \frac{\alpha - 1}{\alpha + 1} \cdot \frac{w}{2} \cdot \frac{Sinh(w \cdot X)}{Cosh(\frac{w}{2})} \qquad \text{(Equation 2.6)}$$

where T is the load, b is the width of the joints and l is the bonded length.

$$w^2 = (1 + \alpha) \cdot \emptyset \qquad \text{(Equation 2.7)}$$

$$\alpha = \frac{t_o}{t_i} \qquad \text{(Equation 2.8)}$$

$$\emptyset = \frac{G_c \cdot l^2}{E \cdot t_o \cdot t_c} \qquad \text{(Equation 2.9)}$$

$$X = \frac{x}{l} \quad -\frac{1}{2} \leq X \leq +\frac{1}{2} \qquad \text{(Equation 2.10)}$$

where t_o and t_i are the outer and inner adherent thickness, respectively, t_c is the adhesive thickness, E is the adherent modulus and G_c is the adhesive shear modulus.

Subsequently, Goland and Reissner [24] considered bending and transverse loads, as well as axial loads, in the substrate by introducing a bending moment factor, k, and a transverse force factor, k'. Both factors were used to relate the force applied in the adherent, T, to the rotation of the joint due to the bending moment, M, and the transverse force, V, as shown in Equations 2.11 and 2.12.

$$M = k \cdot \frac{P \cdot t_{o-i}}{2} \qquad \text{(Equation 2.11)} \qquad V = k' \cdot \frac{P \cdot t_{o-i}}{l} \qquad \text{(Equation 2.12)}$$

The analytical formulations proposed by Völkersen and Goland and Reissner were the first theories that allowed for the analysing of the shear stress distribution of adhesively bonded joints. Most of the analytical solutions proposed hereon after were developed from these theories.

Hart-Smith [25,26], developed Völkersen's analysis for double lap joints and Goland-Reissner's analysis for single lap joints by including plasticity within the adhesive. However, these analytical formulations do not take into account the shear and normal deformations through the thickness which are particularly important in adherents such as composites.

Ojalvo and Eidinoff [27] extended the Goland and Reissner's formulation using a more complex shear strain and displacement equations to study the influence of the adhesive thickness on the stress distribution. Their study concluded that the main difference in formulations that take into account the adhesive thickness lies in the stress distribution at the ends of the overlap bonds. With this consideration, the shear stress increases and the peel stress decreases at the ends of the bonded joint. It was found that the effect of the adhesive thickness was more significant for relatively short overlap bonds, thick adherents and high stiffness adhesives.

Moreover, other analytical formulations, such as the theories presented by Allman [28] and Chen and Cheng [29], considered the stress-free condition that occurs at the ends of the overlap length. These theories took into account the zero shear stress at the end of the adhesive layer and it was determined that the distance from the maximum shear stress to the end of the adhesive layer depends on the flexibility among the materials involved in the joint. Chen and Cheng pointed out that this distance is usually 20% of the adhesive thickness. Later, Tsai et al. [30] incorporated shear strains in the substrates assuming a linear evolution through the adherent thickness. It was shown that the improved solution provided a better prediction for the adhesive shear stress distribution than the classical solutions, especially for adherents with low transverse shear stiffness, which is the case of laminated composite materials. Due to its relevance to the present research, the theoretical formulation of Tsai et al. for double lap joints is presented as follows in Equations 2.13 - 2.16.

$$\tau_i = A \cdot Sinh(\beta \cdot x) + B \cdot Cosh(\beta \cdot x) \qquad \text{(Equation 2.13)}$$

where A and B are coefficients which depend on the boundary conditions, and β is a parameter which depends on the geometry of the bonded joint and the mechanical properties of the materials involved.

$$A = \frac{\beta \cdot l \cdot \tau_{avg}}{Cosh(\beta \cdot l)} \cdot \left[\frac{1 - \frac{E_i \cdot t_i}{2 \cdot E_o \cdot t_o}}{1 + \frac{E_i \cdot t_i}{2 \cdot E_o \cdot t_o}} \right] \qquad \text{(Equation 2.14)}$$

$$B = \frac{\beta \cdot l \cdot \tau_{avg}}{Sinh(\beta \cdot l)} \qquad \text{(Equation 2.15)}$$

$$\beta^2 = \frac{\frac{G_c}{t_c} \cdot \left(\frac{2}{E_i \cdot t_i} + \frac{1}{E_o \cdot t_o} \right)}{\left[1 + \frac{G_c}{t_c} \cdot \left(\frac{t_i}{6 \cdot G_i} + \frac{t_o}{3 \cdot G_o} \right) \right]} \qquad \text{(Equation 2.16)}$$

where τ_{avg} is the average shear stress along the bonded joint, E_0 is the elastic modulus in the longitudinal direction of the outer adherent, E_i is the elastic modulus in the longitudinal direction of the inner adherent, G_0 is the shear modulus in the longitudinal direction of the outer adherent, G_i is the shear modulus in the longitudinal direction of the inner adherent.

However, the formulations presented above have been mainly used for plane geometry bonded joints. These need to be extended to accommodate circular geometries such as the anchors being considered in this research.

Other analyses of increasing complexity were proposed to obtain more general closed-form solutions which require the use of a computer for a solution. These analyses consider the shear and normal deformations through the thickness of the adherents. One of these analyses was conducted by Adams and Mallick [31]

where the authors proposed a formulation which considered an elastic response on symmetrical unidirectional composite adherents and an elasto-plastic response on the adhesive layer. The adherents also could be dissimilar with different geometry and mechanical properties. Also, Sawa et al. [32,33] completed a comprehensively analysis of the stresses on the adherent-adhesive interface. Da Silva et al. [34][35] have collected and compared many of these analytical approaches.

In addition, stress distributions of mixed adhesive joints were also investigated. This technique considers using several adhesives of different stiffness to obtain a more uniform stress distribution on the adherent-adhesive interface. Raphael [36] considered that the adhesive failure occurs when the adhesive shear strain exceeds a certain value. This research proposed using a ductile adhesive at the ends of the overlap length due to the higher adhesive shear strains, whereas a less ductile adhesive could be used in the middle of the joint. Later, Srinivas [37] studied the effect of the overlap length on mixed adhesive joints. It was found that the stresses on the adherent-adhesive interface can be reduced when a long overlap for the stiff adhesive is used in comparison to the overlap for the flexible adhesive.

Also, three-dimensional analyses were conducted by Adams and Peppiatt [38] and, more recently, by Oterkus et al. [39] where the Poisson's ratio was included and the transverse stress distributions along the width of the bonded joint was analysed.

Moreover, more advanced analyses were carried out using the finite element method which enables adhesive and substrate non-linearities, progressive damage and coupled hygro-mechano-thermal effects to be included [40–43]. Non-linear response in adhesively bonded joints can generally be modelled through continuum damage response, von Mises plasticity [44] and Drucker-Prager plasticity [45].

The continuum damage response considers that the fracture is mainly caused by nucleation, growth, and merging of voids in ductile materials. This concept was first developed by Gurson [46], where a yield criterion and flow rule for a material containing a given volume fraction of voids was proposed and, later, extended by Tvergaard and Needleman [47] who included void nucleation and growth. Efforts were made to extend this approach in order to model the continuum damage response with the finite element method (FEM) [48–51]. Recently, Hua et al. [52] proposed a continuum damage model to undertake progressive damage modelling in adhesive joint systems. The model proposed was able to predict the initiation and propagation of the damage, as well as, the failure load of the joints.

Also, polymers usually exhibit higher yield stresses in compression to tension. This allows for hydrostatic yield dependency to be used through Drucker-Prager plasticity. The Drucker-Prager model was first developed for determining the pressure dependent yield failure of soils which enables the characterising of the yield surface and predicting the effect of compressive hydrostatic stress on yielding. Recently, the Drucker-Prager model was mathematically modified to take into account both tensile and compressive hydrostatic stresses [53] and utilised successfully for adhesively bonded joints [54–57].

Progressive damage can also be used to analyse adhesively bonded joints through the cohesive zone model (CZM). In 1959, the CZM was originally introduced by Barenblatt [58,59] based on the Griffith's theory of brittle fracture. This was followed by Dugdale [60] who introduced a relationship between the process zone at the crack, or cohesive stress, and the plastic yield stress of the materials involved. The cohesive forces were taken to be the same as the yield stress. The CZM was first implemented by Hillerborg et al. [61] through the FEM. As it can be seen in Figure 2.11, the basic idea of the CZM is that the cohesion forces between two atomic planes increase at the same time as the distance between both mentioned atomic planes increases up to a maximum cohesion force is reached. At this point, damage starts and further separation of the atomic planes results in a rapid increase of the damage and decrease of the cohesion forces.

Usually the damage propagation phase or strain softening branch after damage is defined as linear, although it could be defined multi-linear. Tvergaard and Hutchison [62,63] used a trapezoidal shape traction-separation in order to study the crack growth of elastic solids. Also, Yang et al. [64–66] used the trapezoidal shape traction-separation to model progressive damage in adhesively bonded joints.

An important advantage of CZM for adhesively bonded joint analysis lies in the possibility of it being used in interfaces as it does not represent any physical material, but allows for the cohesive forces between two materials that are pulled apart to be described. By inserting a layer of cohesive elements between two continuum elements throughout the potential crack path, a progressive damage can be successfully utilised to study adhesively bonded joints, especially when the crack path is known in advance.

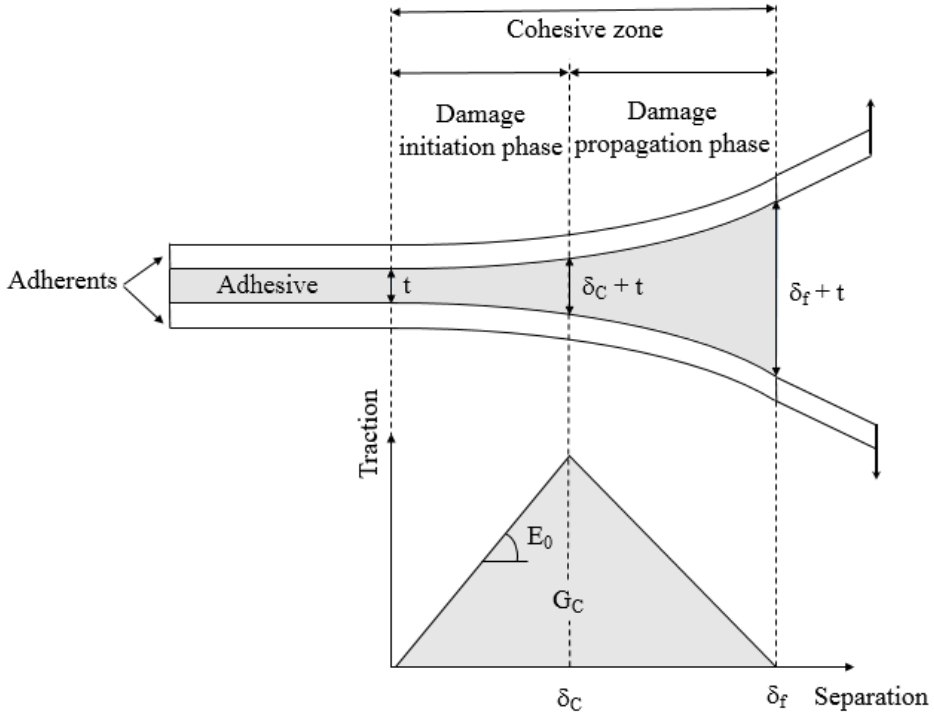

Figure 2.11. Bi-linear traction-separation law CZM in adhesively bonded joint.

Ouyang et al. [67] used a cohesive zone model for adhesively bonded pipe joints under torsional loading. Bi-linear cohesive laws were utilised with isotropic materials in order to obtain a first understanding of the joint response. Furthermore, Li et al. [68] proposed an analytical solution for bond anchorages for FRP tendons under axial load. The analytical formulation was based on a bi-linear cohesive zone model placed in the adhesive layer. It was experimentally and analytically found that the adhesive thickness was the main factor affecting the strength tensile capacity. In addition, the authors concluded that the characteristic strength bond was also dependent on the properties of the adhesive, the geometry and surface conditions of the tendon, as well as the radial stiffness of the confining medium. This work indicated that the cohesive zone method can be used to predict the tensile capacity of the bond anchorages under quasi-static loading.

Moreover, there are many theoretical models developed by Wang [69] and Yue and Looi [70] regarding the pull-out of fibres in the literature based on either fracture energy or shear stress analysis. However, these models are developed in order to understand the mechanics of the debonding process of a single fibre from a brittle matrix.

2.3.3.4 Time-dependent response of adhesively bonded joints

Adhesives usually exhibit both elastic and viscous properties when subjected to deformation. An immediate elastic strain response is obtained when a load is applied whereas a slow increase of strain is observed as a function of time due to the viscous characteristics of the material. These materials are called time-dependent materials or viscoelastic materials. Time-dependent effects can be observed by the phenomena of creep under constant stress or stress relaxation under constant strain. Also, even though the applied forces are constant, time-dependent phenomena may have a considerable effect on the stress distribution developed [71]. The stress or strain at a particular point can vary substantially with time and for this reason bond anchorages need to be studied whilst taking into account the viscoelastic phenomena. Time-dependent behaviour of materials can be studied experimentally through three different tests; creep, stress relaxation and constant rate stressing. However, the most common method used to assess time-dependent behaviour is uniaxial creep testing.

Creep response of adhesively bonded joints

Creep phenomenon is the tendency of a solid material to deform continuously under the influence of a constant load (below the yield strength of the material) over long periods of time. Usually, the strain-time curves exhibit three characteristic stages (see Figure 2.12).

- Primary or transient creep. Once the load is applied and the instantaneous elastic strain occurs (ε_0), the material deforms rapidly but at a decreasing rate. The duration of this stage is usually relatively short as it reaches a constant deformation rate quickly.

- Secondary or steady-state creep. The creep strain reaches a minimum deformation rate and remains approximately constant over a relatively long period of time.
- Tertiary Creep. The creep strain rate accelerates rapidly until the failure of the material is reached (rupture). The material in unable to withstand the load and fails.

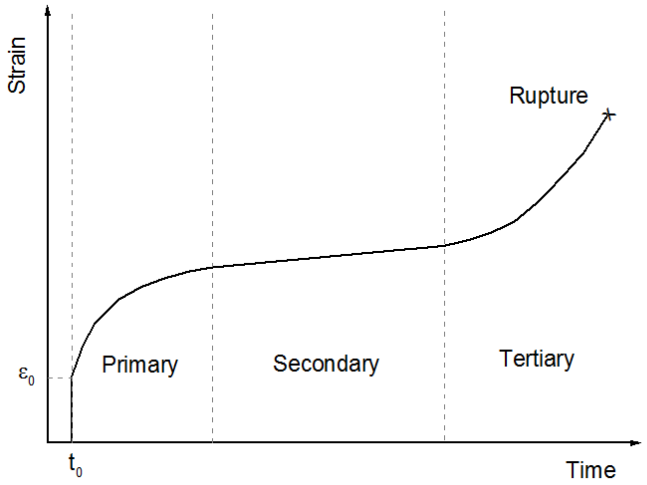

Figure 2.12. Characteristic creep stages.

Regarding the composite material, Yamaguchi et al. [72] conducted creep tests with GFRP, CFRP and AFRP tendons. The bars were tested experimentally at different loads. The results indicated that there was a linear relationship between stress and the logarithm of the creep time to failure. Through a linear extrapolation, it was shown that it was possible to stress CFRP tendons over 80% of their ultimate tensile strength to obtain a lifespan of over 50 years. However, the bonded joint is more sensitive to suffering premature failure caused by creep.

Most stress analyses of adhesives and adhesively bonded joints are generally carried out using time-independent plasticity materials models where the yield surface is used to define the onset of inelastic strains. Von Mises [44] and Druker-Prager yield criteria [45] that are often used to predict the creep phenomenon in polymers and adhesively bonded joints. As mentioned in the quasi-static section, the latter allows for the inclusion of a hydrostatic term which associates the plastic flow with an increase in volume. The yield function for von Mises theory is defined as follows in Equation 2.17.

$$F = q - \sigma_0 \cdot \left(\varepsilon_{eq}^{pl}, \theta\right) = 0 \qquad \text{(Equation 2.17)}$$

where q is the von Mises equivalent stress, σ_0 is the uniaxial tensile stress and the ε^{pl}_{eq} is the equivalent plastic strain corresponding to the tensile stress. On the other hand, the yield function for Druker-Prager theory is defined in Equation 2.18.

$$F = a \cdot q^b - p - p_t \cdot \left(\varepsilon_{eq}^{pl}, \theta\right) = 0 \qquad \text{(Equation 2.18)}$$

where a and b are material parameters to be determined from available data, p_t is the initial hydrostatic stress strength of the material (hardening parameter), p is the equivalent pressure stress and q is the von Mises equivalent stress.

It is worth noticing that the plasticity models described above are independent of strain rate effects. However, a rate dependent yield strength can be combined with these models to include rate-dependent plasticity. This rate dependency can be introduced in many different ways. One of the most used theories was proposed by Norton [73] and Bailey [74], better known as creep power law. The creep power law model is presented in Equation 2.19.

$$\dot{\varepsilon}_{eq}^{cr} = A \cdot q^B \cdot t^m \qquad \text{(Equation 2.19)}$$

where $\varepsilon^{cr}{}_{eq}$ is the uniaxial equivalent creep strain rate, q is the von Mises equivalent stress, t is the total time and A, B and m are material parameters to be determined from available data.

Although the presented models have been used to successfully represent the creep phenomenon in adhesives and bonded joints, the main limitation lies in the inability to model substantial strain recovery on unloading. In situations where the strain recovery is required, an alternative approach must be utilised. There are many visco-elastic [75,76] and visco-plastic [77,78] models able to accurately predict the non-linear volumetric deformation. However, most of them do not take into account the hydrostatic stress sensitivity and do not allow for a varying volume of non-linear deformation. Also, a large experimental campaign is required in order to correctly calibrate all the parameters of the mentioned theories.

Creep phenomenon in adhesively bonded joints has mainly been studied through single lap joints (SLJs) and double lap joints (DLJs) [54,79,80] where different creep models for finite element analysis were investigated and compared with available experimental data in order to investigate the main parameters involved in the damage initiation and propagation, and the creep time to failure of bonded joints. Creep experimental tests on either SLJs or DLJs are usually based on a double cantilever with a specified load ratio (ordinarily of 10:1). Specimens are attached to the shortest horizontal cantilever whereas a sustained dead weight is placed on the longest end. The load remains constant until the failure of the specimen occurs. The use of a cantilever test setup is a well-known technique for creep testing [71].

Su and Mackie [81] developed a two dimensional finite element model to simulate the creep phenomenon in adhesively bonded joints. A viscoplastic model was used for the adhesive and the creep was modelled by reducing the plastic yield stress to zero. When the specimen was loaded, a peak was observed in normal and shear stress distributions along the bond line. Creep led to a more even distribution of the stresses, reducing these peaks and showing a large increase of strains with time.

Some other models [82,83] studied the stress distribution in adhesive joints at high temperatures, where the increasing rate of creep strain is even higher. The aim of these investigations was based on finding the best adhesive joint design at high temperatures. In this sense, in order to enhance the mechanical properties of adhesive joints, especially the creep behaviour, Khalili et al. [79] proposed the reinforcement of the adhesively bonded joints by adding carbon fibres to the bond line with a fibre orientation ±45º.

Stress relaxation response of adhesively bonded joints

Time-dependent phenomena are usually studied through uniaxial creep testing because of its simplicity. For this reason, stress relaxation tests are rarely carried out to study time-dependent behaviour. However, there are several studies worth mentioning.

Adhesively single lap joints were studied under stress relaxation by Tomblin et al. [84]. Calibrated stressing rings were used to keep the displacement between the ends of the specimen constant. The ends of the SLJs were fixed in the inner part of the ring. The stress relaxation tests were conducted by monitoring the strain of the outer part of the rings exerted during the load application. However, this test setup is more suitable for small specimens. Other studies conducted the stress relaxation tests by using actuators or testing machines [85]. In these cases, short duration of analysis is usually recommended due to the cost of carrying out an experimental test lasting days or even weeks.

Moreover, partial elements of a structure can be tested under stress relaxation when the whole structure in service is subject to being tested. A partial element is prestressed and the rest of the structure keeps this element under tension. In this sense, Delhomme et al. [86] carried out a stress relaxation study on anchoring systems used for ski-lift pylons by using a concrete block which was part of the structure in service. The concrete block allocated the bolt and the ends of the bolt were fixed by locking plates. This is appropriate for relatively small structures. In addition, these structures were simulated using Abaqus where time-dependent behaviour was taken into account in a viscoelastic analysis using a power law creep model based on the Bailey-Norton law [87].

In spite of time-dependent phenomena being studied in adhesively bonded joints, especially through experimental creep tests, there is still a lack of knowledge of these phenomena relating to bond-type anchorages for composite materials.

2.3.3.5 Fatigue response of adhesively bonded joints

Although fatigue is a phenomenon associated with metals, it is also present in polymers and ceramic materials. Most composite materials are also sensitive to cyclic fatigue loads, which can lead to premature failure of the structure. Fatigue failure in composite materials arises from different damage mechanisms that appear in different zones of the material throughout its life. The combination of these local damages

causes the degradation of the mechanical properties globally [88]. Although composite materials may exhibit a reasonable fatigue performance, the major concern in this work lies in the adhesive bond [89].

Adhesively bonded joints under fatigue load have primarily been studied through single lap joints, double lap joints and laminated doublers in bending (LDB) [73,89–95]. Usually, experimental tests are combined with predictive numerical models in order to reduce time and costs of the final design. The typical variables assessed are the maximum fatigue load, the load ratio *(R*) and the frequency. The effect of the maximum fatigue load and the load ratio generally determine the fatigue response of adhesively bonded joints, whilst the loading frequency is often less important over the range 1-10Hz, as mentioned by Crocombe et al. [90].

Different methods have been employed to model the fatigue damage in the adhesive joints based on the stress singularity or fracture mechanics. Quaresimin and Ricotta [91,96,97] experimentally studied SLJs, which consisted of Carbon/epoxy laminates bonded with epoxy adhesives, under fatigue loading. Extensive research of the stress intensity factors (SIFs) and strain energy release rate (SERR) was investigated. The authors proposed a life prediction methodology based on the actual mechanics of the fatigue damage evolution which described the lifetime of the bonded joint as a sequence of a crack nucleation phase. However, this approach cannot successfully study progressive damage during the initiation phase. Also, it is based on the elastic stress field, which might not be completely appropriate for adhesives with plastic response.

Other approaches, such as the investigations conducted by Gilbert et al. [98] and Xu et al. [99], were based on the fracture mechanics where the damage propagation phase was considered, predicting the number of cycles to failure of adhesively bonded joints. However, these theories do not take into account the damage initiation.

The cohesive zone model (CZM) has recently been considered for predicting fatigue response where the crack path is known in advance. The cohesive elements consider damage initiation (once the cohesive elements reach the maximum traction allowed) and damage propagation (that can be defined as a function of the fracture energy or the displacement at failure).

Maiti et al. [100] and Nguyen et al. [101] modelled fatigue loading using cohesive zone modelling with a damage evolution equation which was evaluated cycle by cycle. This was computationally very expensive and limited to low cycle fatigue. More recently, the fatigue damage response of adhesively bonded was modelled with cohesive elements with progressive fatigue damage degrading the parameters of the cohesive elements [92–94] (see Figure 2.13). The damage evolution law was assessed for blocks of cycles. This allows an efficient use of computing resources to be acquired and can simulate high cycle fatigue. For each block of cycles, the cohesive element properties were degraded following a cyclic fatigue damage evolution law. These parameters were calibrated with experimental data.

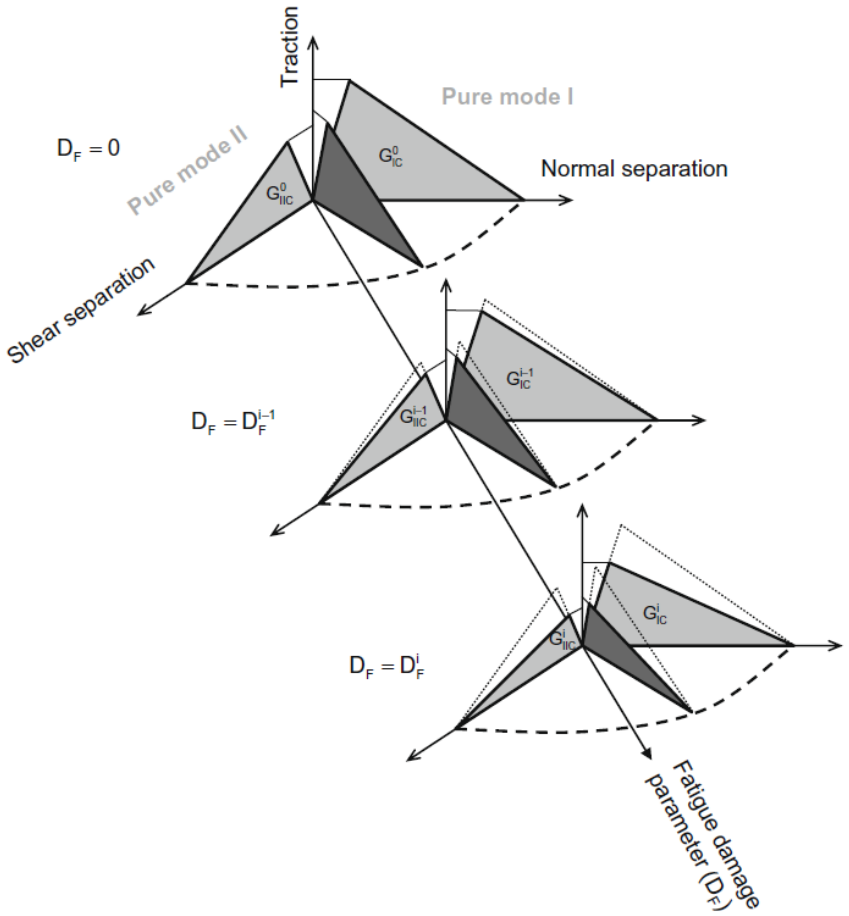

Figure 2.13. Fatigue degradation of cohesive element properties [94].

Khoramishad et al. [94] proposed the fatigue analysis of adhesively bonded joints through a cohesive zone between the adhesive and the substrate. As mentioned earlier, the influence of fatigue was simulated by assessing the evolution law for blocks of cycles and degrading the traction-separation response of the cohesive elements. The fatigue degradation process was implemented through Equation 2.20 and 2.21.

$$\frac{\Delta D}{\Delta N} = \begin{cases} \alpha \cdot (\varepsilon_{max} - \varepsilon_{th})^{\beta}, & \varepsilon_{max} > \varepsilon_{th} \\ 0, & \varepsilon_{max} \leq \varepsilon_{th} \end{cases} \qquad \text{(Equation 2.20)}$$

$$\varepsilon_{max} = \frac{\varepsilon_n}{2} + \sqrt{\left(\frac{\varepsilon_n}{2}\right)^2 + \left(\frac{\varepsilon_s}{2}\right)^2} \qquad \text{(Equation 2.21)}$$

where ΔD is the increment of damage and ΔN the increment of cycles, ε_n and ε_s are the averaged bond line normal and shear strains, ε_{max} is a combination of these normal and shear strain components, ε_{th} is a threshold value which specifies the minimum strain to initiate the fatigue damage, and α and β are material constants.

It was found that the numerical fatigue damage model gave a consistent match with the available experimental data. However, this approach is valid for applications were the load ratio does not significantly influence the fatigue response of the adhesively bonded joint.

Khoramishad et al. [92,93] later considered the load ratio and variable fatigue loading effect in their formulation. This was included by introducing a parameter, n, to accommodate the ductility of the adhesive and a correction factor, γ, which relates the maximum fatigue load, P_{max}, the static strength, P_s, and the fatigue ratio, R. Equations 2.20 and 2.21 present the fatigue damage law used for predicting fatigue damage modelling of adhesively bonded joints under variable amplitude loading.

$$\frac{\Delta D}{\Delta N} = \begin{cases} \alpha \cdot [(\varepsilon_{max} - \varepsilon_{th}) \cdot \gamma^n]^{\beta}, & \varepsilon_{max} > \varepsilon_{th} \\ 0, & \varepsilon_{max} \leq \varepsilon_{th} \end{cases} \quad \text{(Equation 2.20)}$$

$$\gamma = \frac{\frac{(1-R)}{2}}{1 - \left[\frac{P_{max}}{2 \cdot P_s} \cdot (1+R)\right]^m} \quad \begin{matrix} \text{m=1, Goodman} \\ \text{m=2 Gerber} \end{matrix} \quad \text{(Equation 2.21)}$$

2.4 Brief summary of prestressed concrete structures with FRP tendons

In the 1970s, the deterioration caused by the reinforcement corrosion, especially in bridges, raised the interest in new strategies to reduce the susceptibility of structures in corrosive environments. This section summarises the most outstanding constructions of concrete structures prestressed with composite tendons.

Research activities began in Germany with the aim to use glass fibres for prestressed applications. As a result of this research, in 1978, Strabag-Bau and Bayer developed a GFRP tendon called Polystal and an anchoring system for post-tensioning. Polystal tendons consisted of a set of 19 rods with a characteristic diameter of 7.5mm each rod and a fibre fraction of 68% by volume. These tendons were incorporated in several bridges in Germany and Austria. The first bridge with prestressed Polystal tendons was built in Düsseldorf in 1986 where a total of 59 tendons with a capacity of 600kN per tendon were utilised.

The interest in the non-metallic tendons continued raising during 1980. In 1983, AKZO, a chemical manufacturer, and Hollandsche Beton Groep HBG, developed an AFRP tendon. In 1989, ninety AFRP tendons were used for prestressing pillars of an acoustic screen along a road in Schiedam (Netherlands). Although the behaviour of the pillars was satisfactory, small cracks appeared in the outer surface of the pillars due to thermal expansion of the tendons.

In addition, several European projects were conducted during the last two decades which focused on investigating new composite materials, researching the durability of composite materials in aggressive environments and developing of design guides and feasibility of projects. The most important activities in Europe were summarised by Taerwe and Matthys [102,103].

In 1980, Japan also started a comprehensive national program to study the use of FRP tendons in concrete structures. Researches focused on developing GFRP tendons and their application in concrete structures. The main aim was to replace the steel reinforcement bars for composite tendons. The investigations undertaken in Japan were summarised by Fukuyama [104], and details of the recent projects were included in the Advanced Composites Centre (ACC).

Furthermore, in 1988 a new anchorage for the GFRP tendon was developed by Iyer and Kumaraswamy in the United States [105]. The anchorage was based on the systems for steel tendons with several modifications. In 1990, the first prestressed bridge with GFRP in the United States was built in Rapid City using the Iyer anchorage [106]. In 1992, the Iyer anchorage was comprehensively studied by Sen et al. [107] in order to prestress pillars with GFRP tendons in marine environments. This research culminated with the first conference focused on FRP composites for civil engineering applications.

Much of the research on prestressed structures with FRP tendons in the United States was conducted by different researchers. The most important works were carried out by Charles W. Dolan [108,109], Antonio Nanni [8,109,110] and Nabil F. Grace [111,112]. The latter work allowed for the designing and building of the first traffic bridge with CFRP tendons in the United States (see Figure 2.14). These investigations led to developing commercial systems tendons, many of which were summarised in the First International Symposium for FRP in Reinforced Concrete Structures.

In Canada, several researchers, especially within the ISIS Canada Resource Centre, investigated the application FRP tendons in prestressed concrete structures. The Canadian Society for Civil Engineering Technical Sub-Committee on Advanced Composite Materials (ACM) was formed in 1989. As a result, the Beddington Trail Bridge (Calgary, Alberta) was the first road bridge built in Canada with some of the concrete beams prestressed with CFRP tendons. It was also the first bridge which utilised an integrated optical sensor system to measure and monitor the behaviour of the prestressed beams with composite materials. The building of the bridge was completed in 1994.

Figure 2.14. First traffic bridge with CFRP tendons built in United States [111,112].

It is worth mentioning that mechanical anchorages were utilised in all the applications in order to attach the FRP tendons to the concrete structure due to their similarity with the current anchorage systems for steel tendons.

2.5 Concluding remarks

A review of anchorage systems for prestressing composite tendons under quasi-static, dynamic and time-dependent loads has been performed. The state of the art has primarily focused on the most noteworthy analytical and numerical modelling methods of anchorage systems for FRP tendons. Also, the fundamentals of the prestressing method and a brief summary of prestressed concrete structures with composite materials have been presented. Based on the literature review provided in this chapter, the following conclusions, which directly affect this research, were drawn;

1. It has been observed that one of the most important causes of deterioration of prestressed structures is the corrosion suffered by the steel reinforcement. In recent decades, researchers around the world have conducted studies with the aim to replace the traditional steel tendons for alternative materials with high resistance to corrosion.
2. The most suitable alternative materials for prestressing applications are FRP materials due to their high mechanical properties, light weight and high resistance to degradation in harsh environments. Several studies have investigated the feasibility of utilising Carbon Fibre Reinforced Polymers (CFRP), Glass Fibre Reinforced Polymers (GFRP) and Aramid Fibre Reinforced Polymers (AFRP) for prestressed applications. It has been seen that CFRP provides higher mechanical properties in comparison to steel tendons and a similar stiffness, unlike other FRP systems.
3. Due to the anisotropic nature of composite materials, the conventional anchoring systems cannot be used. There are two main anchoring systems for composite materials: mechanical anchors and adhesively bonded anchors.
4. Mechanical anchorages for FRP tendons are based on the current anchoring systems for steel prestressing rods. Several modifications have been considered in order to homogenise the radial pressure acting transversally on the tendon, which generally causes a premature failure of the tendon in the anchorage area. Because of their similarity with the current systems for steel, compactness, ease of assembly, reuse and reliability, these anchoring systems have been extensively investigated and used in real applications. For this reason, the present research mainly focuses on the investigation of adhesively bonded anchorages although a preliminary experimental work with mechanical anchorages for FRP tendons has been undertaken in order to confirm the main conclusions obtained by different researches.
5. An adhesive bond-type anchorage for composite tendons consists of a metallic housing inside which single or multiple rods are bonded with an adhesive. The quasi-static response has been

experimentally studied with failure occurring in the bond line. For this reason, the stress distributions on the adhesive layer have been investigated by many researches under different loadings. The analytical formulations for adhesively bonded joints were mostly formulated for plane geometries, such single lap joints or double lap joints. It was found that the theoretical solution of Tsai et al. [30] allows obtaining a good prediction of the shear stress distribution on the adhesive-adherent interface, particularly when the adherent is a composite materials. Also, analytical formulations for bonded joints have not been extended to tubular bonded anchorages.

6. Different techniques have been investigated in order to numerically model adhesively bonded joints for composite materials in plane geometries. These analyses consider non-linearities, continuum damage, coupled hygro-mechano-thermal effects or progressive damage. It was found that using a cohesive zone model for adhesively bonded joints allows for the accurate prediction of the damage initiation of the bonded joint and the damage propagation throughout a potential crack path.
7. Time-dependent phenomena have mainly been studied through the creep response of plane geometries of adhesively bonded joints. Time-independent plasticity material models and time dependent visco-elastic and visco-plastic models have been described and discussed. It was found that a model which uses a multi-axial visco-plasticity theory is able to precisely model the creep phenomenon by reducing the plastic yield properties of the adhesive layer.
8. Fatigue response of adhesively bonded joints has primarily been studied through SLJs, DLJs and LDB. Stress singularity factor and fracture mechanics have been used to study the lifetime of bonded joints. However, these models do not allow both damage initiation and propagation damage to be obtained. Moreover, it was found that the cohesive zone model efficiently permits indication of the evolution of damage and predicts the onset and growth of damage to bonded joints under fatigue loading with constant or variable amplitude.
9. Although many researchers have experimentally studied straight bond-type anchorages, little attention has been paid to the failure mechanism and its analytical and numerical modelling. Also, the straight bond-type anchorage has not been extensively studied under constant fatigue and time-dependent loading. The present research aims to investigate all these aspects experimentally and numerically.

Chapter 3. Specimens manufacture

3.1 Introduction

Experimental work was carried out in order to study the bond-type anchorage behaviour under quasi-static, fatigue and time-dependent loading. As it was described in the research methodology, single lap joints (SLJs) were tested under creep loading in order to provide an experimental creep law, double lap joints (DLJs) were considered for the quasi-static experimental investigation with the aim to study the shear stress distribution along the adherent-adhesive interface, and straight bond-type anchorages were tested under quasi-static, fatigue and time-dependent loading in order to investigate the mechanical response of the anchorages for FRP tendons. For this purpose, three types of specimens were manufactured during this research work: single lap joints, double lap joints and straight bond-type anchorages. This chapter presents the manufacturing techniques of all these configurations, details of each specimen geometry and the mechanical properties of the materials involved.

Moreover, mechanical anchors with and without sleeve material were also tested as preliminary experimental work to discuss the quasi-static behaviour reported in the state of the art. However, the preparation of specimens with mechanical anchors is not described in this section due to its assembling simplicity just before testing.

3.2 Materials

As the stress analysis of an adhesively bonded joint typically requires the knowledge of material properties of all the components involved, Table 3.1 and

Table 3.2 summarise the available information provided by manufacturers of the adhesive systems and the adherents used in this research work, respectively. All the adhesives were two component resins based on methacrylate, polyurethane or epoxy since the shear strength is higher. Two component adhesives feature a high versatility in application and performance. These systems consist of a resin and a hardener and may be cured either at ambient temperatures or at elevated temperatures for more rapid cures. The adhesives were prepared using a mechanical mixer at the revolutions per minute specified by the manufacturer, usually no more than 400rpm. The mixing procedure with the mechanical mixer was sustained until a uniform paste was obtained.

Although, GFRP structural rods have been used in this study, the main study focuses on CFRP because of its higher mechanical properties. The composite materials used in this study for the SLJs, DLJs and the anchor rods were manufactured using a pultrusion process. The composite material were MBrace Laminate LM [113] for the SLJs and DLJs, and MBar Galileo [114] and Aslan GFRP [115] for the anchors. The contents of fibre and resin were 65% and 35% by volume, respectively. The composite material was provided with a peel ply that was removed immediately prior to bonding. No other preparation in the FRP laminates and rods was required. In addition, the composite material had shallow depressions on the surface in order to optimise the bond with the adhesive (see Figure 3.1).

Moreover, numerical modelling was undertaken in order to predict the behaviour of the SLJs and straight bond-type anchorages joined with adhesive 02. For this reason, Table 3.3 summarises the tensile and compressive properties of the adhesive 02 needed to model the adhesive layer. Tensile and compressive data of the bulk adhesive were provided by the company performed through ASTM D 638 and ASTM D 695.

Table 3.1. Nomenclature and mechanical properties of the adhesives used in this work.

Adhesive	Commercial name	Elastic modulus, E [MPa]	Poisson coefficient, ν [-]	Viscosity [mPa·s]	Density, ρ [g/cm^3]	Resin curing time [days]
Adhesive 01	Basf Apogel 1360	3,380	0.45	250	1.10	3
Adhesive 02	Basf MBrace Primer	700	0.42	250	1.10	3
Adhesive 03	Basf MBrace Adhesivo	3,000	0.40	90,000	1.70	3
Adhesive 04	ITW Plexus MA300	1,000	-	60,000	1.00	1
Adhesive 05	ITW Plexus MA420	1,200	-	80,000	1.00	1
Adhesive 06	Resoltech 3050CT & 3054CT	-	-	40,000	1.05	7
Adhesive 07	Huntsman Araldite 2011	1,900	-	45,000	1.05	1
Adhesive 08	Huntsman Araldite 2029	570	-	60,000	1.32	1
Adhesive 09	Resoltech 3040 & 3045	-	-	45,000	1.40	7
Adhesive 10	Scott Bader Crestabond M1-05	700	-	120,000	-	1

Table 3.2. Nomenclature and mechanical properties of the adherents used in this work.

Adherents	Elastic modulus, E [GPa]	Transversal modulus, G [MPa]	Poisson coefficient, ν [-]	Ultimate tensile strength [MPa]	Ultimate tensile force [kN]
CFRP (MBar Galileo & MBrace Laminate BASF)	E_x= 141 E_y= 3.3 E_y= 3.3	G_{yz}= 1,190 G_{zx}= 1,930 G_{xy}= 1,930	ν_{yz}= ν_{zx}=0.007 ν_{xy}= ν_{xz}=0.288 ν_{zy}= ν_{yz}=0.374	2,500	Tendon ϕ8mm=125 Laminate50x1.5mm=187
GFRP (Aslan FRP Hughes Brothers)	E_x=40.8	[-]	[-]	1,000	Tendon ϕ6mm=28 Tendon ϕ10mm=75
Steel housing	E=200	G=80	0.3	355	[-]

Figure 3.1. MBar Galileo bar.

Table 3.3. Tensile and compressive data of the bulk adhesive (Basf MBrace Primer).

Properties	Yield strength [MPa]	Strain at yield [%]	Ultimate Strength [MPa]	Rupture strain [%]
Tensile	14.5	2.0	17.2	40
Compressive	26.2	4.0	28.3	10

All the specimens (SLJs, DLJs and straight bond-type anchorages) were cured at room temperature, according to the specifications of the adhesive manufacturer. Standard laboratory conditions were assured during the curing process. This includes a temperature of 23±2ºC and a relative humidity of 50±5%.

3.3 Single lap joint (SLJ)

Manufacturing of SLJs were based on ASTM D3165 [116]. Four configurations of single lap joints were prepared in the laboratory to be tested under creep loading. The dimensions of the SLJs are shown in Figure 3.2. The overlap length, the width and thickness of the bond line are summarised in Table 3.4. SLJs were tested in order to obtain additional information of the bonded joint to model the straight bond-type anchorage. As the primary parameter of interest in the anchorages was the adhesive thickness, different thicknesses in SLJs were investigated. However, as the overlap length of the anchorages was large enough for the full adhesive stress field to be developed, the joint superposition length was not studied in SLJs. All the specimens were made up using the adhesive MBrace Primer [117], a low viscosity polyamine cured epoxy. The low viscosity of the adhesive usually enables an easy preparation of the joints avoiding air cavities and undesirable imperfections. This allows manufacturing of the joint by pouring the adhesive into the overlap length unlike adhesives with high viscosity which require a more complex procedure.

It is worth mentioning that SLJs were manufactured with no adhesive spew fillets. Adhesive spew fillet is the portion of adhesive that is squeezed out from the bonded area and forms a bead at the ends of the substrates assembled. Even though the spew fillet is normally present in an adhesive joint, it is usually neglected in the stress analysis of adhesively bonded joints. However, the presence of spew fillets can reduce peak stresses in function of their shape and size, and thus the joint strength can be increased. As

adhesive spew fillets were not considered in the straight bond-type anchorage, SLJs were made up without spew fillets in order to transfer results between both geometries.

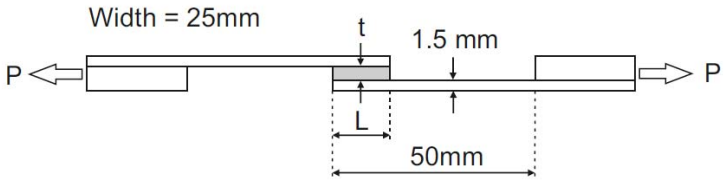

Figure 3.2. Dimensional details of SLJ.

Table 3.4. Geometric characteristics of SLJ.

Specimen	Adhesive	Repetitions	Length, L[mm]	Width [mm]	Thickness, t [mm]
SLJ_01_02	02	3	10	25	1.6
SLJ_02_02	02	4	10	25	3.2
SLJ_03_02	02	3	10	25	4.8
SLJ_04_02	02	3	10	25	6.4

SLJs were prepared in the laboratory according to the following procedure:

1. The CFRP laminates were cut and machined in the laboratory according to the dimensions shown in Figure 3.2.
2. The peel ply provided to protect the composite material surface was removed carefully ensuring the good condition of the surfaces to be bonded.
3. Joints were made up in a working glass area (see Figure 3.3 left). Square end spacers were used to make up the SLJs with no adhesive spew fillets. The overlap length and the bond layer thickness of the SLJs were controlled by the spacers.
4. The CFRP laminates were placed *edge-on* on the glass support. Once the required dimensions of the specimens were ensured with the spacers, a thermoplastic glue gun was utilised to seal all the sides of the overlap length.
5. The thermoplastic glue gun was plugged in for a few minutes before applying in order to ascertain that the glue was hot enough to flow out of the nozzle. The sides of the joints were then sealed with the sealant. The top side of the SLJs remained open in order to pour the adhesive in later (see Figure 3.3 left).
6. Once the sealant was totally cured, after approximately 30 min., the spacers were removed and the overlap dimensions were checked. If the dimensions were not suitable, the procedure was started again from step number 3 after removing the glue. Only in a few cases the dimensions of the joints were found not to be appropriate.
7. The adhesive was prepared with a mechanical mixer and poured into the overlap gap. The application of the adhesive was carried out slowly to avoid the formation of voids or gaps in the

bond layer. It is important to mention that pouring was realised within a short period of time as the adhesive pot-life was between 30 and 60 minutes.

8. Specimens were cured at room temperature for three days as suggested by the manufacturer before testing (see Figure 3.3 middle).
9. The sealant was removed of the SLJs and the specimens were ready to be tested. Specimens were named indicating the adhesive thickness and specimen number (see Figure 3.3 right).

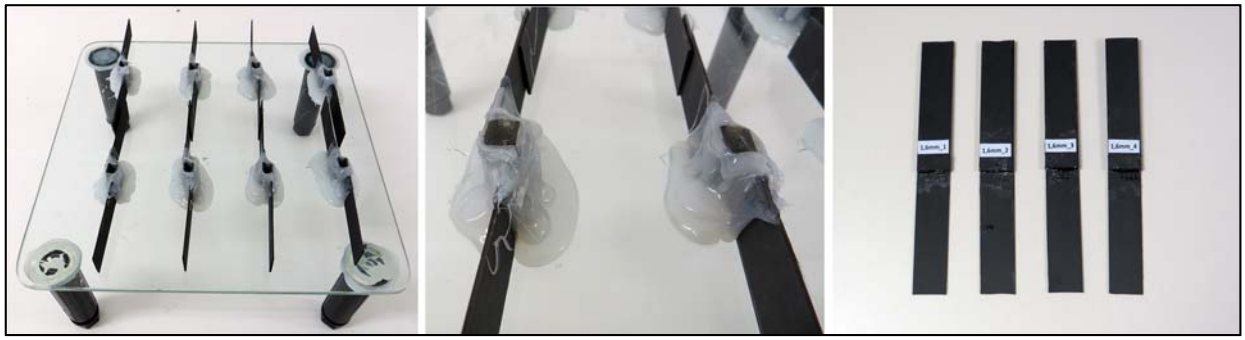

Figure 3.3. Preparation method of SLJ.

3.4 Double lap joint (DLJ)

Double lap joints were based on ASTM D3528 [118]. Seven configurations of double lap joints were prepared in the laboratory with three adhesive systems [117,119,120] to be tested under quasi-static loading. Alike SLJs, spew fillets were not considered in the manufacture of DLJs. Dimensional details and geometric characteristics of DLJs are summarised in Figure 3.4 and Table 3.5, respectively.

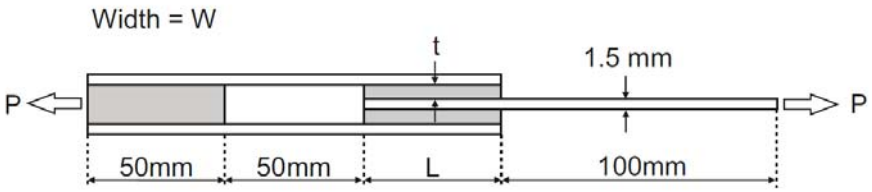

Figure 3.4. Dimensional details of DLJ.

DLJs were prepared in a laboratory environment and different procedures were undertaken depending on the adhesive viscosity. For those adhesives which the viscosity was lower than 1,000mPa·s, the procedure carried out with SLJs was assumed. Steps 1-9 mentioned in the preparation of SLJs were followed. Figure 3.5 (left) shows the two components of the adhesive 02 before mixing. As it can be seen, the different colour hue determines the proportion of each component. Whilst low viscosity adhesives are normally provided individually and the mixing is realised in a mixing recipe not provided by the manufacturers, high viscosity adhesives are frequently provided with a dynamic mixing gun which mixes the two components when applying.

Table 3.5. Geometric characteristics of DLJ.

Specimen	Adhesive	Geometry	Repetitions	Length, L[mm]	Width, W [mm]	Thickness, t [mm]
DLJ_01_01	01	01	4	100	40	1.35
DLJ_01_02	02	01	2	100	40	1.35
DLJ_01_03	03	01	2	100	40	1.35
DLJ_02_01	01	02	1	200	30	1.35
DLJ_03_02	02	03	1	200	40	1.35
DLJ_04_02	02	04	3	200	10	1.35
DLJ_05_02	02	05	3	50	15	1.35

Figure 3.5. Preparation method of DLJ with low density adhesives.

Double lap joints made up with low viscosity adhesives were placed in a glass work area and a thermoplastic gun and square end spacers were used to provide the required dimensions as mentioned with SLJs. The adhesive was set into the overlap length either by pouring the adhesive or by injection moulding with a syringe (see Figure 3.5 middle). Specimens were cured at room temperature according to the manufacturers' specifications and the sealant was removed after curing (see Figure 3.5 right).

On the other hand, a different procedure was adapted for high density adhesives (>1,000mPa·s). Steps 1-2 mentioned earlier were followed in order to obtain the required dimensions of CFRP laminates. The procedure undertaken during the preparation of DLJs with high viscosity adhesives is detailed as follows:

3. Placing the adhesive was not carried out by pouring but by squeezing out the adhesive with a small spatula. For this reason, laminates were placed on the working area horizontally and the sides of the overlap lengths were sealed with squares end spacers and thermoplastic glue. As it is shown in Figure 3.6 (middle) the spacers were fixed in the contour of the bonded joint of the outer adherent. The height of the spacers determined the required thickness of the joint. This procedure was realised for both outer adherents of each specimen.

4. The adhesive was prepared with a mechanical mixer according to the manufacturers' specifications. As it can be observed in Figure 3.6 (left), the consistency of the adhesive was higher than low viscosity adhesives.
5. Once a uniform adhesive paste was obtained, the adhesive was carefully spread on the outer and inner adherents with a small spatula. This step was especially important because an incorrect application of the adhesive could have substantially increased the number of voids, air bubbles and imperfections of the joint. Thin layers of adhesive were continuously placed on the outer adherents until the required thickness was reached. This allowed detecting the formation of bubbles that were removed by applying pressure. One layer was placed on both faces of the inner adherent following the same procedure. It is worth noting that extra layers were placed to guarantee excess adhesive to prevent gaps in the joints. Control of the adhesive layer thickness and imperfections were major factors during the preparation of the joints.
6. Substrates were joined by placing all the adherents according to the required dimensions and squeezing out softly. Excess adhesive flowed between the spacers and the adherent. When the adherents were in contact with the spacers, the manual pressure was released (see Figure 3.6 right).
7. Specimens were cured at room temperature according to the manufacturers' specifications. Afterwards, spacers and thermoplastic glue were removed.

Despite all the effort made to prevent air bubbles formations and voids, a greater number of defects were found in joints with high viscosity adhesives as it can be seen reported in the experimental work. Specimens were named indicating the geometry and adhesive used.

Figure 3.6. Preparation method of DLJ with high density adhesives.

3.5 Straight bond-type anchorage

Straight bond-type anchorage based on ACI 440.3R [121] were prepared in the laboratory. An adhesive bond-type anchorage consisted of a steel housing inside which a single FRP tendon was bonded with an adhesive. Each specimen included one tendon and two steel housings. Steel housings were provided with an external metric screw thread in order to attach both anchors to the clamping system of the actuator and the reaction plate, respectively. Any other system such as a British standard Whitworth thread or a Dywidag

system could have been used instead of the metric screw thread. Anchorages were tested under quasi-static, fatigue and time-dependent loading. Dimensional details are summarised in Figure 3.7 and Table 3.6. Spew fillets were not considered in the manufacture of straight bond-type anchorages. Two different nomenclature were assumed in the experimental work with straight bond-type anchorage. First, all the adhesive systems [117,119,120,122–128] presented in this work were tested in quasi-static loading. Secondly, fatigue and time-dependent experimental work were carried out with the adhesive 02 because of its handling ease and its high mechanical properties.

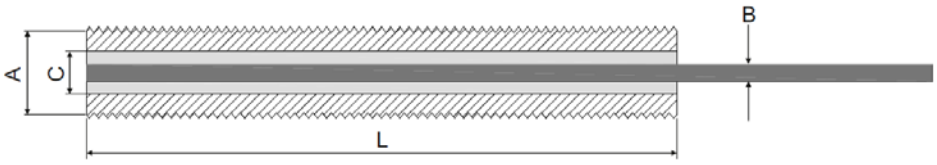

Figure 3.7. Dimensional details of straight bond-type anchorage.

Table 3.6. Geometric characteristics of anchorage.

QUASI-STATIC EXPERIMENTAL WORK							
Specimen	Adhesive	Repetitions	Length, L[mm]	Steel tube outer diameter, A [mm]	Tendon material	FRP rod diameter, B [mm]	Steel tube bore, C [mm]
A_01_02	02	4	200	26	CFRP	8	14
A_02_02	02	2	200	26	CFRP	8	20
A_03_02	02	1	200	26	CFRP	8	24
A_04_02	02	1	200	26	GFRP	6	14
A_05_02	02	1	200	26	GFRP	8	14
A_01_03	03	1	200	26	CFRP	8	14
A_01_04	04	1	200	26	CFRP	8	14
A_01_06	06	2	200	26	CFRP	8	14
A_01_07	07	1	200	26	CFRP	8	14
A_01_08	08	1	200	26	CFRP	8	14
A_01_09	09	1	200	26	CFRP	8	14
A_01_10	10	1	200	26	CFRP	8	14
A_06_04	04	2	300	26	CFRP	8	14
A_06_05	05	1	300	26	CFRP	8	14
A_07_02	02	1	460	26	CFRP	8	14
FATIGUE AND TIME-DEPENDENT EXPERIMENTAL WORK							
Specimen	Adhesive	Repetitions	Length, L[mm]	Steel tube outer diameter, A [mm]	Tendon material	FRP rod diameter, B [mm]	Steel tube bore, C [mm]
A_14	02	5	200	26	CFRP	8	14
A_16	02	5	200	26	CFRP	8	16
A_18	02	6	200	26	CFRP	8	18
A_20	02	6	200	26	CFRP	8	20

As mentioned earlier, two different procedures were undertaken according to the adhesive viscosity. The followed procedure during the preparation of anchorages with high viscosity adhesives is detailed as follows:

1. The FRP rods were cut and machined in the laboratory. Following the recommendations of the guide test ACI 440.3R, a length of three anchors lengths was provided for each specimen to guarantee a smooth stress distribution between anchors. Afterwards, the peel ply provided to protect the composite material surface was removed carefully ensuring there were not impurities on the surface of the rod to be bonded.
2. Steel housings were machined by an external company. Steel housings were cut at the specified length and drilled according to the diameter in Table 3.6. The inner surface of each housing was prepared before attaching the tendon using acetone, a solvent degreasing agent with low hazard rating, to remove any impurities.
3. The first anchor of a specimen was manufactured using a simple beam lying on a support and fixed with nuts and washers (see Figure 3.8). Small centring pieces were placed at both ends of the anchor to subsequently locate the FRP rod and assure co-axiality of the rod inside the steel housing (see Figure 3.9). The bottom of the anchor was also sealed with a thermoplastic sealant to avoid leaks.

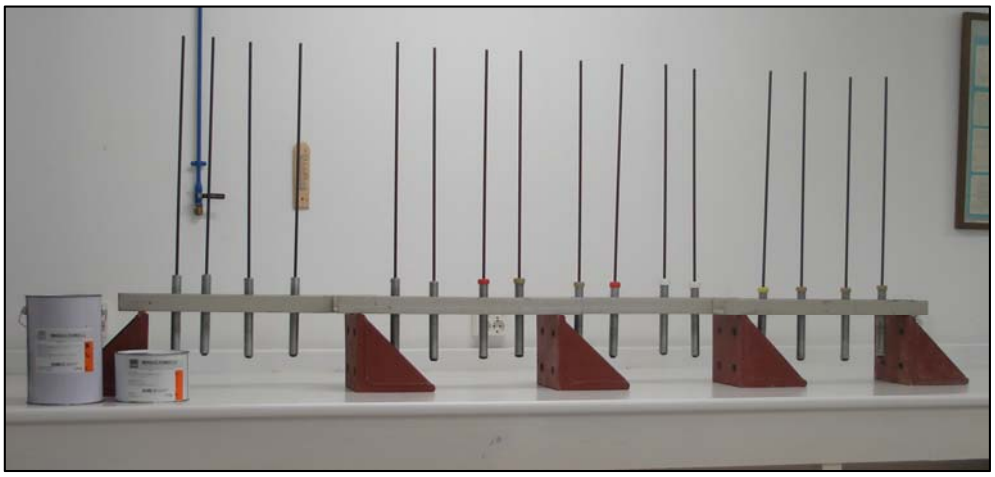

Figure 3.8. Preparation of the first anchor of straight bond-type anchorages.

4. Once the dimensions were ensured with centring pieces, the adhesive was slowly injected with a mixing gun as it can be seen in Figure 3.10 (left). The difficulty of the process lies in the high possibility of air gaps. For this reason, when the anchor was filled with the volume of adhesive required for the joint, the rod was inserted into the steel housing bore and slowly immersed into the adhesive in order to push out the air accumulated into the bore (see Figure 3.10 middle).
5. Manual vibration was applied to the anchor to bring to the surface the small bubbles generated during the process. Afterwards, the necessary adhesive was injected to reach the top of the anchor (see Figure 3.10 right). This step was repeated until there was no evidence of air bubbles or gaps located into the bore.

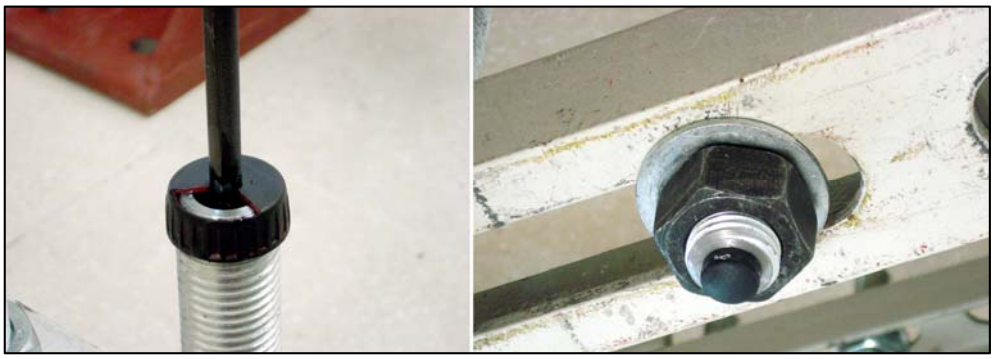

Figure 3.9. Small centring pieces placed at the top (right) and bottom (left) of each anchorage to assure co-axiality of the rod inside the cylinder.

6. The first anchor of the specimen was cured at room temperature according to the manufacturers' specifications. The specimens remained in the beam until the adhesive was completely cured.

Figure 3.10. Preparation method of straight bond-type anchorage with a high density adhesive.

7. Once the first anchor was entirely cured, the other side of the specimen was manufactured using a double-beam (see Figure 3.11). The cured anchor was placed and fixed on the upper beam and in the lower beam the steps 4-6 were repeated to build the anchor of the other end of the specimen.

An easier procedure was adapted for low viscosity adhesives. Steps 1-3 and 6-7 mentioned earlier were followed to prepare the anchors. However, placing the adhesive was realised by injection moulding. This allowed a better quality joint with a lower imperfections rate on the adhesive interfaces. Before applying the adhesive, the rod was placed into the steel housing and the required dimensions were ensured through centring pieces. Afterwards, the adhesive was injected with a syringe until the top of the joint was reached. After curing, the same process was undertaken on the other anchor of the specimen (see Figure 3.12).

Figure 3.11. Preparation of the second anchor of straight bond-type anchorages using a double-beam.

Figure 3.12. Preparation method of straight bond-type anchorage with a low density adhesive.

3.6 Concluding remarks

Single lap joints, double lap joints and straight bond-type anchorages were manufactured and specimens of high quality were obtained. Manufacturing techniques were adapted and modified in order to achieve the best quality for each geometry and adhesive. In all the cases, thickness and overlap length were the main parameters during the preparation of the specimens.

All the specimens were manufactured in a laboratory environment at an average temperature of 23±2ºC and a relative humidity of 50±5%, and techniques depended on the adhesive viscosity. A previous mould was required in all cases in the overlap area in order to maximise the accuracy of the thicknesses and, for low viscosity adhesives, to avoid possible adhesive leaks. For those adhesives with low viscosity (<1,000mPa·s), the adhesive was placed by pouring and injection, whereas for adhesives with high viscosity the adhesive was set by moulding and squeezing.

Due to the procedure, specimens with high viscosity adhesives presented a greater number of imperfections on the interfaces with the adherents than low viscosity adhesives. The main imperfection detected was the accumulation of air bubbles on the interfaces. This caused a reduction of the bonded area and a distortion of the stress distribution. Consequently, the ultimate load and the mechanical properties were decreased.

It is worth mentioning that during the moulding and squeezing procedure, twice the adhesive volume was required for high viscosity adhesives whilst no material was lost when an adhesive of low viscosity was used. Moreover, no other effects such as shrinkage were observed during the adhesive curing which might have changed the geometry and/or mechanical properties of the specimens.

Before testing, specimens were stored in a protective environment away from excessive temperatures and humidity.

Chapter 4. Quasi-static analysis

4.1 Introduction

Experimental tests were undertaken on mechanical anchors, double lap joints (DLJs) and straight bond-type anchorages to study the quasi-static response of the joints. The main study focuses on the ultimate failure load and failure mode for all the joints, as well as the shear stress distribution on the composite material - adhesive interface during the loading process.

A preliminary work was conducted on mechanical anchors in order to assess the general behaviour of this type of anchor and to compare the results with the main conclusions reported in the state of the art. DLJs were performed to analyse and compare the experimental shear stress distribution on the interface with the analytical models of Olaf Völkersen [23] and, Tsai, Oplinger and Morton [30]. Also, an analytical formulation was developed in this research to determine the shear stress distribution on the adhesive interfaces for straight bond type anchorages. The analytical formulation was validated against experimental results in order to provide an approximate distribution of shear stress in the bonded joint for adhesively bonded anchors which behave similarly to linear elastic.

Moreover, numerical modelling was carried out with different adhesive material models in order to investigate the static response of the straight bond-type anchorage and its failure mechanism. The adhesive was modelled with linear elastic properties, von Mises plasticity [44], Drucker-Prager plasticity [45] and progressive damage.

This chapter describes the experimental work, analytical and numerical modelling of mechanical anchors, DLJs and bonded anchors under quasi-static loading.

4.2 Preliminary experimental work

4.2.1 Objectives

Preliminary experimental work was carried out on split-wedge anchorages and double lap joints. The goals of this work were to:

4.2.1.1 Split-wedge anchorages

1. Assess the ultimate load of the split-wedge anchorage system. As mentioned in the state of the art, the transverse force of the wedges tends to cause the premature failure of the tendon. This reduction

of the failure load was assessed and compared among the mechanical anchors with and without a sleeve material.

2. Investigate the failure mode of the anchorage system. Because of the high radial pressure generated by the wedges, the wedges tend to crush and cut the rod in the anchor area at a failure load lower than that specified by the manufacturers. Moreover, failure mode caused by slipping can also occur when the static friction between wedges and the rod cannot equate the load applied to the tendon and the rod is pulled out of the wedges. The ideal failure mode would be the rupture of the fibres along the free length, as this would allow the maximum tensile capacity of the tendon to be reached. The failure modes observed in the experimental work were assessed for mechanical anchors with and without the sleeve material.
3. Analyse the effects of the sleeve material. A copper sleeve material was introduced between the wedges and the rod in order to smoothen the stress concentration at the top of the anchor. Two different thicknesses of sleeve were used and the failure mode as well as ultimate load were studied and compared to the experimental data obtained with mechanical anchors without sleeve material.
4. Analyse the effects of the clamping wedges. As reported in the state of the art, the use of several wedges does not guarantee the same static friction between the wedges and the rod. The failure mode by slipping is usually caused by the non-uniform static friction generated by the wedges of the anchorage. The displacement of the wedges during the experimental tests was also investigated in the preliminary experimental work with mechanical anchors.

4.2.1.2 Double lap joints

1. Study the failure mode of the DLJs. The failure mode of the double lap joints was one of the main goals of the preliminary work. Three different failure mode types may occur with double lap joint. In the first case, the failure takes place in one of the external adherents of the joint. In the second case, the failure is produced by fractures to the adhesive layer, better known as cohesion failure. Finally, the third case, and most common, is the interfacial failure between the adhesive and one of the adherents (adhesion failure). The failure mode was mainly investigated by means of a conventional naked-eye examination of the specimen after failure as well as a thorough microscopy examination of the failure surface.
2. Investigate the stress distribution within the adhesive layer. In order to predict the joint strength, choose an adequate design for each application and know the behaviour of the joints, the stress distribution within the adhesive layer must be known. In this research, the experimental shear stress distribution on the failure surface was obtained through the instrumentation of strain gauges throughout the outer surface of the adherents. The experimental data was compared with the existing analytical formulations of Völkersen and TOM at the failure load in order to find the most suitable failure criterion for the DLJs tested.

3. Investigate the influence of bonded length on the shear stress distribution at the failure load and the ultimate load of the joints, by testing specimens with different adhesive systems and bonded lengths.
4. Develop of an analytical formulation for straight bond-type anchorages. One of the goals that links the experimental work conducted with DLJs and straight bond-type anchorages is the possibility to develop a suitable analytical formulation for straight bond-type anchorages from the analytical formulation that best matches DLJs. The development of an analytical formulation is presented in the straight bond-type anchorage section.

4.2.2 Split-wedge anchorage

A split-wedge anchorage specimen consisted of a CFRP rod of 700mm length and two split-wedge anchorages. The external barrel and wedges were machined by an external company, where the length of the barrel was 128mm and the outer diameter was 117mm. A conical bore was machined in the inner section of the barrel with a large and small bore of 75.8 and 67.3mm, respectively. The evolution of the bore throughout the barrel was linear. Four identical wedges with the same length were machined with an inner bore equal to the tendon diameter. As only CFRP Mbar Galileo tendons were tested with mechanical anchorages, the inner bore of the wedges was 8mm. The outer surface of the wedges was provided with the same angle as the inner bore of the barrel. Split-wedge anchorages for steel tendons generally provide a rough surface in the wedges in contact with the tendon in order to increase the adherence and the load transfer.

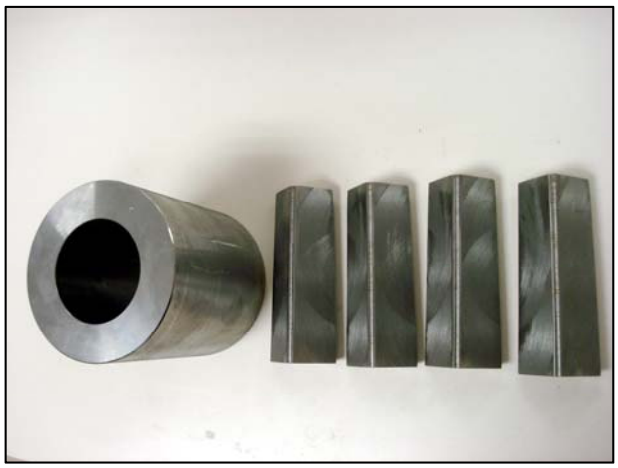

Figure 4.1. Split-wedge anchorage components.

Figure 4.2. Split-wedge anchorage assembly.

As mentioned in the state of the art, one the most accepted modifications is the removal of the roughness of the wedges in order to prevent local damage to the matrix of the composite material and homogenise the stress distribution exerted on the rod. For this reason, the wedge surfaces in contact with the tendon were completely smooth. When a sleeve material was used between the wedges and a barrel, two semi-circular copper tubes of the same rod diameter were attached at each end of the composite material. The length of

the sleeve material was 130mm and the thicknesses tested were 0.5 and 1mm. The split-wedge anchorage components and the assembly with the CFRP tendon can be seen in Figure 4.1 and Figure 4.2, respectively.

4.2.2.1 Test setup

Quasi-static experimental test were undertaken using a universal testing machine with a capacity of up to 200kN. Split-wedge anchorages were tested in tension to failure under force control at 50N/s. The load and displacement were recorded at a frequency of 50Hz using a Suzpecar data acquisition system. The pull-out test setup is shown in Figure 4.3.

Figure 4.3. Quasi-static test setup for split-wedge anchorages.

The specimen was mounted just before testing. The rod was placed among the wedges and the whole was introduced into the barrel. A uniform pressure was manually applied to the bottom of the wedges in order to clamp the tendon. It is worth mentioning, that during the clamping process it was important to clamp all the wedges simultaneously so that relative displacements could be avoided. This allows a proper functioning of all the wedges during the loading process. When a sleeve material was used, the two semi-circular tubes were previously positioned at each end of the rod. The specimen was placed into the universal testing machine and the final clamping process was completed at the same time as the anchorage was loaded. The geometries of all the configurations are summarised in Table 4.1.

Table 4.1. Mechanical anchor configurations.

Specimen	Repetitions	Sleeve material thickness, t [mm]
SW_01	1	-
SW_02	1	0.5
SW_03	3	1.0

The load cell placed on the crosshead of the universal testing machine continuously recorded the force during the test. Also, an external linear variable displacement transducer (LVDT) was placed in the movable crosshead of the testing machine. It is important to notice that the LVDT recorded the rate of extension of

the movable crosshead precisely, and therefore the real displacement of the anchorages might not have been the same. However, the measured displacement can give an approximation of the behaviour of the entire system. In addition, a high-speed recording camera MotionBLITZ was used to record the failure of the specimen.

4.2.2.2 Results and discussion

The experimental load-displacement curve measured from all the split-wedge anchorages and the failure load reached in each case are summarised in and Figure 4.4 and Table 4.2. It can be noticed that the specimen without the sleeve material reached the lowest ultimate load. As mentioned by Nanni et al. [8], Malvar and Bish [6], Sayed-Ahmed et al. [10], Taha et al. [9,14], Schmidt et al. [1] and Bennitz [129], there is a high radial pressure generated by the wedges at the loading end of the anchor which caused the premature failure of the rod. The high stress concentration generally crushes and cuts the tendon fibres at the loading end of the anchor. This result was confirmed during the post-testing examination of the specimen. Figure 4.5 shows a failure detail at the end of the anchor. It can clearly be seen that the failure was caused by crushing and splintering of the tendon. The matrix of the composite material was not able to carry the transverse load generated by the static friction at the loading end of the anchor and it collapsed instantaneously, causing a partial cut across the tendon. Since the ultimate tensile strength of the tendon is 2500MPa (125kN according to its section), the SW_01 configuration approximately reduced its tensile strength in a 35%.

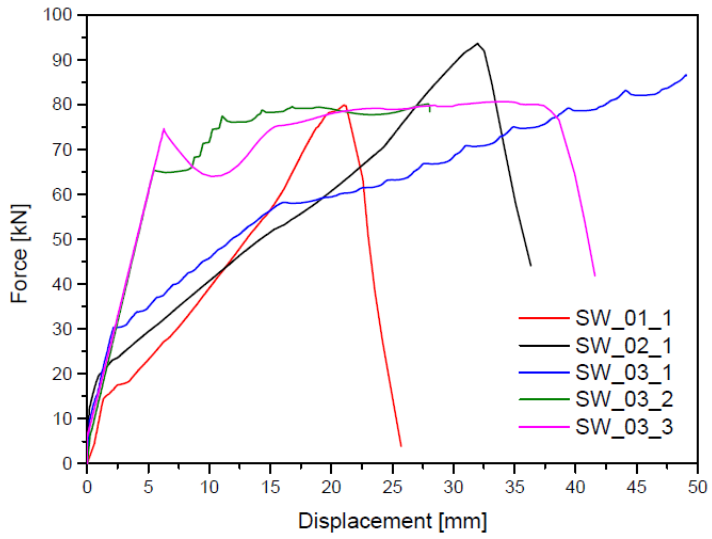

Figure 4.4. Measured load and displacement response of all the specimens with split-wedge anchorages.

As indicated by Malvar and Bish [6], an intermediary material between the tendon and the wedges with a low stiffness smoothens the stress distribution at the loading end of the anchor. This allows for the stress concentration and the premature failure of the tendon by crushing or splintering to be avoided. For this purpose, SW_02 and SW_03 configurations were equipped with a thin layer of copper with an elastic

modulus of 120GPa attached to end of the tendon. As can be seen in Table 4.2, these configurations reached the highest failure load, particularly the specimen SW_02_1 with a copper sleeve thickness of 0.5mm. Even though the failure mode of the specimens was a combination of crushing and slipping, Figure 4.6 shows how the failure of the specimen was closer to the ideal failure of the anchor, where the rupture of the fibres is produced along the free length. In all the cases the failure of the tendon was instantaneous and explosive, releasing all the energy stored in the rod. Figure 4.7 shows the recorded failure of specimen SW_02_1 with the high-speed recording camera which elapsed in 396 msec.

Table 4.2. Summary of experimental failure load of specimens with split-wedge anchorages.

Specimen	Experimental failure load [kN]
SW_01_1	79.96
SW_02_1	93.69
SW_03_1	86.70
SW_03_2	80.17
SW_03_3	80.72

Figure 4.5. Failure detail of the specimen SW_01_1.

Figure 4.6. Failure detail of the specimen SW_02_1.

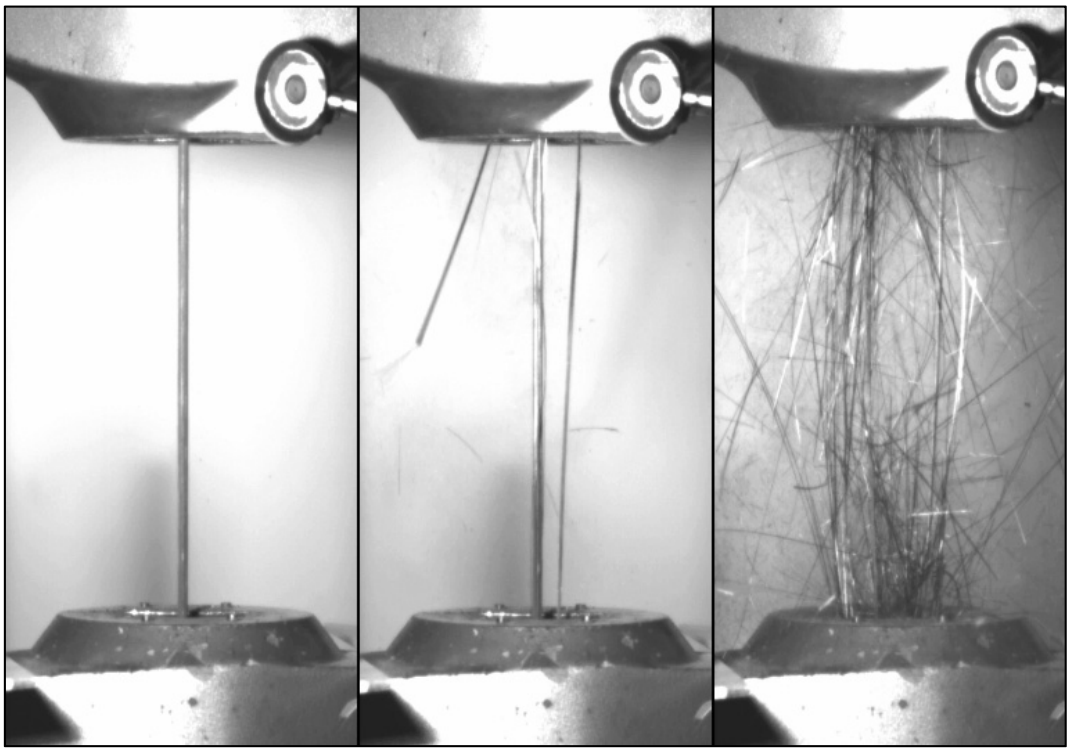

Figure 4.7. Recorded failure of specimen SW_02_1 (396msec)

Although a higher failure load was reached in specimens with the sleeve material, it was not enough to achieve the maximum tensile strength of the rods. The sharp edge of the wedges caused a 25% reduction of the tendon tensile strength. Also, these configurations reached the plastic yield stress of the sleeve material initiating the slipping of the rod until the specimen was not able to carry more load. As the sleeve material enhanced the behaviour of the mechanical anchorages, a material with a higher yield stress is suggested for further research. The yield strength of the copper used in this research was 70MPa. Aluminium alloys, on the other hand have yield strengths ranging from 200MPa to 600MPa and a stiffness of about one-third of steel. This would enable a smooth stress distribution at the loading end of the anchor, allowing the specimens to reach higher loads.

Furthermore, there was a large difference amongst the displacement demonstrated by the specimens during the loading process. As mentioned earlier, a large displacement during loading may cause a premature failure of the joint by slipping and is mainly produced by a non-uniform clamping of the wedges. Although the wedges were positioned carefully, a negligible difference to the naked eye might result in a large displacement difference amongst wedges at high loads. It can be seen in Figure 4.5 how the penetration of the wedges into the barrel was different at the end of the test. This is one of the causes of a premature failure by crushing or slipping. As shown in Figure 4.4, the configurations SW_01 and SW_02 demonstrated a large displacement mainly due to the non-uniform displacement of the wedges. The configuration SW_03, on the other hand, showed a large slip of the tendon because of the non-uniform displacement of the wedges combined with the plastic response of the sleeve material. As illustrated in Figure 4.4, when the plastic

yield stress of the sleeve material was reached, the specimen was not able to keep carrying higher loads and the displacement kept increasing until the premature failure of the tendon was produced.

4.2.2.3 Concluding remarks

A preliminary experimental work with mechanical anchorages was carried out in the laboratory under quasi-static loading until failure. Because of its similarity with the current systems for steel and compactness, a split-wedge anchorage for composite materials was investigated with and without a sleeve material. Based on this study, the following conclusions can be drawn:

1. As mentioned by many researchers, the tapered shape of the wedges introduces a transverse force which tends to damage the matrix of the composite material at the loading end of the anchor. The transverse force generally causes the premature failure of the tendon in the area of the anchorage. In this research, wedges dug into the tendon causing premature failure of the rod. The tensile strength capacity of the rods was reduced by around 25-36% of its maximum tensile strength.
2. Failure modes by crushing or splintering and slipping were observed in this study. When the anchorages were used without a sleeve material, the wedges cut the fibres of the rod transversely at the loading end of the anchor, leading to a crushing failure mode. Placing a copper sleeve between the wedges and the tendon allowed an increase of the failure load to be obtained. Furthermore, the failure mode was closer to the rupture of the fibres along the free length. However, the failure was still located at the anchorage area. In all cases, the failure was instantaneous and catastrophic, rapidly releasing all the energy accumulated in the rods.
3. The sleeve material placed between the wedges and the tendon clearly enhanced the behaviour of the specimen. Nevertheless, the plastic yield stress of the copper was reached during loading which produced the slipping of the tendon. Aluminium alloys are suggested for further research because of their low elastic modulus (70GPa) and their high plastic yield stress (>200GPa). These would allow the stresses at the top of the anchor to be smoothed and the plastic yield stress would not be reached during the loading procedure.
4. The non-uniform displacement of the wedges during the loading caused a premature failure of the rods by crushing and slipping. With the aim of increasing the efficiency of the whole, the uniform penetration of the wedges into the barrel must be guaranteed.

4.2.3 Double lap joint

Double lap joints were manufactured as indicated in Chapter 3 with the adhesives 01, 02 and 03, and tested under quasi-static loading up to the point of failure. It is worth noticing that the experimental campaign on DLJs was undertaken progressively. First, joints with geometry 01 were tested until failure and the rest of the geometries were designed from the results obtained.

4.2.3.1 Test setup

Quasi-static tests on double lap joints, based on ASTM D-3528 [118], were carried out using a Suzpecar electromechanical testing machine. The test setup is shown in Figure 4.8. Pneumatic metallic clamps were used to grip the ends of each specimen which were perfectly aligned to avoid unwanted effects. The surfaces of the grips were provided with shallow hollows so that the load transfer with the specimen could be increased. Although this system seems more suitable for metallic specimens it worked correctly where the grips were in direct contact with the composite material. However, there was a small slip between the grips and the specimen and therefore, the displacement recorded by the movable crosshead was greater than the displacement experimented by the joint.

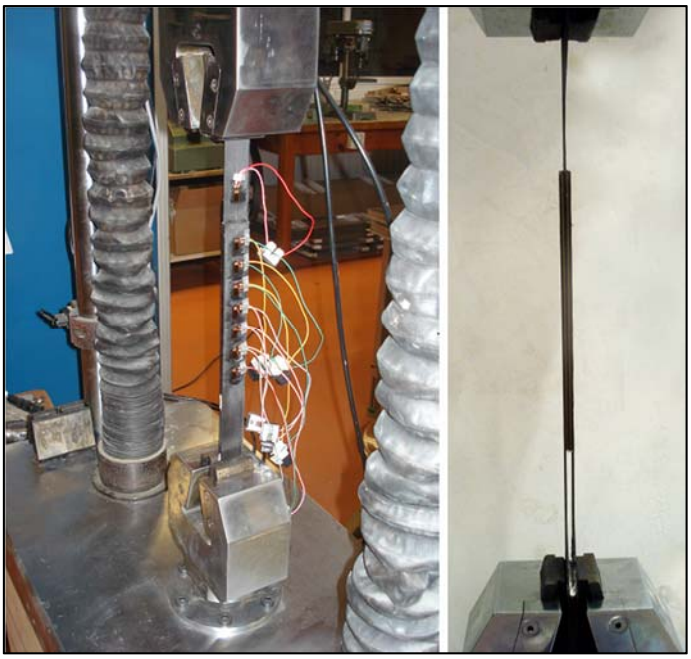

Figure 4.8. DLJ test setup.

In addition, several specimens were instrumented with strain gauges in order to obtain the experimental shear stress distribution on the adherent-adhesive interface. The strain gauges were placed longitudinally every 25mm throughout the outer surface of the composite material in the direction of the bonded length. The strain gauges used in this research had a gauge length of 10mm and a resistance of 350 Ω.The surface beneath the gauges was prepared before attaching the gauges using an abrasive paper (grade 220) and M-Prep Conditioner A immediately followed by M-Prep Neutralizer 5A from Vishay. The gauges were then bonded on the prepared area using a cyanoacrylate adhesive M-bond 200. The specimens instrumented with strain gauges were DLJ_01_01_1, DLJ_01_03_1, DLJ_02_01 and DLJ_03_02. The force, displacement and strain were continuously recorded during the test at a frequency of 50Hz using an MGCPlus acquisition system.

4.2.3.2 Strain data acquisition

The experimental shear stress distribution on the adhesive interface is one of the main aims of the experimental campaign for both double lap joints and straight bond-type anchorages. For this purpose, several specimens were instrumented with strains gauges attached longitudinally in the external face of the outer adherent. Given that the inner adherent cannot be instrumented, the shear stress analysis was carried out on the outer adherent - adhesive interface.

The experimental shear stress distribution on the interface for DLJs was obtained through the experimental data recorded along the outer adherent with the strain gauges. Considering uniaxial stress on the outer adherent allows the normal stress of the outer adherent to be related with the shear stress transferred on the adhesive interface between two strain gauges. The external surface of the outer adherent was divided in several lengths. The position of two consecutive strain gauges defined a length.

The normal strain difference measured between two consecutive strain gauges gave the average normal stress transferred to the adhesive through shear stress for each length. The average shear stress of each length transferred to the adhesive was represented with a unique value in the centre of each length (see Figure 4.9).

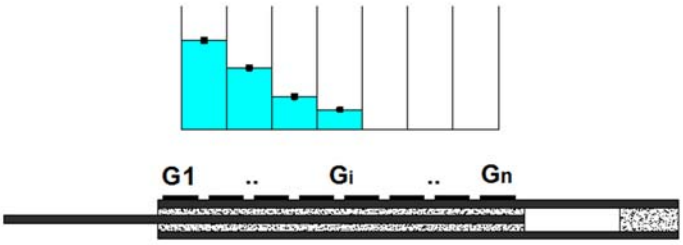

Figure 4.9. Experimental shear stress distribution on the outer adherent - adhesive interface.

The variation of longitudinal force acting on the outer adherent, F_i, can be expressed as follows through Equation 4.1:

$$F_i = A_t \cdot E \cdot \left(\varepsilon_i - \varepsilon_{i-1}\right) \quad \text{(Equation 4.1)}$$

where A_t is the transversal section of the outer adherent, E is the longitudinal elastic modulus of the outer adherent and, ε_i and ε_{i-1} are the strain measures between two consecutive strain gauges. Moreover, the average shear stress on the outer adherent-adhesive interface can be expressed as shown in Equation 4.2:

$$F_i = A_l \cdot \tau_{avg\_i} \quad \text{(Equation 4.2)}$$

where τ_{avg_i} is the average shear stress for each length between two consecutive strain gauges and A_l is the longitudinal section of the outer adherent-adhesive interface for each length. The uniaxial stress hypothesis on the outer adherent allows equating Equations 4.1 and 4.2 (see Equation 4.3).

$$\tau_{avg\_i} = \frac{A_t \cdot E \cdot (\varepsilon_i - \varepsilon_{i-1})}{A_l} \quad \text{(Equation 4.3)}$$

The experimental shear stress distribution of the double lap joints was directly compared with the classical analytical formulations of Olaf Völkersen for double lap joints, which neglects adherent shear deformations, and the improved theoretical solution of Tsai, Oplinger and Morton (TOM), which includes the effect of adherent shear deformations. The comparison of the experimental data and the analytical formulations is discussed in the next subsection.

4.2.3.3 Results and discussion

The experimental failure load of all double lap joints that were tested are summarised in Table 4.3. It is worth noticing that the maximum capacity of the testing machine utilised was 35kN. In the cases where the maximum capacity of the machine was reached, the test was stopped and the failure load of the specimen was not obtained.

Table 4.3. Summary of experimental failure load of double lap joint specimens.

Specimen	Experimental failure load [kN]	Average shear stress on the bonded joint at failure [MPa]	Specimen	Experimental failure load [kN]	Average shear stress on the bonded joint at failure [MPa]
DLJ_01_01_1	21.70	2.70	DLJ_01_03_2	23.65	2.95
DLJ_01_01_2	18.05	2.25	DLJ_02_01	25.60	2.20
DLJ_01_01_3	22.70	2.80	DLJ_03_02	-	>4.50
DLJ_01_01_4	20.30	2.55	DLJ_04_02	23.90[1]	>6.00
DLJ_01_02_1	-	>4.50	DLJ_05_02_1	18.05	12.90
DLJ_01_02_2	-	>4.50	DLJ_05_02_2	16.40	11.70
DLJ_01_03_1	22.90	2.85	DLJ_05_02_3	15.95	11.40

As shown in Figure 4.10, force-displacement curves for specimens with geometry 01 were principally linear up to the instantaneous and explosive failure. Specimens manufactured with adhesives 01 and 03 showed a comparable response under quasi-static loading until failure. This may be primarily due to their similar stiffness. Moreover, as detailed in Table 4.3, the average shear stress on the adhesive-inner adherent joint at the failure load was reported. Similarly, specimens with adhesive 01 and 03 showed a similar maximum average shear stress on the bonded length ranging between 2.50 and 3.00MPa.

[1] The maximum tensile strength of the composite material was reached and thus the failure did not occur in the bonded joint. However, the average shear stress on the bonded joint at failure was 6MPa.

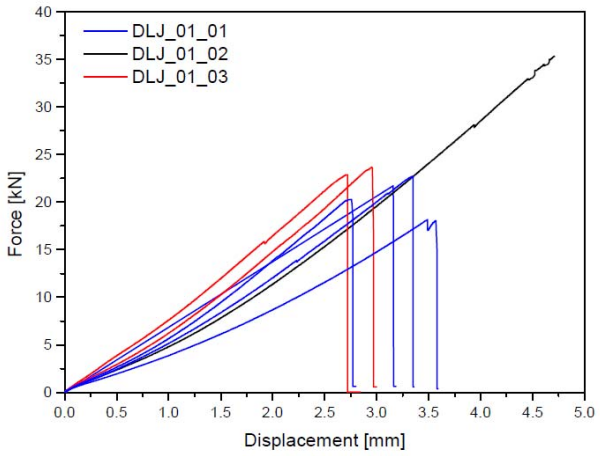

Figure 4.10. Measured load and displacement response of DLJs with geometry 01.

Specimens with adhesive 02 reached the maximum tensile capacity of the tensile machine and the test was stopped. Force-displacement curves were linear up to 35kN. At this point of the investigation, the failure was not reached for specimens with this adhesive and the average shear stress at the failure load was unknown. In all cases where the failure was reached, it occurred within the adhesive but very close to the interface between the adhesive and the adherent. Figure 4.11 shows a representative failure surface of all the specimens with adhesive 01 and 03. It can be seen that the adhesive layer was broken into small pieces. When the failure load was reached, the debonding of the adhesive-adherent interface occurred followed by a release of all the energy stored in the adhesive during the loading process.

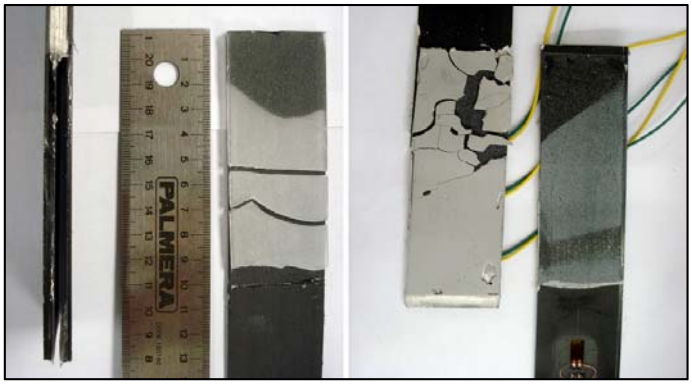

Figure 4.11. Typical failure surfaces in the DLJs for adhesive 01 (left) and adhesive 03 (right).

Due to the symmetry of double lap joints, the load is mainly transferred by shear stress through the adhesive-adherents interfaces. Thus, research has focused on the analysis of the stresses in the adhesive bonded length. Specimens DLJ_01_01_1 and DLJ_01_03_1 were therefore instrumented with strain gauges and the shear stress distribution along the bonded length was obtained at the failure load of each sample. The experimental shear stress distribution on the bonded joint was compared to the classical analytical formulation of Völkersen and the improved theoretical solution of TOM. These comparisons are presented

in Figure 4.12 and Figure 4.13. It can be seen that the prediction from TOM's analytical formulation is more consistent in both cases than the classical analytical formulation. This reflects the importance of considering the shear deformation of the adherents in the analysis for double lap joints.

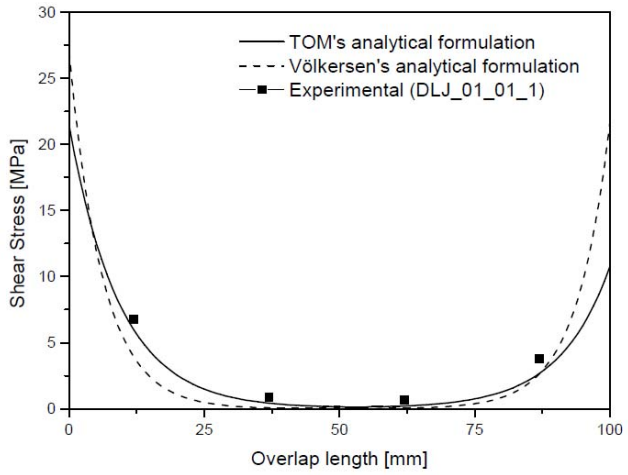

Figure 4.12. Experimental shear stress distribution along the overlap length of specimen DLJ_01_01_1 compared to the analytical formulation of Völkersen and TOM.

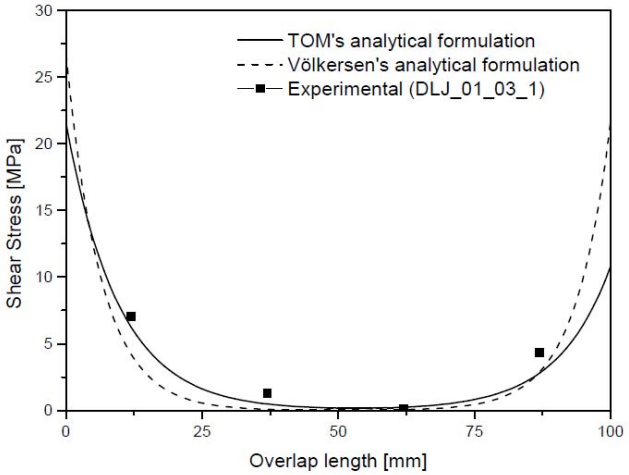

Figure 4.13. Experimental shear stress distribution along the overlap length of specimen DLJ_01_03_1 compared to the analytical formulation of Völkersen and TOM.

According to the experimental data, the shear stress distribution in the centre of the joints remained very close to zero, whereas the highest values of shear stress were located at the ends of the bonded joint (see Figure 4.12 and Figure 4.13). This may be caused by the high stiffness of the adhesives used where the adhesive layer cannot develop large deformations. As the centre of the bond line barely contributed to the load transfer between the adhesive and the adherents, longer bonded joints were manufactured and tested in order to investigate the length influence. As it can be seen in Figure 4.11 (right), a greater number of air bubbles formed during the manufacturing of specimens with high viscosity adhesives. This generates a distortion of the stress distribution along the bond line and a decrease of the failure load. This issue will be

investigated in further detail in the failure surface analysis section. For this reason, and taking into account the similar results between specimens with adhesives 01 and 03, solely adhesive 01 was considered for further investigation.

Returning to the comparison of the shear stress distribution, it can be seen that there was a high non-uniformity of stress distribution along the overlap length. The maximum stresses predicted by the analytical formulations were located at the end of the overlap length where, clearly, the classical analytical formulation overestimated the experimental shear stress at the ends of the joint.

As mentioned before, the geometry 02 was manufactured in order to investigate the length influence of the bonded joint where the width of the specimen was reduced to ensure the failure within the range capacity of the testing machine. In spite the specimen failure not having being reached for samples with adhesive 02, a longer specimen was manufactured and instrumented with strain gauges to investigate the shear stress distribution along the overlap length with the adhesive 02 at the maximum capacity load of the testing machine. Due to its lower stiffness, a somewhat more uniform stress distribution was expected than the other adhesive systems tested. The load-displacement curves recorded during the loading process were fundamentally linear up to either the point of failure, for the specimen DLJ_02_01, or the maximum capacity of the testing machine, for the specimen SLJ_03_02.

Both specimens were longitudinally instrumented with strain gauges along the outer surface of the adherent in order to obtain the experimental shear stress distribution on the adhesive-adherent interface. Figure 4.14 shows the comparison of the experimental data obtained with specimen DLJ_02_01 against the analytical formulations of Völkersen and TOM at the failure load. The same behaviour as in previous tests was observed. The shear stress at the centre of the overlap length was almost zero, whilst the highest values were located at the end of the bonded length. TOM's analytical formulation fitted the experimental data more closely, whereas the classical analytical formulation overestimated the shear stress distribution at the ends of the joint.

Furthermore, increasing the overlap length enlarged the shear stresses close to zero. This suggests that there was an effective bonded length for high stiffness adhesives which in this case was approximately 75mm. The high stiffness of the adhesive did not allow the deformation of the adhesive layer and, consequently, only the ends of the overlap length transferred the load from the inner adherent to the outer adherent through the adhesive layer. Once a maximum value of shear stress was reached on the bonded joint, the failure started and it was rapidly propagated throughout the overlap length causing the collapse of the specimen. This result suggests that high stiffness adhesives are not entirely suitable for straight bond-type anchorages as a short effective overlap length limits the overlap length. It is important to mention that ACI [121] recommends a minimum length of the steel tube ranging between 300 and 460mm.

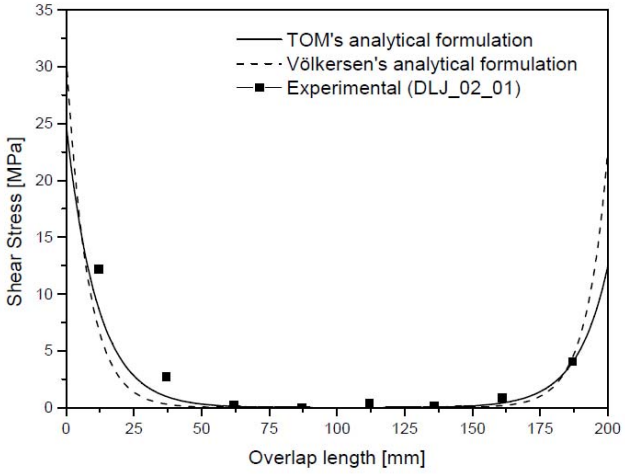

Figure 4.14. Experimental shear stress distribution along the overlap length of specimen DLJ_02_01 compared to the analytical formulation of Völkersen and TOM.

Furthermore, the experimental shear stress distribution on the adhesive-adherent interface of the DLJ_03_02 was obtained at 30kN and compared with the existent analytical formulations as shown in Figure 4.15. It can be seen that TOM's analytical formulation matched with the experimental distribution along the overlap length. The difference between the analytical formulations was higher in this case as the shear stress distribution predicted by the classical analytical formulation was overrated at the ends of the bonded joint and underrated at the centre.

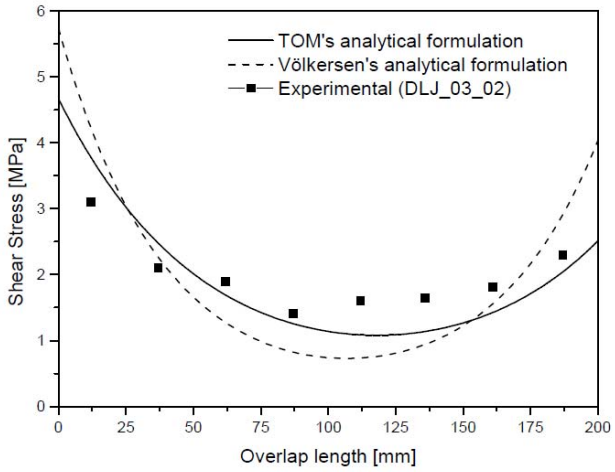

Figure 4.15. Experimental shear stress distribution along the overlap length of specimen DLJ_03_02 compared to the analytical formulation of Völkersen and TOM.

In contrast to previous shear stress comparisons, DLJ_03_02 developed a more uniform stress distribution along the overlap length. This result was mainly caused by the low stiffness of the adhesive allowing the deformation of the adhesive layer along the bonded joint. Clearly, this behaviour of the joint caused by a low stiffness adhesive fitted conveniently with the intended purpose for straight bond-type anchorages as the effective length can be much larger in comparison with high stiffness adhesives.

In order to reach the failure on DLJs with adhesive 02, the geometry 04 was manufactured where the width was reduced four times. However, during the loading process the ultimate tensile strength of the composite material was reached causing the failure of the laminate. For this reason, the geometry 05 was designed with a smaller overlap area and the failure occurred on the bonded joint. Figure 4.16 shows the measured load and displacement of these specimens during the loading process.

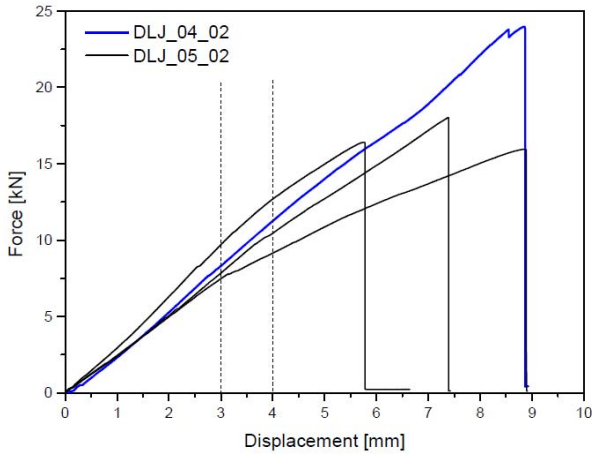

Figure 4.16. Measured load and displacement response of DLJs with geometries 04 and 05.

The load-displacement curves were mainly elastic up to the point of failure, which occurred instantaneously. As it can be seen from curves of specimens DLJ_05_02, there was a significant change in the slope between 3 and 4mm of displacement. This slope change was produced when the average shear stress on the adhesive-adherent interface was greater than 6MPa. This suggests that adhesive 02 might be yielded or damaged before failure. As the average shear stress on the interfaces of the specimen DLJ_04_2 was 6MPa at failure load, this slope change was not perceived. Also, in specimens DLJ_05_02, the failure occurred suddenly on the bonded joint and all the energy accumulated in the adhesive layer was released. However, as shown in Figure 4.17, the adhesive layer remained in one piece due to its higher flexibility.

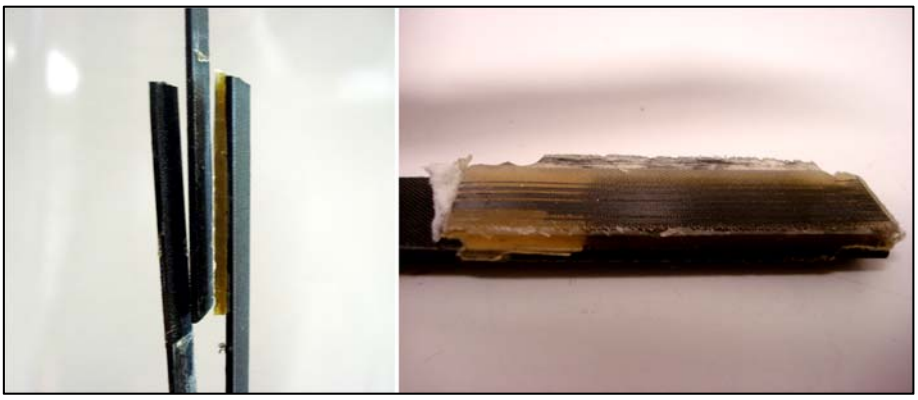

Figure 4.17. Typical failure surfaces in the DLJs with adhesive 02.

Finally, it was determined through DLJ_05_02 specimens that the maximum average shear stress on the interface of the joint was approximately 12MPa. A parametric study was conducted with TOM's analytical formulation in order to determine the effective length of bond line for double lap joints with adhesive 02. The effective length was found to be about 400mm.

4.2.3.4 Failure surface analysis

A failure surface analysis was conducted on DLJs using a stereoscope microscope SCZ-T4P Carton at 20x magnification. Pictures of the failure surface were taken with a USB Microscopic camera Deltapix DP300. DLJs with all three adhesives tested in this preliminary work were examined. Figure 4.18, Figure 4.19 and Figure 4.20 show the results of the failure surface analysis of specimens with adhesive 01, 02 and 03, respectively. The failure surface analyses for each adhesive displayed are representative of the failure mode of all specimens tested. The conventional naked-eye examination after failure showed in Figure 4.11 and Figure 4.17, revealed that the failure in all specimens was produced within the adhesive but very close to the adhesive-adherent interface, better known as adhesive failure. This failure mode was confirmed with the microscopic analysis, where the CFRP laminate (from the failure area) was impregnated with a small layer of adhesive. It also contained adhesive particles due to a local cohesive failure of the adhesive.

It can be seen that the failure surface of specimens with adhesive 01 and 02 was very close to the adhesive-adherent interface where the laminate surface roughness largely remained complete. In these cases, the layer of adhesive impregnated on the laminate was very thin and thus the braided surface of the composite material was visible. The microscopic analysis revealed that the laminate surface roughness contained small air formations in the shallow depressions of the composite material mainly caused by the manufacturing procedure.

Figure 4.18. CFRP laminate failure surface of specimen DLJ_01_01_1 magnified 20x.

Figure 4.19. CFRP laminate failure surface of specimen DLJ_05_02_1 magnified 20x.

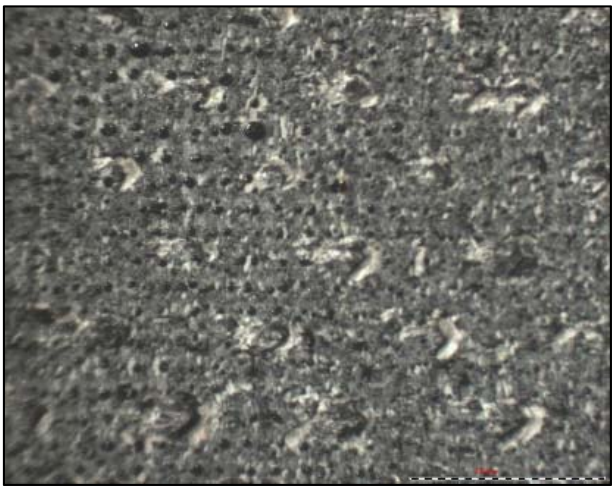

Figure 4.20. CFRP laminate failure surface of specimen DLJ_01_03_1 magnified 20x.

The failure surface of the specimen with adhesive 03 was also close to the adhesive-adherent interface but there was a thicker layer of adhesive on the CFRP laminate. In Figure 4.20 it can be clearly seen that the number of imperfections due to the manufacturing procedure was greater in this case. As mentioned in Chapter 3, low viscosity adhesives (adhesives 01 and 02) were manufactured by pouring and injecting, whereas high viscosity adhesives (adhesive 03) were prepared by moulding and squeezing. The latter generated a greater number of imperfections on the interfaces due to the procedure, as it can be seen in Figure 4.20.

The amount of defects detected on the failure surfaces, mainly formation of voids and air bubbles, were quantified. The commercial software Autocad/CAD 2011 was used to analyse the images and it was found that imperfections caused an area reduction of the overlap bond of 0.9 and 0.7% for specimens with adhesives 01 and 02, respectively. For specimens with adhesive 03 there was an area reduction of the overlap bond of around 11%.

4.2.3.5 Concluding remarks

Preliminary experimental work with double lap joints was conducted in the laboratory under quasi-static loading until failure. The different adhesives that were tested offered an understanding of the failure mechanism and the load transfer behaviour of the bonded joints. The following conclusions can be drawn:

1. In all cases, the failure was produced within the adhesive but very close to the adhesive-inner adherent interface. The damage began at the loading end of the joint and it was propagated very rapidly throughout the overlap bonded length releasing all the energy stored during the loading process.
2. The failure surface analyses with a stereoscope microscope revealed that low viscosity adhesives presented a lower number of defects on the adhesive-adherent interface than high viscosity adhesives due to the manufacturing process undertaken in this research.
3. For all the DLJs, the failure mode occurred instantly and explosively. Double lap joints with adhesives 01 and 03 mainly showed an elastic-linear behaviour up to failure whilst specimens with adhesive 02 showed a slight softening of the stiffness. This might be caused due to the yielding or damaging of the adhesive during the loading process.
4. The experimental shear stress distribution on the failure surface was obtained and compared with the existent analytical formulations for DLJs of Völkersen and TOM. It was found that the TOM's analytical formulation offered a high prediction of the stress distribution on the interface up to failure, highlighting the importance of the adherent shear deformation. The classical analytical formulation, on the other hand, overestimated the shear stress prediction at the ends of the bonded joint.
5. The highest shear stresses on the failure surface at the ultimate load were at the ends of the bonded length whilst the lowest shear stresses were placed at the centre of the joint. For the adhesives with high stiffness, the lowest shear stresses were very close to zero limiting the usable bonded length. Increasing the overlap length for high stiffness adhesive resulted in a length increase of the shear stresses close to zero. Thus, there is an effective bonded length that can be much larger for low stiffness adhesives.

4.3 Straight bond type anchorage

4.3.1 Objectives

Straight bond-type anchorages were experimentally and numerically studied under quasi-static loading up to failure. Also, an analytical formulation was developed to predict the shear stress distribution on the adhesive-inner adherent interface. Notably, the geometry of the anchorages was designed in order to obtain the failure of the joint in the bonded interface between the adhesive and the composite material. This

allowed the failure mechanism of the bonded joint to be investigated. The objectives of this section were as follows:

1. To study the failure mode of the straight bond-type anchorages. As was observed in the preliminary experimental work with DLJs, the failure was expected on the adhesive-adherent interface by adhesion failure. The failure mode was examined after testing through a conventional naked-eye and microscopy examination of the failure surface. In addition, two specimens with GFRP rods were designed and tested in order to study the failure mode in the free length of the rod.
2. To investigate the different mechanical response of anchorages by using different adhesive systems. Ten adhesives were tested and the behaviour during the loading process was assessed. As was seen in the experimental preliminary work, force-displacement curves can show either an elastic-linear behaviour or a change in the slope due to yielding or damage of the adhesive. For this purpose, ten structural adhesives for composite materials with high strength were tested and, force and displacement were measured continuously until failure. The failure load of the specimen as a whole was also assessed.
3. To analyse the influence of the anchor length during the loading process and the failure load by testing specimens with different bonded length. This was then done with straight bond-type anchorages with adhesive 02.
4. To investigate the influence of the adhesive thickness with anchorages with adhesive 02. Three different adhesives thicknesses were tested so that the evolution of shear stress along the overlap bonded length and their influence on the failure load could be studied.
5. To obtain the static strength of the anchor geometries which are studied under time-dependent and fatigue loads. In order to normalise the time-dependent and fatigue experimental data, the static strength of the anchorages is required. However, even though CFRP rods were provided under the same trade name to perform fatigue and stress relaxation testing activities, the superficial roughness of the tendons was differed slightly. For this reason, quasi-static tests were also conducted on the anchors with the rods with the thinnest and thickest adhesive layers of the geometries studied in Chapter 5 and 6 (A_01_02 and A_02_02). The ultimate failure load was evaluated in order to determine whether the superficial roughness had a significant influence on the final failure load of the straight bond-type anchorages.
6. To develop an analytical formulation for straight bond-type anchorages from TOM's analytical formulation for double lap joints. In addition, an anchorage was instrumented with strain gauges on its outer surface in order to compare and validate the proposed analytical formulation.
7. To numerically research the response of straight bond-type anchorages with adhesive 02 under quasi-static loading. The bonded length and adhesive thickness influence was also numerically

investigated. Different adhesive models were investigated and compared with the experimental data in order to obtain a model able to predict the response of the straight bond-type anchorages.

4.3.2 Experimental work

Straight bond-type anchorages with ten different adhesives were experimentally tested under quasi-static loading in the laboratory up to failure. The composite material used in this research was principally CFRP, except for specimens A_04_02 and A_05_02 which were manufactured with GFRP tendons. Due to the lower tensile strength of GFRP, the failure mode in the free length of the tendon was studied. However, the main study focuses on the analysis of the stresses on the adhesive-tendon interface which was achieved through anchorages with CFRP rods.

4.3.2.1 Test setup

Pull-out tests on the anchor models based on ACI 440.3R B.10 [121] were carried out using an MTS actuator. All specimens were tested in tension until failure under displacement control, at 1mm/min. The casings had external metric screw threads which were used to attach the specimens to the test machine. However, the specimen A_03_02_1 was not provided with an external metric screw as it was longitudinally instrumented with eight strain gauges placed every 25mm throughout the outer surface of the steel housing in order to validate the analytical formulation developed in this research.

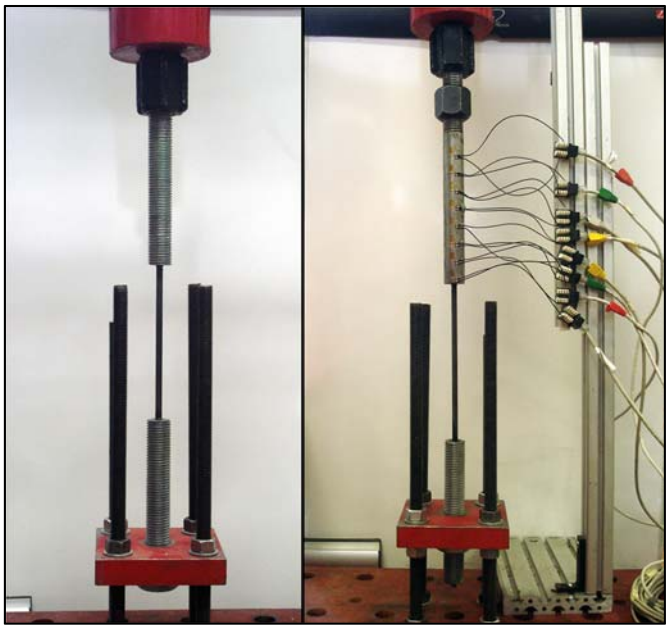

Figure 4.21. Test setup of straight bond-type anchorage.

The strain gauges used in this study had a gauge length of 10mm and a resistance of 350 Ω.The surface beneath the gauges was prepared before attaching them with the use of abrasive paper (grade 220) and M-Prep Conditioner A immediately followed by M-Prep Neutralizer 5A from Vishay. The gauges were then attached to the prepared area of the housing steel using a cyanoacrylate adhesive M-bond 200. The load,

displacement and strain data were recorded at a frequency of 50 Hz using an MGCPlus data acquisition system. The pull-out test specimens, with and without strain gauges, is shown in Figure 4.21. Also, a high-speed recording camera MotionBLITZ was used to record the failure.

4.3.2.2 Results and discussion of CFRP rod anchorages

In all specimens with CFRP rods the failure occurred within the adhesive but very close to the interface between the adhesive and the tendon. The failure produced on the interface allows the failure mechanism of the bonded joint and the influence of the anchor geometry to be studied. Figure 4.22 shows the typical failure phenomenon throughout the bond length. It can be seen how there are still some adhesive particles attached to the CFRP tendon after failure.

Figure 4.22. Typical failure surface in the bonded anchorages with CFRP.

Table 4.4. Summary of experimental failure load of straight bond-type anchorages.

Specimen	Experimental failure load [kN]
A_01_02_1	58.70
A_01_02_2	60.20
A_01_02_3	64.97
A_01_02_4	39.95
A_02_02_1	75.10
A_02_02_2	51.15
A_03_02_1	87.24
A_01_03_1	37.70
A_01_04_1	84.70
A_01_06_1	49.53
A_01_06_2	45.42
A_01_07_1	59.02
A_01_08_1	72.77
A_01_09_1	73.85
A_01_10_1	43.72
A_06_04_1	107.86
A_06_04_2	104.26
A_06_05_1	78.01
A_07_02_1	110.70

Table 4.4 summarises the experimental failure load measured in straight bond-type anchorages with CFRP rod tested under quasi-static loading. Although different failure mechanisms were observed depending on the adhesive used, the experimental failure load was considered as a reference of the maximum tensile strength of each anchorage. All specimens showed similar behaviour during the loading process which was either principally linear elastic up to the point of instantaneous failure or elastic-plastic with a significant change in the slope of force-displacement curve. Figure 4.23 shows the recorded failure of specimen A_01_03_1 with a high-speed recording camera which elapsed in 1.3 sec.

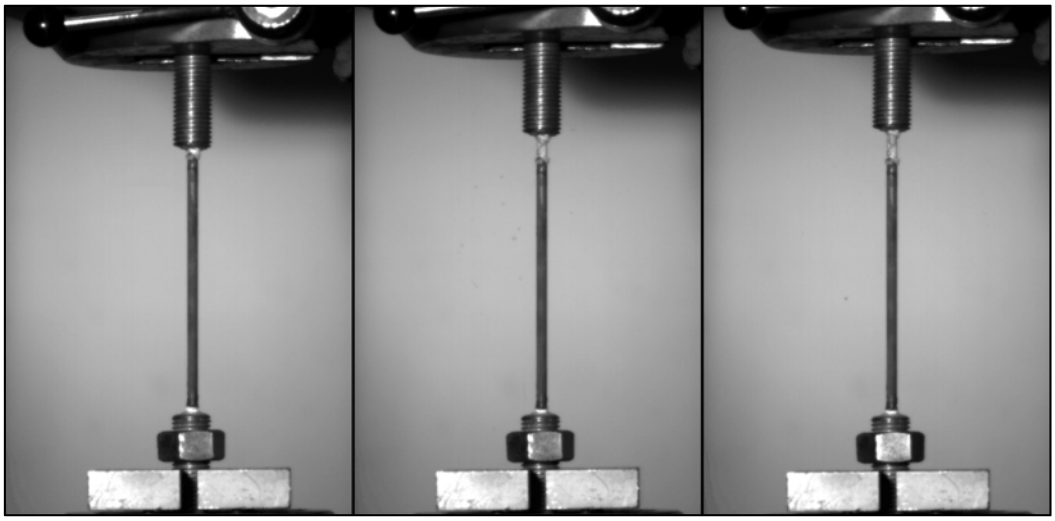

Figure 4.23. Recorded failure of specimen A_01_03_1. (1.3 sec)

Specimens with adhesive 02 were studied more thoroughly where the influence of the overlap length and thickness were assessed. The adhesive 02 was chosen for further investigation due to its high experimental failure load in comparison with other adhesive systems tested. Furthermore, the low viscosity of the adhesive also allowed for specimens of high quality to be manufactured. With low viscosity adhesives, a lower number of imperfections on the adhesive, such as accumulation of air bubbles, than high viscosity adhesives were obtained, avoiding a reduction of the bonded area and a distortion of the stress distribution due to the imperfections.

Figure 4.24 shows the measured load and displacement response of the specimens with adhesive 02. As can be seen, force-displacement curves were generally linear up to the point of failure, which occurred suddenly and explosively. It is worth noticing that the displacement was measured by the internal linear variable differential transformer of the actuator which registered the displacement of the MTS actuator cylinder accurately but did not represent the real displacement of the specimen due to little relative displacements among all the components of the testing system. However, the measured displacement offers an understanding of the behaviour of the specimens under quasi-static loading.

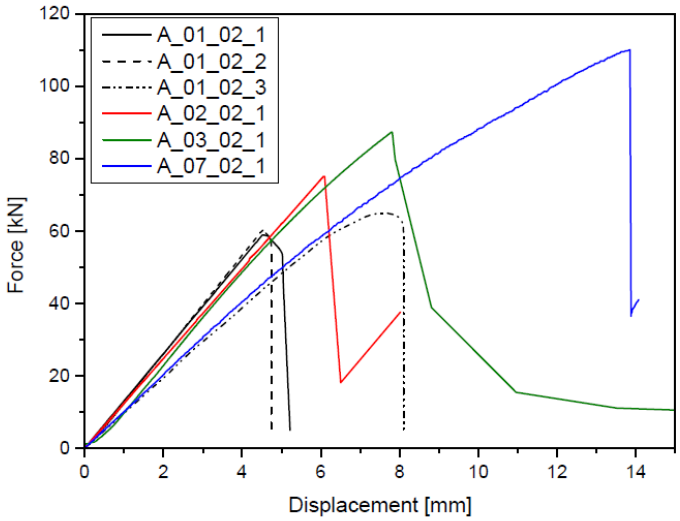

Figure 4.24. Measured load and displacement response of anchorages with CFRP rods and adhesive 02.

On some force-displacement curves there was a slight softening in the slope. This might be due to yielding of or damage to the adhesive before failure. Also, the slope change was more evident for specimens that reached greater failure loads. Furthermore, it can be noticed that the specimens with higher adhesive thickness achieved a higher ultimate force. The relationship between the failure load reached and the adhesive layer thickness was mainly linear. A reason for this result may be that a more uniform distribution of adhesive stress occurred at the top of the bonded joint with the thicker adhesive layers. Moreover, with the same adhesive thickness a higher ultimate force was reached with the longer bonded joint. This was probably due to the fact that there was more load-carrying area of the adhesive in the longer joints.

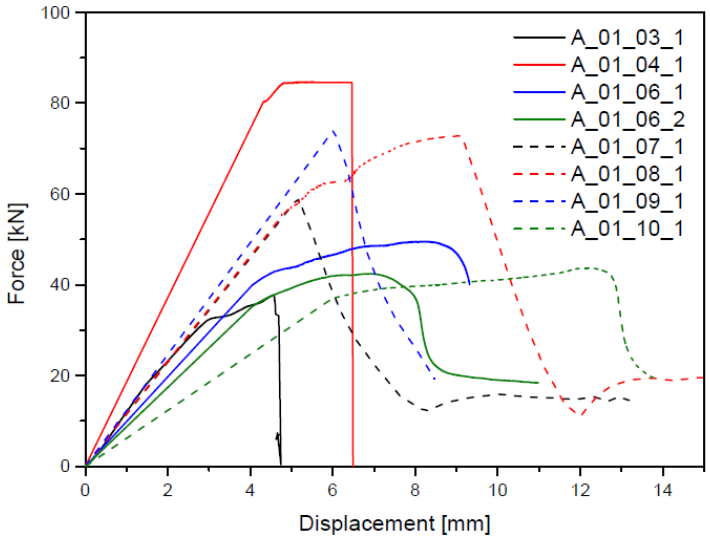

Figure 4.25. Measured load and displacement response of anchorages with geometry 01.hesive 02

Diverse structural adhesives for composite materials with high strength were also tested and assessed. It was observed that the force-displacement curves were mainly linear up to sudden failure. However, a few specimens presented a plastic region before failure. Specifically, specimens A_01_04_1 and A_01_08_1 behaved mostly liner-elastically up to the point that specimens reached a small plastic region very close to the failure load. Specimens A_01_06 and A_01_10_1 showed a larger plastic region when approximately the 80% of the failure load was exceeded. Finally, the specimen A_06_05_1 showed an extensive plastic region when the maximum load was reached. The measured load and displacement responses of all these specimens are shown in Figure 4.25 and Figure 4.26.

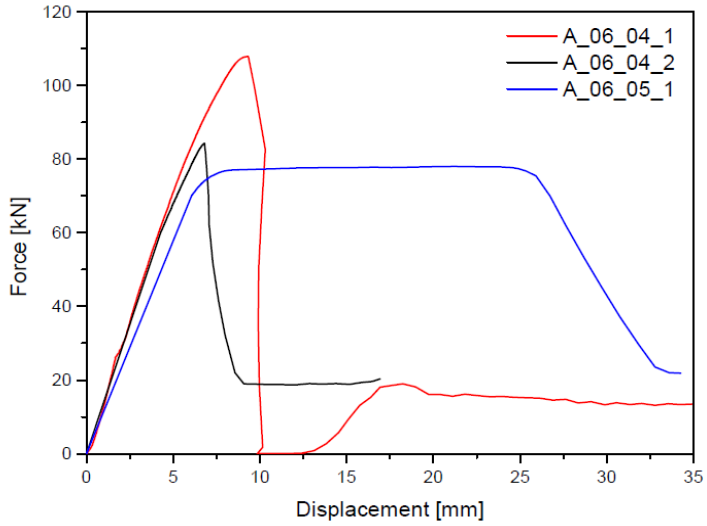

Figure 4.26. Measured load and displacement response of anchorages with geometry 06.

As mentioned in the introduction of this section, the CFRP rods utilised for fatigue and time-dependent analyses were provided with a slightly different superficial roughness. As the static strength of the anchorages is an essential value for normalising the fatigue and time-dependent data, quasi-static tests were conducted on the anchors with the rods with the thinnest and thickest adhesive layers (specimens A_01_02_4 and A_02_02_2). The failure loads obtained were compared with the failure loads of specimens A_01_02 and A_02_02_1. Quasi-static tests were undertaken according to the test setup and static strengths of 39.95 and 51.15kN were obtained for the thinnest and thickest adhesive layers, respectively. It is clear that there was a significant reduction in the ultimate load of the specimens when compared to the experimental results shown in Figure 4.24 (reduction of 30-35%). Therefore, these results will be used solely as static tensile strength of the anchors for fatigue and time-dependent analyses. The force-displacement curves of these specimens are shown in Figure 4.27. Similarly, these specimens behaved mostly linear up to instantaneous failure.

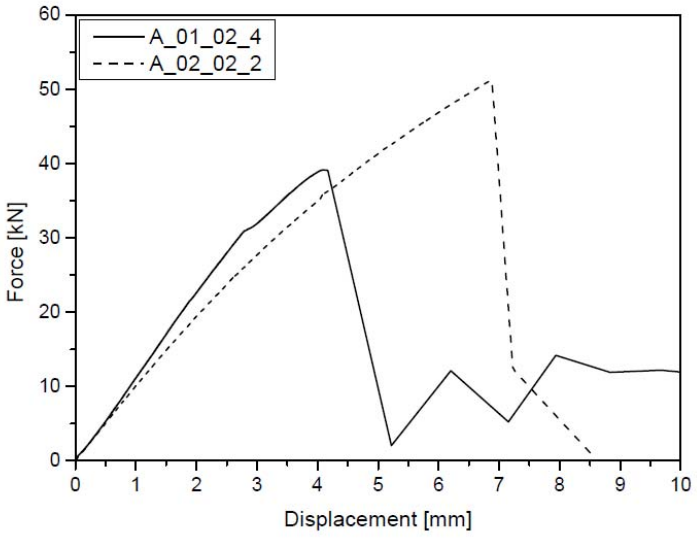

Figure 4.27. Measured load and displacement response of anchorages A_01_02_4 and A_02_02_2.

4.3.2.3 Results and discussion of GFRP rod anchorages

Specimens with GFRP were designed so that the maximum tensile strength of the rod can be reached and that the failure mechanism when it is produced in the free length of tendon can be studied. Figure 4.28 shows the failure of the GFRP tendons in their free length. Due to the lower tensile strength of the GFRP[2] used, the ultimate capacity of the chemical bond was not expected, as the tendon would reach its maximum tensile strength. During the loading process, premature fibre failures in the tendon were noticed as the applied load approached the failure load. When the maximum capacity of the tendon was exceeded, the failure in the free length of the rod was produced rapidly and suddenly. Figure 4.29 shows the recorded failure of specimen A_04_02_1 with high-speed recording camera which elapsed in 332 msec. The failure loads of specimens A_04_02 and A_05_02 were 29.85 and 50.94kN, respectively.

Figure 4.28. Failure mode of straight bond-type anchorages with GFRP.

[2] The tensile strength of the GFRP was 2.5 times lower than CFRP rods used in this research.

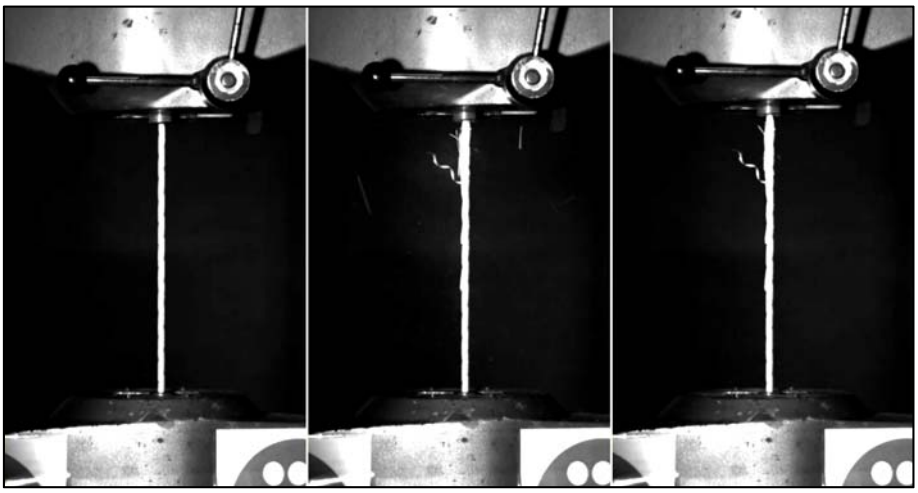

Figure 4.29. Recorded failure of specimen A_04_02_1. (332 msec)

The force-displacement curves of both specimens measured during the loading process up to failure are shown in Figure 4.30. It can be seen that a substantial change occurred in the slope of the specimen A_05_02_1 when approximately 60% of the failure load was exceeded. This may largely be caused by the onset of damage in the adhesive layer. However, the ultimate tensile strength of the tendon was reached before the failure of the chemical bond. Furthermore, the specimen A_04_02_1 showed an elastic-linear behaviour up to sudden failure. This may be caused due to the ultimate tensile strength of the rod was reached before the damage in the adhesive layer was initiated.

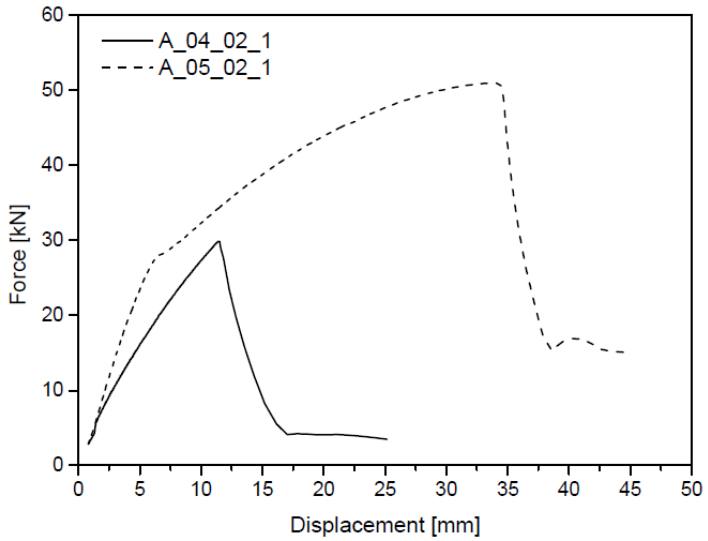

Figure 4.30. Measured load and displacement response of the anchorages with GFRP rods.

4.3.2.4 Failure surface analysis

A failure surface analysis was conducted on straight bond-type anchorages with adhesive 02 using a stereoscope microscope SCZ-T4P Carton with magnification levels ranging from 8x to 20x. Pictures of the failure surface were taken with a USB Microscopic camera Deltapix DP300. Figure 4.31 and Figure 4.32

show the failure surface of the specimen A_01_02_1 magnified x8 and x20, respectively. As mentioned earlier, the failure occurred within the adhesive but very close to the adhesive-rod interface. It can be seen, that the CFRP rod contained a large amount of adhesive particles and it is considered that the adhesive reached its maximum adhesion strength during the loading process causing it to fail very close to the interface. As shown in more detail in Figure 4.32, the tendon contained adhesive particles on its entire surface. The failure surfaces displayed are considered representative of all specimens tested with adhesive 02 under quasi-static loading (excluding specimens A_01_02_4 and A_02_02_2).

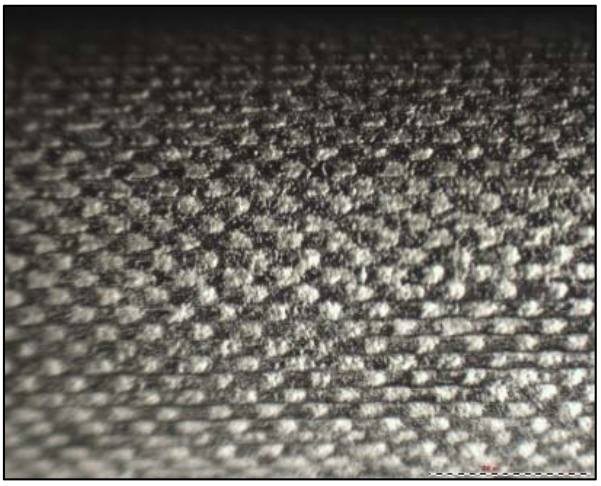

Figure 4.31. CFRP tendon failure surface of specimen A_01_02_1 magnified x8.

Figure 4.32. CFRP tendon failure surface of specimen A_01_02_1 magnified x20.

Figure 4.33 and Figure 4.34 show the failure surface of the specimen A_01_02_1 magnified x8 and x20. As previously mentioned, a second batch of CFRP rods was used in order to study the fatigue and time-dependent behaviour of the straight bond-type anchorages. It was detected that the superficial roughness of these tendons was differed slightly from the first batch and the quasi-static results showed that there was a reduction of the static strength of around 30-35%. As expected, the failure surface analysis revealed that the chemical bond with the composite rod was not completely successful. The strength of attraction between

the adhesive and the rod was reduced, and the number of adhesive particles attached to the failure surface was lower. As mentioned by Packham [130] the surface energies of the adhesive and substrate mainly determine the adhesive bond and the molecular attraction between adhesive and tendon. In this case, the adhesion strength reduction might be caused due to a lower surface energy of the second batch of rods.

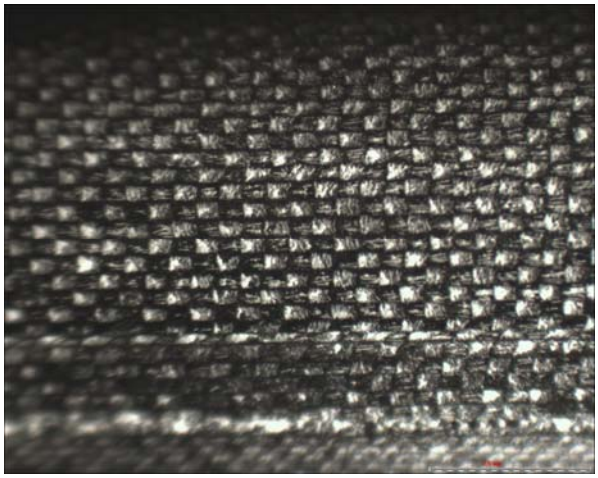

Figure 4.33. CFRP tendon failure surface of specimen A_01_02_4 magnified x8.

Figure 4.34. CFRP tendon failure surface of specimen A_01_02_4 magnified x20.

4.3.3 Analytical modelling

An analytical formulation is proposed in this section in order to determine the shear stress distribution in straight bond-type anchorages. As TOM's analytical formulation offered an accurate prediction of the shear stress distribution in DLJs, the equilibrium equations presented by Tsai, Oplinger and Morton [30] were modified in order to take into account the circular geometry of the anchor. A linear constitutive equation of the materials involved was considered. Also, a linear shear distribution through the thickness of the substrates was assumed.

Only an outline of the analysis is presented in this section, full details are provided in Appendix A. Following the nomenclature of Figure 4.35, the shear stress distribution on the interface between the adhesive and the rod, τ_i can be determined through Equation 4.4.

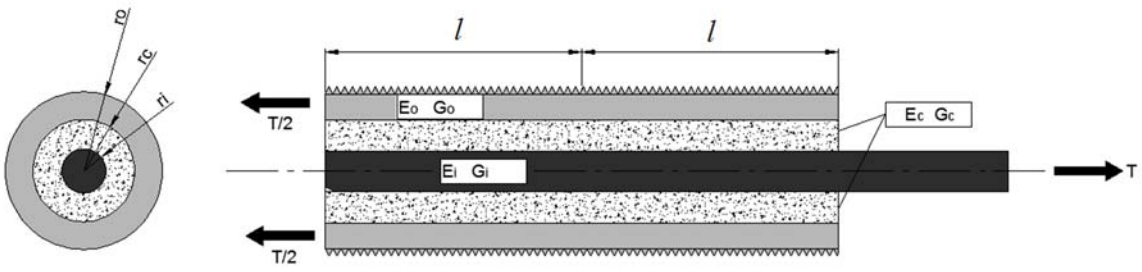

Figure 4.35. Anchor geometry.

$$\tau_i = A \cdot sinh(\beta \cdot x) + B \cdot cosh(\beta \cdot x) \quad \text{(Equation 4.4)}$$

The coefficient β is determined by:

$$\beta^2 = \frac{\frac{G_c \cdot r_i}{(r_c - r_i)} \cdot \left(\frac{2}{E_i \cdot r_i^2} + \frac{2}{E_o \cdot (r_o^2 - r_c^2)} \right)}{1 + \frac{G_c}{(r_c - r_i)} \cdot \left[\frac{5 \cdot r_i}{12 \cdot G_i} + \frac{1}{(r_o^2 - r_c^2)} \cdot \left(\frac{r_i \cdot (r_o - r_c) \cdot (r_o^2 - r_c^2)}{2 \cdot G_o \cdot r_o} - \frac{r_i \cdot (r_o^4 - r_c^4)}{4 \cdot G_o \cdot r_o \cdot (r_o - r_c)} \right) \right]} \quad \text{(Equation 4.5)}$$

where E_0 is the elastic modulus in the longitudinal direction of the steel housing, E_i is the elastic modulus in the longitudinal direction of the FRP tendon, G_0 is the shear modulus in the longitudinal direction of the steel housing, G_i is the shear modulus in the longitudinal direction of the FRP tendon and G_c is the shear modulus in the longitudinal direction of the adhesive layer. The coefficients A and B for a 'Pull-Pull' solution are determined by:

$$A = \frac{\beta \cdot l \cdot \tau_{mi}}{\cosh(\beta \cdot l)} \cdot \left(\frac{1 - \frac{E_i \cdot r_i^2}{E_o \cdot (r_o^2 - r_c^2)}}{1 + \frac{E_i \cdot r_i^2}{E_o \cdot (r_o^2 - r_c^2)}} \right) \quad \text{(Equation 4.6)}$$

$$B = \frac{\beta \cdot l \cdot \tau_{mi}}{\sinh(\beta \cdot l)} \quad \text{(Equation 4.7)}$$

in which τ_{mi} is the average shear stress on the adhesive-rod interface and is defined by Equation 4.8;

$$\tau_{mi} = \frac{T}{2 \cdot \pi \cdot r_i \cdot 2 \cdot l} \quad \text{(Equation 4.8)}$$

It should be noted that this formulation assumes that the adhesive behaves like a linear elastic material. The adhesive used in the experimental tests was ductile and it was likely that a plastic zone may have been developed before final failure. Thus the analytical formulation was validated at lower levels of load for the specimen A_03_02_1, which was instrumented with strain gauges on the outer steel tube (adapted to introduce a region with no thread) for this purpose.

Considering the axial stresses in the steel housing and the steel constitutive equation, the analytical formulation for the shear stress on the adhesive-tube interface can be used to find the normal strain in the steel housing (assumed constant across the wall thickness). This was compared with the experimental recorded data at low values of load where the adhesive remained within its linear region. Figure 4.36 compares the experimental and analytical strains along the external surface of the anchor. It can be seen that the correlation between the two shows a good agreement, thus validating this analysis at lower loads.

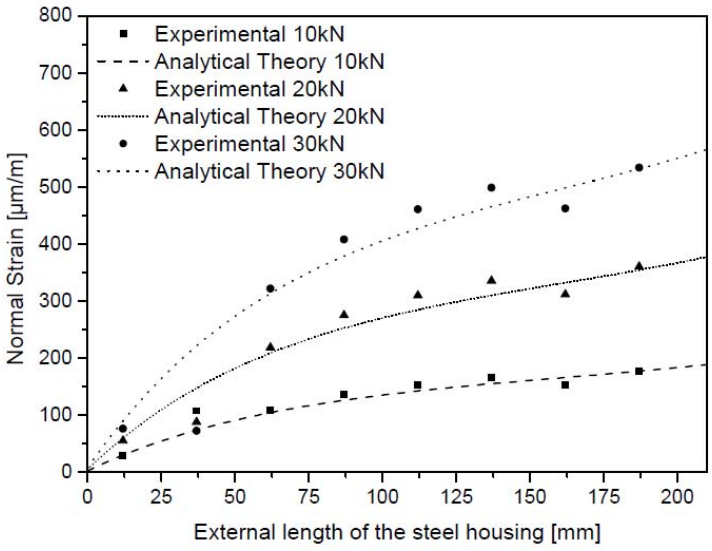

Figure 4.36. Normal stress distribution along the external surface of the steel housing of the specimen A_03_02 at different loads.

In addition, the analytical solution was used to predict the shear stress distribution at the adhesive-rod interface for the four geometries at their respective experimental failure loads presented in Figure 4.24. As anticipated, the maximum shear stresses developed, were considerably in excess of the yield stress for the adhesive. However, it can be seen that the maximum shear stress predicted was common for all the configurations with the same anchor length independent of the adhesive thickness. Thus, in principle, it might be possible to use the analytical solution in order to predict the failure load of the anchor for different thicknesses. However the failure stress would have no physical significance. Further, it would not be applicable for different anchor lengths as can be seen in Figure 4.37 shows that using this elastic analysis a higher “adhesive failure stress” is required for a longer anchor length where the bond length refers to the adhesive-rod interface bond from the loading end of the anchor to the bottom of the anchor. In practice, it

is likely that yielding occurs and that the longer anchor length enables a longer yield zone to be developed, producing higher joint strengths. To investigate this further and model some of these more complex aspects it was necessary to undertake FE modelling, which will be discussed in the next section. Also, the developed solution analysis and the linear finite element method were found to be in very good agreement with each other (see Figure 4.39).

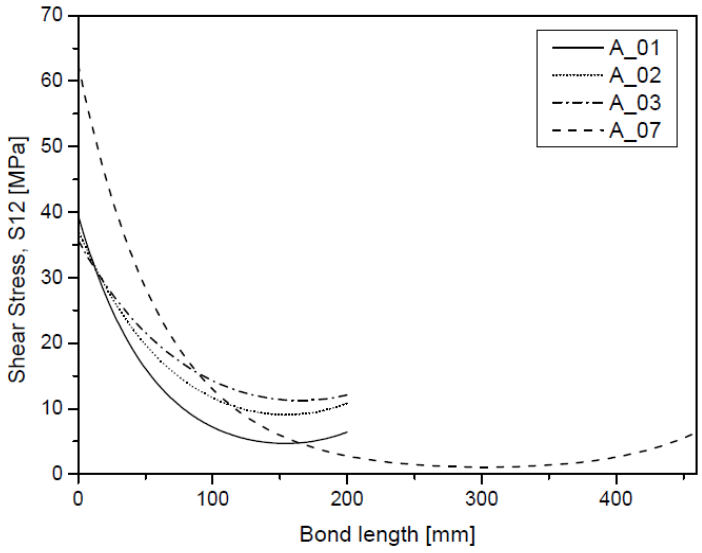

Figure 4.37. Shear stress distribution along the adhesive-rod interface obtained with the analytical formulation.

4.3.4 Numerical modelling

In order to predict the quasi-static response of the bonded anchorage, a finite element model was developed in Abaqus/CAE. This study focuses on the experimental results obtained with straight bond-type anchorages with adhesive 02 shown in Figure 4.24. Owing to the shape of the anchor, a 2D axisymmetric model was used (see Figure 4.38). This simplified the model and hence optimised computing resources. Four different geometries were modelled according to the geometries that were tested experimentally (A_01_02, A_02_02, A_03_02 and A_07_02). The bottom of the steel housing was fully fixed and the top of the CFRP rod was loaded either with an axial force or an axial displacement. Different material models of increasing complexity were investigated for the adhesive layer. Initially the adhesive was modelled with linear elastic properties. Following this, adhesive yielding was modelled using both von Mises plasticity and Drucker-Prager plasticity, the latter enabling the hydrostatic dependency of the adhesive to be included in the modelling. Finally, progressive damage was included in the modelling in order to capture the entire mechanical response of the anchor including the damage initiation and evolution leading to joint failure. Progressive damage modelling with a cohesive zone was investigated where the elements followed a traction-separation law. This section contains a more detailed discussion on a number of these aspects. Geometric non-linearity was included in all the analyses.

A structured mesh composed by four-noded axisymmetric stress elements (CAX4R) with a mesh density of 0.5mm was used for the whole model. When a cohesive zone was used, structured four-node axisymmetric cohesive elements (COHAX4) with a multi-linear traction-separation response were utilised to study the progressive damage in the adhesive bond line. The size of the cohesive element was 0.5x0.5mm throughout the adhesive bond line.

A sensitivity analysis of the mesh was conducted for all the geometries in order to determine the most suitable mesh size for the straight bond-type anchorages. As the experimental failure load was located on the adhesive-tendon interface, numerical modelling work focused on the stress distribution on the adhesive layer. A convergence analysis was undertaken reducing the mesh size until a lower variation of 1% of the maximum shear stress distribution on the adhesive-tendon interface was obtained. The sensitivity analysis was performed through a linear elastic analysis of all the geometries and it was considered suitable for the rest of the analyses.

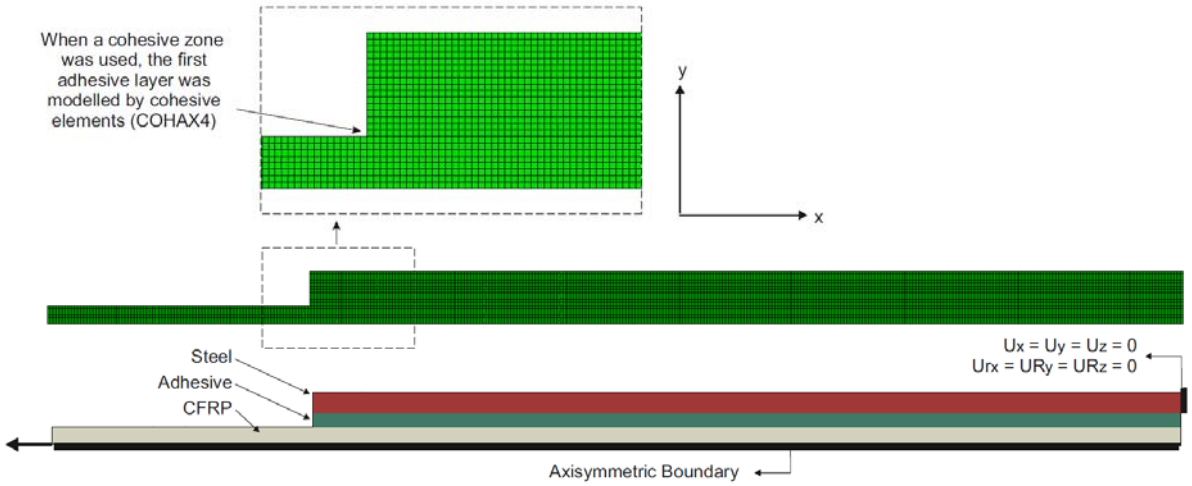

Figure 4.38. Finite element mesh and boundary conditions for the geometry with a bore and length of 14 and 200mm respectively.

Finally, it is worth mentioning that the main objectives of the numerical modelling lied in the stress distribution of the adhesive layer due to the premature failure of the straight bond-type anchorages on the adhesive-tendon interface. For this reason, the composite material tendon was modelled as an elastic orthotropic material in all cases, as the failure mode was not achieved in the rod. The steel housing was also modelled as an isotropic elastic material as there were no evidence of local failures during the experimental campaign.

4.3.4.1 Linear elastic modelling

Initially a linear elastic analysis was undertaken for all four configurations. The material properties required for each material for this analysis were the Young's modulus and Poisson's ratio. The mechanical properties of the materials are summarised in Chapter 3. In these linear elastic analyses the experimental failure load

was applied to the CFRP bar with a linear ramps instead of a displacement. The shear stress distribution along the adhesive-rod interface was assessed at the failure load for all the geometries (see Figure 4.39).

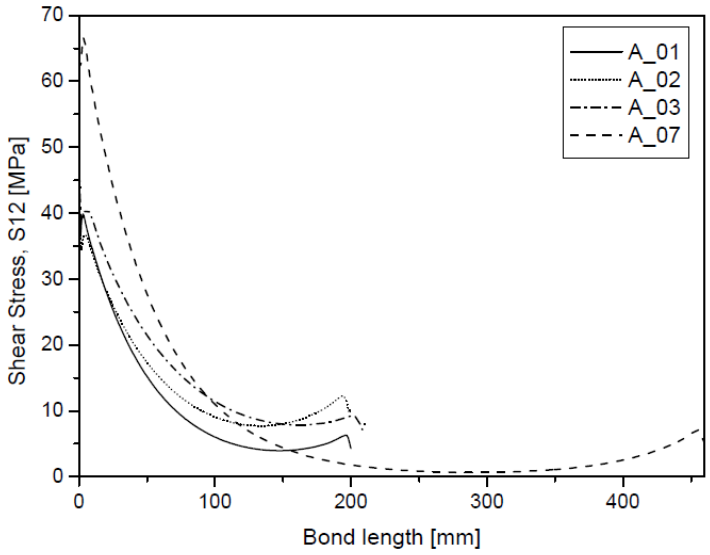

Figure 4.39. Shear stress distribution along the adhesive-rod interface obtained with lineal elastic modelling.

The results were consistent with and confirm the analytical modelling discussed above (compare Figure 4.37 and Figure 4.39). The anchors with the same bonded length but different adhesive thicknesses all reached similar shear stress values when loaded at their respective failure loads even though their geometries were moderately different. According to these results, a higher load can be reached for the same level of maximum stress as the adhesive thickness increases (as noted with the analytical solution proposed). However, the linear elastic finite element analyses showed a perturbation in the stress at both ends of the adhesive layer due to the end effects. The analytical solution was not able to provide this level of detail. Figure 4.40 illustrates the shear stress distribution through the different materials at the top of the anchor where the stresses were at their highest. The in-board peak in the adhesive shear stress, which gave rise to the perturbation discussed above and seen in Figure 4.39, is clearly seen in this more localised view. However, although the maximum adhesive stresses at the failure load were the same for all three anchors of the same length, there are two main drawbacks. The first is that this value is not the same for the longer anchor and the second is that these maximum stresses are well in excess (>40%) of the yield stresses provided by the manufacturer for this adhesive[3]. Both factors suggest that the behaviour of the adhesive cannot be modelled as linear elastic. The adhesive is reasonably ductile and clearly there will be considerable yielding in the joint prior to failure. Consequently, further analyses were carried out considering non-linear behaviour of the adhesive. From the linear analyses it was clear that stress levels in

[3] The tensile and compressive yield stresses for the adhesive MBrace Primer are 14.5 and 26.2MPa respectively.

the CFRP rod and steel were not sufficiently high to cause yielding in these materials and hence linear elastic models were retained for these.

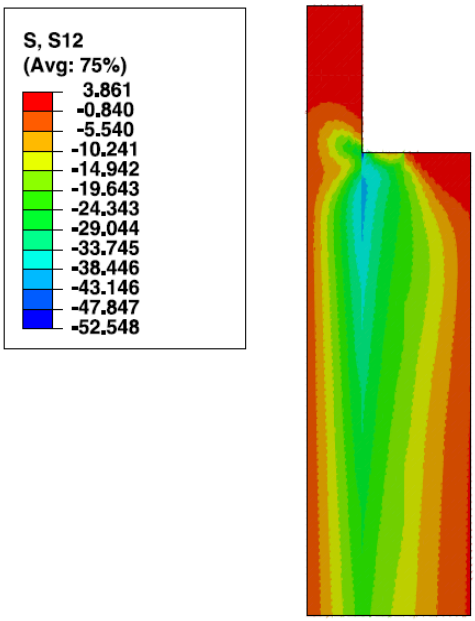

Figure 4.40. Shear stress distribution at the top of the anchor (MPa).

4.3.4.2 Elasto-plastic modelling (von Mises plasticity)

Initial analyses were elastic-perfectly plastic (i.e. no strain hardening) assuming von Mises yielding. The analyses were carried out with the experimental failure load for all the geometries for a range of different adhesive yield stresses from 15 to 45MPa. Figure 4.41 shows the predicted relationship obtained between the adhesive yield stress and the maximum equivalent plastic strain (PEEQ) at the experimental failure load for each of all four configurations. When the yield stresses were below a certain (configuration dependent) value the maximum failure load could not be achieved. This was because global yielding occurred at these yield stresses, at loads below the experimental failure load recorded. When selecting a yield stress above these levels the failure load could be achieved but, for a specified yield stress, a different maximum plastic strain (i.e. a differing extent of yield) was reached in each configuration.

It is clear that the use of a critical plastic strain for predicting the strength of these anchor joints is not possible. Whilst the use of an adhesive thickness dependent failure strain might be feasible it would be difficult to justify physically and the value of these strains are considerably higher than the stated material data provided by the manufacturer. Furthermore, the mismatch in failure strains for the two anchors that have the same adhesive thickness but different overlap length (see Figure 4.41) suggest that this approach is inappropriate.

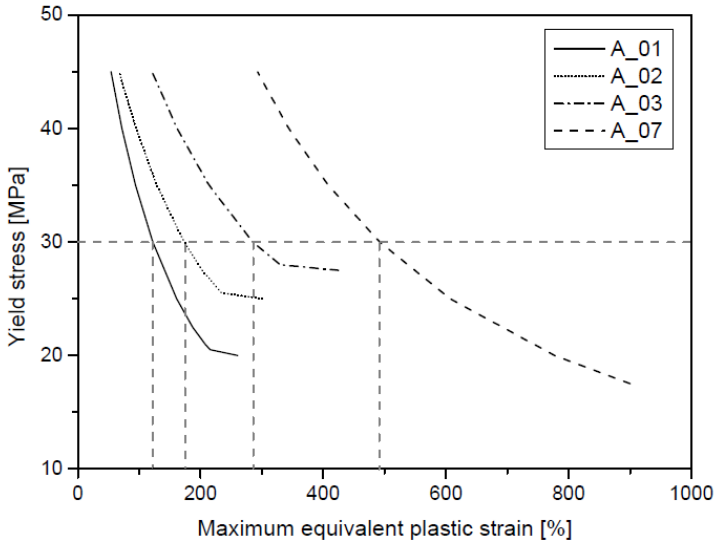

Figure 4.41. Variation of maximum equivalent plastic strain at failure with yield stress (von Mises plasticity).

4.3.4.3 Elasto-plastic modelling (Drucker-Prager plasticity)

As shown in previous studies [131][132], polymers generally exhibit greater yield stresses in compression than in tension. This is certainly the case for the adhesive 02 as the tensile and compressive yield stresses are 14.5 and 26.2MPa, respectively. Therefore, the classical von Mises yield criterion, which has no hydrostatic yield dependency, did not fully model the adhesive. In order to take into account the hydrostatic pressure sensitivity in the adhesive, Drucker-Prager plasticity was considered. The yield criterion for this model was based on the shape of the yield surface in the meridional plane, where the equivalent stress depends on the hydrostatic pressure. The Equation 4.9 gives the Drucker-Prager yield criterion for hydrostatic pressure sensitivity in materials.

$$\zeta \cdot \sigma_{yt}^2 = 3 \cdot J_2 + (\zeta - 1) \cdot I_1 \quad \text{(Equation 4.9)}$$

where ξ is the ratio between the yield stress in compression, σ_{yc}, to the yield stress in tension, σ_{yt}, at the same equivalent plastic strain, J_2 is the second invariant of the deviatoric stress sensor and I_1 is the first invariant of the deviatoric stress tensor. The yield surface can be expressed in Abaqus/CAE as a linear, a hyperbolic or a general exponent form. The linear model offers the most complex form which provides a possibly noncircular yield surface in the deviatoric plane. The hyperbolic and general exponent models use a von Mises section in the deviatoric stress plane, which means that the yield surface in the deviatoric plane is circular. In this research, the general exponent form was used because of the experimental data available for calibration of the model parameters. Also, the exponent form is the most general of the three yield criteria. The yield surface in the meridional plane for the general exponent form is presented in Equation 4.10 and Figure 4.42.

$$F = a \cdot q^b - p - p_t = 0 \quad \text{(Equation 4.10)}$$

where a and b are independent material parameters of the plastic deformation, p_t is the initial hydrostatic stress strength of the material (hardening parameter), p is the equivalent pressure stress and q is the von Mises equivalent stress expressed in Equation 4.11.

$$q = \sqrt{\frac{3}{2} \cdot s_{ij} \cdot s_{ij}} = \sqrt{3 \cdot J_2} \quad \text{(Equation 4.11)}$$

in which s_{ij} are the components of the stress deviator tensor. Comparing Equations 4.10, the yield surface on the meridional plane, and 4.9, the yield criterion for this model, and setting the parameter b=2 (as indicated by Charalambides and Dean [133]), the parameters a and p_t can be obtained as shown in Equation 4.12 and 4.13.

$$a = \frac{1}{3 \cdot (\zeta - 1) \cdot \sigma_{yt}} \quad \text{(Equation 4.12)} \qquad p_t = \frac{\zeta \cdot \sigma_{yt}}{3 \cdot (\zeta - 1)} \quad \text{(Equation 4.13)}$$

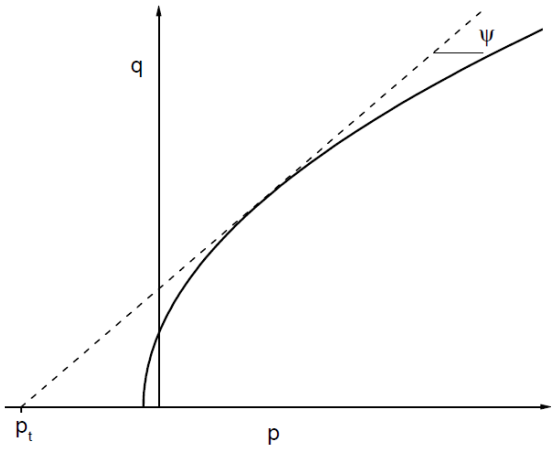

Figure 4.42. Yield surface in the meridional plane in Drucker-Prager plasticity for the general exponent form.

The material parameters used in this Drucker-Prager model are summarised in Table 4.5. The experimental failure load was applied to each of the four joint configurations and the resulting stress and plastic strain distributions were obtained. A plot of the equivalent stress, which was the yield stress for the plastic region, for all the geometric cases at their failure load is shown in Figure 4.43 where the red dash lines divide the plastic region from the elastic region of each geometric case. It can be seen that, unlike the von Mises plasticity, the yield stress varied along the length of the anchor. This was because the hydrostatic pressure varied along the overlap length, tending to be highest towards the overlap ends. Nevertheless, the maximum equivalent stresses are still well in excess of the yield stresses provided by the manufacturer.

Table 4.5. Drucker-Prager plasticity parameters.

Drucker-Prager Parameters	
Type	Exponent form
Material constant *a*	0.02849
Exponent *b*	2
Dilation angle, ψ	24.23

Table 4.6. The equivalent plastic strains at the experimental failure load.

Geometry	PEEQ [%]
A_01	48.2
A_02	29.1
A_03	40.5
A_07	53.6

The equivalent plastic strains corresponding to the failure load of each joint are shown in Table 4.6. It can be seen that the strains were generally lower than those obtained with von Mises plasticity and were more physically reasonable. This was because higher levels of yield stress were sustained due to the hydrostatic pressure. Figure 4.44 illustrates the maximum equivalent strain along the adhesive-tendon interface of each geometry at the corresponding failure load. It can be seen that the maximum values shown in Table 4.6 correspond with the maximum equivalent stress very close to the loading end of the anchorage. Further, there was less variation between the critical strain levels, suggesting that these would predict the anchor loads more accurately. However, even with this model the loads would not be better predicted than around +/- 20%.

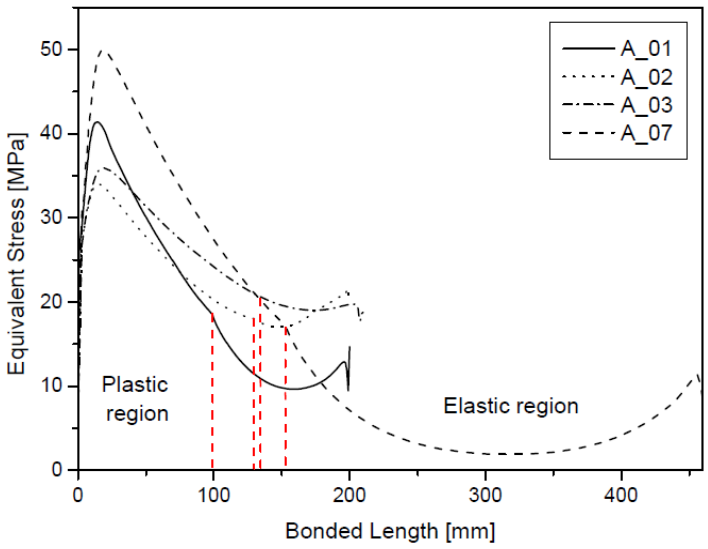

Figure 4.43. Equivalent stress distribution along the adhesive-rod interface (Drucker-Prager plasticity).

The fact that an elasto-plastic model with a critical plastic strain was unable to properly explain the effect of anchor length on joint strength suggests that a more complex failure mechanism might be active. Specifically, failure might occur in the more stressed regions followed by a frictional force resisting separation at the failed surfaces. Such a mechanism would account for the dependency of the strength on anchor length, but in a way that better matched the measured experimental data. To consider this further, it was necessary to undertake progressive damage modelling where the material can reach a peak, fail, and

then experience further deformation at a reduced level of (frictional) load. This is reported in the progressive damage modelling subsection.

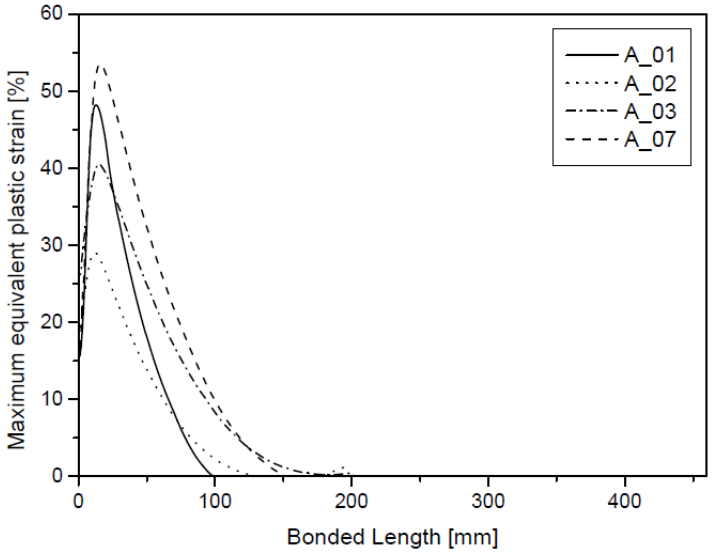

Figure 4.44. Maximum equivalent plastic strain along the adhesive-rod interface (Drucker-Prager plasticity).

4.3.4.4 Progressive damage modelling

The adhesive was modelled with a progressive damage model (CZM) where the constitutive behaviour of the cohesive element was defined by a traction-separation response. This is implemented by following the assigned elastic curve until a point of damage initiation. Subsequently, the stress is modified by a damage parameter that ranges between 0 (no damage) and 1 (fully damaged). There are various ways of defining damage. In this work it was defined as a function of separation to give a sharp drop (to simulate fracture) followed by a long region of constant but high damage (to simulate the friction process). A multi-linear traction-separation response was utilised to simulate the loading, failure and subsequent (post-failure) friction between both materials. This is illustrated in Figure 4.45, which shows the resulting traction-separation response calibrated with the experimental results.

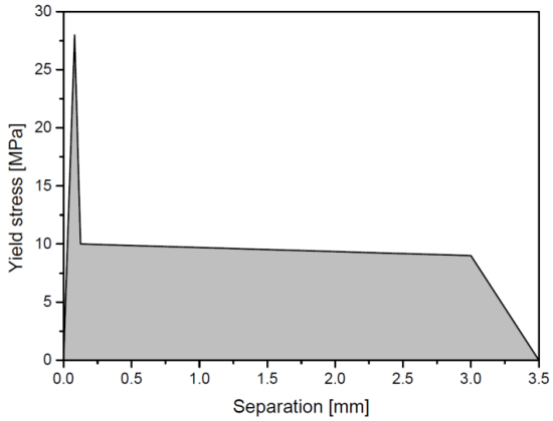

Figure 4.45. Progressive damage modelling response used in CZM in the normal direction.

Damage initiates in the cohesive elements when a quadratic interaction function involving the nominal stress ratios reaches a value of one. Unlike other criteria, this criterion considers the interaction of all the nominal stresses instead of only one nominal stress. A quadratic interaction damage initiation criterion was used to link the tractions as outlined in Equation 4.14.

$$\left\{\frac{\langle t_n \rangle}{t_n^0}\right\}^2 + \left\{\frac{t_s}{t_s^0}\right\}^2 + \left\{\frac{t_t}{t_t^0}\right\}^2 = 1 \quad \text{(Equation 4.14)}$$

where ‹› is the Macaulay bracket meaning that the compression stress state does not contribute to damage initiation, t_n, t_s and t_t are the stress components predicted by the elastic traction-separation without damage, and t_n^0, t_s^0 and t_t^0 are the nominal threshold stresses which specify the maximum traction allowed. The normal and shear yield stress were set at 28.30 and 16.34MPa, respectively, as it was considered that the chemical bond allows reaching the ultimate strength of the adhesive provided by the manufacturer.

The damage after the point of initiation was defined to increase with displacement up to complete failure at a critical value of displacement. The damage evolution for a linear softening is expressed through the equation proposed by Camanho and Davila (see Equation 4.15) [134].

$$D = \frac{\delta_m^f \cdot (\delta_m^{max} - \delta_m^o)}{\delta_m^{max} \cdot (\delta_m^f - \delta_m^o)} \quad \text{(Equation 4.15)}$$

where δ_m^{max} refers to the maximum value of the effective displacement during each loading increment, δ_m^f specifies the effective displacement at complete failure and δ_m^0 specifies the effective displacement at damage initiation. The effective displacement in all the cases was defined as the quadratic interaction of the displacement components as shown in Equation 4.16.

$$\delta_m = \sqrt{\langle \delta_n \rangle^2 + \delta_s^2 + \delta_t^2} \quad \text{(Equation 4.16)}$$

where ‹› is the Macaulay bracket, δ_n, δ_s and δ_t are the displacement components predicted and δ_m is the effective displacement predicted. In addition, the displacement components were defined as the nominal strain components multiplied by the original thickness of the cohesive elements.

However, in this research a tabular damage evolution was utilised to simulate the friction process. For a tabular softening, the damage, D, was directly defined as a function of the effective displacement relative to the effective displacement at damage initiation. Ten points of damage were defined (see

Table 4.7) where the damage between consecutive points was linearly obtained through Equation 4.15.

Table 4.7. Tabular damage evolution

Damage	$\delta_m^{max} - \delta_m^0$
0.00	0.000
0.50	0.015
0.78	0.030
0.89	0.060
0.95	0.180
0.98	0.540
0.99	1.500
1.00	4.000

Furthermore, severe convergence difficulties were found during solving, due to the damage evolution and stiffness degradation specified. In this sense, Abaqus/CAE allows regularising the traction-separation laws using a viscous parameter permitting the stresses to be slightly outside of the limits set by the traction-separation law. This regularisation process involves the consideration of a viscous stiffness degradation parameter, D_v, which depends on the viscosity parameter, μ, and the degradation variable considered in Equation 4.15. It is worth noticing that the viscosity parameter must be a small value compared to the characteristic time increment in order to improve the convergence of the model without compromising results. In this work, a viscosity parameter of 0.001 was considered for a characteristic time increment of 0.1. The stress components predicted by the traction-separation elements were affected by the viscous stiffness degradation after damage initiation as described in Equations 4.17.

$$\boldsymbol{t} = (1 - D_v) \cdot \bar{\boldsymbol{t}} \quad \text{(Equation 4.17)}$$

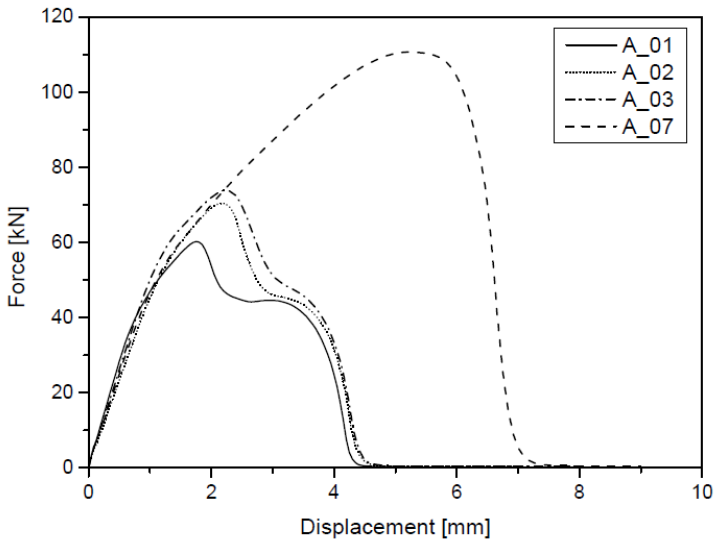

Figure 4.46. Force – displacement diagram obtained with CZM.

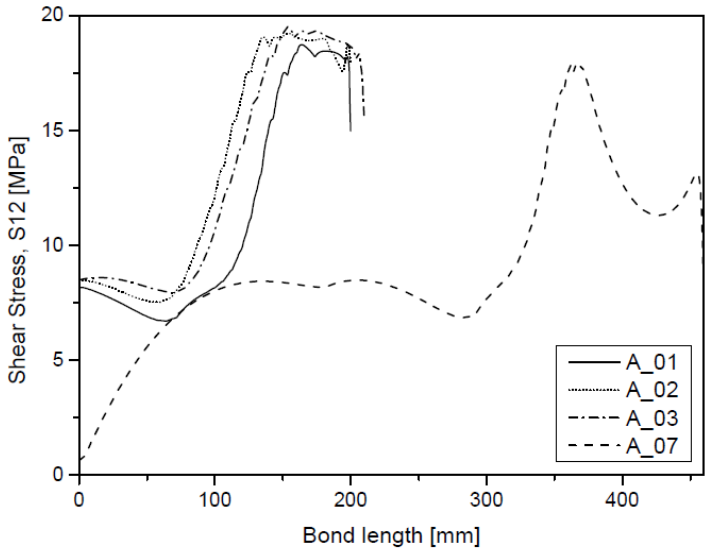

Figure 4.47. Shear stress distribution along the adhesive-rod interface obtained with CZM.

When damage was initiated, the maximum stress moved down the adhesive-rod interface. The predicted load-displacement response for each of the four joints is shown in Figure 4.46 and is discussed in more detail later. Figure 4.47 shows the shear stress distribution along the CFRP interface at the maximum load reached in each of the geometries (as shown in Figure 4.46). Damage spreads in from both ends of the bond but mainly from the end where the CFRP was loaded (0mm bond length in Figure 4.47). The region where the shear stress was at its maximum (at about 18MPa) indicates the current damage front (i.e. damage has spread about 150mm in the 200mm long anchors and about 350mm in the 460mm long anchor). Material to the left of this front was damaged and to the right remained undamaged (until the other end was approached). The rapid fall in shear stress corresponds with the rapid damage in the traction-separation model whilst the plateau lower level corresponds to the friction region. In the shorter anchors the damage was spread furthest in the anchor with the thinnest adhesive layer. It can be seen that the maximum load in each anchor was reached when the maximum stress was close (less than 50mm) to the bottom of the bonded joint. The longer "friction" region in Figure 4.46 for the 460mm long anchor enabled this configuration to sustain the higher failure load observed experimentally.

Moreover, Figure 4.48 illustrates three different stages of the damage front evolution and its shear stress distribution in the adhesive section for the anchor with the thickest adhesive[4]. Point "a" shows the shear stress distribution when damage started at the top of the joint. The corresponding force at this stage was slightly greater than 37kN. Below this force, the joint behaved completely linearly with the maximum shear stress occurring at the top of the bonded joint. When damage was initiated, the maximum shear stress travelled along the joint towards the bottom. At the point "b", the damage front and the maximum values

[4] Geometry A_03.

of shear stress reached around the middle of the joint. It can be noticed that the top of the bonded joint was highly damaged with values between 0.9 and 1. This damage zone was transmitting the lower frictional loads. Finally, point "c" shows the shear stress distribution in the adhesive when the joint reached the maximum damage it can sustain. The force at this stage was very close to the experimental failure load. The maximum values of shear stress occurred at the bottom of the joint where most of the overlap length was in the frictional region.

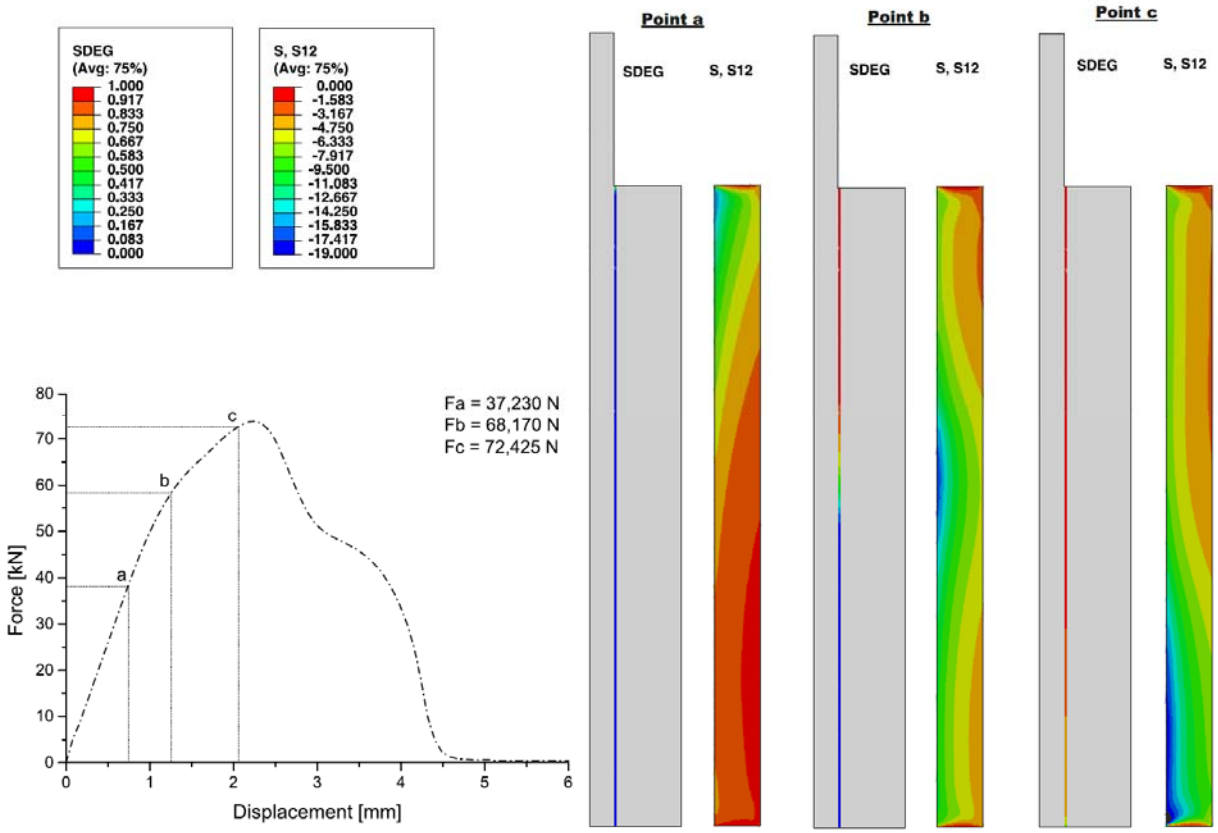

Figure 4.48. Damage and shear stress evolution along the cohesive layer and adhesive section respectively for the geometry 24_200mm.

Returning to consider the predicted failure loads in Figure 4.46, as discussed in the elastic analysis, for joints of the same length, initial damage (at a given stress) occurred at higher loads for the larger adhesive thicknesses due to a more uniform stress distribution along the adhesive length. This results in the joints with thicker adhesive layers having the higher predicted strengths seen in Figure 4.46. These features match the measured joints strengths very well and show good correlation between the measured and predicted strengths of the four anchor geometries.

Finally, geometric cases corresponding to specimens A_01_02_4 and A_02_02_2 were also simulated with progressive damage evolution. Experimental data under quasi-static loading showed that, in both cases, there was a reduction of 30-35% of the static failure load in comparison with the experimental results obtained in Figure 4.24. This was mainly caused by the batch of CFRP tendons intended for the fatigue and

stress relaxation analyses presented a slightly different superficial roughness. In these cases, the strength of attraction between the adhesive and the rod decreased and thus did not allow the ultimate strength of the adhesive provided by the manufacturer to be reached due to a premature failure in the tendon-adhesive interface. For this reason, the traction-separation law response was recalibrated for these specimens reducing the normal and shear yield stresses proportionally, as well as the tabular damage evolution.

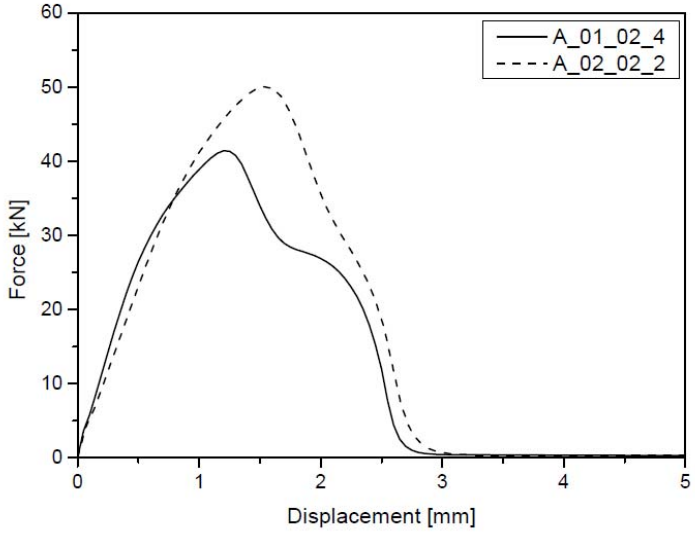

Figure 4.49. Force – displacement diagram obtained with CZM for specimens A_01_02_4 and A_02_02_2.

As shown in Figure 4.49, the progressive damage evolution provided a predictive failure load very close to the experimental data recorded. Predicted static strengths of 41.30 and 50.10kN were obtained for the thinnest and thickest adhesive layers, respectively. The recalibrated normal and shear yield stresses, which provided a predictive failure close to the experimental data, were 17.20 and 9.93MPa, respectively. The tabular damage evolution parameters were also readjusted and summarised in Table 4.8. It is worth mentioning that all these parameters will be used in Chapter 6 in order to simulate the fatigue behaviour of the straight bond-type anchorages.

Table 4.8. Tabular damage evolution for specimens A_01_02_4 and A_02_02_2.

Damage	$\delta_m^{max} - \delta_m^0$
0.00	0.000
0.50	0.009
0.78	0.018
0.89	0.036
0.95	0.108
0.98	0.324
0.99	0.900
1	2.400

Moreover, Figure 4.50 illustrates the shear stress distribution along the adhesive-rod interface at the failure load of each geometric case. As mentioned earlier, the damage was initiated at the loading end of the

anchorage (0mm bond length) and propagated throughout the overlap joint from the top to the bottom of the anchorage (200mm bond length). The maximum shear stresses (at about 12MPa) indicate the current front damage, which is placed at the bottom of the bonded joint. At this stage, the failure load of each specimen was reached, although the material placed on the left of the front damage corresponds to the damaged bonded length, which represents the friction region of the traction-separation law of the cohesive elements (at about 5MPa).

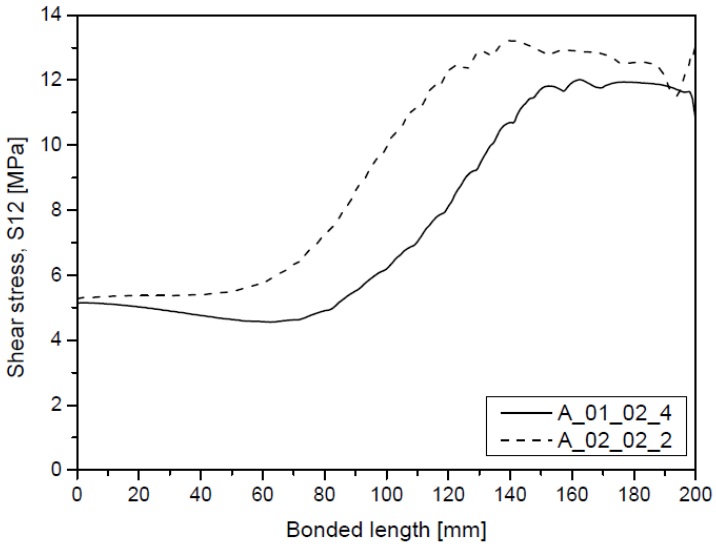

Figure 4.50. Shear stress distribution along the adhesive-rod interface obtained with CZM for specimens A_01_02_4 and A_02_02_2.

4.3.5 Concluding remarks

In this section, experimental, analytical and numerical results of the tensile characteristics of straight bond-type anchorages for CFRP tendons under quasi-static loading have been investigated. Based on the experimental results, the following conclusions can be drawn:

1. In all specimens with CFRP tendons, a premature failure of adhesive-tendon interface was observed. The failure started at the top of the anchorage (loading end) and was quickly propagated to the bottom of the joint throughout the overlap length. The naked-eye examination and the microscopic analysis revealed that the failure surface occurred within the adhesive but very close to the interface.
2. Force-displacement curves were largely linear up to the point of failure, which occurred rapidly and explosively. However, several specimens showed a significant change in the slope revealing that nonlinearities in the adhesive must occur. This was the case with adhesive 02 which was considered for further investigation.
3. Different geometries of adhesively bonded anchors were tested in tension to failure and higher failure loads were reached when either the adhesive thickness or the bonded length was higher.

Moreover, an analytical formulation from TOM's theoretical solution was developed and validated with experimental data at low loads in order to predict the shear stress distribution in circular anchorages. From the analytical modelling, it can be drawn that:

4. The analytical solution proposed for the adhesive stresses in the anchor was able to predict the stress state in the anchor for low values of load but not at higher loads, where the material yields. For this reason, this formulation allows providing an approximate distribution of shear stress in the bonded joint for circular anchors for adhesives which mainly behave linear elastic up to failure.

Finally, numerical modelling was conducted to predict the static strength and the failure mechanism of straight bond-type anchorages with adhesive 02. From the numerical modelling, the next conclusions can be drawn:

5. An axisymmetric FE model was developed to assess the anchor under static tensile loading. Elastic analyses were unable to successfully predict the measured responses as the required stresses where physically unreasonable and were different for different anchor lengths.
6. Similarly, when using von Mises plasticity there was no correlation between the maximum equivalent plastic strains of the adhesive at the point of failure of each configuration.
7. When the adhesive was modelled with Drucker-Prager plasticity, the scatter in the adhesive failure strains, although improved, was still too high to enable reliable strength prediction to be made.
8. A cohesive zone model with progressive damage and a "frictional" post-damage region was shown to provide predicted joint strengths that correlate closely with the measured experimental data. This model was able to successfully describe the different failure loads with different thicknesses and lengths of adhesive layer.

Chapter 5. Time-dependent analyses

5.1 Introduction

Adhesives and bonded joints often exhibit time-dependent mechanical properties which may affect the functionality and durability of a structure. These effects can be observed by the phenomena of creep under constant load or stress relaxation under constant strain. Also, time-dependent effects may vary the stress or strain noticeably at a particular point which may lead to a malfunction of the structure or, in the worst-case scenario, an unexpected premature failure.

Therefore, the adhesively bonded anchorage needs to be investigated under time dependent phenomena in order to determine the durability of the anchorage and the stress field variation of the adhesive during its lifespan. This chapter summarises the experimental work and numerical modelling of straight bond-type anchorages for CFRP tendons with the adhesive 02 under creep and stress relaxation loading.

5.2 Creep analysis

5.2.1 Introduction

The creep phenomenon is the continuous deformation of a solid material under the action of a constant load or mechanical stress over long periods of time. As mentioned in the state of the art, there are three characteristic stages of creep. In the first stage, known as primary creep, the material deforms quickly but slows with increasing time until a relatively uniform rate of deformation is reached. The second stage or secondary creep is the dominant phase of the creep phenomenon. It is also the most studied and understood stage of the creep phenomenon. In the last stage or tertiary creep, the deformation rate increases and the material fails due to a large amount of strain. In this research the straight bond-type anchorage was studied under axial creep loading with the aim to investigate the influence of constant loads over long periods of time.

Experimental creep tests on single lap joints (SLJs) with the adhesive 02 were undertaken. The variables assessed were the adhesive thickness and the creep loading. In addition, the creep response of the SLJs was predicted using Finite Element Analysis. A visco-plastic material model, based on the Bailey-Norton law (creep power law) [74,135] was calibrated with the experimental data and utilised to predict the creep time until failure of SLJs. The effect of creep damage was modelled by degrading the adhesive plastic yield stress.

The creep model developed was also applied to the straight bond type anchorage with the aim to study the creep aspects requiring consideration in the anchorages. Furthermore, creep times to failure on anchorages were assessed at the average fatigue loads utilised in this research in order to investigate the influence of the creep phenomenon on the fatigue testing activities carried out in this investigation.

5.2.2 Objectives

Single lap joints with the adhesive 02 were experimentally and numerically studied under creep loading up to failure. Different adhesive thicknesses were tested with the same overlap length in order to obtain a creep law able to predict the creep failure time. The parameters of the creep law were calibrated with the experimental data obtained from the SLJs. Finally, the creep law was used to predict the creep time to failure of the bonded anchorages. The objectives in this section are drawn in the flowchart presented in Figure 5.1 and described as follows:

1. To obtain an experimental creep law. Single lap joints were tested under creep loading up until failure. The parameters assessed include the adhesive thickness of SLJs and creep loads. Although the joint superposition length, also known as overlap length, is a well-known influencing variable in bonded lap joints, it has not been included as a variable. SLJs were tested in order to obtain additional information about the bonded joint to model the straight bond-type anchorage. In this sense, the overlap length of the anchorages was large enough for the full adhesive stress field to be developed. Thus the primary parameter of interest in the anchorages was the adhesive thickness and not the overlap length. This was the reason why only the adhesive thickness was varied in the SLJ. It was considered that the overlap length in the short overlap SLJ would not add significant information. The most suitable mathematical formulation of creep was used in order to fit the experimental creep response obtained.
2. To develop a numerical model considering time-dependent phenomena for SLJs and straight bond-type anchorages. As was mentioned in the state of the art, the model proposed by Su and Mackie [81], which was able to simulate adhesively bonded joints under time-dependent loading by reducing the plastic yield stress of the adhesive layer to zero, was found to fit the boundary conditions of the topic covered in this chapter. A numerical model, which follows the main features of the model developed by Su and Mackie, was investigated for SLJs and straight bond-type anchorages.
3. To predict the creep times until failure of the anchors that were tested under fatigue loading by using the numerical model. The aim of this study lies in the possible influence of time-dependent phenomena during the fatigue testing activities. Creep times to failure of the anchorages were obtained at the mean fatigue loads and compared with the longest times to failure of fatigue test in

order to evaluate whether it was necessary to include time-dependent effects on the fatigue analysis (Chapter 6).

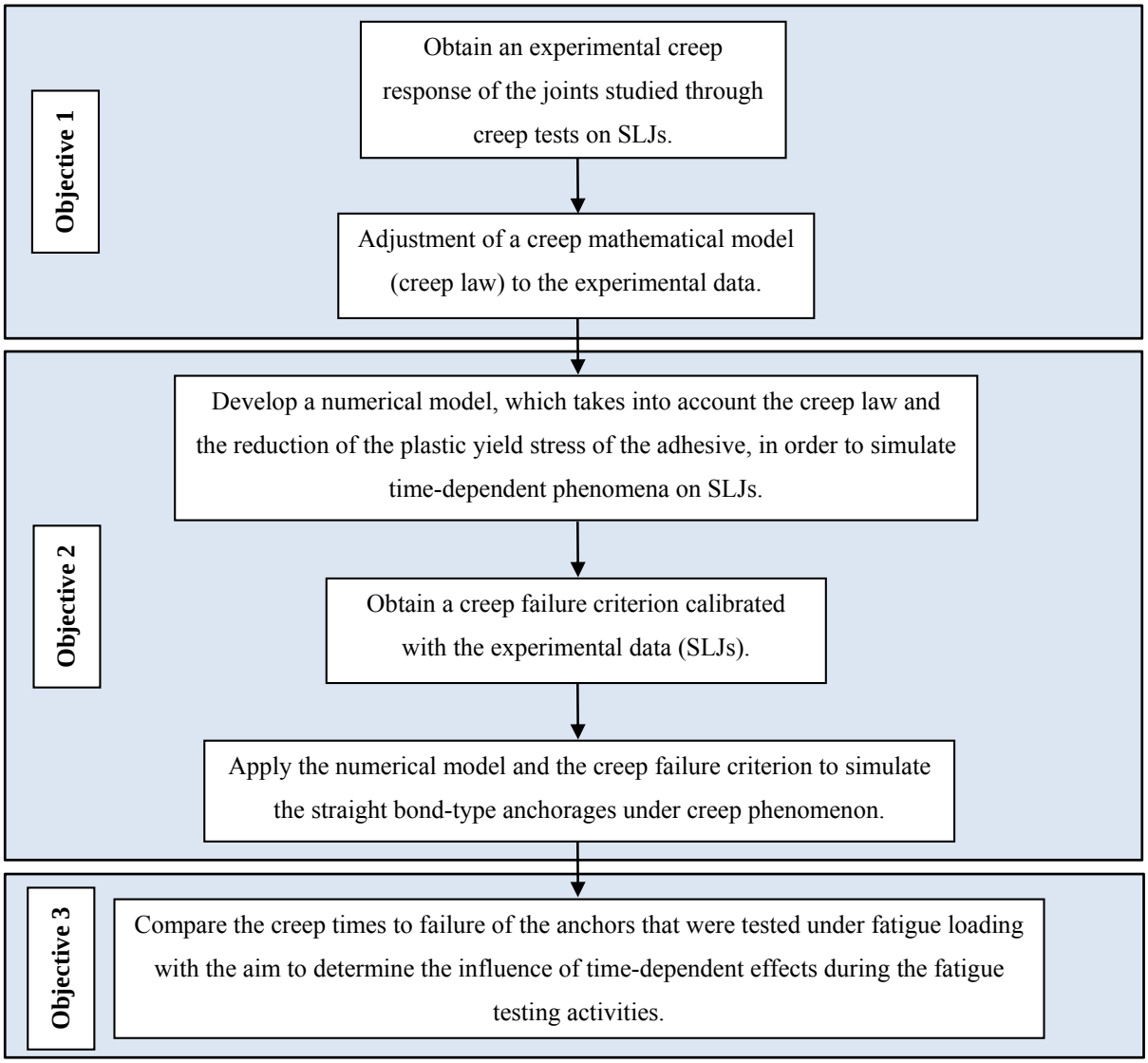

Figure 5.1. The flowchart of the creep analysis objectives.

5.2.3 Experimental work

5.2.3.1 Test setup

With the aim to determine the most suitable creep loads, pull-out tests on SLJs were undertaken to determine the static strength. The static tests were carried out using an MTS actuator under displacement control at 0.5mm/min. Force and displacement were recorded at a frequency of 50 Hz using an HBM MGCPlus data acquisition system. One specimen of each geometry was tested up to failure in order to obtain the static strength. The overlap length, the width and thickness of the bond line are summarised in Chapter 3.

Moreover, creep tests on the SLJs based on ASTM D2294 [136] were undertaken. The creep test machine was based on a levered beam with a load ratio of 10:1, as seen in Figure 5.2. SLJs were attached to the shortest arm of the beam and the specimens were aligned vertically in order to avoid unwanted bending effects. Specimens were loaded by applying a dead weight at the other end of the beam. The weight was gradually applied by hand over a short timespan so that any sharp impulse on the beam could be avoided. The load remained constant after application until failure of the specimen. The use of a levered beam test setup is a well-known technique for creep testing [71].

Figure 5.2. Creep test setup for SLJs.

Time to failure was recorded using an HBM Spider 8 acquisition system. When the specimen failed, the loading weight on the other side of the beam fell on an aluminium plate. This plate was instrumented with a strain gage and the values of strain were continuously recorded at a very low frequency (1 Hz). When the loading weight fell, a large jump in the strain was recorded. This enabled the time, when the specimen failed, to be accurately determined. The creep test setup for the SLJs is shown in Figure 5.2. The different loads assessed were the 80, 60 and 40% of the average static strength of the SLJs for all the geometries and an additional load of 20% for the geometry SLJ_02_02.

A detailed view of the test setup is shown in Figure 5.3. It can be seen that the specimen was mainly loaded under shear stresses. It is worth noticing that the non-symmetric geometry of SLJs also introduced a bending moment on the joint. In this sense, metallic square spacers were placed between the grips in order to avoid the load eccentricity and reduce the effect of bending moment on the adhesive layer. The thickness of the metallic square spacers utilised were equal to the thickness of the adhesive layer as well as one substrate for each geometric case.

Figure 5.3. Detail of creep test setup for SLJs.

5.2.3.2 Results and discussion

In all the specimens, failure occurred within the adhesive but very close to the interface between the adhesive and the composite material. Figure 5.4 shows the typical failure phenomenon throughout the bond length for the single lap joints. Detailed pictures of the failure surface can be seen in the next subsection (failure surface analysis).

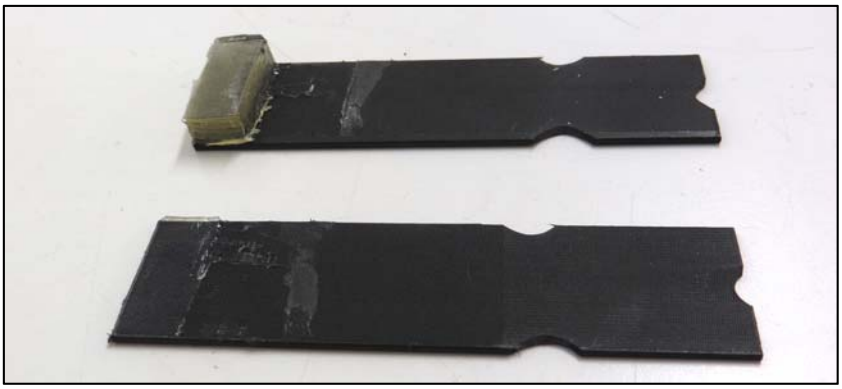

Figure 5.4. Typical failure surfaces in the SLJs.

In the pull-out tests, the experimental force-displacement curves were largely linear up to the point of failure, which occurred suddenly. The average static strength obtained from all four specimens was 1,563N. This result defined the creep loads assessed which were 1250, 940, 625 and 325 N as they represented the 80, 60, 40 and 20% of the average static strength of SLJs.

Moreover, the experimental creep times to failure obtained from the single lap joints are shown in Figure 5.5 and Table 5.1. Clearly, the average shear stress is the same for all the specimens which were loaded

with the same load. Generally, the increased load eccentricity associated with the thicker adhesive layers introduced an increased bending moment and hence increased the adhesive stresses. This resulted in thicker specimens tending to have a shorter lifetime than thinner specimens at the same creep load. The experimental results were assessed with the aim to obtain individual curves for each geometric case, however the experimental tests were limited and the trends obtained were not wholly consistent. In this approach, introducing a thickness dependent creep failure strain accommodated the effect of adhesive thickness. For this reason, the experimental data were combined into one unique linear curve, giving the relation between the average shear stress and the creep time to failure (see Figure 5.5). As the average stress was reduced, the lifespan was increased.

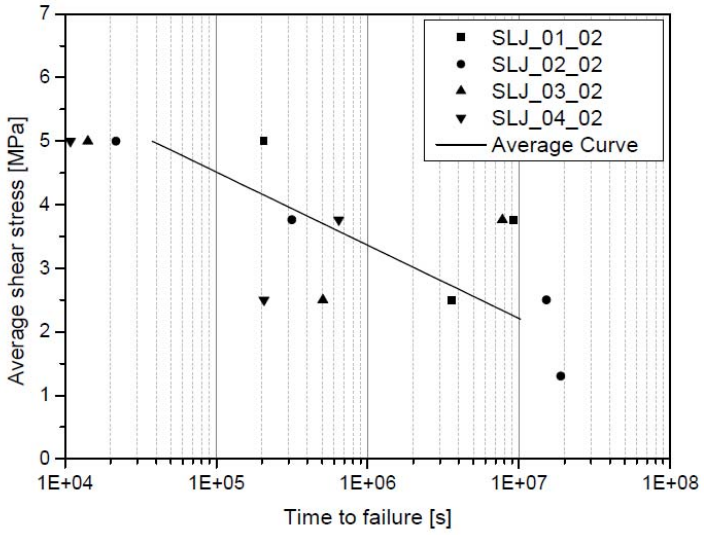

Figure 5.5. Experimental load-life creep data for the single lap joints.

Table 5.1. Experimental creep time to failure of SLJs.

Specimen	Average shear stress [MPa]	Creep load [N]	Creep time to failure [hours]
SLJ_01_02_1	8.95	1,250	57.17
SLJ_01_02_2	6.70	940	2552.89
SLJ_01_02_3	4.50	625	999.84
SLJ_02_02_1	8.95	1,250	6.04
SLJ_02_02_2	6.70	940	87.88
SLJ_02_02_3	4.50	625	4232.95
SLJ_02_02_4	2.25	312	5262.34
SLJ_03_02_1	8.95	1,250	3.94
SLJ_03_02_2	6.70	940	2163.32
SLJ_03_02_3	4.50	625	140.68
SLJ_04_02_1	8.95	1,250	3.02
SLJ_04_02_2	6.70	940	179.25
SLJ_04_02_3	4.50	625	57.41

5.2.3.3 Failure surface analysis

Failure surface analyses were conducted on single lap joints using a stereoscope microscope SCZ-T4P Carton with magnification levels ranging from 10x to 25x. Pictures of the failure surface were obtained with a USB Microscopic camera Deltapix DP300. Figure 5.6, Figure 5.7 and Figure 5.8 show the most characteristic SLJ failure surfaces after testing.

The conventional naked-eye examination revealed that the failure occurred in the adhesive-adherent interface due to adhesive failure. It was observed that the CFRP laminates contained small adhesive particles which indicated local failures caused by adhesive cohesive failure, similar to DLJs and anchorages experimentally studied in Chapter 4. As discussed earlier, the strength of the chemical bond mainly depends on the surface energy and can therefore be revealed in the failure surface analysed. In Chapter 4 it was seen that specimens, which were considered to reach the maximum adhesion strength during the loading process, contained adhesive particles on their entire failure surface. Specimens, which reached lower static strength due to lower attraction strength between the adhesive and the rod, contained a lower number of adhesive particles on their failure surface.

Figure 5.6 shows the failure surface of the CFRP laminate magnified x10. The failure mainly occurred because of adhesion failure, although there are several adhesive particles attached to the composite material due to local cohesive failures of the adhesive. These small adhesive particles were spread on the failure surface of SLJs, covering their entire surface. The failure surfaces of the SLJs were found to be analogous to the failure surfaces observed in specimens A_01_02_4 and A_02_02_2, where the surface energy was lower (see Chapter 4). This result allows for the use of the experimental load-life data from the SLJs in order to predict the time-dependent behaviour of the straight bond-type anchorages.

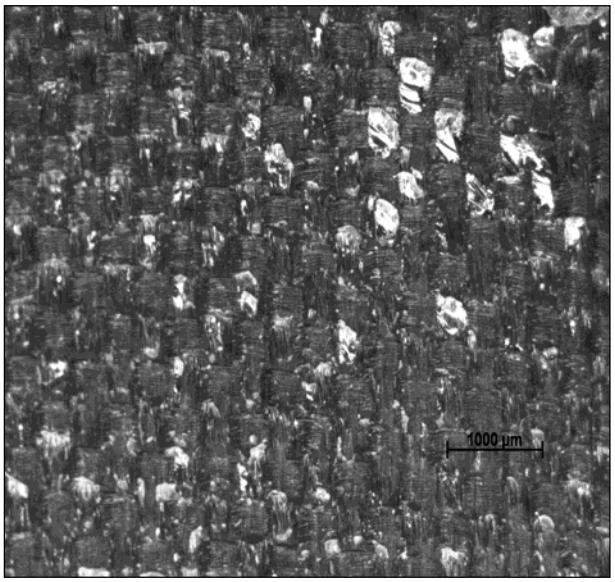

Figure 5.6. CFRP laminate failure surface of specimen SLJ_04_1 magnified x10.

Moreover, the conventional naked-eye examination of the SLJ failure surfaces occasionally detected different local failure modes worth mentioning. Figure 5.7 shows a local failure surface on the adhesive layer where the cohesive failure of the adhesive was more evident, especially at the top of the image. This local failure was solely detected in the specimen SLJ_04_01 and located at the end of the overlap bonded length. Further, Figure 5.8 shows the adhesive layer surface where the epoxy resin acquired the shape of the shallow hollows of the composite material and, locally, some particles of the CFRP laminate attached to the adhesive layer.

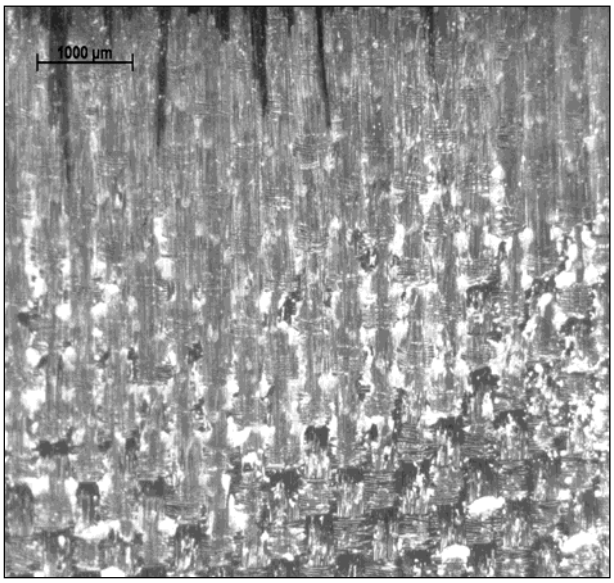

Figure 5.7. Adhesive failure surface of specimen SLJ_04_1 magnified x10.

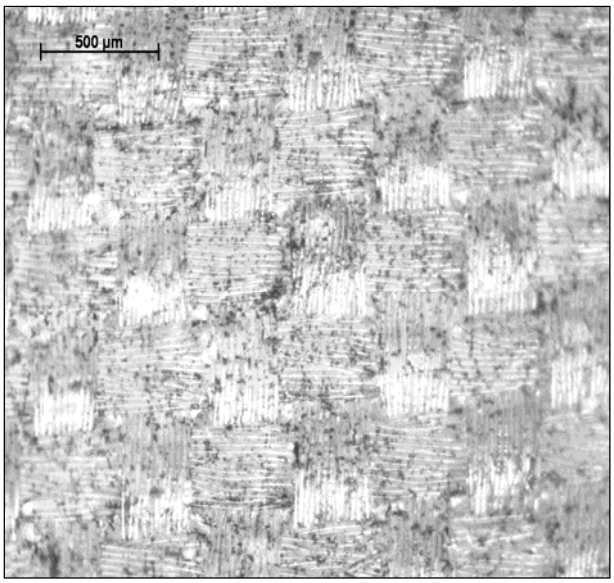

Figure 5.8. Adhesive failure surface of specimen SLJ_01_1 magnified x25.

5.2.4 Numerical modelling

Finite element models were developed in Abaqus/CAE for SLJs and anchors in order to develop a model able to predict the creep response of the straight bond-type anchorages. A 2D plane stress finite element model, shown in Figure 5.9, was developed to predict the SLJ behaviour under creep loading. Four different geometries were modelled according to the geometries tested experimentally presented in Chapter 3. A convergence analysis of the mesh was undertaken for all the geometries to determine the most suitable mesh size for the single lap joints. The mesh size was progressively reduced until a lower variation of 1% of the maximum shear stress distribution on the adhesive-adherent interface was obtained. Four-noded plane stress elements (CPS4R) with a mesh density of 0.1mm were used for the whole model. One end of the substrate was assigned an encastre constraint. At the other end the transverse displacement and the rotation were constrained and the (axial) creep load was applied.

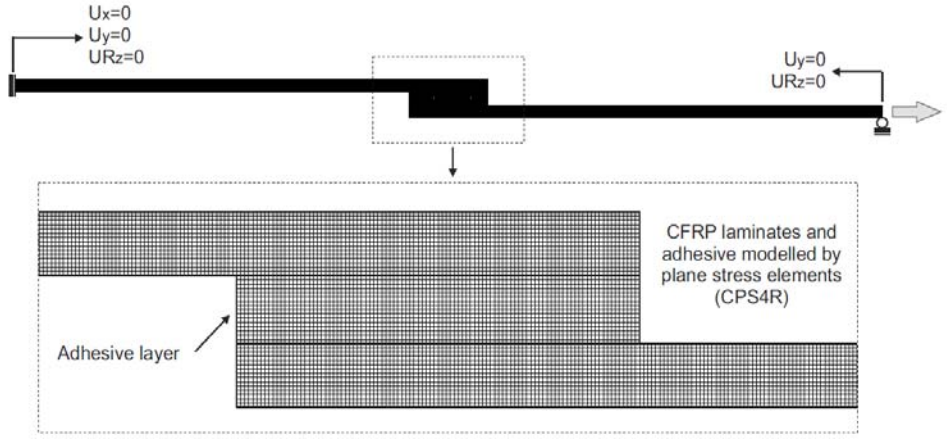

Figure 5.9. Finite element mesh and boundary conditions for the geometry SLJ_01_02.

Furthermore, a 2D axisymmetric model was developed for the anchor (see Figure 5.10). An axisymmetric model, rather than a full 3D model, was considered to minimise the computational effort. The anchorage geometries were experimentally tested under fatigue and stress relaxation loading was modelled[5]. The bottom of the steel housing was entirely fixed and the top of the CFRP was loaded with an axial force. The anchor models were used to predict the creep time to failure of the geometries in order to assess the creep influence during the fatigue analysis (see Chapter 6). Four-noded axisymmetric stress elements (CAX4R) with a mesh density of 0.1mm were used for the creep model. It is worth mentioning that the same mesh density as the SLJs was used for the anchors. Even though the mesh produced is, possibly, sufficient, the same mesh was required as the maximum creep strain from the SLJs simulations was taken to determine the creep failure time of the anchors. This is more valid if the meshes are the same size in both cases.

[5] Geometries A_14, A_16, A_18 and A_20.

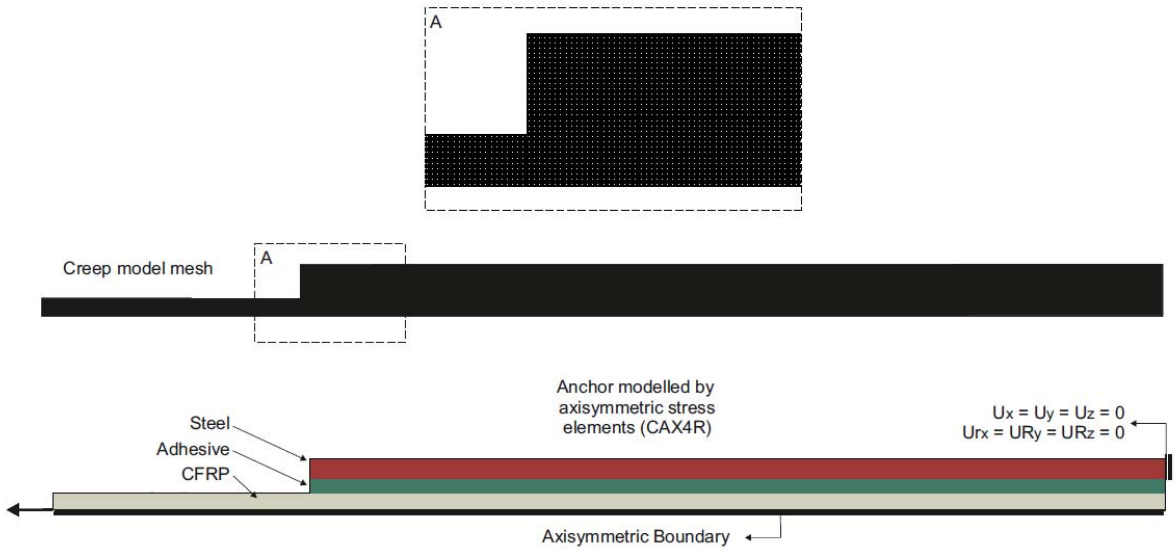

Figure 5.10. Finite element mesh and boundary conditions for the anchor with a bore and length of 14 and 200mm respectively.

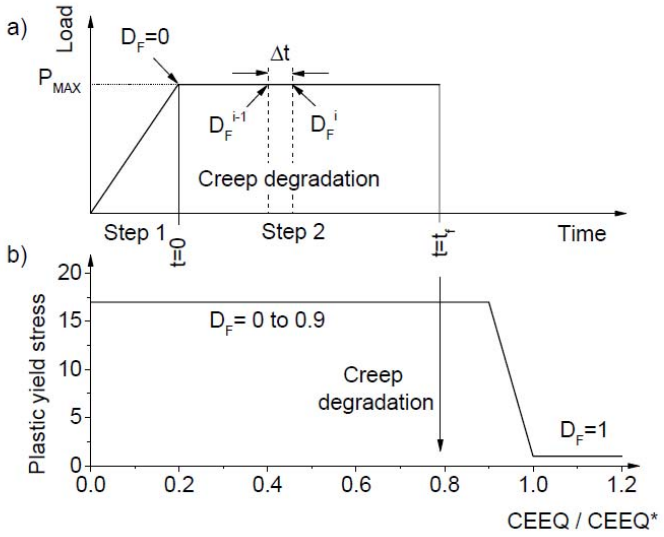

Figure 5.11. a) Steps applied in the creep modelling b) Creep degradation scheme implemented.

The creep modelling of both models (SLJs and anchors) were conducted considering elastic-perfectly plastic von Mises plasticity, creep and progressive damage for the adhesive. An elastic-perfectly plastic model was deemed a reasonable starting point for two reasons a) the post-yield hardening was relatively modest and b) the elastic-plastic model parameters were to be degraded by the accumulated creep strain and so the exact form of plasticity is less critical as in an analysis where the plasticity is not degraded. A time-dependent analysis was required to consider the creep phenomenon. As can be seen in Figure 5.11a, two steps were applied. In the first step, the force was applied linearly from 0 to P_{max} in 1 second. In the second step, much longer, the force remained constant until the creep failure of the joint was reached. In

the SLJs, P_{max} was based on the experimental creep loads used. As there was no experimental creep data for the anchors, forces used in the anchor modelling were equal to the mean force applied in the fatigue experimental tests. This anchor modelling was undertaken in order to assess whether the predicted creep time to failure was long enough for creep damage to be neglected, when compared with the fatigue damage in the fatigue modelling. Although the anchor and the SLJ do not experience the same mode mix of loading both experience peel and shear stresses at the site of failure and thus the material response generated from the SLJ was applied directly to the anchor modelling.

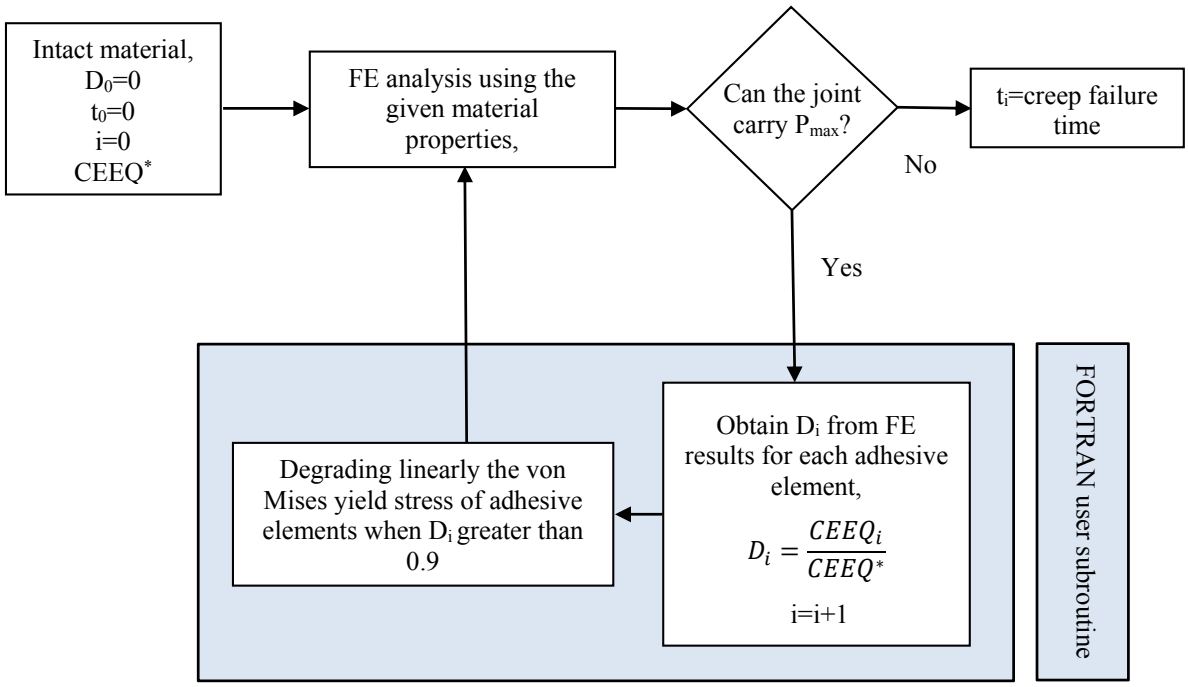

Figure 5.12. The flowchart of the creep model in Abaqus/CAE.

The von Mises yield stress for the adhesive was defined initially at 17.20MPa as this was the maximum strength obtained in the quasi-static analysis of the joints (see Chapter 4). In order to simulate the damage in the joint, a subroutine in FORTRAN was implemented to take into account a progressive damage based on the reduction of the yield stress. Figure 5.11b shows the creep degradation scheme implemented. Once the equivalent creep strain, *CEEQ*, was greater than 90% of the maximum equivalent creep strain allowed, *CEEQ**, the yield stress, initially set at 17.20MPa, was degraded linearly to 1MPa, thus effectively producing local adhesive failure.

The creep model is illustrated in more detail in a flowchart form in Figure 5.12. The maximum equivalent creep strain was set at the beginning of the simulation when both damage and time increment were still zero. The time-dependent analysis started in the first time increment of the second step (see Figure 5.11a) and the equivalent creep strain of each adhesive element was obtained. The damage of each adhesive element was calculated through the user subroutine and the adhesive plastic properties were linearly degraded if the damage was greater than 0.9. Once the damage and plastic yield stress of each adhesive

element was updated, a new time increment was evaluated. This loop was repeated until the joint was not able to keep carrying the load applied.

5.2.4.1 Creep modelling of SLJ

A creep mathematical model was utilised in order to fit the average curve obtained from the SLJ experimental data (see Figure 5.5). This permitted implementing the creep in the numerical model to simulate the joint under the creep phenomenon. A commonly used creep model response is provided by the Bailey-Norton law, also known as creep power law. The classical power law for creep allows for the characterisation of the primary and secondary creep regimes whereas a tertiary creep regime is not considered. The creep power law is presented in Equation 5.1.

$$\frac{d\varepsilon_{cr}}{dt} = A \cdot \sigma^{B} \quad \text{(Equation 5.1)}$$

where A and B are material constants, ε_{cr} is the creep strain, t is the creep time and σ is the normal tensile stress at which the specimen is subjected. The experimental creep times to failure obtained from the single lap joints were used to find the material constants of the creep power law. The power law multiplier, A, and the equivalent stress order, B, were found to be 1.75E-13 and 7, respectively. It can be seen in Figure 5.13 that the creep power law fits the average experimental stress-time to failure data very well (see Figure 5.5).

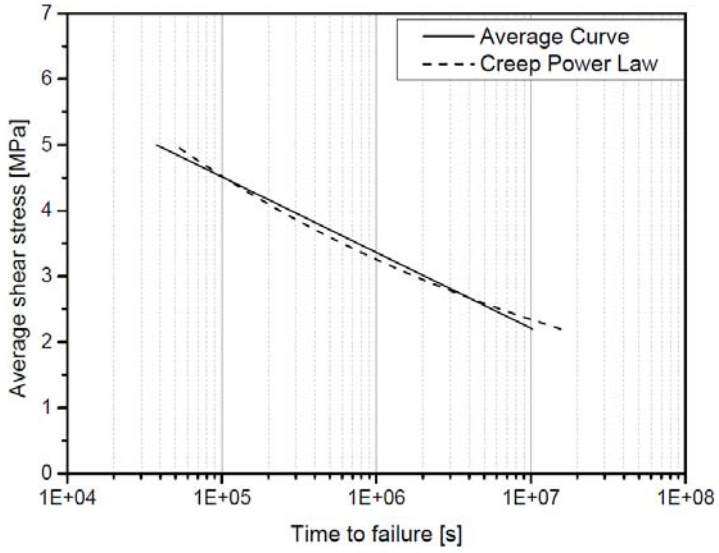

Figure 5.13. Creep power law and average.

However, the maximum local equivalent creep strain (*CEEQ**) in each geometry at failure was unknown. The maximum local equivalent creep strain was determined for each single lap joint geometry with the aim to obtain the failure time of the joint according to the experimental creep law. This was undertaken in an iterative manner, i) selecting a value of *CEEQ**, ii) using progressive damage FEA to determine the time to failure for that *CEEQ**, iii) adjusting the value of *CEEQ** accordingly and repeating the process. The

value of *CEEQ** required was found to be adhesive thickness dependent. As the number of SLJs tests was limited, it was not possible to fit curves to individual thicknesses and the data were insufficient to obtain consistent trends. For this reason, a single regression line was adopted where the creep failure strain was found to be thickness dependent. Figure 5.14 shows the variation of *CEEQ** as a function of the adhesive thickness. These data were used to determine the maximum equivalent creep strain allowed for the anchors of different adhesive thicknesses. The anchor thicknesses studied were 3, 4, 5 and 6mm and the maximum equivalent creep strain allowed for the creep modelling of the anchorages were obtained through a quadratic polynomial equation (as shown in Figure 5.14), which is displayed on the graph. The maximum equivalent creep strains used in this research for both SLJs and anchorages are summarised in Table 5.2.

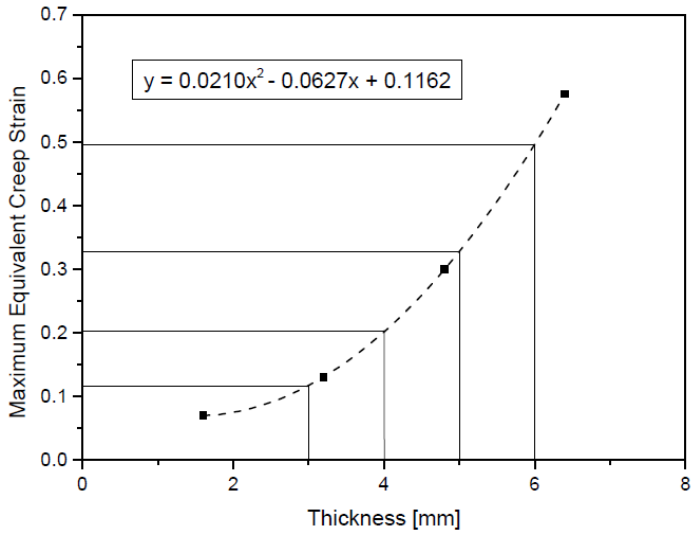

Figure 5.14. Maximum equivalent creep strain allowed as a function of the adhesive thickness.

Table 5.2. Maximum equivalent creep strain for SLJs and anchorages.

Geometry	CEEQ*
SLJ_01_02	0.0700
SLJ_02_02	0.1300
SLJ_03_02	0.3000
SLJ_04_02	0.5750
A_14	0.1171
A_16	0.2014
A_18	0.3277
A_20	0.4960

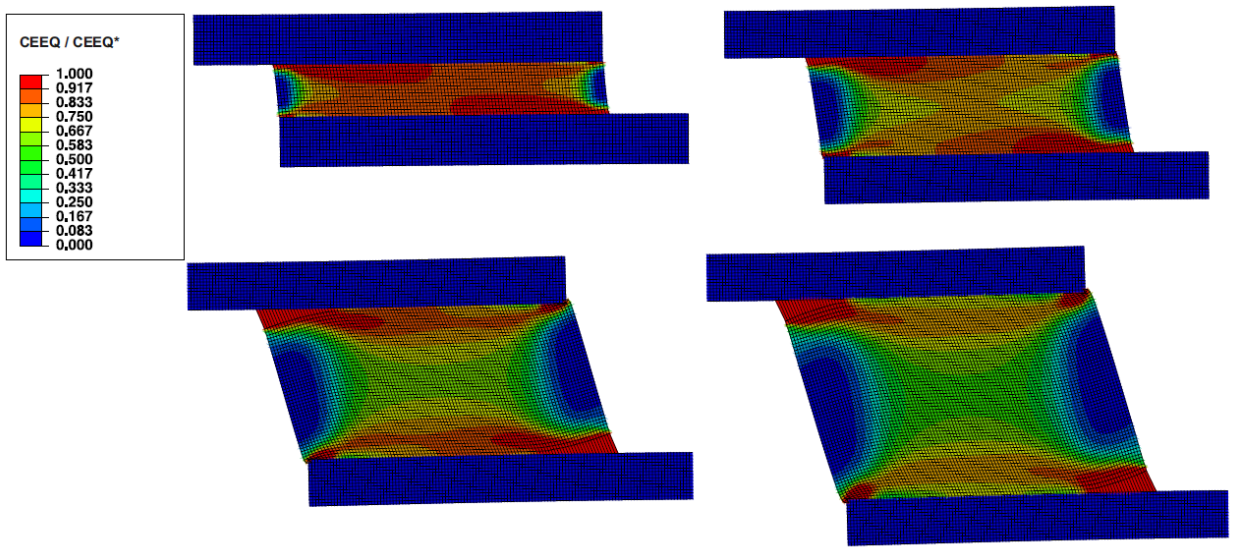

Figure 5.15. The ratio CEEQ/CEEQ* at creep failure for all SLJs at the lowest creep load.

Figure 5.15 shows the creep strain distribution (normalised by the creep failure strain) at the point of failure for all SLJs at the lowest creep load. This is representative of the mode of failure in all the SLJs at all the creep loads. In all joints, the damage initiated at the ends of the joint and grew towards the centre on both interfaces. Both damage fronts were joined in the centre of the joint when they were adjacent to each other. When this occurred, the values of *CEEQ*/*CEEQ** on the adhesive-substrate interfaces were greater than 0.9 and the joint was not able to carry the load specified because of the degradation of the plastic yield stress and thus failure was predicted.

5.2.4.2 Creep modelling of straight bond-type anchorage

The anchors were modelled using the same creep power law as the SLJs. It is known that the secondary bending is one of the key factors which influence the peel stress distribution in SLJs, whilst the effect of Poisson's ratio at the entry point of the bonded anchorages introduces peel stresses. Even though the mode mix in the SLJ and the anchor were not the same, they both experienced peel and shear stresses and thus it was considered that the results could be transferable. The maximum equivalent creep strain was determined according to the geometry of the anchor (see Figure 5.14). In these models the creep time to failure was the unknown variable which was determined in the same way as in the SLJ (i.e. by the evolution of the localised creep failure). Therefore, the anchors were modelled until the joint was no longer able to carry the load specified. As mentioned earlier, the creep modelling of the anchorages was used to predict the creep time to failure of each geometry to assess the creep influence during the fatigue analysis. For this reason the mean fatigue loads which were used in fatigue testing activities, were utilised in this section. The forces assessed were 24 and 36kN.

In the same way as in the SLJs, the damage initiated at the top of the adhesive-tendon interface where stresses were highest, and grew along the bonded length towards the bottom. Figure 5.16 shows the shear stress distribution at the last time increment of each anchor on the adhesive-tendon interface at a creep load of 24kN. The damage front travelled along the joint until it reached the bottom of the joint. At this point the joint was no longer able to carry the load and the failure of the anchor was assumed. It is worth mentioning that the damage front started to travel when the elements were not fully damaged. This means that these elements still had some capacity to sustain load. This is perfectly reflected in Figure 5.16 where the lowest values of shear stress were about 3MPa.

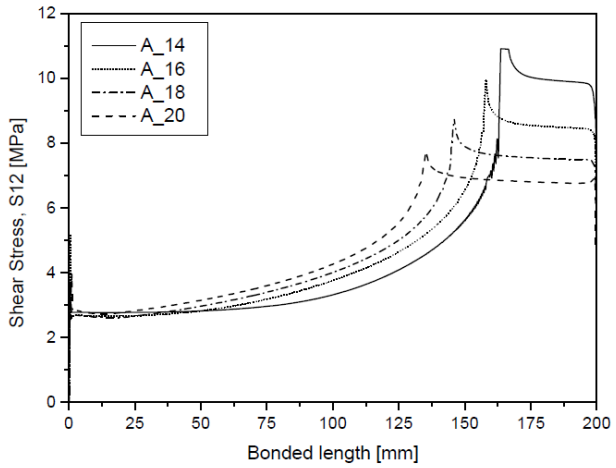

Figure 5.16. Shear stress distribution along the adhesive-rod interface at the last time increment at a creep load of 24kN.

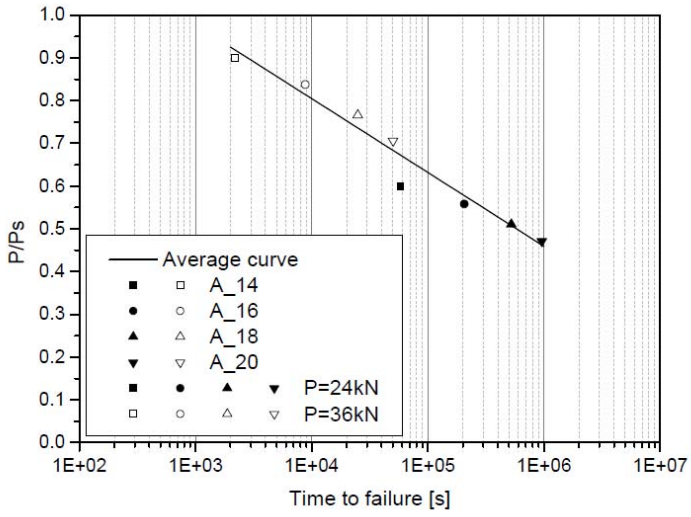

Figure 5.17. Predicted creep failure times for all the geometries.

Figure 5.17 and Table 5.3 show the predicted creep failure times for all the geometries at the two loads. In Figure 5.17 the creep loads were normalised by the static failure load of each anchor (see Chapter 4). The predicted creep failure times of each geometry gave a unique curve showing a consistent trend. As can be

seen in Table 5.3, the predicted creep failure times were greater for each geometry (by a factor ranging between 1.5 to 17.5) than the experimental fatigue tests. This suggests that in many of the cases considered, creep may not significantly influence the fatigue experimental tests. Thus, the creep phenomenon was not considered in the subsequent fatigue modelling (see Chapter 6). This should be considered a starting point and subsequent research should address the combination of creep and fatigue damage.

It can be concluded from Figure 5.17 and Table 5.3, that the adhesively bonded anchors for CFRP rods, might suffer failure by creep at short values of time for high loads. This suggests the anchors should preferably be loaded at low loads so that the creep phenomenon does not become a problem.

Table 5.3. Predicted creep failure times and longest experimental fatigue tests.

Specimens	Time to failure at 24 kN		Time to failure at 36 kN	
	Predicted creep failure time [s]	Longest experimental fatigue test [s]	Predicted creep failure time [s]	Longest experimental fatigue test [s]
A_14	58,453	6,311	1,920	64
A_16	206,020	138,845	8,644	1,567
A_18	524,775	160,586	24,865	1,986
A_20	956,942	271,616	50,122	2,876

5.2.5 Concluding remarks

Creep tests at different loads were conducted on SLJs of various geometries. The creep model, developed from SLJs and applied to the anchors, was based on a time-dependent analysis where the progressive damage and final creep failure were implemented by degrading the plastic yield stress of the adhesive material. Regarding the creep analysis, the following conclusions can be drawn:

1. Creep tests conducted on SLJs showed that specimens with thicker adhesive layers tended to have a shorter lifespan than specimens with thinner layers at the same creep load. The load eccentricity associated with the non-symmetric geometry of SLJs introduced a bending moment which increased the adhesive stresses depending on the adhesive layer thickness. An experimental creep law, which related average shear stress of the bonded joint and time to failure, was obtained and utilised to calibrate the numerical model.
2. A creep power law based on the Bailey-Norton law was utilised in the numerical work. The parameters of the creep power law were calibrated with the experimental data available and it was found that the maximum equivalent creep strain in the SLJs at failure load was thickness dependent. The thickness dependency was mainly caused by the utilisation of a single load-time regression curve of the experimental data. Although, it is considered that this thickness dependency might be physically non-existent, this solution is an artificial way allowing the bonded joints to be simulated under the creep phenomenon. A quadratic polynomial equation which related both variables (CEEQ* and thickness) was found and utilised to obtain the maximum equivalent creep strain most suitable for the thicknesses used in the anchorages.

3. Creep modelling of the straight bond-type anchorages was undertaken successfully. This revealed that the lifespan of the anchors was short at high loads suggesting that they should be loaded at low loads in order to increase their lifespan in real structures.
4. The large predicted creep time to failure at the mean fatigue loads indicated that the creep loading aspect during fatigue testing activities should not significantly influence the fatigue lifetime. Consequently, the influence of the creep phenomenon was not considered in the fatigue modelling (see Chapter 6).

5.3 Stress relaxation analysis

5.3.1 Introduction

The stress relaxation phenomenon is the stress relief of a solid material under the action of a constant strain. The rate of relaxation is usually higher just after the constant strain is applied and it is progressively reduced until a near to constant rate of relaxation is reached. The rate of relaxation is mainly determined by several mechanisms including grain boundary slipping, movement of dislocations, and the formation of vacancies or free volumes.

The long-term load loss in prestressed structures is an important factor which is usually estimated and incorporated into the calculation together with the effective stress. The relaxation stress losses of the prestressing cables mainly depend upon the type of tendon, the anchorage and the initial stress. For this reason, the adhesively bonded anchorage investigated in this research has been studied under the effect of stress relaxation.

On one hand, experimental stress relaxation tests were undertaken on anchorages with adhesive 02 where the main parameter assessed was the adhesive thickness of the anchorage. Ten specimens were prestressed at three different initial tensioning forces and the displacement was held constant in order to study the experimental load loss in the specimens. During this time, seven specimens were additionally restressed to the original tensioning load when the load loss was stabilised and constant.

On the other hand, the creep power law found in the creep analysis was used to predict the stress relaxation of the anchors. The model was implemented in Abaqus/CAE and the load loss of each anchor was simulated during the relaxation process before restressing, and compared with the experimental data.

5.3.2 Objectives

Straight bond-type anchorages were experimentally and numerically investigated under stress relaxation loading. Different geometries were tested at three different initial tensioning forces[6]. The initial tensioning

[6] The initial tensioning forces were 16, 24 and 32kN.

forces were approximately distributed equidistantly within the static strength range of the anchorages. Also, the geometries cases were simulated numerically using the numerical model found in the creep analysis section from SLJs. The main objectives of this section are described as follows:

1. To design and propose a test setup for long term tests in order to study the stress relaxation on straight bond-type anchorages after applying the initial tensioning force. The system mainly consists of a tubular support, which kept a constant distance between both anchorages of each specimen, and a load cell that continuously recorded the tensioning force.
2. To investigate the load loss experimented by the anchorages when an initial loading force was applied. The tendency and the relationship between the load loss and the different geometries was studied. The influence of the different initial tensioning forces in the load loss evolution was also investigated.
3. To study the restressing technique on straight bond-type anchorages. Several specimens were restressed up to four times at their corresponding initial tensioning force once the load loss was stabilised and constant. The load loss evolution after restressing was experimentally studied.
4. To predict the stress relaxation of the different geometries of the straight bond-type anchorages by using the numerical model described in the creep analysis section. The model was implemented in Abaqus/CAE through the Bailey-Norton creep law and the load loss of each anchor was investigated and compared to the experimental results during the relaxation process before restressing.
5. To establish the most relevant recommendations for a potential use of straight bond-type anchorages in prestressing applications by discussing the experimental and numerical results.

5.3.3 Experimental work

5.3.3.1 Test setup

A new system was developed in order to measure the load loss when the displacement between anchorages is fixed. Figure 5.18a shows half a section of the specimen and its system for keeping the displacement constant. Specimens were located into a tube and both ends were fixed. At one end, a load cell of 100kN was placed to continuously measure the tensioning force of the anchor. Through a thread adapter, this anchor of the specimen was completely attached to the load cell. At the other end, a reaction steel plate, nut and washer were placed but not attached to the anchor. The specimen was pulled with a hydraulic jack for stretching cables. However, the jack did not prestress the anchor directly. Instead, a prestressing steel cable, which was attached to the anchor through a cable-anchor connector, was used. It is worth noticing that during the prestressing process, the jack produced the action over the steel cable (tensioned) and the reaction over the reaction plate 2, the double H-beam (also known as double I-beam) and the reaction plate 1 (compressed). The double H-beam was chosen because its cross section allowed the free movement of the

steel cable between its webs during the prestressing process. As the double H-beam did not allow the access for screwing the nut to the reaction plate 1, separating wedges were introduced between the reaction plate 1 and the double H-beam. This allowed for the nut to be accessed. Once the specimen reached the desired tensioning force, the reaction plate 1 was attached to the specimen through the nut and washer and the force made for the hydraulic jack was released and transferred to the reaction plate 1. The tubular support kept the distance between load cell and reaction plate 1 constant. As in a real prestressed concrete structure, the tubular support was the compressed element. For this reason, the tube has to be thick enough to assure that the load loss is caused primarily by the large adhesive deformation in comparison with the steel tube deformation. The length and thickness of the tubular support used in this research were 720 and 4mm, respectively. The procedure for pulling the specimen and all the components can be seen in Figure 5.18b.

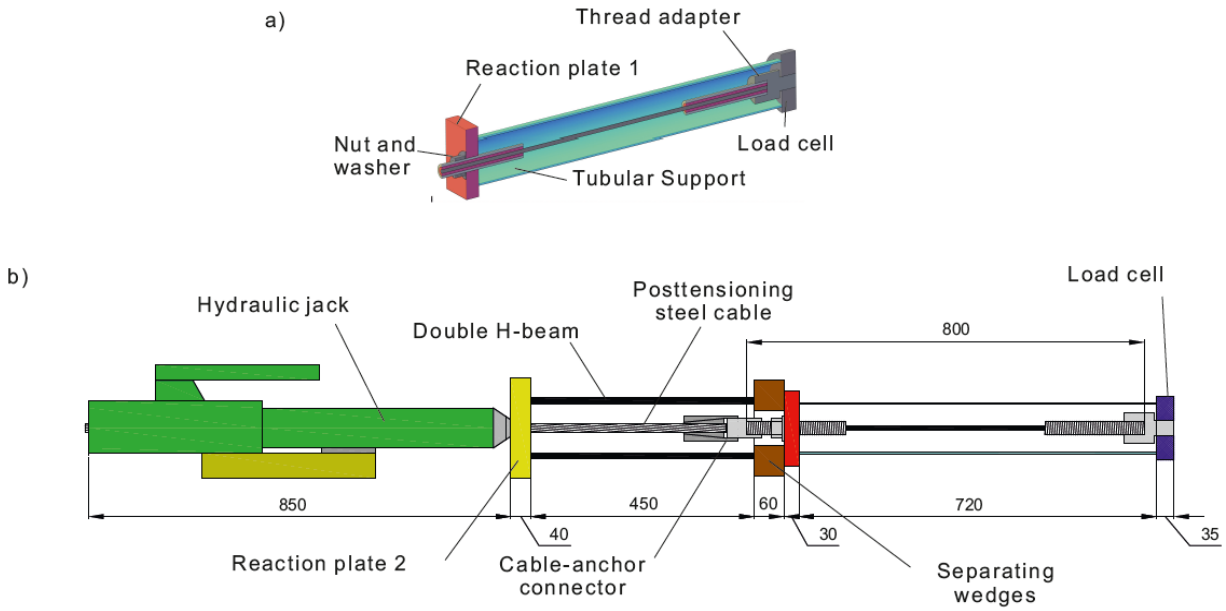

Figure 5.18. a) anchor dimensional details b) scheme of the stress relaxation test setup b) scheme of the tensioning process. All the dimensions in millimetres.

A 250kN CTT-Stronghold hydraulic jack was used to pull the specimens. Force and time were recorded at a frequency of 1 Hz using an HBM Spider 8 acquisition system. Despite there being an equivalence between the pressure of the jack and the pulled force, the values of the load cell were used during the prestressing procedure to determine at what point the specimen should be attached to the reaction plate 1. The hydraulic jack was manually controlled at approximately 5 kN/min. The anchors were pulled at three different loading forces; 16, 24 and 32kN. When the specified force was reached, the jack pressure was locked and the specimen was attached to the reaction plate 1. Then, the force was unloaded with the hydraulic jack and was transferred to the structure (see Figure 5.18a).

The stress relaxation setup and posttensioning system are shown in Figure 5.19. Four different geometries were assessed under stress relaxation in the present work, where the main parameter assessed was the

adhesive thickness of the anchorage. The specimens tested, and the initial tensioning force (target and experimentally achieved), are summarised in Table 5.4. The last number of the nomenclature used for the specimens refers to the repetitions of each geometry. Geometries A_14 and A_16 were evaluated under two initial tensioning forces (16 and 24kN) whilst geometries A_18 and A_20 were studied under three initial tensioning forces (16, 24 and 32kN). It is worth noticing that not all the specimens of the same group had exactly the same initial tensile load. This was due to a loss of load during the manual load transfer between the hydraulic jack and the structure (see Table 5.4). Also, seven specimens were restressed up to four times at the same initial tensioning force when the load loss was lower than 0.5% per day of each specimen's initial tensioning force in order to evaluate whether the evolution of the load loss was similar for all the stressing steps. Three specimens were not restressed to assess the long-term influence (specimens A_16_1, A_14_2 and A_16_2).

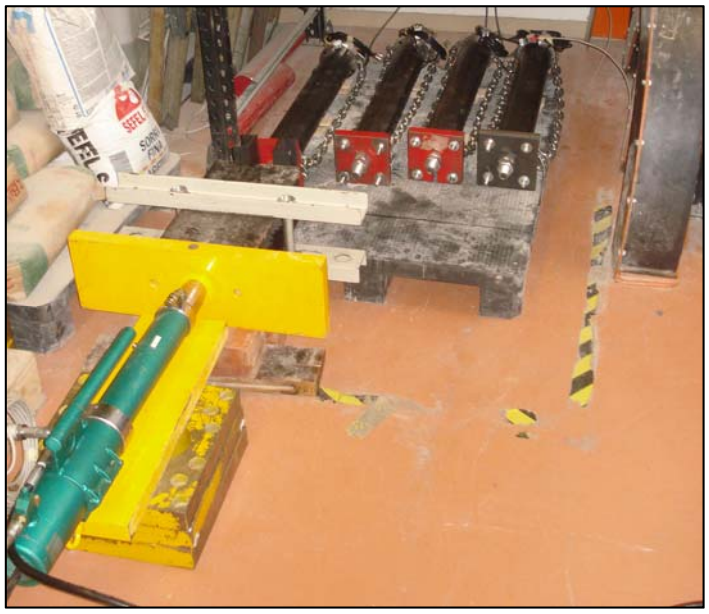

Figure 5.19. Loading process of the specimens.

Table 5.4. Target and experimental initial tensioning forces.

Specimen	Initial force target [kN]	Experimental initial force [kN]
A_14_1	16.00	15.52
A_16_1	16.00	11.64
A_18_1	16.00	16.78
A_20_1	16.00	17.01
A_14_2	24.00	21.40
A_16_2	24.00	24.05
A_18_2	24.00	22.42
A_20_2	24.00	26.13
A_18_3	32.00	31.43
A_20_3	32.00	30.83

5.3.3.2 Results and discussion

The static strength of the anchorages was required to normalise and compare the experimental stress relaxation data amongst the different geometries. For this reason, in the quasi-static analysis of the anchorages, static tests were conducted on the anchors with the thinnest and thickest adhesive layer (see Chapter 4). Static strengths of 39.95 and 51.15kN were obtained for the thinnest and thickest adhesive layer respectively. From these values, a linear interpolation was considered between the adhesive thickness and static strength, as it was observed in previous works [137].

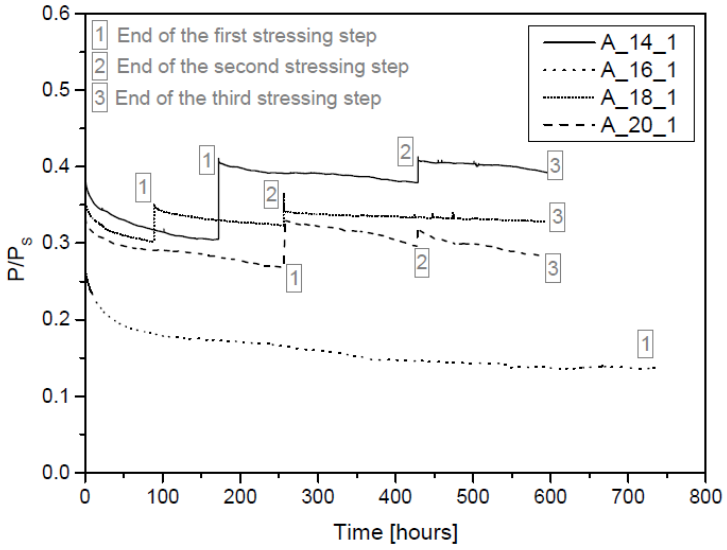

Figure 5.20. Experimental normalised load-time data for the anchors tensioned at 16kN.

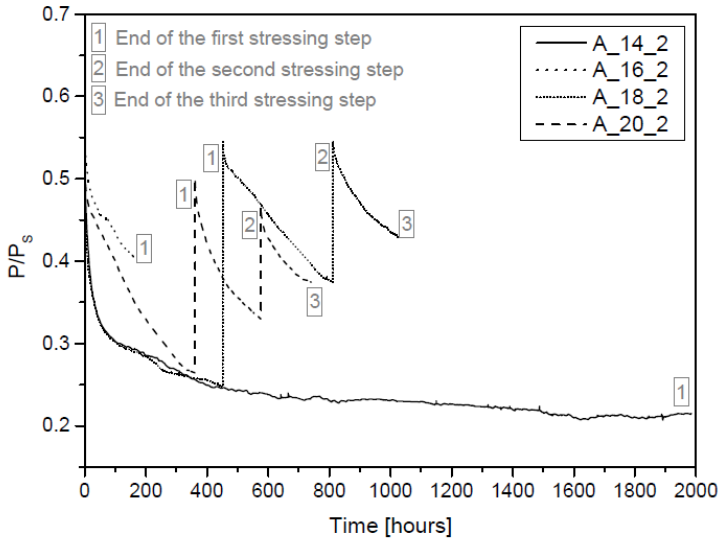

Figure 5.21. Experimental normalised load-time data for the anchors tensioned at 24kN.

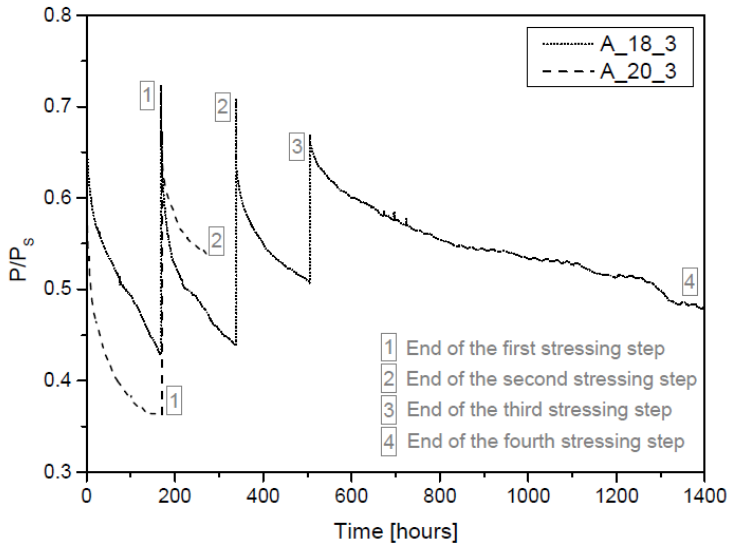

Figure 5.22. Experimental normalised load-time data for the anchors tensioned at 32kN.

Figure 5.20, Figure 5.21 and Figure 5.22 show the experimental normalised load-time data at three different initial tensioning forces (16, 24 and 32 kN) where the recorded load, P, was normalised by the static failure load of the anchorage, P_s. In general, it was observed that the load loss was similar for all the specimens with the same initial tensioning force but different amongst those with different initial tensioning forces. The greater the tensioning force, the greater was the load loss recorded. Moreover, restressed specimens show a lower load loss in each stressing step. This might be caused by the reduced mobility of the polymer chains of the adhesive after successive tensioning. Whereas the specimens which remained with the same tensioning force show that the load loss was gradually stabilised until a constant load loss rate was reached.

Figure 5.23 shows the normalised load loss of the all the specimens during the first 300 hours of the first stressing step. The normalised load loss was calculated through the Equation 5.2, which gave the normalised load loss ratio per unit of time. The specimens were grouped into three main groups according to the initial tensioning forces under which they were stressed (16, 24 and 32 kN). The maximum load loss for all the specimens occurred at the beginning of the test. Then, the ratio load loss decreased until a constant load loss ratio of 0.00125 per hour was reached. This constant load loss ratio was reached approximately after 25 hours of testing. From this value towards either the end of the test or the end of the stressing step, the load loss ratio remained constant for all specimens.

$$Normalised\ load\ loss = \frac{\left|\frac{P_{i+1}}{P_s} - \frac{P_i}{P_s}\right|}{t_{i+1} - t_i} \quad \text{(Equation 5.2)}$$

where Pi is the current loading force in the step i, Ps is the static failure load of the anchorage and t is the time in the step i. Figure 5.24 is a zoom-in of the load loss during the first 25 hours of testing where the load loss was markedly more pronounced. It can be seen, that there was an experimental trend for each

initial loading force. A three-term exponential equation was used to match the experimental stress relaxation data as it usually provides a reasonably good fit for expressing the relaxation curve as mentioned by Rudra [138]. The normalised load loss during the first 25 hours was more significant for the highest initial tensioning force (32kN). As the initial tensioning force was lower, the normalised load loss was reduced. The increase of load loss at the beginning of the test was found to be non-proportional whilst the initial stress increased proportionally (increments of 8 kN). A physical reason of this result might be the molecular rearrangement in the adhesive layer. The overall molecular structure of a cured epoxy is a disordered crystalline structure [139]. The epoxy resin and hardener (polyamines for MBrace Primer) are mixed together in a liquid state (not crystalline state). Once they are mixed, the crosslinking process, between polymer chains, starts through ionic bonds. The resultant network is a three-dimensional block with a disordered molecular structure. This results in significant spaces in the molecular structure called free volume. As a viscoelastic material combines both viscous and elastic characteristics, when a load is applied, creep or stress relaxation phenomena appear as a molecular rearrangement [71]. When the loading process started, crystalline structures were deformed due to the load stress. At the same time, due to the disorder of the crystalline chains (free volume), these were rearranged very rapidly. As the load increased during the loading process, the molecules kept being rearranged at a lower rate because of the crystalline structure's compaction

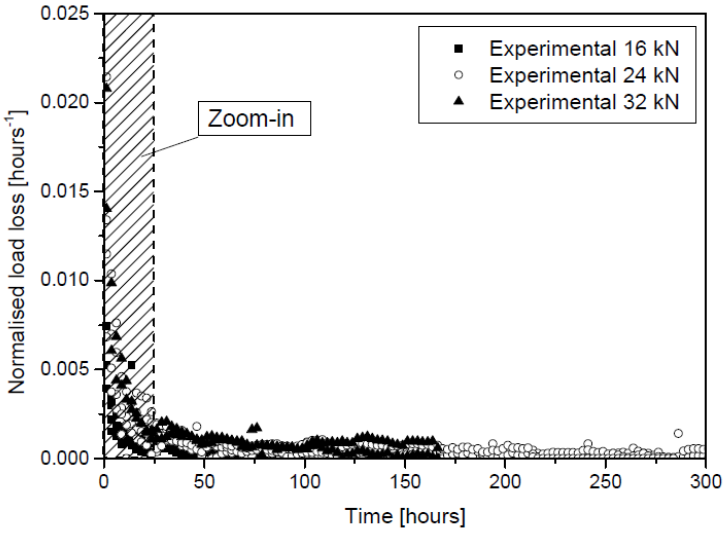

Figure 5.23. Experimental normalised load loss of all the anchors during the first 300 hours grouped according to the three initial tensioning forces.

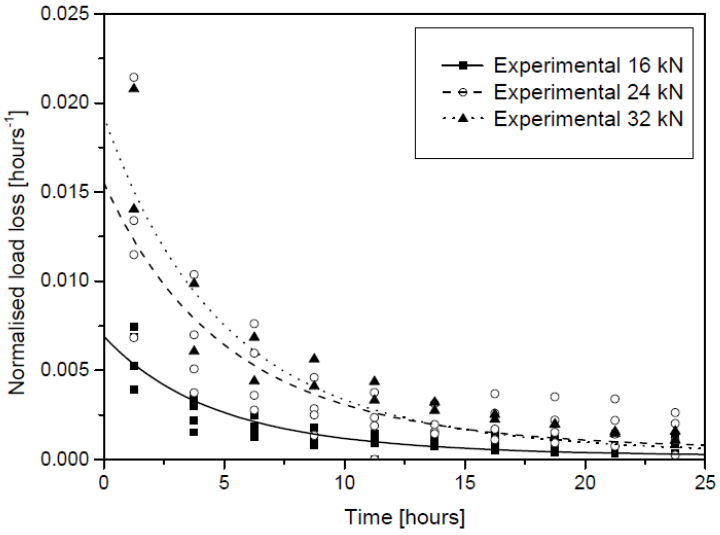

Figure 5.24. Experimental normalised load loss of all the anchors during the first 25 hours grouped according to the three initial tensioning forces and experimental trend curves.

Additionally, the influence of restressing was experimentally studied. Seven specimens were restressed up to four times when the load loss was lower than 0.5% per day of the initial tensioning force of each specimen. As discussed previously, creep or stress relaxation phenomena mainly appear as a molecular rearrangement. As can be seen in Figure 5.25, Figure 5.26 and Figure 5.27, the load loss was more accentuated just after the load was applied (first stressing step). Once the specimens were restressed again to the original tensioning force, the molecular rearrangement rate increased but not as strongly as in the first restressing. This was because the molecules were already rearranged and the spaces between the chains were reduced.

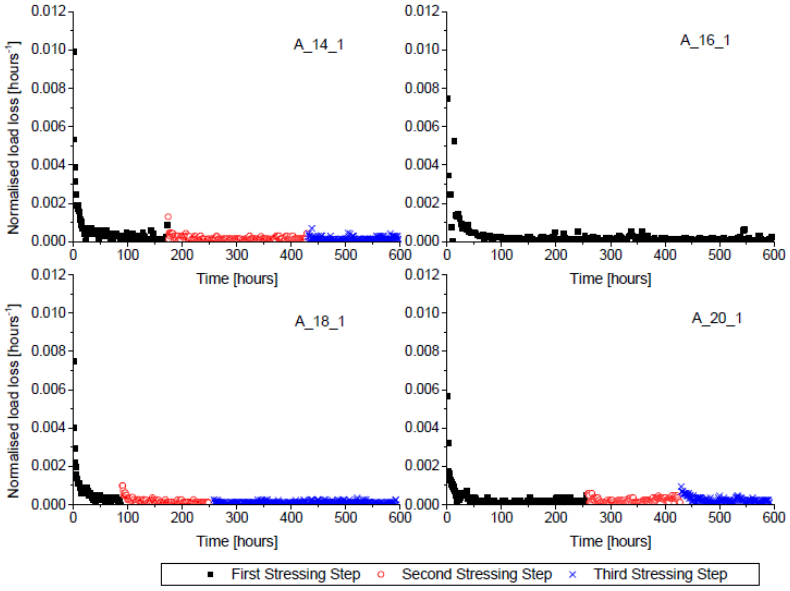

Figure 5.25. Experimental normalised load loss of all the anchors loaded at 16kN.

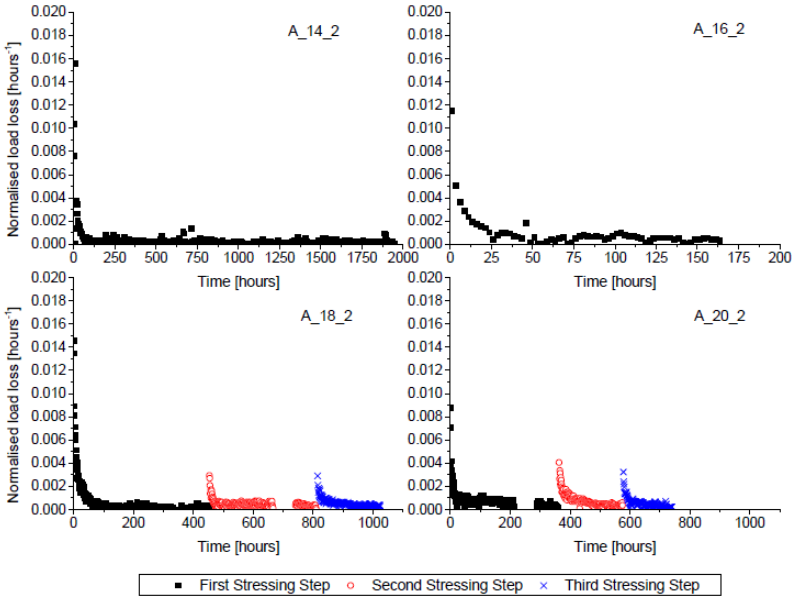

Figure 5.26. Experimental normalised load loss of all the anchors loaded at 24kN.

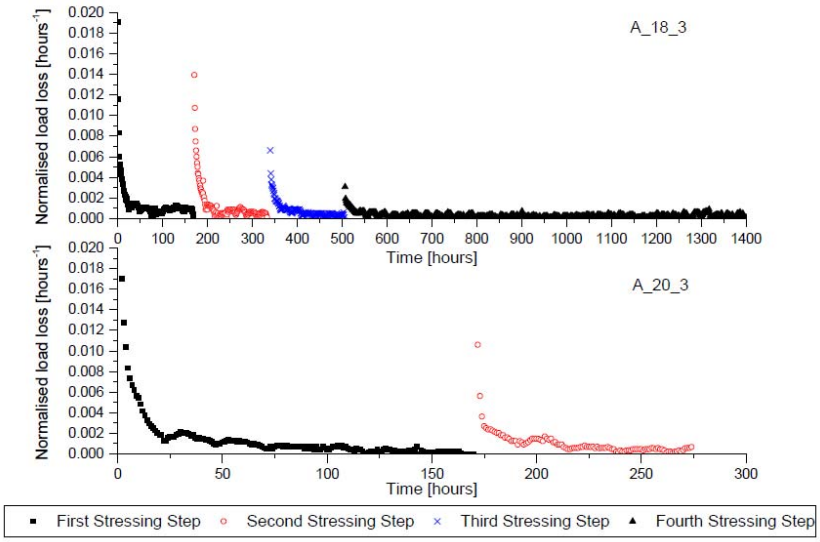

Figure 5.27. Experimental normalised load loss of all the anchors loaded at 32kN.

It was observed that the load loss after restressing remained at a very low rate for specimens stretched at low initial tensioning forces. In these cases, restressing allowed the specimens to reach the working tensioning force without increasing the load loss ratio. This suggests that spaces between molecular chains did not increase and so the load loss ratio was largely kept at the same value. Figure 5.25 shows how the load loss rate at the second and third stressing step of the restressed specimens mainly remained constant. The results demonstrate that the restressing technique allows the desired working tensioning force to be reached once it has been reduced by time-dependent phenomena. For adhesively bonded anchorages loaded up to 40% of the static failure load of the anchorage, one restressing permitted the initial tensioning force to be reached almost without increasing the load loss ratio.

For higher initial tensioning forces (anchorages loaded more than 40% of the static failure load of the anchorage), the load loss ratio was increased during the second, third and fourth restressing, once it was established in the previous stressing step. This may be due to high initial tensioning forces allowing for a higher molecular rearrangement when the specimens were restressed. Nevertheless, in each stressing step the load loss ratio was lower than the previous stressing step. This can be observed in Figure 5.26 and Figure 5.27 where the load loss achieved the lowest rate after successive restressing.

It is worth noticing that this increase of the load loss ratio was lower for each extra prestressing step. However, attention has to be paid with strain failure criteria as these consider that the material fails when it exceeds a certain strain limit in a given area. In this study, strain effects were not a limitation.

Finally, three specimens were not restressed and the long-term influence was assessed. As previously mentioned, the maximum load loss and, therefore, the highest molecular rearrangement rate for these specimens occurred at the beginning of the test. The ratio load loss then decreased until the specimens reached a constant load loss ratio up to the end of the test.

5.3.4 Numerical modelling

A finite element model was developed in Abaqus/CAE to predict the stress relaxation response of the bonded anchorage. A 2D axisymmetric model was used (see Figure 5.28) in order to simplify the geometry and optimise the computing resources. Four different geometries were modelled according to the geometries tested experimentally[7]. The bottom of the steel housing was fully fixed and the top of the CFRP rod was loaded with an axial displacement.

A sensitivity analysis of the mesh was conducted in order to determine the most suitable mesh size for the straight bond-type anchorages under stress relaxation loading. It is worth noticing that the mesh density used for the anchorages in the creep analysis was the same mesh used with SLJs (0.1mm). Using the same mesh density for both cases (anchorages and SLJs) was more valid in the creep analysis as the results from the SLJs simulation were used to determine the maximum equivalent creep strain allowed for the anchors. However, the same mesh density was not required for the anchorages under stress relaxation loading as the maximum equivalent creep strain depending on the thickness was not used. The converge analysis revealed that a variation of the maximum equivalent creep strain (*CEEQ*) and maximum shear stress distribution on the adhesive-tendon interface, between the mesh density utilised in the creep analysis (0.1mm) and the optimum mesh size obtained in quasi-static modelling of the anchors (0.5mm), was lower than 0.5%.

Therefore, four-noded axisymmetric stress elements (CAX4R) with a mesh density of 0.5mm were used for the whole model. Geometric non-linearity was included in all the analyses. A time-dependent analysis

[7] Geometries A_14, A_16, A_18 and A_20.

was required to consider the viscoelastic phenomenon. The Young's modulus and Poisson's ratio used for each material are summarised in Chapter 3. Elastic-perfectly plastic von Mises response was assumed in the adhesive and the plastic yield stress was defined at 17.20MPa as this was the maximum strength obtained in the quasi-static analysis (see Chapter 4).

In the first step, the displacement was applied linearly from 0 to d_{max} in 1 second. A different d_{max} was used for each specimen in order to obtain the experimental initial load of each tested anchor (see Table 5.4). In the second step, the displacement remained constant and the stress relaxation was analysed.

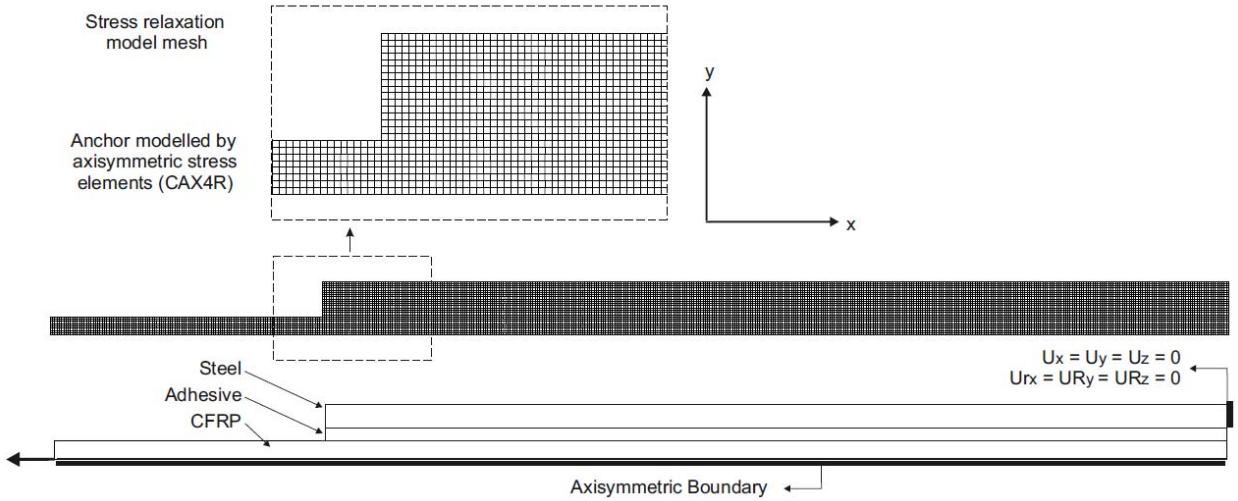

Figure 5.28. Finite element mesh and boundary conditions for the anchor with a bore of 14mm and length of 200mm.

The viscoelastic properties of the adhesive were assumed through the Bailey-Norton power law, better known as creep power law. The power law is presented in Equation 5.3.

$$\frac{d\varepsilon_{cr}}{dt} = A \cdot \sigma^{B} \quad \text{(Equation 5.3)}$$

where *A* and *B* are material constants, ε_{cr} is the creep strain, *t* is the creep time and σ is the normal tensile stress at which the specimen is subjected. As discussed in the creep analysis section, the experimental creep times to failure from the single lap joints were used to find and calibrate a creep power law able to predict the creep failure time in anchorages [140]. The power law multiplier, A, and the equivalent stress order, B, were found to be 1.75E-13 and 7, respectively.

The time-dependent behaviour of viscoelastic materials must be expressed by a constitutive equation which includes time as a variable, in addition to the stress and strain variables. Therefore, the power law presented in Equation 5.3 can be adapted to describe the stress relaxation phenomenon where there is a variation of stress with respect to time. Due to the fact that the displacement between anchors was held constant in this study, the total strain differential with respect to time must be zero. Thus, the Equation 5.4 can be written:

$$\frac{d\varepsilon_{el}}{dt} = -\frac{d\varepsilon_{cr}}{dt} \quad \text{(Equation 5.4)}$$

where ε_{el} is the elastic strain and ε_{cr} the creep strain. Moreover by Hooke's law is known that;

$$d\varepsilon_{el} = \frac{d\sigma}{E} \quad \rightarrow \quad \frac{d\varepsilon_{el}}{dt} = \frac{1}{E} \cdot \frac{d\sigma}{dt} \quad \text{(Equation 5.5)}$$

where E is the elastic modulus of the adhesive. Combining Equations 5.3 and 5.5 into the Equation 5.4, the creep power law for stress relaxation can be written:

$$\frac{d\sigma}{dt} = -A \cdot E \cdot \sigma^{B} \quad \text{(Equation 5.6)}$$

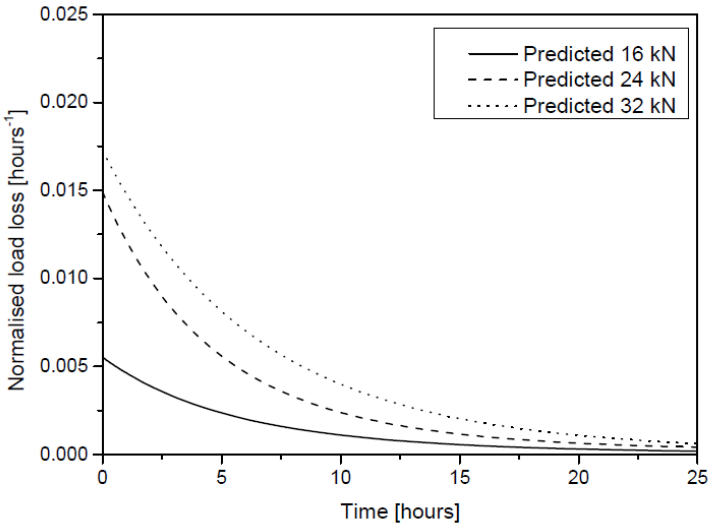

Figure 5.29. Predicted average curves of the normalised load loss for each initial tensioning force during the first 25 hours.

Equation 5.6 was implemented into the model which was utilised to predict the load loss of the first stressing step for each anchor. All the geometries were simulated at their experimental initial tensioning forces (see Table 5.4) with the parameters mentioned earlier. The predicted normalised load loss was obtained for all the geometries during the first 25 hours of the first stressing step. Similarly to the experimental data, the predicted stress relaxation curves for all the specimens of each initial tensioning force were grouped in an average curve. The average curves of each initial tensioning force are shown in Figure 5.29. Analogous behaviour was numerically observed in all the average curves, with no sudden changes. Consistent with the experimental data, the load drop was greater for the highest initial tensioning force and smaller for the lowest initial tensioning force. Also, the increase of load loss at the beginning of the test was found to be non-proportional with the initial tensioning force.

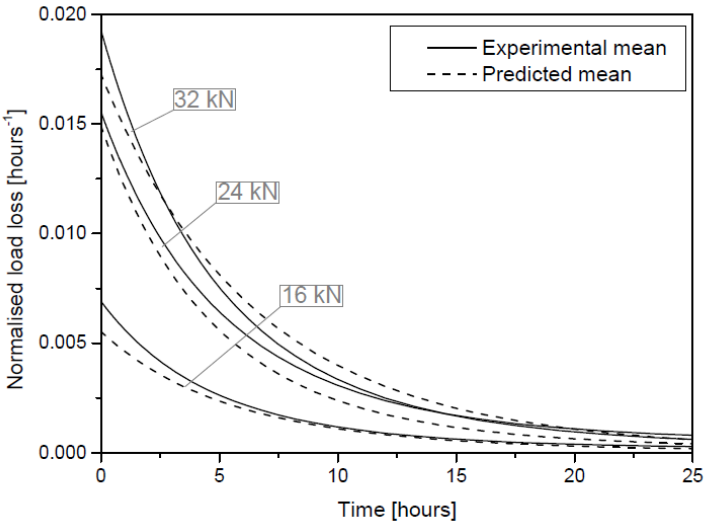

Figure 5.30. Experimental and predicted average curves of the normalised load loss for each initial tensioning force during the first 25 hours.

Comparing Figure 5.24 and Figure 5.29, the experimental results were broadly consistent with the numerical data along the load drop. This is illustrated in Figure 5.30. On the whole, there is a slight difference between both curves of each initial tensioning force that decreases over time. Once the curves reach stabilisation at around 25 hours, experimental and numerical trends are practically at the same value of normalised load loss per unit of time.

Figure 5.31 illustrates five different time stages of the predicted shear stress distribution in the adhesive layer during the stress relaxation process for the anchor with the thickest adhesive layer (A_20_3) at the highest initial tensioning force. The behaviour of this anchor was representative of the behaviour of all the anchors. On the left, shear stress contour plots on the adhesive layer are displayed whereas on the right, the shear stress distributions along the rod-adhesive interface are plotted. Also, in each time stage displayed in Figure 5.31, time, *t*, and the predicted resulting loading force, *P*, normalised by the static failure load of the anchorage, *Ps*, are provided. Time step "A" shows the shear stress distribution in the first second of the simulation. At this point there was not enough time for the molecular rearrangement to occur in the bonded joint and so the joint behaved entirely with no time-dependent effects. Although the plastic yield stress was reached at the first elements of the top of the bonded joint, the rod-adhesive interface mainly behaved linear-elastically with the maximum stresses occurring at the top of the bonded joint as can be seen in the plot. After approximately two minutes, at the time step "B", the shear stress peak at the top of the bonded joint suffered a quick reduction that affected the first 25mm of the bonded length. As shown in the plot, the maximum value of shear stress was reduced by about 20% of its initial value (reduction of 2.5MPa). Subsequently, the shear stress distribution kept reducing but in a lower ratio. At the time step "C", after 75 minutes, the shear stress distribution was completely flat within the first 75mm of the bonded joint. The maximum value of shear stress was reduced by around 40% of its initial value (total reduction of 4.5MPa)

and the shear stress distribution was more uniform. Time steps "D" and "E" show the shear stress distribution after 675 and 10,000 minutes. At these stages, the distribution was practically flat along the overlap length and the load loss per unit of time was very small.

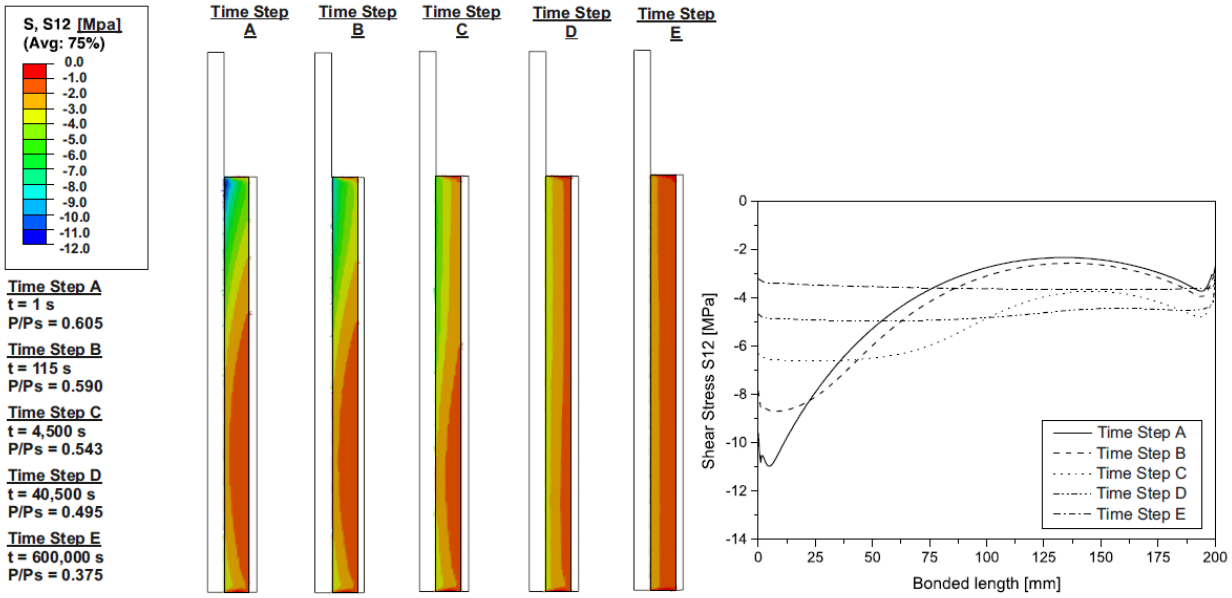

Figure 5.31. Shear stress evolution along the adhesive layer for the geometry A_20_3.

5.3.5 Concluding remarks

Adhesively bonded anchors under stress relaxation were examined experimentally and numerically at three different initial tensioning forces. Ten specimens were tested, seven of which were restressed up to four times at the initial tensioning force when the load loss rate was stabilised. Regarding the experimental normalised load-time data the following conclusions can be drawn:

1. The load loss was similar for all the geometries of each initial tensioning force. A unique and clear experimental trend for all the geometries of each initial loading force was found.
2. The load loss was found to be different among the initial tensioning forces. The greater the initial tensioning force, the greater was the load loss recorded. Also, this increase of load loss was non-proportional to the increase of initial stress.
3. Restressed specimens showed that restressing might increase the molecular rearrangement among molecular chains of the adhesive layer and thus, this results increasing the load loss ratio once it was stabilised in the previous stressing step.
4. The increase of load loss ratio for each restressing was found to be lower for each successive restressing. However, specimens might fail if the adhesive ultimate strain is reached for a given area.

A finite element model was developed in Abaqus/CAE to predict the stress relaxation response of the bonded anchorage using a time-dependent analysis. Elastic-perfectly plastic von Mises response was assumed in the adhesive layer and the time-dependent behaviour of the adhesive was considered through the Bailey-Norton law. From the prediction of the first stressing step of load loss of each anchor, the following conclusions can be drawn:

5. Stress relaxation modelling of anchors was undertaken successfully. The creep power law has provided a predicted joint time-dependent behaviour that correlate closely with the experimental trend curves for the first stressing step.
6. It was observed experimentally and numerically that the anchors suffered the highest molecular rearrangement on the adhesive layer once the load was applied. Afterwards, the molecular rearrangement was gradually reduced until a constant load loss rate was reached. For all the specimens, the stabilisation of the load loss rate was reached approximately 25 hours after the loading force was transferred.

To conclude, experimental and finite element modelling results provide valuable information in order to develop future design recommendations for adhesively bonded anchorages for CFRP tendons with the specified configuration in this study. The most notable recommendations are described below.

1. The restressing technique allows for the working load of the composite bar to be increased by successive restressing once time-dependent phenomena has reduced the initial tensioning load.
2. The load loss rate caused by the stress relaxation reaches a stabilised and constant value after approximately 25 hours. Restressing is suggested when the load loss rate has been stabilised after each restressing.
3. The load loss achieves the lowest rate after the fourth consecutive restressing for initial loading forces ranging between 60 and 70% of the static failure load of the joint.
4. The load loss achieves the lowest rate after the third consecutive restressing for initial loading forces ranging between 45 and 55% of the static failure load of the joint.
5. For the anchorages loaded up to 40% of the static failure load of the joint, one restressing allows the initial tensioning force to be reached without further load loss.

Chapter 6. Constant amplitude fatigue analysis

6.1 Introduction

One of the most visible prestressed concrete products is the prestressed girder in large infrastructures such as bridges. These structures are usually subjected to cyclic loading below their maximum strength. However, the repeated loading and unloading may cause certain damage mechanisms that may lead to the unexpected failure of the structure. For this reason, fatigue is an important factor which needs to be considered in prestressed structures.

Experimental fatigue tests on straight bond-type anchorages were undertaken with failure occurring on the adhesive-tendon interface. Four different adhesive thicknesses were evaluated under three constant amplitude fatigue loadings. The experimental fatigue response of adhesively bonded anchorages was discussed and an experimental load-life average curve was obtained for all the anchorages.

The fatigue response of the straight bond-type anchorages was also predicted using Finite Element Analysis. A multi-linear traction-separation cohesive zone model was implemented at the adhesive-tendon interface when simulating the fatigue loading of the anchorages. The cohesive law obtained in the quasi-static analysis in Chapter 4 was used in the fatigue model. The fatigue damage model used in this research was based on the degradation of the cohesive elements taking into account the fatigue damage evolution.

This chapter summarises the experimental work and numerical modelling of the straight bond-type anchorages under constant amplitude fatigue.

6.2 Objectives

Adhesively bonded anchorages for CFRP tendons with adhesive 02 were experimentally and numerically studied under constant amplitude fatigue loading. Four geometric cases were assessed under three different fatigue loading spectra. The main objectives of this analysis were to:

1. Obtain an experimental load-life curve for the straight bond-type anchorages. Specimens with different adhesive thickness were experimentally tested under three fatigue loading spectra. The influence of the adhesive thickness during the loading process and the number of cycles to failure of each specimen was investigated. With the aim to normalise the experimental data, the influence of the maximum load and the loading range was also assessed.

2. Analyse the failure mode of anchorages under constant amplitude fatigue. As it has been seen in previous chapters, the specimen failure was expected on the adhesive-tendon interface, mainly due to adhesion failure. For this reason, a failure surface analysis of specimens was also carried out through a conventional naked-eye and microscopic examination after testing.
3. Develop a numerical fatigue model to predict the number of cycles to failure of straight bond-type anchorages under constant amplitude fatigue loading. The models presented by Khoramishad et al. [92–94] for SLJs were investigated in order to accommodate a cohesive zone between the adhesive layer and the tendon. The influence of fatigue was simulated by assessing the evolution law for blocks of cycles and degrading the traction-separation response of the cohesive elements. The multi-linear traction-separation law found in the quasi-static analysis for circular straight bond-type anchorages was used.

6.3 Experimental work

6.3.1 Test setup

Fatigue tests on the anchor joints were carried out using an MTS actuator by applying a sinusoidal waveform controlled by force at a loading frequency of 4 Hz. The loading frequency was chosen according to the investigation conducted by Crocombe et al. [90] where it was found that, in many cases, the maximum fatigue load and the load ratio determine the fatigue response of adhesively bonded joints when the frequency ranges between 1-10Hz. The number of cycles, load, displacement and time were recorded at a frequency of 100 Hz using an MGCPlus acquisition system. The fatigue test setup is shown in Figure 6.1.

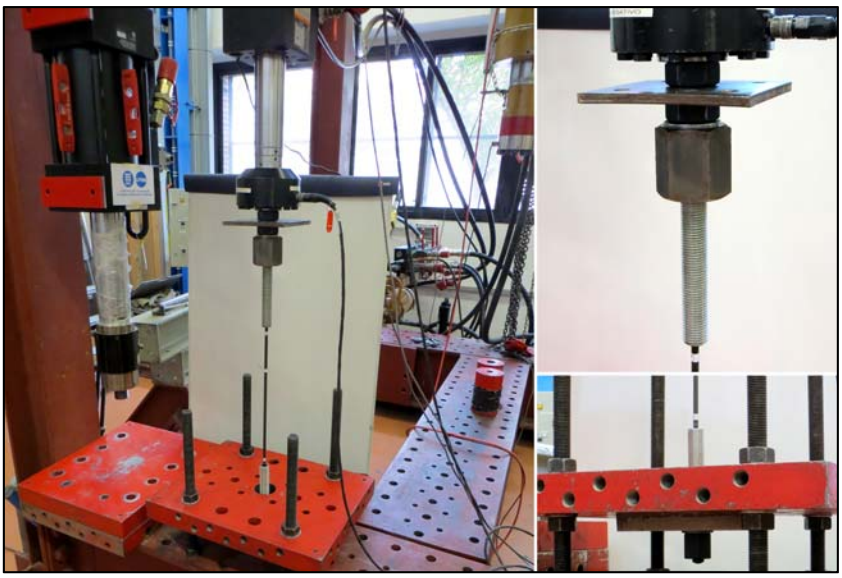

Figure 6.1. Fatigue test setup for anchors.

First, one anchorage of the test specimen was completely attached with nuts and washers to the MTS actuator load cell, whereas the other anchorage remained free. The displacement of the actuator was then

adjusted to place the second anchorage of the specimen through the reaction plate hole. Subsequently, this anchorage was fixed with nuts and washers. Once both anchorages of the test specimen were fixed, the MTS actuator was manually controlled to reach the specified average load of each test. During this process the alignment was carefully verified and confirmed in order to avoid unwanted effects such as a bending moment due to an eccentricity. Once the average load was reached, the fatigue test started and was controlled by the MTS actuator. The fatigue loading spectra that were assessed are summarised in Table 6.1.

Table 6.1. Fatigue loading spectra conditions.

Fatigue loading spectra	$R=P_{min}/P_{max}$	P_{min} [kN]	P_{mean} [kN]	P_{max} [kN]
A	0.84	33	36	39
B	0.77	21	24	27
C	0.92	23	24	25

6.3.2 Results and discussion

As anticipated in previous chapters, the failure occurred in the adhesive-tendon interface by adhesive failure. Figure 6.2 shows slippage of the composite rod relative to the adhesive due to the pull-out of the tendon. It can be seen that small particles of the adhesive remained attached to the CFRP tendon after failure.

Figure 6.2. Typical failure surface in the bonded anchorages with CFRP under fatigue loading.

Table 6.2 summarises the experimental number of cycles to failure of straight bond-type anchorages tested under fatigue loading. It is worth mentioning that three specimens did not reach the failure by the end of the fatigue test. The case with the lowest cycles was due to a clamping system failure halting the test. In the remaining two cases this was because the maximum number of cycles ($1x10^6$) was reached. The maximum number of cycles that were recorded in these three cases are specified in Table 6.2.

Table 6.2. Experimental fatigue results.

Specimen	Fatigue loading spectra	Number of cycles to failure
A_14_3	A	254
A_14_4	B	14,058
A_14_5	C	25,242
A_16_3	A	6,269
A_16_4	B	22,209
A_16_5	C	555,382
A_18_4	A	7,946
A_18_5	B	50,127
A_18_6	C	642,345
A_20_4	A	> 11,506
A_20_5	B	> 615,700
A_20_6	C	> 1,086,463

In the present work, the maximum fatigue loads were approximately set from the usual stress levels of steel tendons for prestressing. According to the static strength of the geometries tested, the maximum fatigue load of the static strength of the anchorage bonded joints ranged between 50%, for the lowest average fatigue load applied to the anchorage with the thickest adhesive layer, and 90%, for the highest average fatigue load applied in the anchorage with the thinnest adhesive layer.

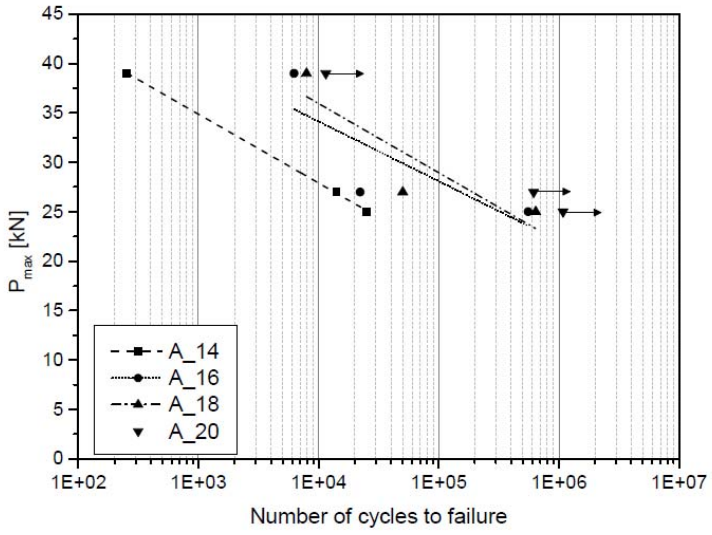

Figure 6.3. Experimental non-normalised load-life fatigue data for the anchors.

The experimental fatigue results are plotted in Figure 6.3. The maximum fatigue load, P_{max}, has been plotted against the number of cycles to failure. From the experimental fatigue test results of the anchors, it was observed that the specimens with a higher adhesive thickness generally achieved a higher number of cycles to failure. This is probably due to the fact that the thicker adhesive layers produced a more uniform distribution of adhesive stress along the bonded anchor. It is worth noticing that the three specimens which

did not reach the failure are marked with arrows in the figure. These "unfailed" joints were not considered in determining the trend curves for the fatigue load-life data.

In order to normalise the experimental load-life fatigue data, the quasi-static strength of the anchorages was used. The normalised fatigue results are plotted in Figure 6.4 and Figure 6.5. The first figure shows the fatigue life plotted against the maximum fatigue load, P_{max}, of the anchors, normalised by the quasi-static failure load, P_s. The latter shows the fatigue life plotted against the loading range, ΔP, normalised by the quasi-static failure load.

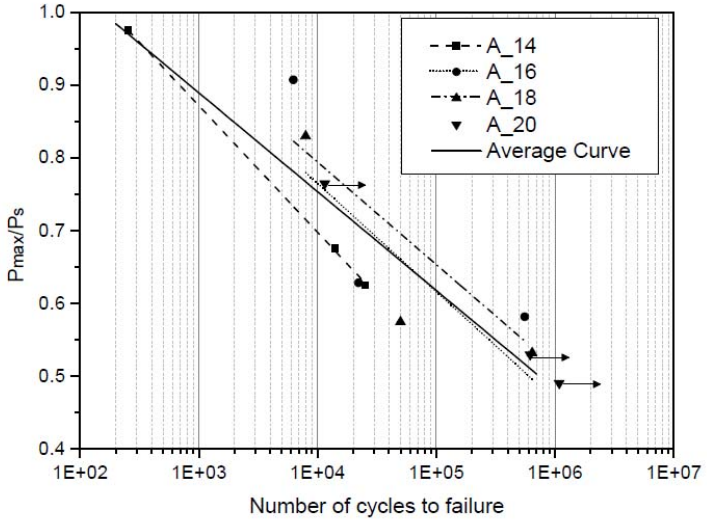

Figure 6.4. Experimental normalised load-life fatigue data for the anchors (loading characterised by the maximum load).

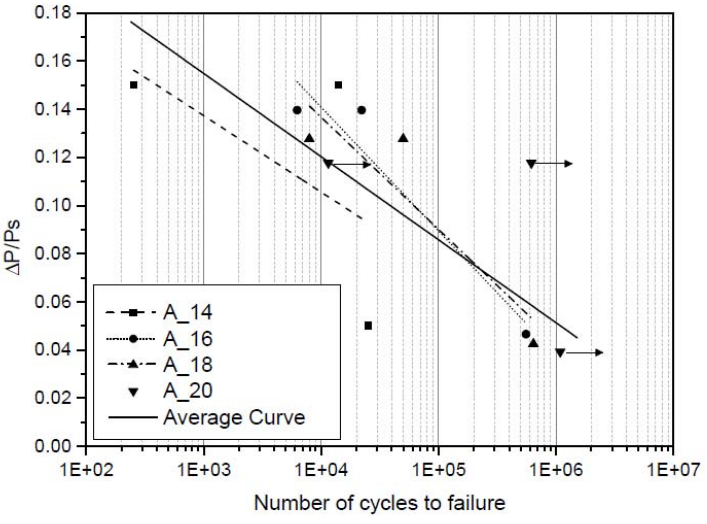

Figure 6.5. Experimental normalised load-life fatigue data for the anchors (loading characterised by the load range).

The experimental dispersion was calculated through the relative standard deviation. It was found that the relative standard deviation to the mean was 10.57% when normalising by the maximum fatigue load whilst

it was 30.51% when normalising by the loading range. As can be observed, when the fatigue loading was defined by the maximum fatigue load (see Figure 6.4), the experimental data dispersion was much lower than when using the loading range (see Figure 6.5). This suggests the maximum load may be the most appropriate way of characterising the fatigue loading applied in this research.

As it was concluded in Chapter 5, the predicted creep time to failure was greater than the longest experimental fatigue tests. For this reason, it was considered that the creep phenomenon did not influence the fatigue tests conducted on straight bond-type anchorages significantly. Nevertheless, the specimen A_16_5 was investigated in more detail, as it was one of the longest fatigue tests carried out. The experimental fatigue time to failure of this specimen was also the closest to its corresponding predicted creep time to failure.

Figure 6.6 shows load-time and displacement-time curves recorded during the fatigue test of specimen A_16_5. As the MTS actuator was controlled by force, the force range remained constant from the beginning of the test to the fatigue failure of the specimen. However, a small variation of displacement was observed throughout the fatigue test. In this case, the fatigue mean load experimented a displacement of approximately 0.5mm from the beginning of the test to the fatigue failure. This suggests that the creep loading effect during the fatigue test might have an unimportant influence in the fatigue lifetime. Also, it is worth mentioning that the displacement was measured by the internal LVDT of the MTS actuator cylinder and did not only measure the real displacement of the specimen as it also took into account small relative displacements amongst all the components of the testing system.

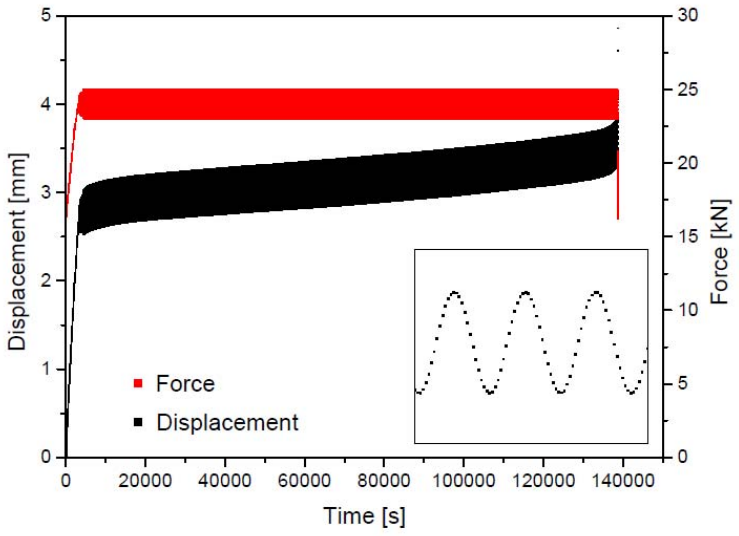

Figure 6.6. Measured load-time and displacement-time curves of specimen A_16_5 under fatigue loading.

This research is therefore primarily concerned with the experimental and numerical fatigue analyses of the straight bond-type anchorage where time-dependent effects did not have a significant influence. The fatigue

loads appeared to be dominant and the test durations were not long enough for time-dependent phenomena to be developed. Even though this consideration is reasonable as a starting position, it is worth noticing that in a real application time-dependent damaging must be taken into account during fatigue analysis. This concept is developed in-depth in next chapter (future work).

6.3.3 Failure surface analysis

The fatigue failure surfaces of the straight bond-type anchorages are shown in Figure 6.7 and Figure 6.8. A stereoscope microscope SCZ-T4P Carton with magnification levels ranging from 10x to 25x was used to conduct the failure surface analysis. Pictures of failure surfaces were taken through a USB Microscopic camera Deltapix DP300.

Figure 6.7. CFRP tendon failure surface of the specimen A_14_3 magnified 10x

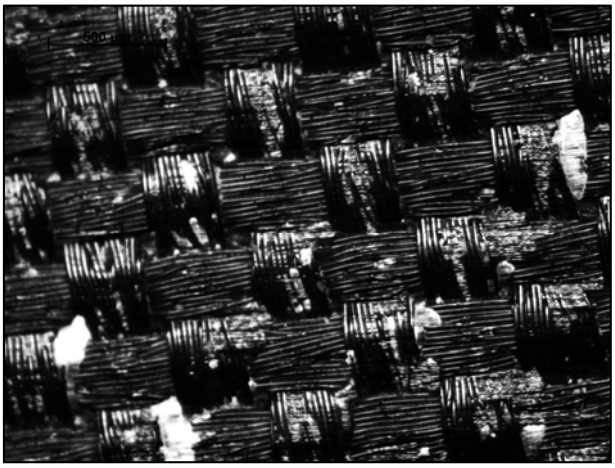

Figure 6.8. CFRP tendon failure surface of the specimen A_14_3 magnified 25x.

It is worth mentioning that a second batch of CFRP rods was provided by the manufacturer, with the aim to study the time-dependent and fatigue behaviour of the straight bond-type anchorages. A naked-eye examination revealed that the superficial roughness of the second batch of CFRP tendons was slightly different. This led to the realisation of quasi-static tests for the geometries with the thinnest and thickest

adhesive layers (geometries A_14 and A_20) in order to compare the quasi-static strengths and failure surfaces between anchorages with tendons with different surface roughness (see Chapter 4). It was found that there was a reduction of the static strength of about 30-35% for the specimens with CFRP rods from the second batch. Also, the microscopic analysis revealed that the number of adhesive particles attached to the failure surface was lower.

As was seen in the naked-eye examination (see Figure 6.2), the failure surfaces for the fatigue tests were mostly caused by adhesion failure. Nevertheless, small particles remained attached to the composite tendon after failure, indicating local cohesive failures of the adhesive. Although the small adhesive particles were spread on the whole failure surface of the rod, this was not entirely covered by adhesive particles revealing that the maximum adhesion strength between the adhesive and the rod was not fully reached. This result was found to be broadly analogous to the microscopic analyses carried out in the specimens with CFRP rods from the second batch (specimens A_01_04_4 and A_02_02_2 tested under quasi-static loading). This equivalence allows for the use of the multi-linear traction-separation parameters of these specimens, which were found in Chapter for 4, in order to model the cohesive layer in the adhesive-tendon interface in the fatigue numerical modelling.

6.4 Numerical modelling

In order to predict the fatigue response of straight bond-type anchorage, a finite element model was developed in Abaqus/CAE. Due to the revolution geometry of the anchorages, a 2D axisymmetric model was considered with the aim to optimise computing resources. The geometry cases tested experimentally under constant amplitude fatigue loading were modelled[8], where the bottom of the steel housing was entirely fixed, and the top of the CFRP was loaded with an axial force. Four-noded axisymmetric stress elements (CAX4R) with a mesh density of 0.5mm were used for the fatigue model. In the fatigue model, a cohesive layer was used adjacent to the adhesive-rod interface, as it was determined from the experimental observations that the failure always occurred in this adhesive-rod interface region. Four-node axisymmetric cohesive elements (COHAX4) with a multi-linear traction-separation response were utilised to study the progressive damage in the adhesive bond line. The size of the cohesive element was 0.5 x 0.5mm along the entire adhesive bond line. Geometric non-linearity was included in all the analyses (see Figure 6.9).

According to the sensitivity analysis of the mesh conducted in Chapter 4, the most suitable mesh size for the straight bond-type anchorages was found to be 0.5mm for obtaining a lower variation of 1% of the maximum shear stress distribution on the adhesive-tendon interface. The same mesh size was used for fatigue modelling.

[8] Geometries A_14, A_16, A_18 and A_20.

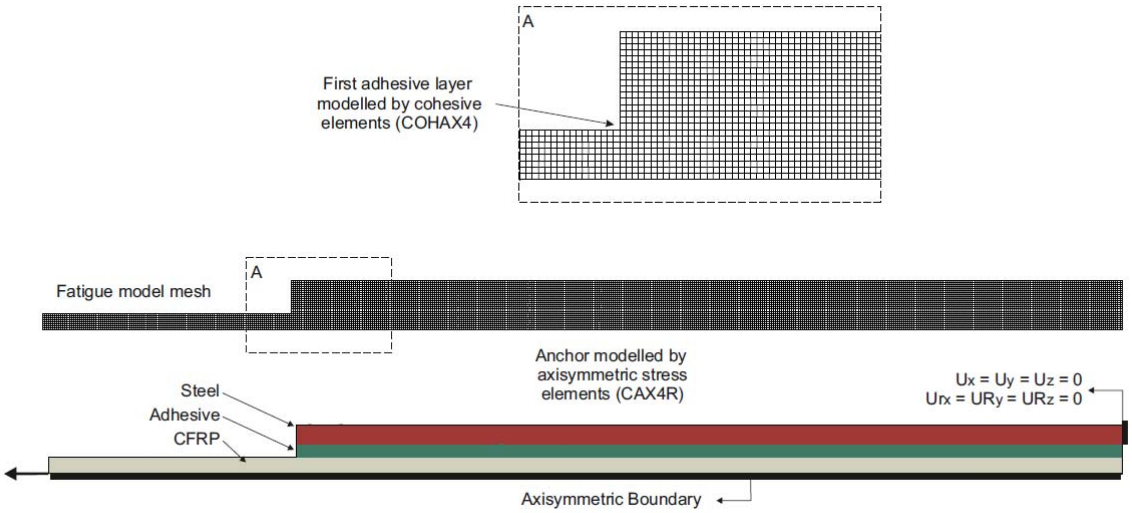

Figure 6.9. Finite element mesh and boundary conditions for the anchor with a bore and length of 14 and 200mm, respectively.

Fatigue modelling of the anchors was undertaken using a progressive damage cohesive zone model (CZM) adjacent to the adhesive-rod interface. Von Mises plasticity was not considered in the adhesive material as the maximum tractions in the cohesive layer along the entire bond line essentially limited the maximum stress on the remaining adhesive continuum. The constitutive behaviour of the cohesive element was defined by traction-separation response. A quadratic interaction damage initiation criterion was used to link the tractions as outlined in Equation 4.14 (see Chapter 4).

The same progressive damage model features applied in the quasi-static modelling were considered in the fatigue modelling. A multi-linear damage evolution was used to simulate the friction process caused by the bearing forces after damage initiation. The damage was directly defined as a function of the effective displacement relative to the effective displacement at damage initiation, where the damage between consecutive points was linearly obtained through Equation 4.15 (see Chapter 4). Also, in order to avoid convergence difficulties, a viscous parameter was used to allow the stresses to be slightly exterior to the limits established by the traction-separation model (see Equation 4.17, Chapter 4).

The fatigue damage model developed by Khoramishad et al. [94] was used to predict the fatigue response of the straight bond-type anchorage. The maximum fatigue load of the actual cyclic loading defined the sinusoidal fatigue loading and degrading the multi-linear traction-separation cohesive properties simulated the influence of the fatigue damage. The fatigue damage evolution law describing the fatigue damage on the adhesive-rod interface is presented in Equation 6.1.

$$\frac{\Delta D}{\Delta N} = \begin{cases} \alpha \cdot (\varepsilon_{max} - \varepsilon_{th})^{\beta}, & \varepsilon_{max} > \varepsilon_{th} \\ 0, & \varepsilon_{max} \leq \varepsilon_{th} \end{cases}$$

$$\varepsilon_{max} = \frac{\varepsilon_n}{2} + \sqrt{\left(\frac{\varepsilon_n}{2}\right)^2 + \left(\frac{\varepsilon_s}{2}\right)^2} \qquad \text{(Equation 6.1)}$$

where ΔD is the increment of damage and ΔN is the cycle increment. The parameters ε_n and ε_s are the averaged bond line normal and shear strains, ε_{max} is a combination of these normal and shear strain components, ε_{th} is a threshold value which specifies the minimum strain to initiate the fatigue damage. The parameters α, β and ε_{th} are calibrated with experimental results.

In this model, changing β modifies the slope of the fatigue load-life (P-N) curve, decelerating the damage evolution and increasing the lifetime when β is increased, having a greater effect at higher strains (loads). When changing the constant α, the P-N curve is shifted horizontally. When α is increased, the damage evolution is accelerated and the lifetime is reduced.

It is worth noticing that the fatigue damage is a function of the number of cycles and the maximum principal strain, the latter depending on the maximum fatigue load applied. As the experimental fatigue results were found to better correlate with the maximum fatigue load (P_{max}) than the load range (ΔP) (see Figure 6.4 and Figure 6.5), this load parameter was used in the modelling (see Figure 6.10a). This formulation was successfully conducted by Khoramishad et al. [94] and a simpler form of this was also utilised satisfactorily by Graner et al. [95].

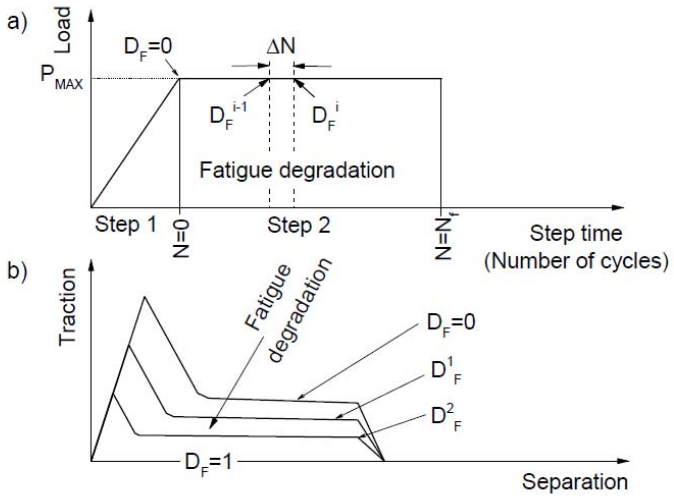

Figure 6.10. a) Steps applied in the fatigue modelling b) Fatigue degradation of the CZM.

Figure 6.10a shows the steps applied in the FE solution and Figure 6.10b the fatigue degradation of the cohesive zone model. In the first step, the force was ramped linearly from 0 to P_{max} in 1 second. In the

second step, the load remained constant and a fatigue damage variable was introduced into the model until the joint failed. Three different levels of fatigue loading were modelled, following the experimental tests (see Table 6.1). Figure 6.10b shows the multi-linear traction-separation cohesive elements utilised, as well as the effect of the degradation. During the second step, the fatigue damage variable at each element integration point was evaluated and linearly degraded according to the level of damage reached through Equation 6.1. According to Chapter 4, the initial normal and shear traction of the cohesive elements were established at 17.20 and 9.93MPa, respectively. The tabular damage evolution parameters are summarised in Table 4.8 (see Chapter 4).

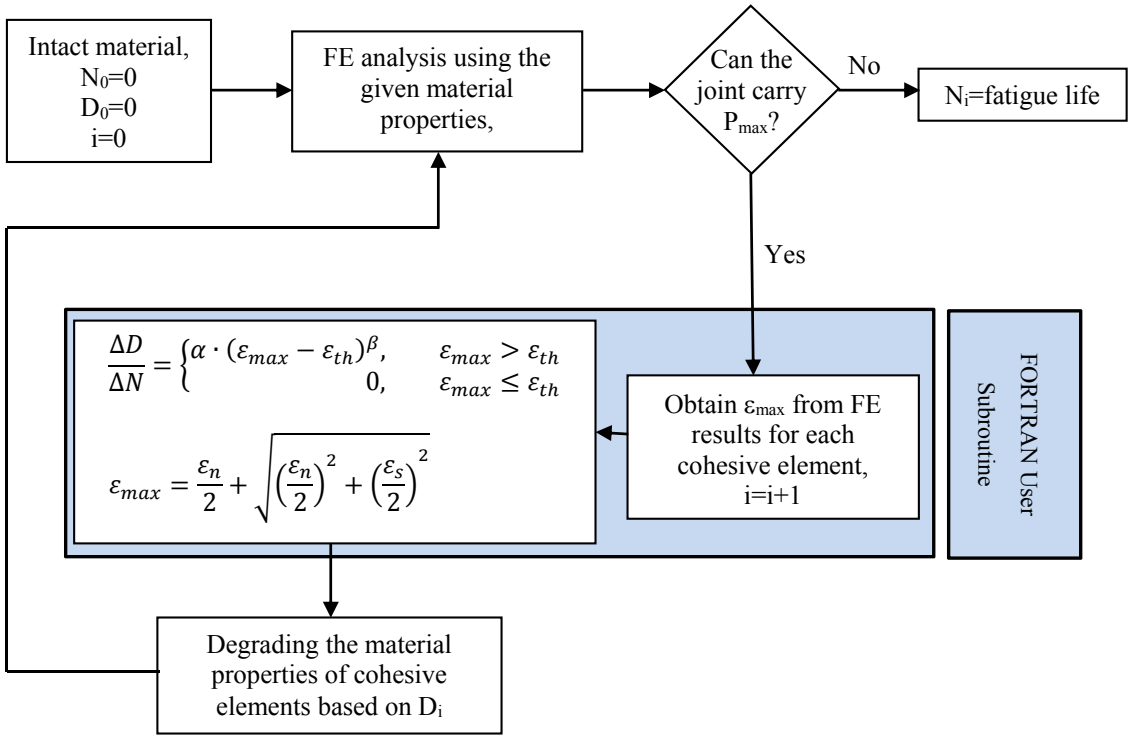

Figure 6.11. The flowchart of the fatigue damage model in Abaqus/CAE.

The progressive damage in the joint was implemented by coupling Abaqus/CAE with a FORTRAN subroutine. The fatigue model is illustrated in more detail in a flowchart form in Figure 6.11. The fatigue analysis started in the first increment of the second step, when the number of cycles was still equal to zero (see Figure 6.10). This provided the state at the beginning of the fatigue test. The maximum principal strains of the cohesive elements were then obtained using the subroutine *GETVRM and compared with the minimum strain to initiate the fatigue damage. If the maximum principal strain was higher than the threshold strain, the multi-linear traction-separation cohesive properties were linearly degraded according to Equation 6.1. Once the parameters were updated, a new increment of cycles was evaluated. For each increment of cycles (ΔN), this loop was repeated where Equation 6.1 was evaluated and the damage accumulated and stored at every cohesive element integration point, until the joint was not able to keep carrying the

maximum fatigue load applied. In this research, each increment of cycles consisted in a block of 1000 cycles.

Also, an iterative approach was undertaken to assess the effect of the fatigue damage model parameters on the fatigue response of the different geometries of the anchors. The fatigue damage model parameter values that matched the experimental fatigue response of the anchors are summarised in Table 6.3.

Table 6.3. Fatigue damage model parameters.

α	β	ε_{th}
0.7	3.5	0.0225

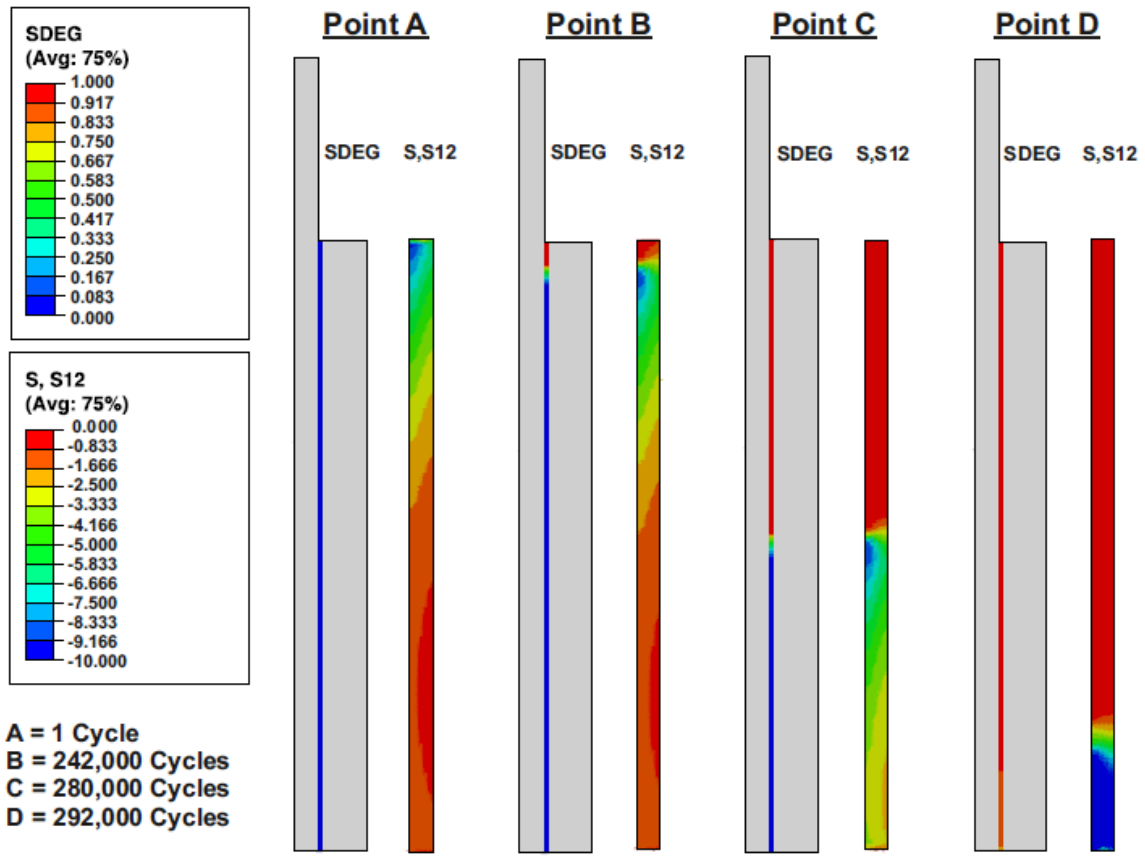

Figure 6.12. Damage and shear stress evolution along the cohesive layer and adhesive section respectively for the geometry A_14 loaded at 24kN.

Like the quasi-static and time-dependent analyses, stresses were initially highest at the end of the joint where the rod was loaded. When damage was initiated, the maximum stress moved down the adhesive-rod interface. As the damage front approached the bottom of the joint, the anchor was not able to carry the applied maximum load specified (24 or 36 kN), and this was taken as the point of final fatigue failure. This is illustrated in Figure 6.12 through four different stages of the fatigue damage front evolution and the corresponding shear stress distributions in the adhesive section for the anchor with the thinnest adhesive thickness (specimen A_14) loaded at 24kN. This is representative of the mode of failure in all the anchors.

Point “A” shows the shear stress distribution in the first fatigue cycle. At this point there was no damage in the bonded joint and so the joint behaved entirely linearly with the maximum stresses occurring at the top of the bonded joint. Once the damage was reached in the first elements of the cohesive layer, both damage front evolution and maximum shear stress moved down the bond line, as can be seen in the points “B”, “C” and “D”. Eventually, the bonded joint was not able to carry the maximum applied fatigue load and the fatigue failure was reached (point “D”).

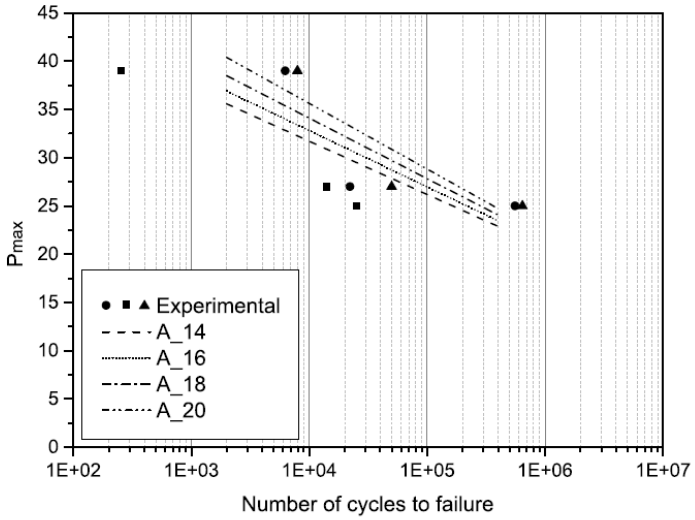

Figure 6.13. Experimental and numerical non-normalised load-life fatigue results for the anchors.

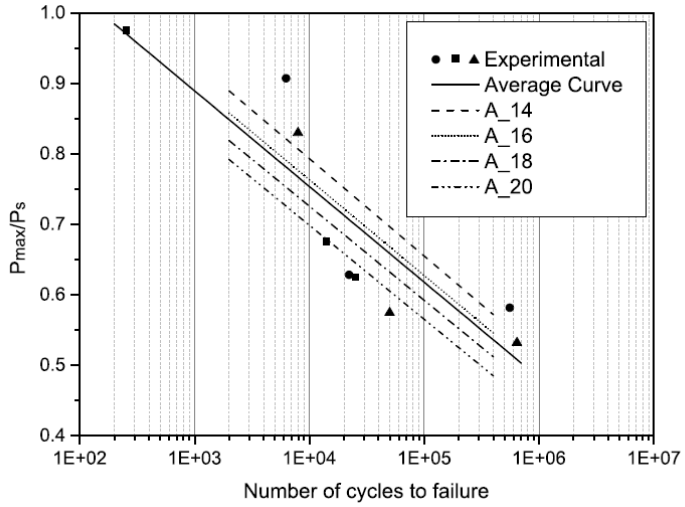

Figure 6.14. Experimental and numerical load-life fatigue data for the anchors normalised by the quasi-static failure load.

The predicted load-life data of each geometry correlated well with the experimental data, as shown in Figure 6.13. Figure 6.14 shows the results normalised by the experimental quasi-static load for each anchor configuration. As mentioned in the fatigue experimental work, the predicted fatigue results showed that the anchors with a larger adhesive thickness reached a greater number of cycles to failure for the same level of

load. An illustration of this can be seen in Figure 6.13, where the non-normalised results are shown. However, as shown in Figure 6.14, when the maximum fatigue load, P_{max}, of the anchors, is normalised by the respective quasi-static failure load, the anchors with a thinner adhesive layer achieved higher number of cycles to failure for the same normalised load. Therefore, when the adhesive thickness was higher, the number of cycles to failure increased proportionally less than the quasi-static failure load.

As shown in Figure 6.13and Figure 6.14, the proposed fatigue damage model for anchors gave a consistent match with the experimental fatigue data in terms of life. This can provide confidence in the model in order to explore the fatigue life of other geometries and load cases.

6.5 Concluding remarks

Fatigue tests were experimentally undertaken on straight bond-type anchorages with different load ratios, maximum fatigue loads and different adhesive thicknesses with failure occurring in the bond line. Also, a fatigue model based on a multi-linear traction-separation cohesive zone model, located throughout the adhesive-tendon interface, was developed and controlled using a fatigue evolution damage law by degrading the cohesive properties of the elements according to the level of damage. From this section, the following conclusions can be drawn:

1. In all fatigue tests the failure of adhesive-tendon interface of the straight bond-type anchorage was observed. The failure started at the loading end of the anchor and travelled rapidly to the bottom of the anchorage throughout the bonded length. The naked-eye examination and the microscopic analysis revealed that the failure surface occurred in the adhesive-tendon interface mainly caused by adhesion failure.
2. Experimental fatigue results were more consistent when considering the maximum fatigue load than the loading range. If the quasi-static strength is known, the normalised results with the maximum fatigue load could be used to estimate the fatigue life of other configurations as a reasonably consistent normalised load-life curve was obtained.
3. The predicted fatigue results using a multi-linear traction-separation cohesive zone model with a fatigue damage evolution model were compared with the experimental results. It was found that the numerical model could successfully predict the fatigue life of adhesively bonded anchors for CFRP rods.
4. A parametric study was conducted in order to obtain the fatigue model parameters required for the degradation of the cohesive element properties. An iterative approach was used to obtain the required parameters that better matched the experimental load-life data. It was qualitatively found that the fatigue model was very sensitive to small variations on β and ε_{th} whilst greater variation on α was required for obtaining a different response in the fatigue model.

5. It was observed experimentally and numerically that the anchors with thicker adhesive layers showed a higher number of cycles to failure at the same fatigue load. Nevertheless, for the same normalised fatigue load, anchors with thinner adhesive thickness were able to reach a greater number of cycles before failure.

Chapter 7. Conclusions and future research

7.1 Summary of the chapter

In this research, straight bond-type anchorages for CFRP tendons were experimentally and numerically investigated under quasi-static, fatigue and time-dependent loads. A multi-linear traction-separation description of the cohesive zone model was successfully used for simulating the progressive damage of the anchorages under quasi-static and fatigue loading whilst a creep power law combined with von Mises plasticity was utilised for predicting time-dependent phenomena on the anchorages. In all cases, the predicted data were calibrated and compared with the experimental results and proved a good agreement.

Split wedge anchorages and double lap joints (DLJs) were also studied experimentally. The first one allowed for the most relevant parameters found in the literature review, which affect the mechanical anchorage for composite materials, to be studied and confirmed. The second permitted finding the most suitable analytical formulation to predict the shear stress distribution on the adhesive-adherent interface for DLJs which was developed in order to obtain an analytical model for straight bond-type anchorages with adhesives that behave primarily in an elastically-linear manner.

This chapter summarises the main conclusions drawn from this investigation and provides suggestions for future work research.

7.2 Conclusions

Numerous investigations have been carried out in the last decades in order to replace the conventional steel tendons with alternative materials that are highly resistant to corrosion. In this sense, FRP tendons provide a suitable alternative for this purpose due to their high mechanical properties in the fibre's direction, light weight and high resistance to corrosion. In addition, CFRP tendons stand out over other FRP systems, due to their higher mechanical properties and a similar stiffness in comparison with steel tendons.

Although FRP tendons can provide higher mechanical properties in the fibres' direction than current steel tendons, the anisotropic nature of composite material does not allow for the conventional anchoring systems to be utilised, as FRP tendons would be damaged in the transverse direction causing a premature failure of the system. For this reason, two main anchoring systems for FRP rods have been considered in the literature review: mechanical anchors and adhesively bonded anchors.

Mechanical anchorages for FRP rods are usually based on the current anchoring systems and have been extensively studied because of their similarity, compactness, and ease of assembly, reuse and reliability. A mechanical anchorage principally consists of a barrel housing or steel plates which grip the tendon through a transverse force. As the weakest mechanical properties of the FRP tendons lie in the transverse direction, the wedges or plates, which grip the tendon, tend to dig into the composite material causing a premature failure. For this reason, investigations on mechanical anchorages have mainly focused on the contact surface between the wedges or plates and FRP tendons.

Several modifications of the contact surface have been proposed in the literature with the aim to homogenise the pressure exerted by the wedges or plates on the tendon. These modifications generally consist of removing the hardened teeth (which are included in conventional anchoring systems) for steel tendons, introducing a sleeve material between the wedges and the tendon in order to smoothen the stresses at the loading end of the anchorage, introducing a small differential slope between the barrel and the wedges, and rounding of the sharp inner edges of the wedges.

In this research, split-wedge anchorages for CFRP tendons with and without sleeves have been experimentally tested under quasi-static loading. It was confirmed that the tapered shape of the wedges introduces a transverse force which damages the matrix of the composite material at the loading end of the anchor causing a reduction of the tendon strength. The tensile strength capacity of the rods was reduced by around 25-36% of its maximum tensile strength provided by the manufacturer.

Also, it was seen that in all the cases the failure was sudden and explosive, releasing all the energy stored in the rod rapidly. When the anchoring system was used without the sleeve material a crushing failure mode of the tendon was obtained. Introducing a copper sleeve between the wedges and the tendon permitted an increase of the ultimate load to be obtained and the failure mode to be closer to the rupture of the fibres along the free length.

In addition, it was observed that the uniform penetration of the wedges into the barrel during the prestressing process must be guaranteed with the aim to avoid a premature failure of the system caused by slipping and crushing.

Adhesive bond-type anchorages for composite tendons generally consist of a metallic housing inside which single or multiple tendons are bonded with an adhesive agent. The quasi-static response of adhesively bonded anchorages has been experimentally investigated by many researches with failure occurring in the bond line. For this reason, in this research the shear stress distribution along the overlap length has been studied and compared to the existent analytical formulations.

As the analytical formulations for adhesively bonded joints were mostly formulated for plane geometries, DLJs were manufactured and tested under quasi-static loading. The experimental shear stress distribution

was obtained through strain gauges installed on the external surface of the adherents and compared to the existent analytical formulations. The failure surface analyses with a stereoscope microscope revealed that DLJs bonded with low viscosity adhesives present a lower number of defects on the adhesive-adherent interface than high viscosity adhesives due to the manufacturing process undertaken in this research.

It is worth mentioning, that for the adhesives with a viscosity lower than 1,000mPa·s, the adhesive was placed by pouring and injection, whereas for adhesives with higher viscosity, the adhesive was set by moulding and squeezing. Due to this procedure, specimens with high viscosity adhesives presented a greater number of imperfections on the interfaces with the adherents than low viscosity adhesives.

Comparing the experimental shear stress distributions from DLJs against the analytical formulations for DLJs of Völkersen and TOM revealed that TOM's analytical formulation offered a more accurate prediction of the stress distribution on the interface where the highest shear stresses on the interface were at the ends of the bonded joint and the lowest shear stresses were placed at the centre of the joint.

As the analytical formulation of TOM was found to be consistent with the experimental shear stress distribution obtained for DLJs, an analytical formulation for straight bond-type anchorages was developed from the formulation of TOM where a third differential equation in the force balance was introduced to take into account the circular section of the anchorages. The analytical solution was validated against the experimental data and it was found that the proposed formulation provides an approximate distribution of shear stress in the bonded joint for circular anchorages with adhesives which behave elastically-linearly up to failure.

Also, different geometries of circular straight bond-type anchorages were investigated under quasi-static loading up to failure using different adhesives systems. As mentioned in the literature review, in most cases a premature failure of adhesive-tendon interface was observed. The failure started at the top of the anchorage and it was quickly propagated to the bottom of the joint throughout the overlap length. The naked-eye examination and the microscopic analysis revealed that the failure surface occurred within the adhesive but very close to the interface by adhesion failure.

The force-displacement curves showed that anchorages behaved largely linearly up to the point of failure, which occurred rapidly and explosively. However, several specimens showed a significant change in the slope revealing that nonlinearities in the adhesive must occur. Finally, it was determined from the experimental campaign that higher failure loads can be reached when either the adhesive thickness or the bonded length are higher.

Moreover, the literature review showed that different techniques have been investigated to model adhesively bonded joints for composite materials. The majority of these have been intended for plane

geometries, such as single lap joints and double lap joints. These analyses consider non-linearities, continuum damage, coupled hygro-mechano-thermal effect or progressive damage.

In this investigation, a numerical modelling work was conducted to predict the static strength and the failure mechanism of straight bond-type anchorages with adhesive 02. Different material models of increasing complexity were investigated for the adhesive layer. Initially the adhesive was modelled with linear elastic properties. However, this analysis was unable to effectively predict the measured responses as the required stresses were physically unreasonable and were different amongst the geometric cases that were studied.

Adhesive yielding was then modelled using, in the first place, von Mises plasticity followed by Druker-Prager plasticity. Similarly to the elastic analysis, when using von Mises plasticity there was no correlation between the maximum equivalent plastic strains of the adhesive at the point of failure of each configuration. Also, these strains were substantially higher than the stated material data provided by the manufacturer. Furthermore, as mentioned in the literature review, Druker-Prager plasticity, which enables the hydrostatic dependency of the adhesive, is normally used to model polymers which exhibit higher yield stresses than tension in compression. Even though, the predicted adhesive failure strains were reduced when using Drucker-Prager plasticity, they were still too high to enable a reliable strength prediction to be made.

Finally, progressive damage was included in the modelling in order to capture the entire mechanical response of the anchor including the damage initiation and evolution leading to the anchorage failure. As the crack path was known in advance, a layer of cohesive elements was implemented between the adhesive and tendon. The cohesive layer simulated the chemical adhesion of the joint by following the assigned elastic curve until a point of damage initiation. Once the damage started, the bearing forces were simulated by a multi-linear softening which was utilised to simulate the subsequent (post-failure) friction between adhesive and CFRP tendon. It was found that the cohesive zone model with progressive damage and a "frictional" post-damage region was shown to provide predicted joint strengths that correlate closely with the measured experimental data. This data successfully described the different failure loads with different thicknesses and lengths of adhesive layer.

Moreover, it was found in the literature review that time-dependent phenomena have also been investigated in adhesively bonded joints especially through plane geometries. Time-independent plasticity material models and time dependent visco-elastic and visco-plastic models have been studied in order to provide a time-dependent response in adhesives and bonded joints. According to the purpose of this research, it was found that a visco-plasticity model, which predicted the lifespan of bonded joints under creep loading by degrading the plastic yield properties of the adhesive layer, was able to accurately model the creep phenomenon in plane adhesive joints.

Creep tests at different loads were conducted on single lap joints (SLJs) with four different adhesive thicknesses where the creep time to failure of each specimen was recorded. It was observed that samples

with a thicker adhesive layer tended to have shorter lifespans than samples with thinner layers at the same creep load. The increased load eccentricity, associated with the thicker adhesive layers, introduced an increased bending moment and hence increased the adhesive stresses. The experimental results permitted an experimental creep law which related the average shear stress of the bonded joint and creep lifetime to be obtained.

Based on the state of the art, a creep power law based on the Bailey-Norton law was utilised in the numerical work. The parameters of the creep power law were calibrated with the experimental data available. Also, the adhesive plastic yield stress was linearly degraded when the equivalent creep strain was greater than 90% of the maximum equivalent creep strain allowed. The numerical results showed that the maximum equivalent creep strain in the SLJs at failure load was thickness dependent. However, a quadratic polynomial equation which related both variables was found with the aim to obtain the maximum equivalent creep strain most suitable to be implemented in the model in function of the adhesive thickness.

The creep phenomenon was not experimentally investigated on the straight bond-type anchorages. However, the creep model was utilised for predicting the creep time to failure of the anchorages under the loads used in the fatigue experimental campaign. It was revealed that the creep loading aspect during the fatigue testing activities did not have a significant influence and thus it was not considered in the fatigue modelling work. It was also found that the lifespan of the anchors was relatively short at high loads, suggesting that these anchors should be loaded either at low loads in order to increase their lifespan in real structures or at higher loads in temporary prestressed concrete structures or auxiliary structures where the properties of the tendon are unique for their purpose.

Moreover, the time-dependent phenomenon was directly investigated on straight bond-type anchorages through experimental stress relaxation tests. Four geometric cases were tested under three initial tensioning forces. It was observed that the experimental normalised load loss was similar for all the geometries of each initial tensioning force. For this reason, a unique experimental trend for all the geometries was obtained for each initial tensioning force. However, the normalised load loss was found to be different among the initial tensioning forces. The greater the initial tensioning force, the greater the load loss recorded. Also, this increase of load loss was non-proportional to the increase of initial stress.

For all the specimens, it was observed that the anchorages suffered the highest load loss rate or molecular rearrangement on the adhesive layer once the load was applied. Afterwards, the molecular rearrangement was gradually reduced until a constant load loss rate was reached. The stabilisation of the load loss rate was reached approximately 25 hours after the loading force was transferred to the anchorage.

The experimental campaign also showed that the restressing technique allows for a higher stabilised load to be achieved as the load loss ratio was found to be lower for each successive restressing. It is suggested

that the straight bond-type anchorage is restressed when the load loss rate is stabilised, after approximately 25 hours.

It was also seen that the number of restressings to achieve a desired stabilised load in the anchorage depends on the initial tensioning force. The normalised load loss achieves the lowest rate after four consecutive restressings for initial loading forces ranging between 70 and 60% of the static failure load whereas three consecutive restressing are required for initial loading forces ranging between 55 and 45%. Solely one restressing is needed for initial tensioning forces under 40% of the static failure load.

Additionally, a numerical model was utilised to predict the stress relaxation response of the bonded anchorage and compared with the experimental data obtained. Similarly to the creep modelling, elastic-perfectly plastic von Mises response was assumed in the adhesive layer and the time-dependent behaviour of the adhesive was considered through the Bailey-Norton law. The numerical model provided a predicted time-dependent behaviour of the straight bond-type anchorage that correlate closely with the experimental trend curves for the first stressing step.

Finally, the fatigue response of adhesively bonded anchorages has been studied in this research. It was found in the literature review, that a cohesive zone model permits the accurate onset and growth of damage of bonded joints under fatigue loading with constant or variable amplitude. It was studied on adhesive plane geometries where the lifespan under fatigue loading was simulated by degrading the properties of the cohesive elements.

In this research, the numerical model was applied to straight bond-type anchorages where a multi-linear traction-separation law was considered in order to take into account the influence of the bearing forces between the adhesive and tendon once the chemical bond failed.

Fatigue tests were experimentally undertaken on straight bond-type anchorages with different load ratios, maximum fatigue loads and different adhesive thicknesses with failure occurring in the bond line. The experimental data were normalised with the maximum fatigue load instead of the loading range as the dispersion was lower. This permitted a consistent load-life curve to be obtained which allows for the fatigue life of other configurations to be estimated if the quasi-static strength is known.

As previously mentioned, a multi-linear traction-separation cohesive zone was modelled between the adhesive and the tendon, as the crack path was known. The fatigue model parameters required for the degradation of the cohesive element properties were calibrated with the experimental load-life curve obtained in the fatigue experimental campaign. It was found that the predicted fatigue results obtained were able to successfully predict the fatigue life of adhesively bonded anchors for CFRP rods.

It was also observed, experimentally and numerically, that the anchors with thicker adhesive layers showed a higher number of cycles before failure at the same fatigue loading. Nevertheless, anchors with thinner

adhesive thickness were able to reach a greater number of cycles to failure at the same normalised fatigue load. This suggest that the increase of quasi-static strength of the joint, produced when the anchorage adhesive thickness increases, is non-proportional to the increase of the fatigue time to failure.

7.3 Future research

The adhesively bonded anchorages for CFRP tendons have been experimentally and numerically investigated under quasi-static, fatigue and time-dependent loads. The main parameters studied in this research have been the adhesive thickness and the bonded length (solely in the quasi-static analysis) of the straight bond-type anchorage within certain limits.

More detailed experimental work will be useful with the aim to more accurately assess and validate the integrity of the numerical work. This includes a great variety of geometric cases to be assessed under quasi-static, fatigue and time-dependent loads. Also, the number of SLJs tests were limited and the results appeared to be thickness dependent. This did not permit fitting curves to individual thicknesses, as the data were insufficient to acquire a consistent trend. As the creep failure strain is physically expected to be a material characteristic and not thickness dependent, further experimental research is needed in order to investigate and discuss this aspect in depth.

Moreover, further research is also required for the numerical models developed in this research, in order to extend the use of these models in more general configurations of adhesively bonded anchorages. In this research, a continuum approach was used for the time-dependent analyses whereas a cohesive zone modelling was utilised for quasi-static and fatigue analyses. As these analyses were not combined in a single analysis, it was reasonable to adopt different damage approaches. However, it would be of interest to develop a time-dependent cohesive zone model combining both time-dependent model and a cohesive zone model (utilised in the quasi-static and fatigue analyses) into one unique model. This would provide a significant improvement for modelling straight bond-type anchorages under different types of loads acting simultaneously, which is more representative of a real application.

Finally, it would be very interesting to experimentally investigate the behaviour of a prestressed concrete structure with CFRP tendons using straight bond-type anchorages. This would provide valuable information in order to design and apply this prestessing system in real applications. The numerical simulation of the whole would however require a lot of computer power which cannot be carried out on ordinary computers.

References

[1] Schmidt JW, Täljsten B, Bennitz A, Pedersen H. FRP tendon anchorage in post-tensioned concrete structures. Concrete Repair, Rehabilitation and Retrofitting 2009:1181–6.

[2] Benatar A, Gillespie JJ, Kedward K. Advanced composites manufacturing. New York: 1997.

[3] Jones RM. Mechanics of composite materials. 2n ed. New York: CRC Press; 1999.

[4] Schmidt JW, Bennitz A, Täljsten B, Goltermann P, Pedersen H. Mechanical anchorage of FRP tendons - A literature review. Construction and Building Materials 2012;32:110–21.

[5] 440R-07 A. Report on Fiber-Reinforced Polymer (FRP) Reinforcement for concrete structures. ACI 2007:1–104.

[6] Malvar LJ, Bish J. Grip effects in tensile testing of FRP bars. 2nd International symposium, Non-metallic (FRP) reinforcement for concrete structures, 1995, p. 8.

[7] 440.4R-04 A. Prestressing Concrete Structures with FRP Tendons. ACI 2004:1–35.

[8] Nanni A, Bakis CE, O'Neil EF, Dixon TO. Performance of FRP tendon anchor systems for prestessing concrete structures. PCI Journal 1996;Jan-Feb:34–44.

[9] Taha MR, Shrive NG. New Concrete Anchors for Carbon Fiber-Reinforced Polymer Post-Tensioning Tendons - Part 1 : State-of-the-Art Review / Design. Aci Structural Journal 2003:86–95.

[10] Sayed-Ahmed, Y. E, Shrive NG. A new steel anchorage system for post-tensioning applications using carbon fibre reinforced plastic tendons. NRC Canada 1998;25:113–27.

[11] Shrive NG, Y. E, Sayed-Ahmed, Damson E, Tilleman D, Tadros G. Prestressing anchorage system for fiber reinforced plastic tendons, 2000.

[12] Pincheira JA, Woyak J. Anchorage of Carbon Fiber Reinforced Polymer (CFRP) Tendons Using Cold-Swaged Sleeves. PCI Journal 2001;Nov-Dec:100–11.

[13] Campbell TI, Shrive NG, Soudki KA, Keatley JP, Reda Taha MM. Design and evaluation of a wedge-type anchor for fibre reinforced polymer tendons. NRC Canada 2000;992:985–92.

[14] Taha MR, Shrive NG. New Concrete Anchors for Carbon Fiber-Reinforced Polymer Post-Tensioning Tendons - Part 2 : Development / Experimental Investigation. Aci Structural Journal 2003:96–104.

[15] Burningham CA. Development of Carbon Fiber Reinforced Polymer prestressing system for structural applications. University of Utah, 2011.

[16] Katz A. Bond mechanism of FRP rebars to concrete. Materials and Structures 1999;32:761–8.

[17] Baldan A. Adhesion phenomena in bonded joints. International Journal of Adhesion and Adhesives 2012;38:95–116.

[18] Cosenza BE, Realfonzo R. Behavior and modeling of bond of FRP rebars to concrete. Journal of Composite Materials 1997;2:40–51.

[19] Bahei-El-Din YA, Dvorak GJ. New designs of adhesive joints for thick composite laminates. Composites Science and Technology 2001;61:19–40.

[20] Benmokrane B, Zhang B, Chennouf A. Tensile properties and pullout behaviour of AFRP and CFRP rods for grouted anchor applications. Construction and Building Materials 2000;14:157–70.

[21] Zhang B, Benmokrane B. Design and evaluation of a new bond-type anchorage system for fiber reinforced polymer tendons. NRC Canada 2004;26:14–26.

[22] Fang Z, Zhang K, Tu B. Experimental investigation of a bond-type anchorage system for multiple FRP tendons. Engineering Structures 2013;57:364–73.

[23] Volkersen O. Die Niet kraftverteilung in zugbeanspruchten Nietverbindungen mit konstanten Laschen querschnitten. Luftfahrtforschung 1938;15:41–7.

[24] Goland M, Reissner E. The stresses in cemented joint. Journal of Applied Mechanics 1944:17–27.

[25] Smith H. Adhesive-bonded single-lap joints. NASA Langley Contract Report NASA CR-112236 1973;January:116.

[26] Smith H. Adhesive-bonded double-lap joints. 1973.

[27] Ojalvo IU, Eidinoff HL. Bond thickness effects upon stresses in single lap adhesive joints. The American Institute of Aeronautics and Astronautics 1978;16:204–11.

[28] Allman DJ. A theory for elastic stresses i adhesive bonded lap joints. Quarterly Journal of Mechanics and Applied Mathematics 1977;30:415–36.

[29] Chen D, Cheng S. An analysis of adhesive-bonded single lap joints. The American Institute of Aeronautics and Astronautics 1983;50:109–15.

[30] Tsai MY, Oplinger DW, Morton J. Improved theoretical solutions for adhesive lap joints. International Journal of Solids and Structures 1998;35:1163–85.

[31] Adams RD, Mallick V. A method for the stress analysis of lap joints. Journal of Adhesion 1992;38:199–217.

[32] Sawa T, Nakano K, Toratani H. A two-dimensional stress analysis of single lap adhesive joints subjected to tensile loads. Journal of Adhesion Science and Technology 1997;11:1039–62.

[33] Sawa T, Liu J, Nakano K, Tanaka J. A two-dimensional stress analysis of single-lap adhesive joints of dissimilar adherends subjected to tensile loads. Journal of Adhesion Science and Technology 2000;14:43–66.

[34] Silva LF da, Neves PJ das, Adams RD, Spelt JK. Analytical models of adhesively bonded joints—Part I: Literature survey. International Journal of Adhesion and Adhesives 2009;29:319–30.

[35] Silva LF da, Neves PJ das, Adams RD, Wang A, Spelt JK. Analytical models of adhesively bonded joints—Part II: Comparative study. International Journal of Adhesion and Adhesives 2009;29:331–41.

[36] Raphael C. Variable-adhesive bonded joints. Journal of Applied Polymer Science Applied Polymer Symposium 1996;3:99–108.

[37] Srinivas S. Analysis of bonded joints. NASA Langley contract report NASA TN D-7855, 1975, p. 53.

[38] Adams RD, Peppiatt NA. Effect of Poisson's ratio strains in adherends on stresses of an idealized lap joint. Journal of Strain Analysis for Engineering Design 1973;8:134–9.

[39] Oterkus E, Barut A, Madenci E, Smeltzer SS, Ambur DR. Bonded lap joints of composite laminates with tapered edges. International Journal of Solids and Structures 2006;43:1459–89.

[40] Bigwood D, Crocombe AD. Non-linear adhesive bonded joint design analyses. International Journal of Adhesion and Adhesives 1990;10:31–41.

[41] Tong L. Bond strength for adhesive-bonded single-lap joints. Acta Mechanica 1996;117:101–13.

[42] Crocombe AD, Ashcroft IA. Simple Lap Joint Geometry. In: Silva LF da, Ochsner A, editors. Modeling of Adhesively Bonded Joints, 2008, p. 3–23.

[43] Crocombe AD, Ashcroft IA. Environmental Degredation. In: Silva LF da, Ochsner A, editors. Modeling of Adhesively Bonded Joints, 2008, p. 225–41.

[44] Mises V. Mechanik der festen Körper im plastisch deformablen Zustand. Göttin Nachr Math Phys 1913;1:582–92.

[45] Drucker DC, Prager W. Soil mechanics and plastic analysis or limit design. Quarterly of Applied Mathematics 1952;10:157–65.

[46] Gurson AL. Continuum Theory of Ductile Rupture by Void Nucleation and Growth: Part I - Yield Criteria and Flow Rules for Porous Ductile Materials. Journal of Engineering Materials and Technology 1977;99:2–15.

[47] Tvergaard V, Needleman A. Analysis of the cup-cone fracture in round tensile bar. Acta Metallurgica 1984;32:157–69.

[48] Bonora N. A nonlinear CDM model for ductile failure. Engineering Fracture Mechanics 1997;58:11–28.

[49] Hambli R, Badie-Levet D. Damage and fracture simulation during the extrusion processes. Computer Methods in Applied Mechanics and Engineering 2000;186:109–20.

[50] Bonora N, Gentile D, Pirondi A, Newaz G. Ductile damage evolution under triaxial state of stress: theory and experiments. International Journal of Plasticity 2005;21:981–1007.

[51] Che HY, Zhu L, Sun DZ, Chen JH, Zhu H. Characterization and modeling of aluminium extrusion damage under crash loading. Thin-Walled Structures 2007;45:383–92.

[52] Hua YX, Crocombe AD, Wahab MA, Ashcroft IA. Continuum damage modelling of environmental degradation in joints bonded with EA9321 epoxy adhesive. International Journal of Adhesion and Adhesives 2008;28:302–13.

[53] Wang CH, Chalkley. Plastic Yielding of A Film Adhesive Under Multiaxial Stresses. International Journal of Adhesion and Adhesives 2000;20:155–64.

[54] Zgoul M. Characterising the rate dependent response of adhesively bonded structures. University of Surrey, 2002.

[55] Sugiman S. Combined environmental and fatigue degradation of adhesively bonded metal structures. University of Surrey, 2011.

[56] Liljedahl CDM, Crocombe AD, Wahab MA, Ashcroft IA. Modelling the environmental degradation of adhesively bonded aluminium and composite joints using a CZM approach. International Journal of Adhesion and Adhesives 2007;27:505–18.

[57] Yu XX, Crocombe AD, Richardson G. Material modelling for rate-dependent adhesives. International Journal of Adhesion and Adhesives 2001;21:197–210.

[58] Barenblatt GI. Equilibrium cracks formed on a brittle fracture. Doklady Akademii Nauk SSSR 1959;127:47–50.

[59] Barenblatt GI. Mathematical theory of equilibrium cracks in brittle fracture. Advances in Applied Mechanics 1962;7:55–129.

[60] Dugdale DS. Yielding of steel sheets containing slits. Journal of Mechanics and Physics of Solids 1960;8:100–4.

[61] Hillerborg A, Modeer M, Petersson PE. Analysis of crack formation and crack growth in concrete by menas of fracture mechanics and finite elements. Cement and Concrete Research 1976;6:773–82.

[62] Tvergaard V, Hutchinson JW. The relation between crack growth resistance and fracture process parameters in elastic-plastic solid. Journal of Mechanics and Physics of Solids 1992;40:1373–97.

[63] Tvergaard V, Hutchinson JW. The influence of plasticity on mixed mode interface toughness. Journal of Mechanics and Physics of Solids 1993;41:119–1135.

[64] Yang QD, Thouless MD, Ward SM. Numerical simulation of adhesively- bonded beams failing with the extensive plastic deformation. Journal of Mechanics and Physics of Solids 1999;47:1337–53.

[65] Yang QD, Thouless MD, Ward SM. Elastic-plastic mode-II fracture of adhesive joints. International Journal of Solids and Structures 2001;38:3251–62.

[66] Yang QD, Thouless MD. Mixed-mode fracture analyses of plastically- deforming adhesive joints. International Journal of Fracture 2001;110:175–87.

[67] Ouyang Z, Li G. Cohesive zone model based analytical solutions for adhesively bonded pipe joints under torsional loading. International Journal of Solids and Structures 2009;46:1205–17.

[68] Li F, Zhao QL, Chen H Sen, Wang JQ, Duan JH. Prediction of tensile capacity based on cohesive zone model of bond anchorage for fiber-reinforce dpolymer tendon. Composite Structures 2010;92:2400–5.

[69] Wang C. Fracture mechanics of single-fibre pull-out test. Journal of Materials Science 1997;32:483–90.

[70] Yue CY, Looi HC. Factors which influence the reliability of the assessment of interfacial bonding in fibrous composites using the pull-out test. International Journal of Adhesion and Adhesives 2001;21:309–23.

[71] Findley WN, Lai JS, Onaran K. Creep and relaxation of nonlinear viscoelastic materials. Elsevier; 1989.

[72] Yamaguchi T, Kato Y, Nishimura T, Uomoto T. Creep rupture of FRP rods made of Aramid, Carbon and Glass fibers. Proceeding of the Non-metallic (FRP) reinforcement for concrete structures International symposium, 1997, p. 8.

[73] Lazzarin P, Quaresimin M, Ferro P. A two-term stress function approach to evaluate stress distributions in bonded joints of different geometries. The Journal of Strain Analysis for Engineering Design 2002;37:385–98.

[74] Bailey RW. The utilization of creep test data in engineering design. London: Institution of Mechanical Engineers; 1935.

[75] Roy S, Reddy JN. Non-linear analysis of adhesively bonded joints. Computers & Structures 1988;29:1011–31.

[76] Majda P, Skrodzewicz J. A modified creep model of epoxy adhesive at ambient temperature. International Journal of Adhesion and Adhesives 2009;29:396–404.

[77] Cernocky EP. Comparison of the unloading and reversed loading behavior of three viscoplastic constitutive theories. International Journal of Non-Linear Mechanics 1982;17:255–66.

[78] Chiu WK, Jones R. Unified constitutive model for thermoset adhesive FM 73. International Journal of Adhesion and Adhesives 1995;15:135–6.

[79] Khalili SMR, Jafarkarimi MH, Abdollahi MA. Creep analysis of fibre reinforced adhesives in single lap joints-Experimental study. International Journal of Adhesion and Adhesives 2009;29:656–61.

[80] Finogenov GN. Creep assessment procedure for adhesive joints. Polymer Science Series C 2007;49:106–7.

[81] Su N, Mackie RI. Two-dimensional creep analysis of structural adhesive joints. International Journal of Adhesion and Adhesives 1993;13:33–40.

[82] Da Silva LFM, Adams RD. Joint strength predictions for adhesive joints to be used over a wide temperature range. International Journal of Adhesion and Adhesives 2007;27:362–79.

[83] Melcher RJ, Johnson WS. Mode I fracture toughness of an adhesively bonded composite–composite joint in a cryogenic environment. Composites Science and Technology 2007;67:501–6.

[84] Tomblin J, Senevirante W, Escobar P, Yap Y-K. Fatigue and Stress Relaxation of Adhesives in Bonded Joints. 2003.

[85] Hariharan K, Majidi O, Kim C, Lee MG, Barlat F. Stress relaxation and its effect on tensile deformation of steels. Materials & Design 2013;52:284–8.

[86] Delhomme F, Debicki G, Chaib Z. Experimental behaviour of anchor bolts under pullout and relaxation tests. Construction and Building Materials 2010;24:266–74.

[87] Delhomme F, Debicki G. Numerical modelling of anchor bolts under pullout and relaxation tests. Construction and Building Materials 2010;24:1232–8.

[88] Majó JAM. Estudio constitutivo de materiales compuestos laminados sometidos a cargas cíclicas. 2003.

[89] Ashcroft IA. Fatigue. In: Adams RD, editor. Adhesive bonding: Science, technology and applications, Woodhead publishing limited and CRC press LLC; 2005, p. 209–39.

[90] Crocombe AD, Richardson G. Assessing stress state and mean load effects on the fatigue response of adhesively bonded joints. International Journal of Adhesion and Adhesives 1999;19:19–27.

[91] Quaresimin M, Ricotta M. Life prediction of bonded joints in composite materials. International Journal of Fatigue 2006;28:1166–76.

[92] Khoramishad H, Crocombe AD, Katnam KB, Ashcroft IA. Fatigue damage modelling of adhesively bonded joints under variable amplitude loading using a cohesive zone model. Engineering Fracture Mechanics 2011;78:3212–25.

[93] Khoramishad H, Crocombe AD, Katnam KB, Ashcroft IA. A generalised damage model for constant amplitude fatigue loading of adhesively bonded joints. International Journal of Adhesion and Adhesives 2010;30:513–21.

[94] Khoramishad H, Crocombe AD, Katnam KB, Ashcroft IA. Predicting fatigue damage in adhesively bonded joints using a cohesive zone model. International Journal of Fatigue 2010;32:1146–58.

[95] Graner Solana A, Crocombe AD, Ashcroft IA. Fatigue life and backface strain predictions in adhesively bonded joints. International Journal of Adhesion and Adhesives 2010;30:36–42.

[96] Quaresimin M, Ricotta M. Fatigue behaviour and damage evolution of single lap bonded joints in composite material. Composites Science and Technology 2006;66:176–87.

[97] Quaresimin M, Ricotta M. Stress intensity factors and strain energy release rates in single lap bonded joints in composite materials. Composites Science and Technology 2006;66:647–56.

[98] Gilbert CJ, Dauskardt RH, Ritchie RO. Microstructural mechanisms of cyclic propagation in grain-bridging ceramics. Ceramics International 1997;23:413–8.

[99] Xu G, Argon AS, Ortiz M. Nucleation of dislocations from crack tips under mixed mode of loading: implications for brittle against ductile behaviour of crystals. Philosophical Magazine A 1995;72:415–51.

[100] Maiti S, Geubelle PH. A cohesive model for fatigue failure of polymers. Engineering Fracture Mechanics 2005;72:691–708.

[101] Nguyen O, Repetto EA, Ortiz M, Radovitzky RA. A cohesive model of fatigue crack growth. International Journal of Fracture 2001;110:351–69.

[102] L. Taerwe, S. Matthy. FRP for Concrete Construction: Activities in Europe. Concrete International 1999;21:33–6.

[103] Taerwe L, Matthys S. Use of FRP in concrete structures: Trends and challenges. Symposium PAGUE 2011, 2011, p. 1071–84.

[104] Fukuyama H. FRP Composites in Japan. Concrete International 1999;21:29–32.

[105] Iyer SL, Kumarswamy C. Performance evaluation of Glass Fiber Composite Cable for prestressing concrete units. Proceedings of the Thirty Third International SAMPE Symposium, 1988, p. 844–57.

[106] Iyer SL. First composite cable prestressed bridge in the USA. Proceedings of the Thirty-Eight International SAMPE Symposium, 1993, p. 1766–1764.

[107] Sen R, Issa M, Mariscal D. Feasibility of fiberglass pretensioned piles in a marine environment. 1992.

[108] Dolan CW. Developments in non-metallic prestessing tendons. Prestressed Concrete Institute 1990:80–8.

[109] Dolan CW, Hamilton HR, Bakis CE, Nanni A. Design recommendations for concrete structures restressed with FRP tendons. 2001.

[110] Micelli F, Nanni A. Durability of FRP rods for concrete structures. Construction and Building Materials 2004;18:491–503.

[111] Grace N, Collavino L, Navarre FC, Nacey RB, Bonus W. Design-Construction of Bridge Street Bridge – First CFRP Bridge in the United States. 2002.

[112] Grace N, Roller JJ, Navarre FC, Nacey RB, Bonus W. Load testing a CFRP reinforced bridge. Concrete International 2004:1–7.

[113] BASF Construction Chemicals BS. MBrace Laminate - Product information. 2009.

[114] BASF Construction Chemicals BS. MBar Galileo - Product information. 2009.

[115] Hughes-Brothers. Aslan FRP Series - Fiberglass Rebar - Product information. 2010.

[116] ASTM-D3165. Standard test method for strength properties of adhesives in shear by tension loading of Single-Lap-Joint laminated assemblies 2007;02:4.

[117] BASF Construction Chemicals BS. MBrace Primer - Product information. 2008.

[118] ASTM-D3528. Standard test method for strength properties of double lap shear adhesive joints by tension loading 2002;96:4.

[119] BASF Construction Chemicals BS. Concresive1360 - Product information. 2008.

[120] BASF Construction Chemicals BS. MBrace Adhesivo - Product information. 2008.

[121] 440.3R-04 A. Guide Test Methods for Fiber-Reinforced Polymers (FRPs) for Reinforcing or Strengthening Concrete Structures. ACI 2004:1–40.

[122] Adhesives PS. Plexus MA300 - Porduct information. 2011.

[123] Adhesives PS. Plexus MA420 - Porduct information. 2011.

[124] Resoltech ATR. Resoltech 3050C & 3050CT - Porduct information. 2011.

[125] Huntsman. Araldite 2011 - Porduct information. 2011.

[126] Huntsman. Araldite 2029 - Porduct information. 2011.

[127] Resoltech ATR. Resoltech 3040 & 3045 - Porduct information. 2011.

[128] Scott-Bader SA. Crestabond M1-05 - Porduct information. 2011.

[129] Bennitz A. Externally Unbonded Post- Tensioned CFRP Tendons. Lulea University of Technology, 2011.

[130] Packham DE. Surface energy, surface topography and adhesion. International Journal of Adhesion and Adhesives 2003;23:437–48.

[131] Crocombe AD, Richardson G, Smith PA. Measuring hydro-static dependent constitutive behaviour of adhesives using a bend specimen. The Journal of Adhesion 1993;42:209–23.

[132] Crocombe AD, Richardson G, Smith PA. A unified approach for predicting the strength of cracked and non-cracked adhesive joints. The Journal of Adhesion 1995;49:211–44.

[133] M.N. C, G.D. D. Constitutive models and their data requirements for use in Finite Element Analysis of adhesives under impact loading. NPL Report CMMT(A) 1997;59.

[134] Camanho PP, Dávila CG. Mixed-mode decohesion finite elements for the simulation of delamination in composite materials. NASA Langley Research Center, TM-2002-211737, 2002, p. 42.

[135] Norton FH. The creep of steel at high temperatures. New York: McGraw-Hill book company; 1929.

[136] ASTM-D2294. Standard test method for creep properties of adhesives in shear by tension loading 2002;96:2.

[137] Puigvert F, Crocombe AD, Gil L. Static analysis of adhesively bonded anchorages for CFRP tendons. Construction and Building Materials 2014;61:206–15.

[138] R.P.Rudra. A curve fitting program to stress relaxation data. Canadian Agricultural Engineering 1987;29:209–11.

[139] Odegard GM, Bandyopadhyay a. Physical aging of epoxy polymers and their composites. Journal of Polymer Science Part B: Polymer Physics 2011;49:1695–716.

[140] Puigvert F, Crocombe AD, L.Gil. Fatigue and creep analyses of adhesively bonded anchorages for CFRP tendons. Accepted for Publication in International Journal of Adhesion and Adhesives 2014.

Appendix A. Analytical formulation for circular adhesive bonded joints

A.1 Analytical formulation

A theoretical solution for circular adhesively bonded joints are proposed in this annex. In this formulation, the adhesive layer was considered to carry only shear stresses needed to transfer the longitudinal forces from the inner (FRP tendon) to the outer (steel housing) adherents. However, linear shear and normal stress distributions through the thickness of the adherents were adopted. Figure A.1 shows the configuration and material parameters of the adhesive anchor.

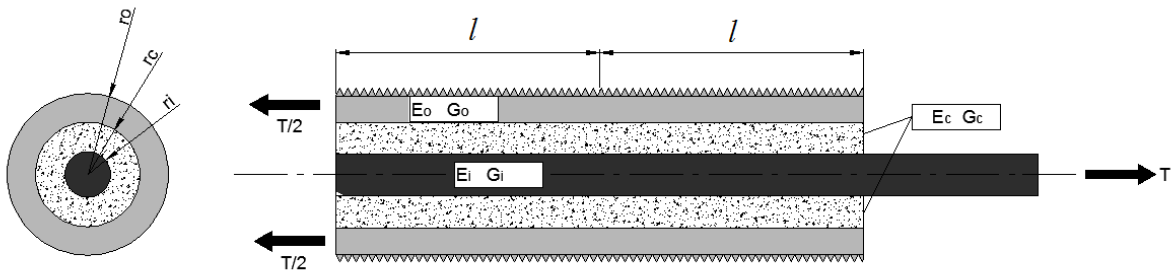

Figure A.1. Configuration bond-type anchorage.

E_0 Elastic modulus in the longitudinal direction of the outer adherent (steel housing).

G_0 Shear modulus in the longitudinal direction of the outer adherent (steel housing).

E_c Elastic modulus in the longitudinal direction of the adhesive.

G_c Shear modulus in the longitudinal direction of the adhesive.

E_i Elastic modulus in the longitudinal direction of the inner adherent (FRP tendon).

G_i Shear modulus in the longitudinal direction of the inner adherent (FRP tendon).

r_o Outer radius of the steel housing.

r_c Outer radius of the adhesive layer.

r_i Outer radius of the FRP tendon.

T Longitudinal forces acting at the outer and inner adherents.

l Bonded length. The bonded length is considered *2l.*

Figure A.2 shows a differential element of the bonded joint. Due to its symmetry, only half of the anchor was considered. In each material element the equilibrium must be balanced according to Equation A.1.

$$\sum F_x = 0 \qquad \text{(Equation A.1)}$$

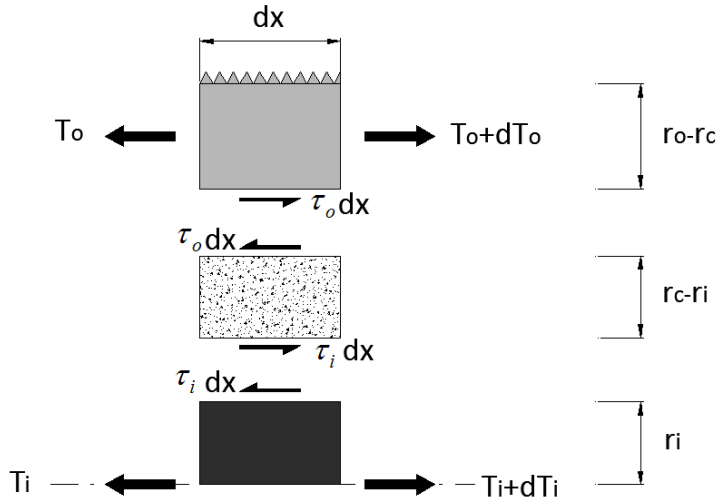

Figure A.2. Geometry and parameters for the basic elements.

The equilibrium equations for the basic elements of the outer and inner adherents can be written as follows:

$$\frac{dT_o}{dx} + \tau_o \cdot 2 \cdot \pi \cdot r_c = 0 \qquad \text{(Equation A.2)} \qquad \frac{dT_i}{dx} - \tau_i \cdot 2 \cdot \pi \cdot r_i = 0 \qquad \text{(Equation A.3)}$$

where T_o and T_i represent the longitudinal forces per unit of width acting on the adherents. In addition, the balance in the adhesive element leads to the Equation A.4.

$$\tau_i \cdot 2 \cdot \pi \cdot r_i \cdot dx = \tau_o \cdot 2 \cdot \pi \cdot r_c \cdot dx \qquad \text{(Equation A.4)} \qquad \text{therefore} \rightarrow \quad \tau_o = \tau_i \cdot \frac{r_i}{r_c} \qquad \text{(Equation A.5)}$$

Equation A.5 is used to rewrite Equation A.2 and allows for the writing of differential equations of equilibrium (Equations A.2 and A.3) based on the same value of inner shear stress, τ_i. This stress was considered more significant because it acts on the surface with less area and thereby with higher shear stresses.

$$\frac{dT_o}{dx} + \tau_i \cdot 2 \cdot \pi \cdot r_i = 0 \qquad \text{(Equation A.6)}$$

Therefore, the differential equations of equilibrium that will be used to determine the shear stress distribution on the tendon-adhesive interface are Equations A.6 and A.3.

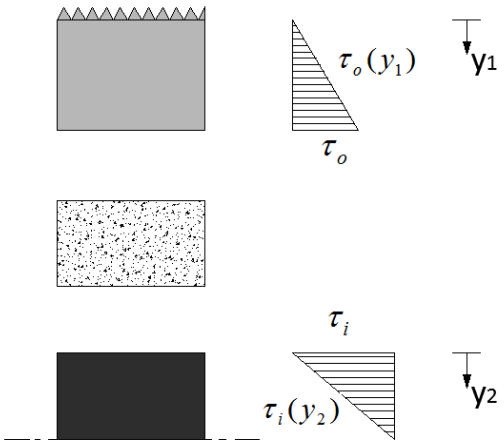

Figure A.3. Shear stress distribution through the thickness of adherents.

According to the hypothesis of Tsai, Oplinger and Morton, the shear stress distribution was considered linear along the thickness of the steel housing and tendon as shown in Figure A.3. Therefore, τ_0 represents the maximum shear stress for the outer adherent and τ_i represents the maximum shear stress for the inner adherent. Due to the circular geometry of the anchor, the maximum shear stress for the adherents are different between them. Thus, the shear stresses for the adherents can be expressed as:

$$\tau_o(y_1) = \frac{\tau_o}{(r_o - r_i)} \cdot y_1 \qquad \text{(Equation A.7)} \qquad \tau_i(y_2) = \tau_i \cdot \left(1 - \frac{y_2}{r_i}\right) \qquad \text{(Equation A.8)}$$

where y_1 and y_2 are a local coordinate system with the origin at the top surface of the outer and inner adherents, respectively. In the inner adherent, the shear stress will be zero when y_2 is r_i and maximum when y_2 is zero. In the outer adherent, the shear stress will be zero when y_1 is zero and maximum on the adhesive-outer adherent interface.

As mentioned earlier, Equations A.7 and A.8 can be written in function of the inner shear stress. Therefore, Equation A.7 can be rewritten using Equation A.5.

$$\tau_o(y_1) = \frac{\tau_i \cdot r_i}{r_o \cdot (r_o - r_i)} \cdot y_1 \qquad \text{(Equation A.9)}$$

Moreover, a linear material constitutive relationship for the adherents was considered where the constitutive equations are determined by the Equation A.10.

$$\sigma_{ij} = C_{ijkl} \cdot \varepsilon_{kl} \qquad \text{(Equation A.10)}$$

where σ_{ij} is the stress tensor, C_{ijkl} is the elastic constitutive tensor and ε_{ij} is the strain tensor. Considering the shear component of the constitutive equation (see Equation A.11), it is possible to rewrite Equations A.8 and 9 in function of the shear strain of the outer and inner adherents.

$$\tau = G \cdot \gamma \qquad \text{(Equation A.11)}$$

where G and γ are the shear modulus and the shear strain in the longitudinal direction, respectively.

$$\gamma_i(y_2) = \frac{\tau_i}{G_i} \cdot \left(1 - \frac{y_2}{r_i}\right) \qquad \text{(Equation A.12)} \qquad \gamma_o(y_1) = \frac{\tau_i \cdot r_i}{G_o \cdot r_o \cdot (r_o - r_c)} \cdot y_1 \qquad \text{(Equation A.13)}$$

The longitudinal displacement functions for the outer and inner adherents are shown in Figure A.4.

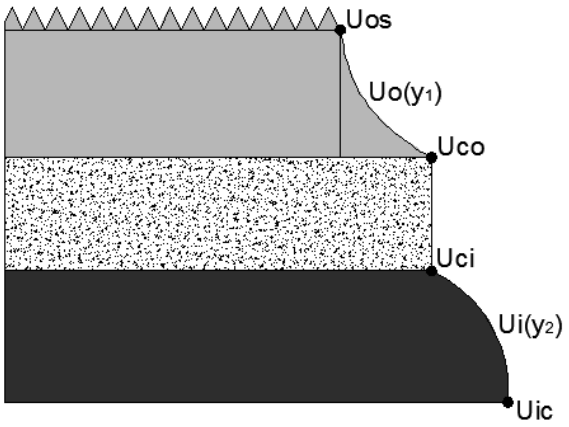

Figure A.4. Longitudinal displacement of the materials involved in the adhesive bond

The longitudinal displacement of the outer adherent, $u_o(y_1)$, can be expressed as follows:

$$u_o(y_1) = u_{co} = u_{os} + \int_0^{y_1} \gamma_o(y_1)\, dy_1 \qquad \text{(Equation A.14)}$$

where u_{os} is the displacement at the top of the outer adherent, u_{co} is the displacement at the bottom of the outer adherent and γ_o is the shear strain of the outer adherent. It is worth noting that a perfect bond among the elements was considered and therefore, the displacements are continuous on the interfaces. Consequently, the Equation A.15 is obtained by integrating and rearranging.

$$u_o(y_1) = u_{co} - \frac{r_i \cdot \tau_i \cdot (r_o - r_c)}{2 \cdot G_o \cdot r_o} + \frac{r_i \cdot \tau_i}{G_o \cdot r_o \cdot (r_o - r_c)} \cdot \frac{y_1^2}{2} \qquad \text{(Equation A.15)}$$

By means of the general theory of the elasticity, the longitudinal strain for the outer adherent, ε_{xxo}, can be obtained from the longitudinal displacement (see Equation A.16).

$$\varepsilon_{xxo} = \frac{du_o}{dx} = \frac{du_{co}}{dx} - \frac{d\tau_i}{dx} \cdot \frac{r_i \cdot (r_o - r_c)}{2 \cdot G_o \cdot r_o} + \frac{d\tau_i}{dx} \cdot \frac{r_i}{2 \cdot G_o \cdot r_o \cdot (r_o - r_c)} \cdot y_1^2 \qquad \text{(Equation A.16)}$$

In the same way, the longitudinal displacement of the inner adherent, $u_i(y_2)$, can be expressed as shown in Equation A.17.

$$u_i(y_2) = u_{ci} + \int_0^{y_2} \gamma_i(y_2)\ dy_2 \qquad \text{(Equation A.17)}$$

where u_{ci} represents the displacement at the top of the inner adherent and γ_i represents the shear strain for the inner adherent. By integrating and rearranging, Equation A.18 is obtained.

$$u_i(y_2) = u_{ci} + \frac{\tau_i}{G_i} \cdot \left(y_2 - \frac{y_2^2}{2 \cdot r_i} \right) \qquad \text{(Equation A.18)}$$

By differentiating Equation A.18 with respect to x, the longitudinal strain in the inner adherent can be found, ε_{xxi}.

$$\varepsilon_{xxi} = \frac{du_i}{dx} = \frac{du_{ci}}{dx} + \frac{d\tau_i}{dx} \cdot \frac{1}{G_i} \cdot \left(y_2 - \frac{y_2^2}{2 \cdot r_i} \right) \qquad \text{(Equation A.19)}$$

Moreover, the longitudinal resultant forces acting in the outer, T_o, and inner, T_i, adherents can be written as follows:

$$T_o = \int \sigma_o\ dA = \int_{r_c}^{r_o} \int_0^{2\pi} \sigma_o \cdot r\, d\theta\, dy_1 \qquad \text{(Equation A.20)}$$

$$T_i = \int \sigma_i\ dA = \int_0^{r_i} \int_0^{2\pi} \sigma_i \cdot r\, d\theta\, dy_2 \qquad \text{(Equation A.21)}$$

where σ_o represents the longitudinal normal stress for the steel housing and σ_i represents the longitudinal normal stress for the tendon. It is worth mentioning that both equations consider the circular geometry of the anchor. Also, Equations A.16 and A.19 can be introduced into the longitudinal normal strains of Equations A.20 and A.21 respectively, by previously transforming the longitudinal normal stresses into functions of normal strains. By integrating and rearranging, the longitudinal resultant forces expressed in Equations A.20 and A.21 can then be formulated in function of the longitudinal normal strains (see Equations A.22 and A.23).

$$\frac{du_{co}}{dx} = \frac{T_o}{\pi \cdot E_o \cdot \left(r_o^{\,2} - r_c^{\,2} \right)} + \frac{d\tau_i}{dx} \cdot \frac{1}{\left(r_o^{\,2} - r_c^{\,2} \right)} \cdot \left[\frac{r_i \cdot (r_o - r_c) \cdot \left(r_o^{\,2} - r_c^{\,2} \right)}{2 \cdot G_o \cdot r_o} - \frac{r_i \cdot \left(r_o^{\,4} - r_c^{\,4} \right)}{4 \cdot G_o \cdot r_o \cdot (r_o - r_c)} \right] \qquad \text{(Equation A.22)}$$

$$\frac{du_{ci}}{dx} = \frac{T_i}{\pi \cdot E_i \cdot r_i^2} - \frac{d\tau_i}{dx} \cdot \frac{5 \cdot r_i}{12 \cdot G_i} \qquad \text{(Equation A.23)}$$

Considering the adhesive as a thermosetting polymer with a low viscosity behaviour for short-term loading applications, the adhesive shear strain, γ_c, can be defined linearly as shown in Equation A.24 (see Figure A.5).

$$\gamma_c = \frac{1}{(r_c - r_i)} \cdot (u_{ci} - u_{co}) \qquad \text{(Equation A.24)}$$

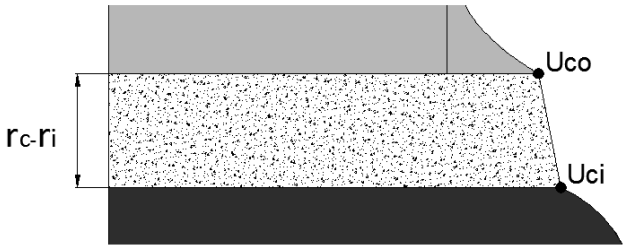

Figure A.5. Longitudinal displacement of the adhesive.

Consequently:

$$\tau_i = \frac{G_c}{(r_c - r_i)} \cdot (u_{ci} - u_{co}) \qquad \text{(Equation A.25)}$$

By differentiating Equation A.25 with respect to *x*,

$$\frac{d\tau_i}{dx} = \frac{G_c}{(r_c - r_i)} \cdot \left(\frac{du_{ci}}{dx} - \frac{du_{co}}{dx} \right) \qquad \text{(Equation A.26)}$$

By substituting Equations A.22 and A.23 (longitudinal normal stresses) into the Equation A.26, the equation becomes,

$$\frac{d\tau_i}{dx} = \frac{G_c}{(r_c - r_i)} \cdot \left(\frac{T_i}{\pi \cdot E_i \cdot r_i^2} - \frac{d\tau_i}{dx} \cdot \frac{5 \cdot r_i}{12 \cdot G_i} - \frac{T_o}{\pi \cdot E_o \cdot (r_o^2 - r_c^2)} \right.$$

$$\left. - \frac{d\tau_i}{dx} \cdot \frac{1}{(r_o^2 - r_c^2)} \cdot \left[\frac{r_i \cdot (r_o - r_c) \cdot (r_o^2 - r_c^2)}{2 \cdot G_o \cdot r_o} - \frac{r_i \cdot (r_o^4 - r_c^4)}{4 \cdot G_o \cdot r_o \cdot (r_o - r_c)} \right] \right) \qquad \text{(Equation A.27)}$$

By differentiating again with respect to x,

$$\frac{d^2\tau_i}{dx^2}=\frac{\frac{G_c}{(r_c-r_i)}\cdot\left(\frac{dT_i}{dx}\cdot\frac{1}{\pi\cdot E_i\cdot r_i^2}-\frac{dT_o}{dx}\cdot\frac{1}{\pi\cdot E_o\cdot\left(r_o^2-r_c^2\right)}\right)}{1+\frac{G_c}{(r_c-r_i)}\cdot\left[\frac{5\cdot r_i}{12\cdot G_i}+\frac{1}{\left(r_o^2-r_c^2\right)}\cdot\left(\frac{r_i\cdot(r_o-r_c)\cdot\left(r_o^2-r_c^2\right)}{2\cdot G_o\cdot r_o}-\frac{r_i\cdot\left(r_o^4-r_c^4\right)}{4\cdot G_o\cdot r_o\cdot(r_o-r_c)}\right)\right]} \qquad \text{(Equation A.28)}$$

By substituting the equilibrium differential Equations A.3 and A.6 into the Equation A.28, Equation A.29 is obtained:

$$\frac{d^2\tau_i}{dx^2}=\frac{\frac{G_c\cdot r_i}{(r_c-r_i)}\cdot\left(\frac{2}{E_i\cdot r_i^2}+\frac{2}{E_o\cdot\left(r_o^2-r_c^2\right)}\right)}{1+\frac{G_c}{(r_c-r_i)}\cdot\left[\frac{5\cdot r_i}{12\cdot G_i}+\frac{1}{\left(r_o^2-r_c^2\right)}\cdot\left(\frac{r_i\cdot(r_o-r_c)\cdot\left(r_o^2-r_c^2\right)}{2\cdot G_o\cdot r_o}-\frac{r_i\cdot\left(r_o^4-r_c^4\right)}{4\cdot G_o\cdot r_o\cdot(r_o-r_c)}\right)\right]}\cdot\tau_i$$

(Equation A.29)

Equation A.29 can be written as follows,

$$\frac{d^2\tau_i}{dx^2}-\beta^2\cdot\tau_i=0 \qquad \text{(Equation A.30)}$$

where,

$$\beta^2=\frac{\frac{G_c\cdot r_i}{(r_c-r_i)}\cdot\left(\frac{2}{E_i\cdot r_i^2}+\frac{2}{E_o\cdot\left(r_o^2-r_c^2\right)}\right)}{1+\frac{G_c}{(r_c-r_i)}\cdot\left[\frac{5\cdot r_i}{12\cdot G_i}+\frac{1}{\left(r_o^2-r_c^2\right)}\cdot\left(\frac{r_i\cdot(r_o-r_c)\cdot\left(r_o^2-r_c^2\right)}{2\cdot G_o\cdot r_o}-\frac{r_i\cdot\left(r_o^4-r_c^4\right)}{4\cdot G_o\cdot r_o\cdot(r_o-r_c)}\right)\right]} \qquad \text{(Equation A.31)}$$

And the general solution for the Equation A.30 is,

$$\tau_i=A\cdot Sinh(\beta\cdot x)+B\cdot Cosh(\beta\cdot x) \qquad \text{(Equation A.32)}$$

Equation A.32 allows for the shear stress distribution along the tendon-adhesive interface at a given load to be obtained, where *A* and *B* are coefficients which depend on the boundary conditions. For circular adhesively bonded anchors, the boundary conditions depend on the stressing system.

Moreover the average shear stress on the tendon-adhesive interface, τ_{mi}, can be defined as shown in Equation A.33.

$$\tau_{mi}=\frac{T}{A}=\frac{1}{2\cdot\pi\cdot r_i\cdot 2\cdot l}\cdot\int_0^{2\pi}\int_{-l}^{+l}\tau_i\cdot r_i\ d\theta\, dz=\frac{T}{4\cdot\pi\cdot r_i\cdot l} \qquad \text{(Equation A.33)}$$

A.2 Pull-Pull model

Boundary conditions for a pull-pull model are shown in Figure A.6 and Equations A.34a and A.34b.

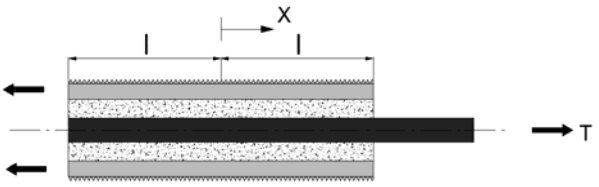

Figure A.6. Pull-Pull model.

$T_o = 0 \qquad T_i = +2\cdot\pi\cdot r_i\cdot 2\cdot l\cdot\tau_{mi} \qquad$ when $x = l$ (Equation A.34a)

$T_o = +2\cdot\pi\cdot r_i\cdot 2\cdot l\cdot\tau_{mi} \qquad T_i = 0 \qquad$ when $x = -l$ (Equation A.34b)

The coefficient B is obtained by introducing Equation A.32 into the shear stress of Equation A.33 and integrating as shown in Equations A.35 and A.36.

$$\frac{1}{2\cdot\pi\cdot r_i\cdot 2\cdot c}\cdot\int_0^{2\pi}\int_{-l}^{+l}\left[A\cdot Sinh(\beta\cdot x)+B\cdot Cosh(\beta\cdot x)\right]\cdot r_i\ dx\,d\theta = \tau_{mi} \qquad \text{(Equation A.35)}$$

$$\frac{1}{2\cdot c\cdot\beta}\cdot\left[A\cdot Sinh(\beta\cdot x)+B\cdot Cosh(\beta\cdot x)\right]_{-l}^{+l} = \tau_{mi} \qquad \text{(Equation A.36)}$$

By rearranging, the coefficient B results,

$$B = \frac{\tau_{mi}\cdot l\cdot\beta}{Sinh(\beta\cdot l)} \qquad \text{(Equation A.37)}$$

The coefficient A is obtained by differentiating Equation A.32 with respect to *x* and equating against Equation A.27, taking into account the boundary conditions equations (Equations A.34a and A.34b). By using the boundary conditions provided either by Equation A.34a or by Equation A.34b, the same value of coefficient A is obtained.

On one hand, differentiating Equation A.32 is provided in Equation A.38.

$$\frac{d\tau_i}{dx} = \beta\cdot A\cdot Cosh(\beta\cdot l)+\beta\cdot B\cdot Sinh(\beta\cdot l) \qquad \text{(Equation A.38)}$$

By substituting the coefficient B (see Equation A.37) into the Equation A.38,

$$\frac{d\tau_i}{dx} = \beta\cdot A\cdot Cosh(\beta\cdot x)+\beta^2\cdot l\cdot\tau_{mi} \qquad \text{(Equation A.39)}$$

On the other hand, Equation A.40 is obtained by applying the boundary condition equations into Equation A.27. In this case, the boundary condition of Equation A.34a was used.

$$\frac{d\tau_i}{dx}=\frac{\dfrac{G_c\cdot r_i}{(r_c-r_i)}\cdot\left(\dfrac{4}{E_i\cdot r_i^{\,2}}\right)}{1+\dfrac{G_c}{(r_c-r_i)}\cdot\left[\dfrac{5\cdot r_i}{12\cdot G_i}+\dfrac{1}{\left(r_o^{\,2}-r_c^{\,2}\right)}\cdot\left(\dfrac{r_i\cdot(r_o-r_c)\cdot\left(r_o^{\,2}-r_c^{\,2}\right)}{2\cdot G_o\cdot r_o}-\dfrac{r_i\cdot\left(r_o^{\,4}-r_c^{\,4}\right)}{4\cdot G_o\cdot r_o\cdot(r_o-r_c)}\right)\right]}\cdot l\cdot\tau_{mi} \qquad \text{(Equation A.40)}$$

By equating and rearranging Equation A.39 against Equation A.40, the coefficient A can be found (see Equation A.41).

$$A=\frac{\beta\cdot l\cdot\tau_{mi}}{Cosh(\beta\cdot x)}\cdot\left(\frac{1-\dfrac{E_i\cdot r_i^{\,2}}{E_o\cdot\left(r_o^{\,2}-r_c^{\,2}\right)}}{1+\dfrac{E_i\cdot r_i^{\,2}}{E_o\cdot\left(r_o^{\,2}-r_c^{\,2}\right)}}\right) \qquad \text{(Equation A.41)}$$

A.3 Pull-Push model

Boundary conditions for a pull-push model are shown in Figure A.7 and Equations A.42a and A.42b.

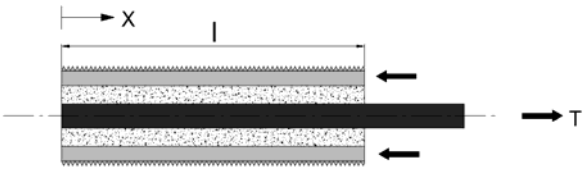

Figure A.7. Pull-Push model.

$T_o=-2\cdot\pi\cdot r_i\cdot 2\cdot l\cdot\tau_{mi}$ $\quad T_i=+2\cdot\pi\cdot r_i\cdot 2\cdot l\cdot\tau_{mi}$ when $x=+l$ (Equation A.42a)

$T_o=0$ $\quad T_i=0$ when $x=-l$ (Equation A.42b)

As mentioned in the pull-pull model, the coefficient B is obtained by introducing Equation A.32 into the shear stress of Equation A.33 and integrating. Hence, the same equation as the pull-pull model allows obtaining the coefficient B.

The same process as used in the pull-pull model is needed to find the coefficient A. This can be found by differentiating Equation A.32 with respect to *x* (through the same process as the pull-pull model) and equating against Equation A.27, taking into account the boundary conditions equations (Equations A.42a and A.42b). As mentioned before, by using the boundary conditions provided either by Equation A.42a or by Equation A.42b, the same value of coefficient A is obtained. In this case, the boundary condition of Equation A.42a was substituted into Equation A.27 and Equation A.43 was obtained.

$$\frac{d\tau_i}{dx}=\frac{\frac{G_c\cdot r_i}{(r_c-r_i)}\cdot\left(\frac{4}{E_i\cdot r_i^{\,2}}+\frac{4}{E_o\cdot\left(r_o^{\,2}-r_c^{\,2}\right)}\right)}{1+\frac{G_c}{(r_c-r_i)}\cdot\left[\frac{5\cdot r_i}{12\cdot G_i}+\frac{1}{\left(r_o^{\,2}-r_c^{\,2}\right)}\cdot\left(\frac{r_i\cdot(r_o-r_c)\cdot\left(r_o^{\,2}-r_c^{\,2}\right)}{2\cdot G_o\cdot r_o}-\frac{r_i\cdot\left(r_o^{\,4}-r_c^{\,4}\right)}{4\cdot G_o\cdot r_o\cdot(r_o-r_c)}\right)\right]}\cdot l\cdot\tau_{mi} \qquad \text{(Equation A.43)}$$

By equating and rearranging Equation A.39 against Equation A.43, the coefficient A can be found (see Equation A.44).

$$A=\frac{\beta\cdot l\cdot\tau_{mi}}{Cosh\left(\beta\cdot l\right)} \qquad \text{(Equation A.44)}$$